The role of the neuronal environment in neurodevelopment and circuit formation in Tuberous Sclerosis Complex



Paula Rocktäschel

St Cross College

University of Oxford

A thesis submitted for the degree of

Doctor of Philosophy

Hillary 2023

Abstract

Background: *Tuberous Sclerosis Complex (TSC)* results from *TSC1* or *TSC2* gene mutations with hyperactivation of the *mechanistic target of rapamycin complex 1 (mTORC1)*. TSC is characterised by benign hamartomas in multiple organs including the brain and neurological symptoms are often amongst the most severe and disabling manifestations. Cortical tubers, histologically characterised by disturbed cortical lamination, dysmorphic neurons, and extensive gliosis, are typical brain tumours in TSC that have been implicated in the generation of seizures.

MTORC1 is a main regulator of cellular metabolism in response to energy and nutrients supply. Malfunctioning of the TSC1:TSC2-mTORC1 pathway can disturb cellular metabolic homeostasis with severe consequences to cellular survival, proliferation, and differentiation. However, the exact impact of mTORC1 hyperactivation on the development of cortical tubers in TSC remains unclear and previous studies demonstrated evidence that tuberigenesis is likely caused by non-genetic factors in addition to disturbances of the TSC1:TSC2-mTORC1 axis.

Aims: In my DPhil project, I examined the impact of extragenetic factors on the development of cortical tubers in TSC. I chose one non-cellular and one cellular factor, namely the availability of extracellular glucose and co-culturing with TSC2-deficient astrocytes, due to two reasons: (i) mTORC1 contributes to cellular energy and glucose metabolism and (ii) elevated levels of potentially malfunctioning astrocytes are a main feature of cortical tubers *in vivo*.

Methods: I used *in vitro* stem cell-derived glial and neuronal cultures to model neurodevelopment and neuronal circuit formation in TSC. Further, I applied a Bayesian computational modelling tool, *dynamic causal modeling (DCM)*, to multi-electrode array (MEA)

recordings from neuronal cultures to extract information on the synaptic foundation of neuronal connectivity in TSC.

Results: *In vitro*, TSC2 deficiency causes developmental disturbances in neural stem cells (NSC) such as prolonged and increased stem cell renewal as well as transcriptional changes in neurons implicating reduced maturity and a tendency towards gliogenesis. However, these changes did not resemble a full cortical tuber-like picture as the late-stage transcriptional abnormalities did not manifest on the protein level.
Limiting cellular glucose supply drives TSC2-deficient neuronal cultures to develop a cortical tuber-like picture including an increased glia-to-neuron ratio and impaired neurogenesis. Glucose deprivation reduces the ability to produce energy through glycolysis and mitochondrial respiration in NSCs with different compensatory coping strategies in TSC2 +/+ and TSC2 -/- cells. TSC2-deficient NSCs upregulate important glycolytic genes such as hexokinase II and lactate dehydrogenase B but fail to activate mitochondrial metabolism. These changes might induce a tendency for proliferation and abnormal survival limiting their neurogenic potential as their transcriptional state in glucose deprivation resembles a cancerous metabolism.
Lastly, I use DCM on MEA data from *in vitro* TSC glio-neuronal co-cultures to examine the impact of astrocytes on neuronal connectivity. First, I demonstrate the suitability of DCM analysis for *in vitro* neuronal recordings in a proof-of-concept study. Second, DCM analysis of recordings from glio-neuronal co-cultures provides preliminary evidence that TSC2-deficient astrocytes increase the parameterised excitation-inhibition ratio in TSC2-deficient neurons.

Conclusion: My study provides evidence that non-genetic factors such as glucose supply and glial co-culture play an important role in the development of cortical tubers. Disturbances to the environment in which TSC2 -/- neurons develop impact their capacity to create healthy neuronal cultures opening up therapeutic strategies aimed at extracellular targets outside of the classic TSC1:TSC2-mTORC1 pathway.

Acknowledgements

I would like to thank my DPhil supervisors Prof Zameel Cader, Prof Arjune Sen, and Prof Rosalyn Moran for their support and guidance throughout the project. Thanks to Prof Cader for introducing the field of stem cell research to me and for your trust in my work. Thanks to Prof Sen for introducing me to the British community of epilepsy professionals and for all your encouragement over six long years. Thanks also to Prof Moran for helping me use Baye's wonderful mathematics to reveal some more secrets about our cells.
I thank everybody at the Cader Lab, especially Philippa Pettingill, Tatjana Lalic, Galbha Duggal, Satyan Chintawar, Tina Wei, Hannah Sleven, Kirk Reardon, Elena Burlacu, Bryan Adriaanse, Gabriel Rocha, David Kelly, Kanisa Arunasalam, and Despoina Charou, for their support and willingness to share insider knowledge and skills that helped me keep cells alive, rescue screwed-up blots, and light DNA.
I especially like to send a big hug to my dear friend and DPhil colleague Emma Mee Hayes. I am not sure how I would have stayed sane without you next to me in the lab and without our long walks and talks in times of sparse social contact. Thank you.
I am very grateful to my friends from the Akerman Lab, Sarah Newey and Anne Heedegard, for sharing their stem cell wisdom with me which made so many things so much easier.

Finally, I would like to thank my family, especially my parents, for their continuing support and for always providing a home where things are just as they should be – good, happy, and safe. *Von ganzem Herzen möchte ich meiner Familie, insobesodere meinen Eltern, danken. Vielen Dank, dass wir immer bei euch einfallen können und dass das Leben bei euch immer so ist, wie es sein soll – gut und einfach glücklich.*

Tim, thanks so much for all we have, they are worth more than anything.

Statement of Originality

I declare that the work presented in this thesis is entirely my own unless otherwise acknowledged. I conducted the work presented here between October 2016 and April 2023 at the University of Oxford, Nuffield Department of Neuroscience. The presented work was not, and will not be, submitted for the award of any other qualification or degree at the University of Oxford or any other institution.

The TSC2 +/+ and TSC2 -/- hES and NSC lines have been genetically engineered at Roche Hoffmann AG. The CRISPR/Cas9 line used in chapter 3 was created at Ben Davies Lab, University of Oxford. Lentiviral constructs used in my thesis were cloned at the WIMM Genome Engineering facility by Philip Hublitz.
The Seahorse experiments in chapter 4 have been performed at Richard Wade-Martin's lab with support and guidance from Brent Ryan and Sophie Morgan.
The DCM analysis in chapter 5 is based on previous computational models created by Prof Rosalyn Moran and colleagues. The cell culture work on control iPSCs for the proof-of-concept study as well as the MEA recordings from the derived neuronal cultures were kindly performed by Tina Liting Wei. The transcriptomics data on neuronal receptor subunit expression displayed in figure 5.4 were generated by colleagues in the Cader Lab prior to my project.

Contents

1 Introduction **1**

1.1 Tuberous Sclerosis Complex 4

1.1.1 Cortical tubers 8

1.2 The molecular pathways forming the basis for this thesis 13

1.2.1 The TSC1:TSC2-mechanistic target of rapamycin complex 1 (mTORC1) pathway 13

1.2.2 Energy-producing metabolism 15

1.3 Stem cell models 20

1.3.1 Stem cell models in neuroscience 20

1.3.2 Stem cell models of TSC 23

1.4 Aims 25

2 Material & Methods **27**

2.1 Ethic statement 27

2.2 Material 27

2.2.1 Cell lines 27

2.2.2 Cell culture materials 28

2.2.3 Constructs 29

2.2.4 Primary and secondary antibodies 30

2.2.5 Primers 30

2.2.6 Molecular biology kits 30

2.3 Cell culture methods and differentiation protocols 31

2.3.1 Human stem cell culture 31

Pluripotent stem cell culture 31

Neural stem cells 32

2.3.2 Neuronal differentiation . . . 33
Neurogenin 2 differentiation . . . 33
Neuronal differentiation via dual SMAD-inhibition. . . . 35
2.3.3 Glial differentiation . . . 37
2.3.4 Lipofection . . . 38
2.3.5 Gene knockdown using an inducible CRISPR/Cas9 induced pluripotent stem cells (iPSC) line . . . 39
Lentiviral transduction of inducible CRISPR/Cas9 iPSCs . . . 39
CRISPR/Cas9 induction . . . 39
2.4 Molecular biology methods . . . 39
2.4.1 Protein extraction . . . 39
2.4.2 DNA extraction . . . 40
2.4.3 RNA extraction and complementary DNA (cDNA) preparation . . . 41
2.4.4 Polymerase chain reaction (PCR) . . . 43
2.4.5 Quantitative reverse transcription polymerase chain reaction (qRT-PCR) . . . 45
2.4.6 Western Blotting . . . 46
2.4.7 Plasmid DNA purification . . . 48
2.4.8 Flow cytometry . . . 50
2.4.9 Immunofluorescence microscopy . . . 51
2.4.10 Colorimetric assays . . . 53
Protein quantification – Bicinchoninic acid (BCA) assay . . . 53
Celltox Green assay of cell death . . . 54
2.4.11 Seahorse experiments . . . 54
2.4.12 Growth curves and doubling time . . . 55
2.5 Multi-electrode array recordings . . . 56
2.6 Underlying biophysical model for DCM of MEA data . . . 56
2.7 Statistical analysis . . . 60

3 The impact of TSC2 on neural development **62**

3.1 Introduction . . . 62
3.2 Aims . . . 66

3.3 Results . . . 68
3.3.1 TSC2 +/+ and TSC2 -/- human embryonic stem cells (hES) and NSC lines. . . . 68
3.3.2 Cortical neuronal differentiation. . . . 74
Dual SMAD-inhibition . . . 75
Neurogenin 2 protocol . . . 84
3.3.3 Glial differentiation. . . . 88
3.3.4 Transient mTORC1 modification. . . . 91
3.3.5 Creation of additional TSC2-mutated stem cell lines. . . . 95
3.4 Discussion . . . 98

4 The impact of glucose/energy metabolism on neural development in TSC 107
4.1 Introduction . . . 107
4.2 Aims . . . 116
4.3 Results . . . 119
4.3.1 Glucose concentrations of different media . . . 119
4.3.2 Glucose deprivation does not affect NSC proliferation . . . 120
4.3.3 Impact of glucose deprivation on neuronal and glial development in TSC2-deficiency . . . 121
Neural differentiation in glucose deprivation. . . . 121
Potential causes for glucose-dependent disturbances in neural differentiation in TSC deficiency . . . 125
4.3.4 Dependency of mTORC1 activity on cell type, glucose supply, and TSC2 genotype . . . 130
4.3.5 Impact of glucose deprivation on energy metabolism in TSC2 +/+ and TSC2 -/- cultures . . . 135
Metabolic gene expression . . . 136
Functional assessment of energy metabolism . . . 139
4.4 Discussion . . . 144

5 The impact of astrocytes on effective connectivity in TSC 155
5.1 Introduction . . . 155
5.1.1 Assessing synaptic connectivity using DCM . . . 157

5.2 Aims . . . 165
5.3 Proof-of-concept study: Establishing DCM on stem cell-derived glio-neuronal co-cultures . . . 166
5.3.1 MEA recordings of a stem cell-derived cortical glio-neuronal co-culture. 167
5.3.2 Model construction. . . . 171
5.3.3 Bayesian model inversion. . . . 173
5.3.4 Generalised linear regression as statistical analysis. . . . 174
5.3.5 DCM on local field potential (LFP) data reveals network changes independent of spiking activity. . . . 177
5.3.6 Model validation. . . . 178
5.4 The impact of astrocytes on neuronal connectivity in TSC . . . 180
5.5 Discussion . . . 186

6 Discussion **192**
6.1 Summary of experimental findings . . . 192
6.2 Is TSC2 knockout sufficient to induce cortical malformation? . . . 193
6.3 Does glucose deprivation drive neuronal differentiation towards cortical malformation in TSC? . . . 199
6.4 Is there a link between energy metabolism and cortical malformation in glucose-deprived TSC2-insufficient neuronal cultures? . . . 202
6.5 Do astrocytes disturb neuronal connectivity in the context of TSC? . . . 204
6.6 Limitations and outlook . . . 206
6.7 Conclusions . . . 208

A Stem cell models in TSC **210**

B Cell culture materials **213**

C Antibodies **216**

D Primer sequences **218**

E Area bins **221**

F Seahorse Background **222**

G Bayes' Theorem and probabilistic inference. 225

H Dynamic Causal Modeling 227

Acronyms 228

Bibliography 231

List of Figures

1.1 Cortical development 2
1.2 Cortical histomorphology in Tuberous Sclerosis Complex (TSC). 9
1.3 The TSC1:TSC2-mTORC1 pathway. 13
1.4 Energy-producing pathways 16

3.1 Characterisation of TSC2 +/+ and TSC2 -/- hES and NSC lines. 69
3.2 Morphological characterisation of TSC2 +/+ and TSC2 -/- hES and NSCs. 71
3.3 Cellular identity of TSC2 +/+ and TSC2 -/- hES. 72
3.4 Cellular identity of TSC2 +/+ and TSC2 -/- Roche NSCs. 74
3.5 Neuronal cortical differentiation via dual SMAD-inhibition. 75
3.6 Rosette formation in neuronal cortical differentiation. 76
3.7 Neural stem cell pool in neuronal cortical differentiation via dual SMAD-inhibition. 78
3.8 Neuronal output in cortical differentiation via dual SMAD-inhibition. . . . 80
3.9 Glio-neuronal balance during cortical differentiation via dual SMAD-inhibition. 82
3.10 Neuronal cortical differentiation via forced neurogenin 2 (NGN2) expression 84
3.11 Neuronal output of the NGN2 differentiation protocol. 86
3.12 Characterisation of NGN2 differentiation in TSC2 +/+ and TSC2 -/- cultures. 86
3.13 STEMCELL Technologies astrocyte differentiation. 89
3.14 Derivation of TSC2 +/+ and TSC2 -/- astrocytes. 90
3.15 Modifications of mTORC1 activity. 92
3.16 Transient mTORC1 modification. 94
3.17 Creation of a TSC2 KO line using an inducible CRISPR/Cas9 system. . . 97

4.1 Downstream targets of mTORC1 109

4.2 Investigations into the effect of combined glucose deprivation and TSC deficiency on the link between disturbed neurodevelopment and energy metabolism 117
4.3 Glucose concentrations of different media 119
4.4 Proliferation of stable NSCs in low glucose media 120
4.5 Investigations into the effect of glucose deprivation combined with TSC deficiency on the link between disturbed neurodevelopment and energy metabolism. 121
4.6 Neuronal cortical differentiation in different glucose media 122
4.7 Impact of glucose deprivation on neuronal output in dual SMAD-inhibition 123
4.8 Investigations into the effect of glucose deprivation combined with TSC deficiency on the link between disturbed neurodevelopment and energy metabolism. 125
4.9 Effect of early glucose deprivation on neuronal output in NGN2 differentiation. 127
4.10 Effect of early glucose deprivation on expression of neuronal progenitor genes. 128
4.11 Effect of glucose deprivation on neuronal death 129
4.12 Investigations into the effect of glucose deprivation combined with TSC deficiency on the link between disturbed neurodevelopment and energy metabolism. 131
4.13 mTORC1 activity in different cell types depending on glucose supply . . . 132
4.14 Effect of rapamycin on mTORC1 activity in glucose-loaded and glucose-deprived NSCs 134
4.15 Investigations into the effect of glucose deprivation combined with TSC deficiency on the link between disturbed neurodevelopment and energy metabolism. 135
4.16 Transcriptomic experiments on genes involved in metabolic pathways . . . 136
4.17 Differently expressed metabolic genes in NSCs and NGN2 neurons 138
4.18 Glycolytic activity in TSC2 +/+ and TSC2 -/- neuronal cells. 142
4.19 Mitochondrial respiration in TSC2 +/+ and TSC2 -/- neuronal cells. . . . 143
4.20 Schematic overview of the metabolic response to glucose deprivation and TSC2 deficiency in NSCs and neurons 148
4.21 Simplified hypothesised mechanism for reduced neuronal output in glucose-deprived TSC2 -/- cultures. 151

5.1 Key steps in DCM analysis. 158
5.2 Principles of Bayesian inference in DCM analysis. 162
5.3 Establishing DCM on iPSC-derived glio-neuronal cultures. 166
5.4 Characteristics of iPSC-derived neuronal cultures. 168

5.5 Influence of γ-aminobutyric acid (GABA) on neuronal firing. 170
5.6 Canonical microcircuit model. 172
5.7 Model fit for GABA and control sources. 174
5.8 Results of the DCM proof-of-concept analysis. 176
5.9 Correlation between spiking parameters and DCM posteriors. 177
5.10 Evaluation of model validity. 179
5.11 Experimental layout for TSC2 glio-neuronal co-culture on MEA. 180
5.12 MEA analysis of TSC glio-neuronal co-cultures. 182
5.13 Modelled effect of TSC2 -/- astrocytes on neuronal connectivity. 183
5.14 Results of DCM analysis in TSC2 glio-neuronal co-cultures. 184
5.15 Model fit in TSC glio-neuronal co-cultures. 185

F.1 Schematic on Seahorse analysis of cellular metabolism. 223

List of Tables

1.1 Diagnosis criteria for TSC 7
1.2 Stem cell studies on TSC published before 2016. 24

2.1 Cell lines used in this study 27
2.2 Cell culture media 28
2.3 Viral constructs 29
2.4 Molecular biology kits 30
2.5 Plating densities of different cell types. 31
2.6 DCM Parameters 61

6.1 Stem cell studies on TSC. 197

A.1 Stem cell models of TSC; stem cell stage 211
A.2 Stem cell models of TSC; glial/neuronal stage 212

B.1 Growth factors, small molecules and media supplements 213
B.2 Coating materials 214
B.3 Detachment agents 214
B.4 Drugs 214
B.5 Other molecular biology agents 215

C.1 Primary antibodies 216
C.2 Secondary antibodies 217

1 | Introduction

The development of the human brain is one of the most fascinating processes in nature as it is not only beautifully orchestrated but also results in a remarkably complex, and for most parts still mysterious, organ. Attempts to discover neurodevelopment were, so far, challenged by the limited availability of developing and developed human brain tissue for research [207]. The advent of human pluripotent stem cells (hPSC) and hPSC-derived neural cells [256] was a turning point in neuroscientific research, especially for research concerning neurodevelopment, as it allows the derivation of a human brain *equivalent* in a laboratory dish for the first time.

Diseases of neurodevelopment, including autism spectrum disorders, epilepsy syndromes or intellectual disability, often have devastating consequences for the respective patient and their families and carers [261]. Understanding the pathological mechanisms underlying neurodevelopmental diseases is key to providing affected individuals with treatment which is the core motivation for all bio-medical research. In my DPhil project, I worked on the neurodevelopmental disorder *tuberous sclerosis complex* and the effect that non-genetic disturbances during neurodevelopment might play in its pathogenesis.

My project focuses on the neurodevelopmental mechanisms underlying the development of cortical tubers in patients with Tuberous Sclerosis Complex (TSC). I will investigate these mechanisms using *in vitro* glio-neuronal models derived from genetically modified hPSCs. The introduction will first give a brief overview of the basic principles of human

neurodevelopment after which I will introduce the neurodevelopmental disorder *tuberous sclerosis complex*. The following introductory section will discuss some critical cellular signalling pathways as my project focuses on molecular biological aspects of TSC. Finally, I will introduce stem cell-derived neuronal model systems highlighting their relevance for modern neuroscientific research in general and present previous stem cell-based studies on TSC in particular.

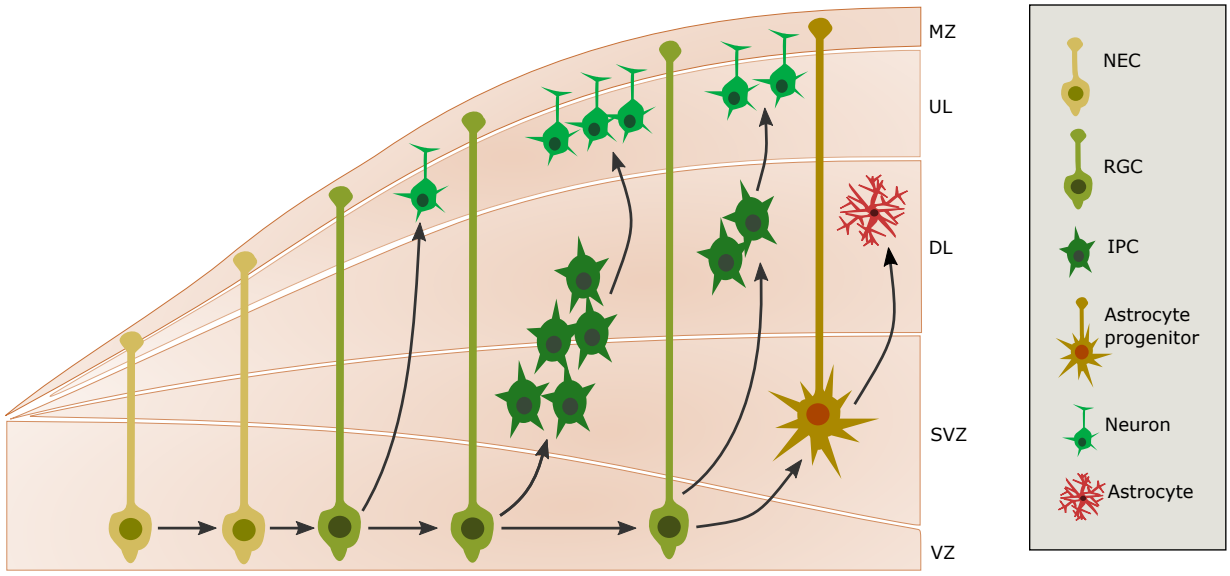


FIGURE 1.1: **Cortical development.** Different pools of neural stem cells build up the human brain inside-out through asymmetric and symmetric divisions. Neuroepithelial cells (NEC) first build the ventricular zone (VZ) and then transform into radial glial cells (RGC) whose proliferation enlarges the VZ and builds the subventricular zone (SBV), predominately through the production of intermediate progenitor cells (IPC). RGC and particularly IPC produce neurons that migrate along RGC processes to build the layered cortex. After neurogenesis, the remaining RGC pool forms the basis for astrogenesis.
MZ, molecular layer; UL, upper cortical layer; DL, deeper cortical layer; SVZ, subventricular zone; VZ, ventricular zone; NEC, neuroepithelial cell; RGC, radial glial cell; IPC, intermediate progenitor cell.

Human cortical development in brief. The structure of the developing brain differs fundamentally from the structure of the developed brain. The developing human brain undergoes enormous changes in its functional and anatomical organisation featuring various time-limited arrangements of dividing neural stem cells, migrating neurons, and emerging transient and more permanent synapses and connections between them (as illustrated in

figure 1.1) [31].

Human neurodevelopment is characterised by an explosive expansion in cell numbers resulting in a thick, layered cerebral cortex with rich folding. This expansion in neuronal numbers is made possible by the formation of multiple layers of neural stem cells (NSC) whose asymmetric and symmetric division with subsequent neuronal migration form the basis for a structured build-up of the human cortex in an inside-out manner [22].

Brain development starts with a single layer of neural epithelial cells (NEC) around the neural tube. As NEC proliferation enhances, the ventricular zone (VZ) emerges with increasing thickness and surface area, especially in the forebrain primordium [23]. Neurogenesis starts when the NEC pool transforms into radial glial cells (RGC) and immature neurons through asymmetric division [94, 191]. RGCs downregulate epithelial features while upregulating glial markers, mostly mediated by a set of genes including forkhead box G1 (FOXG1), LHX2, paired Box 6 (Pax6), and EMX2 [180]. However, RGCs further expand their apical processes to touch the pial surface and act as a guide wire for subsequent neuronal migration [25, 111, 135]. They are interconnected via adherens junctions expressing ZO-1 but lack intercellular tight junctions [1]. RGCs are the direct and indirect progenitors to most neurons and two main glia, oligodendrocytes and astrocytes [7, 159]. Most of their daughter cells are basal progenitors and other intermediate progenitor cells (IPC) that migrate away from the VZ forming the subventricular zone (SVZ) [192] which becomes distinguishable from the VZ after around 6 weeks of gestation [31]. The SVZ is characterised by a high diversity of progenitors including basal progenitors, IPCs, RGCs and outer radial glial cells (oRGC). Evidence suggests that the developmental reason for species-specific cortical characteristics lies within the SVZ as its structure, thickness, and complexity have increased during evolution and the human SVZ is significantly differently organised than rodent SVZ [22]. In fact, proliferation in human SVZ is so significant that

after gestational week 20, the SVZ can be divided into an inner and outer layer. The SVZ becomes the main source of neurogenesis with the contribution towards neurogenesis of progenitors from the VZ gradually decreasing until the VZ only comprises a thin one-cell layer band [22].

Between species, the number of neurons and the degree of cortical folding is a major outcome difference of cortical development [156]. In humans, the remarkable increase in neuronal number is presumably caused by increased NSC proliferation in different layers of the developing brain, particularly the human-specific outer SVZ that accommodates a variety of different NSCs including RGCs and IPCs [156].

The bulk of astrogenesis happens after neurogenesis from the remaining pool of NSCs. Prenatally, astrocytes are produced from RGCs in the SVZ [90]. Postnatally, they are born locally within the cortex due to the division of mature astrocytes and remain capable of mitosis even in adulthood [90].

1.1 Tuberous Sclerosis Complex

Tuberous sclerosis complex (TSC) is a neurodevelopmental disorder caused by inactivating mutations in either the TSC1 or TSC2 gene. Patients with TSC present with benign hamartomas in various organs such as the heart, brain, lungs, and kidneys as well as characteristic skin lesions. TSC affects approximately 2 Million people worldwide [49] and about 3,700 – 11,000 patients in the United Kingdom [266] with an estimated incidence of 1:6000 births [199].

Genetics. TSC is caused by mutations in either the TSC1 (OMIM #605284, 9q34.13) or TSC2 (OMIM #191092, 16p13.3) gene. The smaller TSC1 gene spans 23 exons over 53 kb [223] whereas the bigger TSC2 gene spans 43 kb over 42 exons [223] plus 2 additional, only

later discovered exons 1a and 1b. The TSC1:TSC2 complex is a main regulator for the mechanistic target of rapamycin complex 1 (mTORC1) which will be discussed in more detail in section 1.2.1. Inheritance of TSC follows an autosomal-dominant pattern, however, two-thirds of TSC cases arise from *de novo* germline mutations [229]. TSC2 mutations are overall more common with a TSC1:TSC2 ratio of approximately 1:3.5. Causes for this imbalance could include an ascertainment bias as TSC1 mutations produce a milder phenotype and thus, might be detected at a lower rate. Also, the higher accumulation of mutations within the TSC2 gene might be due to its larger size as well as an inherently higher mutation frequency [229]. In up to 15 % of TSC cases, no mutation in either the TSC1 or TSC2 gene can be identified (no mutation identified (NMI)) [229, 254].

As genetic screens for TSC1 or TSC2 mutations have become reliably available worldwide, pathogenic TSC1 or TSC2 mutations have been labelled as an independent diagnostic criterion sufficient for the diagnosis of TSC without further clinical evidence in the latest TSC diagnostic criteria catalogue in 2021 (see diagnostic criteria for TSC in figure 1.1) [193]. However, due to the 15 % of NMI patients, the absence of a pathogenic mutation is not an exclusion criterion for TSC.

TSC2 mutations translate into the most severe phenotype while TSC1 variants often present with milder symptoms and an even milder phenotype is found in NMI patients. TSC2 mutations are often associated with intellectual disability and renal angiomyolipoma (AML)s, both of which are rare with TSC1 variants [51, 229]. TSC2 mutations also increase the risk for intellectual disability [133], infantile spasms [133], and seizures [133]. Also, patients affected by a TSC2 mutation tend to present earlier in life [133].

Clinical presentation. TSC is a variable disorder that can affect almost every organ of the human body. Variations in severity, clinical features, and burden on the quality of life are high, even amongst related individuals or people with similar mutations. Peo-

ple with TSC develop highly angiogenic but often benign tumours, most commonly in the skin, brain, kidneys, lungs, and heart, and subsequently suffer from organ dysfunction when the normal tissue is replaced by cancerous cells [194]. The disease spectrum ranges from asymptomatic patients, only being identified through genetic testing as a relative of an identified patient with TSC, to severely affected patients presenting with intellectual disability, autism, and seizures starting in early infancy. Typical manifestations include lymphangioleiomyomatosis of the lungs, exclusively found in women [199], cardiac rhabdomyoma [244], and skin lesions such as hypomelanotic macules, angiofibromas, and shagreen patch [194]. The main causes of morbidity and mortality in patients with TSC are the expansion and malignant transformation of neural and renal lesions [10] as well as haemorrhage from a renal AML [47, 237]. Due to the varied nature of the disease, TSC has been widely underdiagnosed in the past [194]. Nowadays, diagnosis can be made clinically due to a combination of major and minor features as illustrated in table 1.1. Identification of pathogenetic TSC1 or TSC2 variants allows for an independent genetic diagnosis to be made, often for individuals detected during screenings for relatives. As the clinical presentation develops over time, this ensures appropriate surveillance and allows to detect disease manifestations as early as possible [193].

Neurological features such as autism, learning disability and seizures are often the most devastating and therapeutically challenging symptoms in TSC. Half of all patients with TSC present with developmental delay and intellectual disability and nearly all patients with TSC show at least one TSC-associated neuropsychiatric disorder (TAND) [136]. Nearly half of all patients with TSC exhibit intellectual disability [146], however, epilepsy is the most common neurological symptom in TSC [107]. Over 80 % of TSC patients develop seizures, often with onset in infancy[78].

In my study, I concentrated on neurological presentations as these are amongst the most

severe and disabling features of TSC. Three types of brain tumours have been identified in TSC, namely *cortical tubers*, *subependymal nodules*, and *subependymal giant cell astrocytomas (SEGAs)* [78]. My study focuses on the development of cortical tubers, thus a more detailed description will follow below.

The identification of either a TSC1 or TSC2 pathogenic mutation in DNA from normal tissue
OR
Definite diagnosis: Two major features or one major feature with ≥ 2 minor features
Possible diagnosis: Either one major feature or ≥ 2 minor features

Major features	Minor features
• Hypomelanotic macules (≥ 3, at least 5-mm diameter) • Angiofibromas (≥ 3) or fibrous cephalic plaque • Ungual fibromas (≥ 2) • Shagreen patch • Multiple retinal hamartomas • Cortical dysplasia (tubers and cerebral white matter radial migration lines) • Subependymal nodules (≥ 2) • Subependymal giant cell astrocytoma • Cardiac rhabdomyoma • Lymphangioleiomyomatosis • Angiomyolipomas (≥ 2)	• "Confetti" skin lesions • Dental enamel pits (> 2) • Intraoral fibromas (≥ 2) • Retinal achromic patch • Multiple renal cysts • Nonrenal hamartomas • Sclerotic bone lesions

TABLE 1.1: **Diagnosis criteria for TSC.** According to the International Tuberous Sclerosis Complex Consensus Conference 2021 [193]

1.1.1 Cortical tubers

Cortical tubers are focal cortical malformations that form due to disturbed neurodevelopment and present as circumscribed thickening of the cerebral or cerebellar cortex [78]. Tubers are characterised by loss of normal cortical lamination, dysmorphic neurons, extensive gliosis, and the existence of giant balloon cells [110]. Approximately 80-90 % of all patients with TSC have tubers, however, tuber load varies from just one to over 20 in the cerebral as well as in the cerebellar cortex [131]. No agreement between studies exists regarding mutation type and tuber burden. Some studies claimed an increased tuber burden with a TSC2 mutation [116] whereas others found similar tuber numbers for both mutated genes [133].

Histologically, cortical tubers are hypomyelinated hamartomas characterised by fewer and dysmorphic neurons, eosinophilic giant balloon cells, calcifications, and an excessive number of astrocytes [122]. Except for calcifications, which are unique to cortical tubers, they share these features with other types of malformation of cortical development (MCD), for example, focal cortical dysplasia (FCD) [11].

Figure 1.2 illustrates non-tuberal and tuberal cortex in TSC compared to the cellular organisation found in healthy individuals. The layered cortical structure is severely disturbed within tubers. Neuronal cell loss and abnormally expressed layer-specific markers can be found in all cortical layers within tubers but upper-layer neurons are notably more impaired suggesting that maturation is particularly affected in TSC [184]. Tuberal neurons further show functional markers of immaturity indicating that lack of development might contribute to tuberigenesis [226]. Various signs of neuronal dysmorphism have been observed in tubers such as abnormal orientation, cytomegaly, multiple nuclei or neurofibrillary tangles [78, 103].

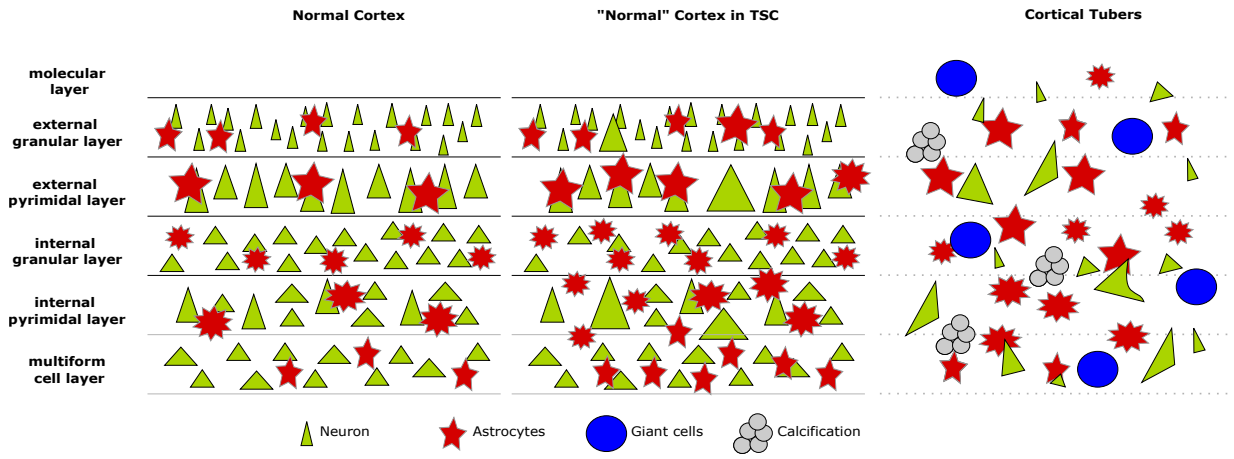


FIGURE 1.2: **Cortical histomorphology in TSC.** In healthy brain tissue, the neocortex comprises six layers with distinct neuronal populations in each layer accompanied by a set proportion of astrocytes (left). Non-tuberal cortex in TSC displays normal cortical layering, yet with an increased astrocytic population throughout all layers (middle). Cortical tubers feature a complete loss of cortical layering, dysmorphic neurons, calcifications, eosinophilic giant cells, and gliosis (right).

The cellular character and functioning of the eosinophilic giant cells remain unclear as they express several neuronal and glial proteins and display mostly glial morphological characteristics, including multipolar processes, storage of glycogen, and the formation of hemidesmosomes with pia and vascular basement membranes [265]. These cells form cellular connections with each other and astrocytes and have occasionally been observed to engage with neuronal synapses as well [103]. Analysis of tubers and their role in the development of TSC symptoms is often hampered by the heterogeneity of tuberal tissue, comprising abnormal and normal neurons and glia alike [78].

Astrocytes likely play a prominent role in the pathogenesis of TANDs, although their precise contribution remains unclear [78]. Cortical tubers often show reactive gliosis and increased GFAP but reduced glutamine synthetase expression [247]. Mouse models with conditional knockout of TSC1 in developing astrocytes present with glial overgrowth, cytomegaly, disturbed cortical lamination and spontaneous seizures, suggesting that astrocytes could contribute significantly to the development of cortical malformations and the neurological presentations in TSC. Astrocyte phenotypes in TSC, and especially from astrocytes found

in cortical tubers, are dynamically changing from a predominantly *reactive* state to *gliotic* astrocytes over time [248]. Similar dynamics are found in astrocyte populations subjected to stress or insult. In TSC, *reactive* astrocytes show mTORC1 hyperactivation and are often found adjacent to giant cells indicating that both cell types might stem from a common progenitor [248]. Astrocytes provide neurons with an optimal extracellular environment by controlling extracellular concentrations of neurotransmitters, ions, and metabolites. In TSC, the ability of astrocytes to facilitate extracellular homeostasis for neurons is impaired, for example, due to malfunctioning of potassium K_{ir} channels [118] or deficiencies in glial glutamate transporters [294], and astrocytes likely contribute to neuronal hyperexcitability in TSC [289].

Perituberal tissue is altered, too, showing hypomyelination, gliosis, and a reduction in axons [103]. Vascularisation and perfusion are altered in FCD as well as cortical tubers compared to normal cortical tissue. Studies have provided mixed evidence on vascularization and metabolism in tubers and other FCD types but the majority of dysplastic lesions, including samples from MCD, FCD and cortical tubers, showed increased vascular density and hypermetabolism. However, one study in 19 patients demonstrated decreased cerebral blood flow detected by cortical IMP-uptake in two-thirds of confirmed tuberal lesions and hypometabolism mostly occurred in tubers suspected to be epileptogenic [257]. Nevertheless, most lesions in TSC, including brain tumours, are highly angiogenic [10]. Macrovasculature, especially the leptomeningeal venous system, is enlarged adjacent to cortical malformations and cortical malformations show changes on the microvasculature level as well [53, 274]. FCD lesions showed higher lesional blood flow compared to the contralateral normal cortex and increased microvessel count [273, 286]. Alterations in white matter microvasculature seem unique to cortical tubers as white matter vascular density

is normal in all other MCD types. In cortical tubers, vascular density correlates with the overall inflammatory response and microglia activation but not with balloon cell count or myelin content [273]. It is debatable whether such vascular alterations correlate with seizure activity in cortical tubers and whether they precede or succeed abnormal neuronal activity.

Neurodevelopmental origin and dynamics. Cortical tubers form in circumscribed cerebral areas. They are present at birth [176] and remain relatively stable in size, although they show dynamic inflammatory and morphological changes [38]. These features suggest their origin lies in early neurodevelopment. Neuronal immaturity and differences in dysmorphology severity between cortical lower and upper layers indicate that a lack of maturation and preserved developmental features contribute to tuberigenesis [184]. In addition, aberrant migration, neuronal cell loss and decreased neurogenesis likely feature in tuberigenesis, although the exact mechanisms remain unclear. The fact that neurons destined for upper cortical layers retain their marker expression profile but can be found in deeper layers indicates that migration is severely affected by TSC1/TSC2 knockout [184]. TSC1/TSC2 mutations cause significant stress levels to neurons, likely increasing their vulnerability and death [56]. The balance between neurogenesis and gliogenesis is also altered in TSC with NSCs showing a tendency for increased gliogenesis in mouse and stem cell-derived models of TSC [78].

Previously, MCDs, including cortical tubers, had been termed *neuronal migration disorders* highlighting the crucial role that disturbed migration plays in their development. However, it has been recognised that the development of cortical tubers and other MCDs is likely more complex with disturbances occurring at various time points during brain development leading to heterogeneous abnormalities in MCDs [11]. Triggers for the development of cortical tubers remain unclear. Most patients with TSC are heterozygous for either TSC1 or

TSC2 mutations, however, investigations from resected tumours revealed a double-hit to TSC1/TSC2 in most of their tumours. These observations sparked the *second-hit hypothesis* assuming that a second allele loss in either TSC1 or TSC2 triggers tumour formation [120]. However, in contrast to tumours of other body parts, the majority of cortical tubers are heterozygous in patients with TSC [214]. Also, homozygous patients with TSC present with localised brain abnormalities despite harbouring the pathogenic mutation universally suggesting that a complete loss of TSC1/TSC2 is not sufficient to induce cortical malformation. Investigations on fetal TSC tissue provided evidence that cortical tubers develop as a consequence of mTORC1 hyperactivation during early embryo development although the exact mechanisms of tuberigenesis remain unclear [212].

Clinically, tuber load correlates with early-onset epilepsy which negatively impacts cognition [121]. However, the relationship between tuber load and neurological presentation remains unclear. Only a poor correlation exists between tuberal numbers and intellectual disability [51], although some studies observed a direct relationship between tuber count and intellectual ability [123]. Tuber size appears to directly affect the severity of cognitive impairment [205]. Other studies observed that not the general tuber load but rather tuber location impacts intellectual development with parietal tubers affecting the patient's cognitive abilities as well as behavioural presentations the most [42]. Tubers whose locations superimpose with focal epileptiform discharges detected on intracranial EEG are framed *hot tubers* [137], and tuberectomy shows good outcomes in what is often pharmacologically refractory epilepsy [74, 75]. It is subject to ongoing debate whether the tuber [39] or the adjacent perituberal tissue [75, 158] functions as the epileptogenic zone in these cases.
Magnetic resonance imaging (MRI) allows the identification of three different tuber types, *type A, B, and C*, according to their T1, T2 and FLAIR signal intensities. The dominant tuber type correlates with the clinical presentation, for example, type A tubers are associ-

ated with less severe phenotypes whereas type C tubers correlate with more severe clinical symptoms and brain abnormalities [87]. However, the causal relationship between tuber load, tuber type, and the clinical picture remains to be elucidated.

1.2 The molecular pathways forming the basis for this thesis

1.2.1 The TSC1:TSC2-mTORC1 pathway

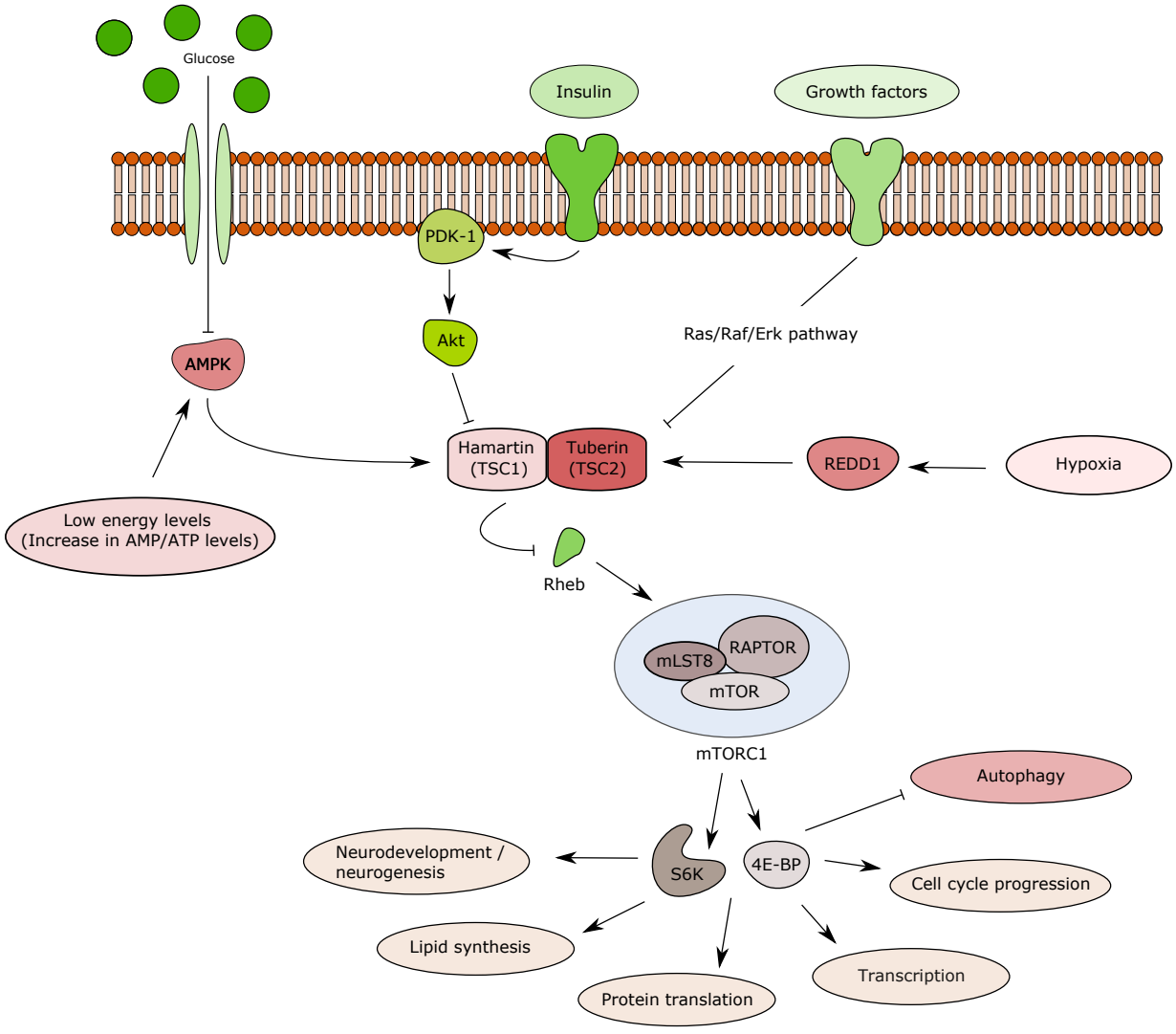


FIGURE 1.3: **The TSC1:TSC2-mTORC1 pathway.** Activity of mTORC1 is linked to glucose supply and extracellular concentrations of growth factor via the TSC1:TSC2 complex. Glucose inhibits AMPK causing suppression of TSC1:TSC2 which dis-inhibits mTORC1 via Rheb. Growth factors such as insulin feed into this pathway via PDK-1 and Akt. Activation of mTORC1 is further regulated by oxygen or amino acids via non-displayed pathways. Activated mTORC1 supports cellular growth via various anabolic processes while reducing anabolic mechanisms such as autophagy.

The mechanistic target of rapamycin (mTOR) is a large serine/ threonine kinase that is ubiquitously expressed and acts as a major regulator of cellular metabolism [106]. The multi-effector kinase is the catalytic unit of two distinct complexes, *mTOR complex 1 and 2 (mTORC1 and mTORC2)*. Complex 1 comprises mTOR together with the regulatory-associated protein of mTOR (RAPTOR) and mammalian lethal with Sec13 protein 8 (mLST8) [231]. Equally, complex 2 consists of mTOR and mLST8 but instead of RAPTOR comprises the rapamycin-insensitive companion of mTOR (RICTOR) [231]. The upstream regulators and downstream targets as well as their cellular functions are much better investigated for mTORC1 whereas mTORC2 is less well understood. As shown in figure 1.3, mTORC1 controls main cellular functions such as cell growth, gene transcription, protein translation, autophagy, and differentiation in response to the supply of growth factors, nutrients and amino acids as well as oxygen levels and other markers of cellular stress [106]. Activation of mTORC1 also plays an important role in neurobiology, particularly in synapse plasticity, neurodevelopment, and learning [288].

MTORC1 regulates cell growth and metabolism primarily by activating gene transcription, protein synthesis, cell proliferation, and cell growth through phosphorylation of its downstream targets ribosomal protein S6 and the translation factor families eukaryotic translation initiation factor 4E-binding protein (4E-BPs) and sterol regulatory element-binding proteins (SREBPs) [60, 82, 141, 231]. In addition, mTORC1 actively inhibits catabolic processes, including autophagy and lysosome biogenesis, when the cell is in a state of good supply [130, 235]. During starvation, mTORC1 activity is low allowing the cell to switch from an anabolic to a catabolic state. mTORC2 exerts its functions through a variety of protein kinases and by interactions with the cytoskeleton [288]. Rapamycin, and related agents (*rapalogs*), are potent inhibitors of mTORC1 with less effect on mTORC2 [147].

The TSC1:TSC2 complex acts as a main upstream regulator of mTORC1 connecting the cellular supply of nutrients and growth factors with mTORC1 activation [43]. The TSC1 corresponding protein *hamartin*, a 130 kDa and 1164 amino acids spanning hydrophilic protein [223], serves as a stabiliser for *tuberin*. Tuberin, the 198 kDa big and 1807 amino acids long gene product of TSC2 [223], is a GTPase activating protein regulating the activity of the Ras superfamily of proteins [223]. Intracellularly, hamartin and tuberin bind into a heterodimer via their coiled-coil domains preventing TSC2 from ubiquitination and degradation [34]. The TSC1:TSC2 protein complex serves as an indirect inhibitor of mTORC1 via the Ras homolog enriched in brain (Rheb) [260]. Activation of TSC1:TSC2 suppresses mTORC1 whereas lack of TSC1:TSC2 dis-inhibits mTORC1 (see pathway overview in figure 1.3).

Regulation of cell metabolism is achieved via a complex network of different cell signalling pathways with mTOR at the centre controlling the delicate balance of catabolism and anabolism. Disturbances of this balance result in pathological cell growth or cell death and mTOR is involved in the pathogenesis of various cancers as well as neurodegenerative diseases.

1.2.2 Energy-producing metabolism

Producing energy in form of adenosine triphosphate (ATP) from metabolites is the basis of cellular growth and proliferation which, in turn, form the foundation for differentiation and development. The mechanisms of how cells balance their energy demands with supply are, thus, crucial and disturbances in cellular energy metabolism can have detrimental impacts on healthy development. As shown in figure 1.4, ATP can be produced by substrate-level phosphorylation (*glycolysis and Krebs cycle / tricarboxylic acid cycle (TCA)*) or oxidative

phosphorylation (*mitochondrial respiration*) [216]. These mechanistically different pathways are interconnected via shared metabolites.

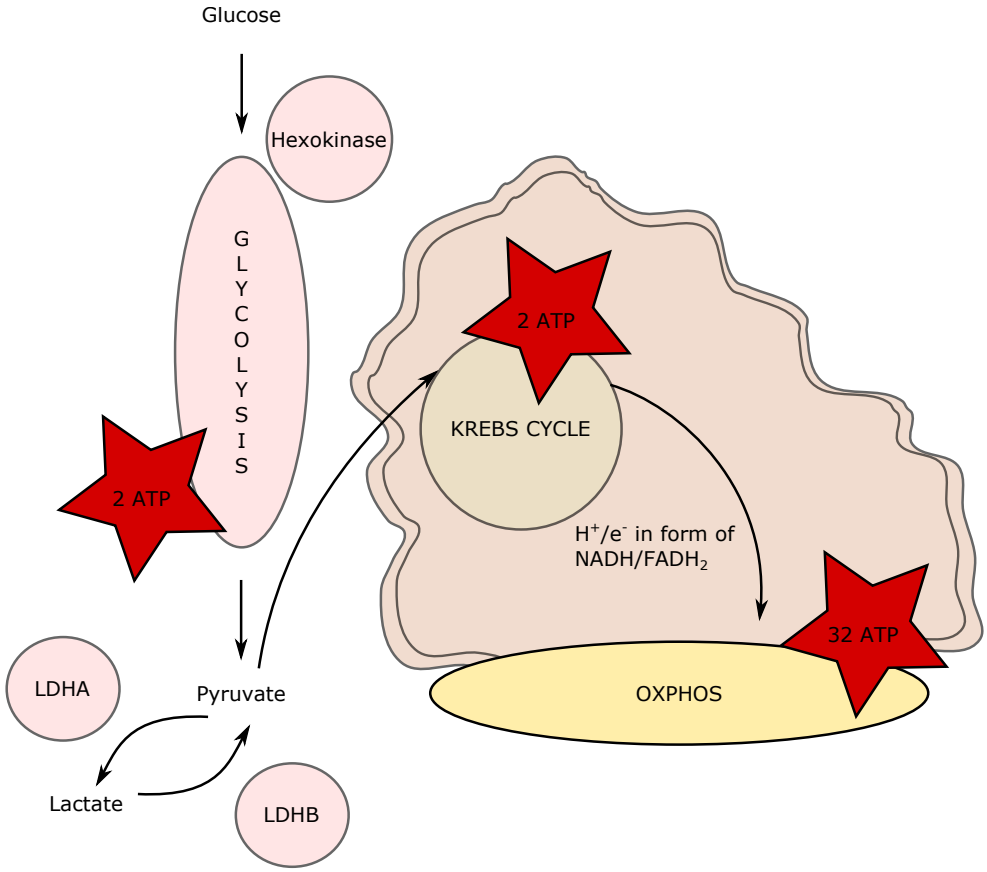


FIGURE 1.4: **Energy-producing pathways.** Schematic overview of the ATP-producing pathways glycolysis (pink), Krebs cycle (green) and oxidative phosphorylation. Glycolysis is located in the cell soma whereas the Krebs cycle and OXPHOS are based in the mitochondria (brown). The number of ATP molecules each pathway produces individually is displayed in the stars.

During **glycolysis**, glucose gets metabolised into pyruvate and lactate while producing two ATP molecules. Although low in ATP yield, glycolysis is fast and further provides cellular building blocks for subsequent anabolic processes.

The **Krebs cycle** is a closed-loop metabolic engine located in the mitochondria [81]. Its functions are diverse as the TCA cycle links glycolytic metabolites to oxidative phosphorylation and provides multiple building blocks for anabolic cellular processes [185]. TCA cycle metabolites have also been discovered to play important roles in the regulation of key non-metabolic processes including immune response as well as pluripotency and cell fate

[166]. For example, the Krebs cycle metabolite a-ketoglutarate acts as an anti-inflammatory agent suppressing pro-inflammatory cellular pathways [155] and further, supports pluripotency in embryonic stem cells [26].

Another important pathway involved in cellular energy production is **oxidative phosphorylation (OXPHOS)**. Protein complexes of the mitochondrial chain build up an electrochemical proton gradient whose potential then releases the energy to phosphorylate ADP to ATP [276]. Compared to glycolysis, OXPHOS is slow and does not provide any additional metabolites, however, yields 32 ATP molecules per glucose.

Two rate-limiting glycolytic enzymes and some of their distinct isoforms will be introduced in the next paragraph as they play a major role at the intersection of energy metabolism, cell survival, and proliferation.

Hexokinase (HK) mediates the first and rate-limiting step of glycolysis, the phosphorylation of glucose to glucose-6-phosphate (G6P). Human HK exists in four different isoforms with varying domains facilitating specific functions in different tissues and conditions. The isoforms differ in their affinity to glucose, with HK 1,2 and 3 displaying higher affinity than isoform 4 [283], as well as in their expression in different tissues. Brain tissue predominantly expresses HK1 [12]. HK2 is expressed in insulin-sensitive tissue such as heart muscle or adipose tissue [40] but is otherwise very little produced in healthy mammalian tissue. In contrast, most tumour cells upregulate HK 2 at an early stage of cancer development, a step which is associated with increased glucose consumption and lactate production (*Warburg effect*) [170]. The HK2 upregulation appears to be transcriptionally regulated through mTORC1 hyperactivation [219]. HK2 plays a crucial role in facilitating high glycolytic rates, even in well-oxygenated conditions and furthermore, increases cell survival and proliferation in numerous cancer types which are often associated with poor

prognosis. Glioblastoma multiforma is such an example of an aggressive glycolytic cancer associated with high HK2 expression levels [287]. HK2, but not HK1, is capable of evading G6P-mediated negative feedback inhibition allowing high catalytic activation under high glycolytic activity [219]. Alongside their cytosolic form, HK1 and 2 exist in a mitochondria-bound form (mitoHK) which allows a tight interaction between glycolysis and oxidative phosphorylation [170]. Especially in glycolytic cancer cells, HK2 is predominately bound to the mitochondrial voltage-dependent anion channel (VDAC) which brings it in close proximity to ATP produced during mitochondrial respiration that can then directly be utilised for glucose phosphorylation in the first steps of glycolysis [219]. In addition, the VDAC-HK2 complex plays an important role in the ability of cancer cells to evade apoptosis and perform increased cell proliferation by inhibiting mitochondria-mediated apoptosis [170]. Apoptosis, physiological cell death, is important to maintain tissue integrity and health as it controls cell number and positioning as well as prevents survival of infected or damaged and thus, potentially harmful cells. Suppression of apoptosis is one of the hallmarks of cancer [20]. Lastly, HK2 but not HK1, acts as an mTORC1 inhibitor enabling autophagy in glucose-deprived environments [219]. Autophagy is an important cellular response mechanism to nutrient starvation and hostile conditions. At early stages of cancer development, autophagy can serve anti-carcinogenic effects by clearing potentially carcinogenic invaders. However, autophagy can switch into a carcinogenic process itself in established cancers as it then provides protection against environmental and drug-induced cellular damage [168].

Lactate dehydrogenase (LDH) is an NAD^+-dependent enzyme that is active in a tetramer formed from two subunits: LDHA, expressed from the LDH-M gene (first discovered in skeletal muscle) and LDHB, encoded in the LDH-H gene (first discovered in heart muscle). Five different tetramere versions exist: H4 (LDH1), M1H3 (LDH2), M2H2 (LDH3), M3H1 (LDH4), M4 (LDH5) [270]. LDHA with a net charge of *-6* has a higher

affinity for pyruvate, thus preferentially converting pyruvate to lactate. The opposite is true for LDHB which, due to a net charge of *+1*, has a higher affinity for lactate and preferentially transforms lactate back to pyruvate [270]. Despite these differences, individual knockout of either subunit does not affect glycolytic flux and lactate production as LDHA and LDHB are capable of functionally replacing their counterpart in various tissue [293]. Double knockout of LDHA and LDHB is required to significantly reduce glycolysis and lactate production and leads to a metabolic shift in affected tissue from glycolysis to OXPHOS [293].

Various cancers, especially those growing in hypoxic conditions, upregulate LDHA facilitating high glucose metabolism and lactate production [80]. The expression of LDHB in cancer is more variable and less well understood [270] but LDHB upregulation has been associated with mTORC1-driven tumourigenesis in TSC2-null mice [296].

LDH also serves a complex role in regulating autophagy and apoptosis in healthy as well as in tumour cells. LDHA as well as LDHB inhibition has been shown to induce apoptosis, in part via mitochondria-dependent pathways [270]. Thus, LDH upregulation could be a potent mechanism to prevent apoptosis in cancer cells. On the other hand, LDHA and LDHB impact differently on autophagy [270]. So far, LDHA has not been found to be involved in the regulation of autophagic activity in cancer cells. In contrast, LDHB inhibition causes a decrease in autophagy in cancer cells indicating that, in turn, elevated LDHB levels might contribute to enhanced autophagy and cell survival in established cancers [270].

In summary, in addition to their immediate role in glucose metabolism, HK2 and LDHA/LDHB are pivotal for most human cancers to allow their high metabolic plasticity, facilitate high glucose metabolism in hypoxic and nutrient-challenging conditions and prevent cell death which overall enables fast-rates of proliferation.

1.3 Stem cell models

1.3.1 Stem cell models in neuroscience

Stem cell-derived neural cultures have significantly transformed the way in which neuroscientists can explore cellular and molecular principles of the human brain. Impressive advances have been made since the first successful isolation of embryonic stem cells from mice in the early 1980s [73] and from human embryos in the late 1990s [262]. Due to groundbreaking discoveries from the Yamanaka group in 2006, it is now possible to convert somatic cells into *induced pluripotent stem cells (iPSC)* in a process termed *reprogramming* [256] and, in theory, differentiate these cells into various different cell types, including neuronal and glial tissue. It is also possible to directly induce neurons from an adult somatic cell without the prior conversion into a stem cell [277]. Similarly, *human embryonic stem cells (hES)* can be differentiated into various human tissues. However, their use is often limited by country-specific legal requirements [211].

Amin and Pasça consider the coincidence of four recent advances in neurobiological techniques as being a catalyst to further our understanding of neurological disease mechanisms: (1) the genomics revolution which allows links between copy number and gene variants to neurological disorders, (2) the development of fast and precise gene editing tools, especially the CRISPR/Cas9 system, (3) the ability to generate patient-specific iPSCs and (4) the possibility to derive 3D neuronal cultures, such as brain organoids, from human stem cells [5]. Neural differentiation of hPSC recapitulates neurodevelopment, especially corticogenesis, remarkably well in many aspects [204]. Human stem cells have an innate tendency to differentiate towards the ectodermal germline layer. This can be advanced by dual SMAD inhibition which blocks endodermal and mesodermal differentiation and subsequently yields

high proportions of neural progenitors and neurons [239]. Otherwise, non-directed neural differentiation of hPSCs spontaneously generates predominantly forebrain cortical neurons of all layers [89]. Specific small molecules and growth factors can pattern other types of neuronal cells, for example, dopaminergic [129, 129] or spinal cord neurons [264].

As they harbour the specific genetic background of patients, iPSCs and derived neuronal cultures enable the study of neurodevelopmental disorders in a dish [204]. Human ES are suitable to explore genetic syndromes as well [44] but require prior gene editing methods to induce the mutation of interest artificially. Since stem cell-based models are not as time-consuming and require fewer laboratory resources than animal models, they are especially well suited for high-throughput target research and drug screenings [69].

To date, stem cell-derived monolayer 2D neuronal cultures have been most frequently applied in neuroscience research. So far, a variety of different brain disorders have been modelled, for example, Huntington's Disease, Parkinson's Disease, Schizophrenia, and different epilepsy syndromes (reviewed in [230]). Despite their advantages, key cellular and tissue characteristics can be disturbed in 2D neuronal cultures including cellular morphology, polarity, molecular signature, proliferation, differentiation potential, and overall functionality [203]. By contrast, 3D cultures, so-called brain organoids, allow much more complex cell-cell interactions leading to higher maturity, greater functionality, a more diverse cellular composition, and an organotypically structured assembly of cells with different regional identities [139]. Cerebral organoids allow us to recapitulate more complex aspects of cerebral cytoarchitecture and achieve higher stages of maturity of corticogenesis.

Various types of cerebral organoids have been introduced, so far. The terms *undirected* or *directed* organoid refer to 3D structures whose assembly has been mostly driven by self-organisation (for example [139]) or by specific mechanical forces and small molecules (for

example [66]), respectively. Fused systems can be generated from region-specific organoids, for example, consisting of cells with forebrain and dorsal pallidum identity [17]. Brain organoids are increasingly applied in hPSC-based research and have been used to model a variety of neurological diseases including TSC [19].

Reprogrammed hPSCs became available to the neuroscientific community a decade ago and important technical questions still need to be solved [292]. Achieving cortical maturation in iPSC-derived neuronal networks is challenging [195] as most 2D differentiation protocols yield immature neurons with fetal-like gene expression patterns [206] associated with slow and incomplete synaptic maturation [195]. Induced neuronal networks are often electrically quiescent and recreate normal cortical activity poorly [196]. Most neural differentiation protocols yield mixed cellular neuronal and glial populations [112] impeding phenotypic identification as well as biochemical and functional analyses [230]. In addition, differentiated cells from different iPSC lines and even from clones of the same line frequently show highly variable behaviour potentially confounding biological meaningful results [83]. This variability is not restricted to 2D cultures as brain organoids themselves show high inter-cell line and inter-batch variability with regards to their cellular composition or molecular signature [275].

Similar to animal *in vitro* neuronal cultures, human iPSC-derived neuronal networks lack important other elements of the human brain such as vascularization, microglia, or myelination [61] which potentially influences synaptogenesis and network formation. Several suggestions have been made to overcome these problems such as transplanting iPSCs into rodent brains to enable maturation *in vivo* [72] or co-culturing iPSC-derived neurons with astrocytes to support synaptic maturation *in vitro* [171]. Cerebral organoids address these

problems to some extent, but do so at the expense of laboratory simplicity, time, scalability, and access to various assays, such as imaging or genome-wide CRISPR–Cas9 screens [203].

1.3.2 Stem cell models of TSC

Modelling TSC has been challenging as germline TSC1/TSC2 mutations are embryonically lethal [132, 198]. Therefore, conditional knockout models are often used where TSC1/TSC2 mutations are introduced in a specific cell population, such as neuronal progenitors [28] or glia [67], only. Different studies have used rodent or human pluripotent stem cells with a TSC genetic background to derive neural cells and build *in vitro* neural model systems to investigate molecular and cellular aspects of neurodevelopment in TSC [18]. However, at the start of my project, only three such studies were available to me, as summarised in table 1.2.

My project is built on the study by Costa and colleagues who differentiated NSCs and cortical neurons from TSC2 +/+, TSC2 +/- and TSC2 -/- hES and investigated their cellular, molecular, and functional properties [44]. Grabole and colleagues [93] performed transcriptional experiments on hES-derived TSC2 +/+ and TSC2 -/- NSCs and the study by Ebrahimi-Fakhari and colleagues [64] investigated iPSC-derived NGN2 neurons regarding their mitochondrial metabolism.

At the start of my project, these studies suggested that the derivation of human neurons with a TSC background might be a suitable tool to study the neurodevelopmental basis of cortical tubers *in vitro*. In these three publications, first evidence was presented that TSC2 loss-of-function mutations lead to developmental disturbances on the transcriptional and translational level resembling findings from cortical tubers *in vivo*. Such abnormalities included larger cells and altered proliferation behaviour, astrocytic propensity, and changes

to synaptic transmission leading to neuronal hypo-excitability [44]. In hPSC-derived NSCs, TSC2-deficiency led to immaturity and glial propensity accompanied by an increase in inflammation and metabolic activation [93]. Further, a stem cell-based TSC study provided evidence that TSC2 loss-of-function impacts mitochondrial homeostasis with decreased mitophagy as well as somatic accumulation but axonal depletion of mitochondria [64]. However, little was known as to how well exactly such hPSC-derived neural models might resemble cortical tubers on a molecular, cellular, or functional level. Also, we had no knowledge of any attempts to derive TSC2-deficient astrocytes and assemble glio-neuronal co-cultures with a TSC background from hPSCs. Furthermore, no investigations into the causes of tuberigenesis in TSC on hPSC-derived cultures had been made at the start of my DPhil project.

Study	**Cell lines**	**Protocol**	Ref
Costa et al. 2016	hES: $TSC2^{+/+}$, $TSC2^{+/-}$, $TSC2^{-/-}$	2D, cortical neurons	[44]
Grabole et al. 2016	hES: $TSC2^{+/+}$, $TSC2^{-/-}$	2D, NSCs	[93]
Ebrahimi-Fakhari et al 2016	iPSCs (Two TSC patients, two matched controls) + TALEN-engineered iPSC TSC2-/- line	NGN2 cortical neurons	[64]
Rocktäschel, started in 2016	hES: TSC2 +/+, TSC2 -/-	2D, NGN2 neurons, NSCs and neurons via dual SMAD-inhibition, astrocytes	[221]

TABLE 1.2: **Stem cell studies on TSC published before 2016.** Three studies using hPSC with a TSC background had been published before the start of my project. This table summarises the starting cell lines as well as the differentiation outcome of these studies as well as my project. Study-specific results are summarised in tables A and A.2.

1.4 Aims

The overall aim of my thesis was to examine the effect of different non-genetic cellular and non-cellular modifications on neuronal differentiation and the development of cortical malformation in TSC. This goal was broken down into these specific aims:

1. Investigate the effect of TSC2 deficiency on hallmarks of neural differentiation such as the balance of NSC renewal and neurogenesis, glio-neuronal composition, and cortical neuronal maturation in a stem cell-derived neuronal model of TSC.

2. Investigate the impact of glucose deprivation on these hallmarks of neurodevelopment as well as on glycolytic and mitochondrial energy production in TSC.

3. Establish a computational model tool – dynamic causal modeling (DCM) – on multi-electrode array (MEA) recordings from glio-neuronal co-cultures to examine effective cortical connectivity *in vitro*.

4. Perform DCM analysis on TSC glio-neuronal co-cultures to examine the impact of TSC2-deficient astrocytes on the synaptic landscape underlying cortical connectivity *in vitro*.

In chapter 2, I will describe the stem cell lines, laboratory materials, and experimental protocols used for this project.
In chapter 3, I will characterise a set of genetically modified TSC2 +/+ and TSC2 -/- hES lines with regards to their genotypic status, morphological features as well as the expression of specific cell type markers indicative of pluripotency and neural features. I utilise these lines to investigate the effect of TSC2 on hallmarks of neurodevelopment by examining different stages of cortical differentiation *in vitro* such as NSC morphology and proliferation, glio-neuronal output as well as neuronal maturation.

In the following two chapters, I will examine the impact of non-genetic modifiers on the development of cortical malformations in TSC. Chapter 4 demonstrates that limited glucose supply causes disturbances to neurodevelopment in TSC2-deficient cultures including decreased neurogenesis and an increase in the glia-to-neuron ratio. In NSCs, glucose deprivation reduces glycolytic and mitochondrial energy production. TSC2-deficiency limits the cellular ability of an appropriate compensatory response to impaired energy levels driving transcriptional changes in glycolytic genes that can be associated with carcinogenesis. The work presented in this chapter resulted in the peer-reviewed first-author publication *Rocktäschel et al. High glucose concentrations mask cellular phenotypes in a stem cell model of tuberous sclerosis complex.* [221].

In chapter 5, I focus on astrocytes, a cellular modifier of neuronal development, and their impact on neuronal circuit formation in TSC. To investigate circuit development and the resulting neuronal connectivity *in vitro*, I first establish a computational modelling tool – DCM – for connectivity analysis and then utilise this tool to investigate the effect of astrocytes on neuronal connectivity in a stem cell-derived *in vitro* model of TSC. Preliminary results suggest that TSC2-deficient astrocytes influence effective connectivity in developing neuronal cultures and their effect is depending on the TSC2 genotypic status of the co-cultured neurons. In response to TSC2-deficient astrocytes, TSC2 +/+ neuronal networks presented with an increase in inhibition whereas TSC2 -/- neuronal networks developed an increased excitation-to-inhibition ratio.

The presented experimental results and their implications for future work will be discussed in chapter 6.

2 | Material & Methods

2.1 Ethic statement

The hES cell lines were used with authorisation from the UK Stem Cell Bank Steering Committee (UK Steering Committee).

2.2 Material

2.2.1 Cell lines

I used the following human cell lines for my DPhil project:

Cell line	Mutation	Cell type	Source
AAVS_N4	TSC2 +/+	hES	Roche Hoffmann AG
N3_22	TSC2 -/-	hES	Roche Hoffmann AG
SA-16B2	TSC2 +/+	NSC	Roche Hoffmann AG
SA-20A	TSC2 -/-	NSC	Roche Hoffmann AG
CPN Cas9	none	iPSC	Ben Davies (University of Oxford)
SBAD-03-01	none	iPSC	STEMBancc

TABLE 2.1: **Cell lines used in this study.** Two hES and two NSC lines with a TSC2 -/- mutation and a TSC2 +/+ control were obtained from Roche Hoffmann AG. A control iPSC line containing an inducible CRISPR/Cas9 system was kindly provided by Dr Ben Davies, University of Oxford – Nuffield Department of Medicine. A second control iPSC line was sourced from the STEMBancc project.

All cell lines were regularly tested for mycoplasma contamination using the testing facility at the Sir William Dunn School of Pathology, Oxford, and were always found to be negative. Cell lines were used at passage numbers between 16 — 25.

2.2.2 Cell culture materials

All cell culture media were prepared under sterile conditions in a flowhood and kept in aliquots in sterile tubes at 4 °C for a maximum of two weeks or at -20 °C for long-term storage. The following cell culture media were used in this study:

mTESR1	
Composition	As purchased from STEMCell Technologies.
Use	To culture human pluripotent stem cells.
NSC medium	
Composition	1:1 mixture of DMEM/F12 GlutaMAX (Invitrogen, 10565018) and Neurobasalmedium (Invitrogen, 211030049) supplemented with 2 % B27 without vitamin A, 1 % N2 and 50 μM β-mercaptoethanol. Media was aliquoted and stored at -20 °C. The following growth factors were added freshly before each usage: 10 ng/mL FGF-2, 10 ng/mL EGF and 20 ng/mL BDNF.
Use	To culture NSCs obtained from Roche Hoffmann AG.
Neural maintenance media (NMM)	
Composition	1:1 mixture of DMEM/F12 GlutaMAX and Neurobasalmedium supplemented with 1 % B27, 0.5 % N2, 50 μM β-mercaptoethanol, 1 mM L-glutamine, 25 U/mL penicillin-streptomycin, 2.5 μg/mL insulin, 0.5 μM sodium pyruvate and 50 μM MEM non-essential amino acids.
Use	Neuronal differentiation via dual SMAD inhibition.
Neural induction media (NIM)	
Composition	NMM supplemented with 1 μM dorsomorphin and 10 μM SB431542.
Use	Induction period of neuronal differentiation via dual SMAD inhibition.
Neurogenin 1 (NGN1) medium	
Composition	DMEM/F12 GlutaMAX supplemented with 1 % N2, 100 U/mL penicillin-streptomycin and 10 μM MEM non-essential amino acids.
Use	Neuronal differentiation with Neurogenin 2.
Neurogenin 2 (NGN2) medium	
Composition	Neurobasalmedium supplemented with 2 % B27, 2 mM GlutaMAX supplement, and 100 U/mL penicillin-streptomycin.
Use	Neuronal differentiation with Neurogenin 2.
Astrocyte differentiation media (ADM)	
Composition	As purchased from STEMCEll Technologies.
Use	Astrocyte Differentiation Protocol.
Astrocyte maturation media (AMM)	
Composition	As purchased from STEMCEll Technologies.
Use	Astrocyte Differentiation Protocol.
Astrocyte Maintenance Media	
Composition	1:1 mixture of Neurobasalmedium and DMEM/F12 GlutaMAX supplemented with 10 % penicillin-streptomycin, 10 % sodium pyruvate and 10 % N2
Use	Maintenance of differentiated human astrocytes.

TABLE 2.2: **Cell culture media** used in this project.

Low glucose versions of NMM, NIM, and NSC media were prepared using a 1:1 mix of no-glucose DMEM (Thermo Fisher, 11966025) and no-glucose Neurobasal-A Medium (Thermo Fisher, A2477501) supplemented with 5 mM glucose. These media were supplemented with GlutaMAX and sodium pyruvate to reach similar concentrations to the respective high-glucose media. All media was prepared under sterile conditions, filtered, and aliquoted into volumes of 40 ml to be stored at -20 °C.

Growth factors and other supplements were made up, if necessary, in the appropriate solvent and sterile filtered through a 0.2 μm wide pored-membrane (Sartorius, Minisart NML 16534) prior to use. Stocks were usually made up in batches and long-term stored at -20 °C or -80 °C. An overview of cell culture materials such as growth factors, media supplements, coating materials, detachment agents, and drugs that I used in this study can be found in appendix B.

2.2.3 Constructs

I used the following genetic constructs:

Construct	**Transduction**	**Source**	**Reference**
NGN2	Lentivirus	Lab stocks	
rt-TA3	Lentivirus	Lab stocks	
pcDNA3-Flag-TSC2	Lipofection	Gift from Brendan Manning (Addgene plasmid 14129)	[160]
pLKO.1-TSC2	Lentivirus	Gift from Do-Hyung Kim (Addgene plasmid 15478)	[272]
Rosa26 CRISPR-sgRNAs	Lentivirus	Ben Davies	
TSC2 CRISPR-sgRNAs	Lentivirus	Ben Davies	

TABLE 2.3: **Viral constructs** used in this project.

2.2.4 Primary and secondary antibodies

I used a variety of different primary and secondary antibodies for immunofluorescence imaging, flow cytometry, and western blotting. Tables C.1 and C.2 list all antibodies used as well as their final concentration for the respective techniques. All antibodies were stored at either 4 °C or -20 °C according to manufacturer's instructions.

2.2.5 Primers

Primers were ordered from Integrated DNA Technologies UK Ltd. I reconstituted these in DNase/RNase-free water to reach a primary stock concentration of 100 μM and diluted the primers further in DNase/RNase-free water towards a secondary stock concentration of 10 μM. All primer stocks were stored at -20 °C. Primer sequences can be found in appendix D.

2.2.6 Molecular biology kits

Throughout this project, I used the following commercially available kits for molecular biological assays:

Kit	**Purpose**	**Supplier**	**Supplier Ref**
EndoFree Plasmid Maxi Kit	Plasmid DNA purification	Qiagen	12362
Direct-zol RNA Micro Prep	RNA extraction	Zymo Research	R2062
DNeasy Blood & Tissue Kit	DNA extraction	Qiagen	69504
Pierce BCA Protein Assay Kit	BCA assay	Thermo Scientific	23225
Glutamate Assay Kit	Glutamate uptake assay	Sigma Aldrich	MAK004

TABLE 2.4: **Molecular biology kits** used in this project.

2.3 Cell culture methods and differentiation protocols

2.3.1 Human stem cell culture

All cells were cultured on culture plates from Corning in cell culture incubators in humidified 5 % CO_2 and at 37 °C. Where stated, cells were counted in a hematocytometer using Trypan Blue 0.4 %. Cells plating densities are given in table 2.5.

Cell type	**Protocol / Experiment**	**Plating density**
Roche NSCs	NSC characterisation	25,000 cells / cm^2
hES	NGN2 transfection	20,000 - 25,000 cells / cm^2
NGN2-transfected hES	NGN2 protocol	25,000 cells / cm^2
Dual SMAD inhibition NSCs	Dual SMAD inhibition final plating (Day 30-35)	30,000 cells / cm^2
Dual SMAD inhibition NSCs	Astrocyte protocol single-cell passage (Day 18-25)	15,000 cells / cm^2
Astrocytes	STEMCell Technologies Astrocyte Differentiation Kit	15,000 cells / cm^2
Dual SMAD inhibition NSCs	Drop-plating for MEA recordings	100,000 cells / cm^2
Astrocytes	Glio-neuronal co-culture for MEA recordings	100,000 cells / cm^2

TABLE 2.5: **Plating densities of different cell types.** Overview of plating densities of cell types used in my studies depending on protocol and experiment.

Pluripotent stem cell culture

Human embryonic stem cells (hES) and induced pluripotent stem cells (iPSC) were grown on matrigel-coated wells in mTESR1 media with 100 % media changes every day.

Matrigel coating: One aliquot of matrigel was diluted in 25 mL of cold KnockOut-DMEM. Plates were coated with 100 $\mu L/cm^2$ and incubated at 37 °C for 1 - 20 h.

Thawing: One cryovial of cell suspension was quick-thawed in the water bath at 37 °C for

1-3 min. Then, the cell suspension was transferred into 9 mL PBS and spun at 400 g for 5 min. After supernatant removal, the cell pellet was re-suspended in 4 mL mTESR1 and 10 μM rock inhibitor and distributed in two wells of a 6-well plate.

EDTA passaging: When reaching 90 - 100 % confluency, pluripotent cell cultures were split at a 1:3 ratio by EDTA passaging. The mTESR1 culture media was removed and cells were incubated in 100 μL/cm^2 of 0.5 % EDTA in PBS for 4-5 min at 37 °C until loosening of the cells. After careful removal of EDTA, cells were washed off with mTESR1 media before plating on matrigel-coated wells.

Freezing: Six wells of a 6-well plate were frozen into 15 cryovials. Pluripotent cells were loosened with EDTA as described above. The cells were washed off with mTESR1 and suspended in an ice-cold 1:1 mix of mTESR1 and 2X freezing media (60 % ES-FBS, 20 % DMSO, 20 % KnockOut-DMEM). The cell suspension was distributed in pre-cooled and labelled cryovials and cooled in Mr. Frosty devices to -80 °C. Afterwards, cells were long-term stored in liquid nitrogen.

Neural stem cells

Neural stem cells (NSCs) from Roche Hoffmann AG were grown on PLO/Laminin-coated wells in NSC media with 100 % media changes every other day.

PLO/Laminin coating: Wells were incubated in 200 μL/cm^2 of a 1/6 Poly-L-ornithine (PLO)-solution in PBS for 6 - 24 h at 37 °C. After PLO removal and two PBS washes, PLO-coated plates were additionally incubated in 200 μL/cm^2 of 20 μg/mL laminin in PBS for 4 - 24 h at 37 °C. PLO/Laminin-coated plates could be kept at 37 °C for 3 days prior to cell plating.

Thawing: NSCs were thawed following the similar thawing protocol as for pluripotent stem

cells with two changes: Cells were spun in PBS at 400 g for 8 min and the resulting cell pellet was resuspended in NSC media prior to plating. Cells were plated at 25,000 cells/cm^2.
Trypsin passaging: After removal of NSC culture media, cells were detached through incubation in 50 μL/cm^2 TrypLE for 4 min at 37 °C. Then, cells were washed off with PBS and spun at 400 g for 8 min. The supernatant was discarded and the cell pellet was resuspended in 1 mL of NSC media. Cells were plated at a density of 25,000 cells/cm^2 onto PLO/Laminin-coated plates.
Freezing: Six wells of a 6-well plate were frozen into 10-12 cryovials. Steps of the TrypLE passaging protocol were followed until the creation of a cell pellet. The cell pellet was then suspended in ice-cold NSC media and 10 % DMSO. This cell suspension was distributed in pre-cooled and labelled cryovials and cooled down in Mr. Frosty devices to -80 °C. Afterwards, cells were long-term stored in liquid nitrogen.

2.3.2 Neuronal differentiation

Neurogenin 2 differentiation

Neuronal differentiation with forced Neurogenin 2 expression (NGN2 protocol) was carried out starting from hES. Cells were cultured on matrigel-coated plates throughout differentiation.

Single-cell plating. After reaching 90 % confluency, hES were single-cell passaged with accutase. After removal of mTESR1 media, cells were washed with PBS once and incubated at 37 °C in pre-warmed 50 μL/cm^2 accutase for 5 min. Afterwards, the cells were washed off with PBS and spun at 400 g for 5 min. Subsequent removal of the supernatant left a cell pellet which was further suspended in mTESR1 media. Cells were plated onto matrigel-coated plates at a density of 20,000 - 25,000 cells/cm^2. Prior to lentiviral trans-

fection, cells were incubated at 37 °C overnight.

Lentiviral transfection. Appropriate safety precautions were taken to ensure the safe handling of lentiviral samples.

Lentiviral transfection was carried out with two constructs, NGN2 and rt-TA3, whose optimum concentration was determined for each viral batch in an optimisation experiment prior to transfection of large batches of cells. Cells were incubated in respective volumes of both viral constructs simultaneously in mTESR1 media for 24 h at 37 °C. After this, the virus-containing media was replaced with fresh mTESR1 and cells could be expanded and passaged up to five times without loss in viral activity to create a large batch of transfected hES.

Differentiation.

Day 0: Thawing/Final Plating. Transfected hES were single-cell plated with accutase as described above at 25,000 cells/cm^2 onto matrigel-coated plates and incubated in mTESR1 at 37 °C overnight.

Day 1: Induction. Culture medium was removed and replaced with fresh NGN1 medium supplemented with 10 ng/mL NT-3 (Peprotech, 450-03-1-10UG), 20 ng/mL BDNF and 4 μg/mL doxycycline.

Day 2: Puromycin selection 1. A full media change was performed with fresh NGN1 medium supplemented with 10 ng/mL NT-3, 20 ng/mL BDNF, 4 μg/mL doxycycline and 0.4 μg/mL puromycin.

Day 3: Puromycin selection 2. Culture medium was changed fully to NGN2 medium supplemented with 10 ng/mL NT-3, 20 ng/mL BDNF, 4 μg/mL doxycycline and 0.4 μg/mL puromycin.

From Day 4: Half medium changes every other day. Half media changes with NGN2 medium supplemented with 10 ng/mL NT-3 and 20 ng/mL BDNF were performed every other day. When applying the fresh media, the plate was tilted and media was added at low speed to avoid washing off the often only loosely attached cells.

Neuronal differentiation via dual SMAD-inhibition.

For this neuronal differentiation, I followed the protocol introduced by Shi and colleagues with lab-specific modifications [238].
Human ES were maintained as described until they reached 100 % confluency which marked the start of this differentiation protocol. Complete confluency is important as non-confluent parts will be more prone to develop neural crest cells.

Induction: Upon confluency, a full media change to NIM was performed. Cultures were maintained with daily full media changes with NIM for 10-12 days.

Dispase passaging: Between days 10 and 12, the developed neuroepithelial sheet was passaged in clumps using a manual dispase passaging technique. Under the hood-based microscope, the sheet was cut with a pipette tip into pieces (approx. 25 pieces per well of a 6-well plate). After that, 200 μL of 10 mg/mL dispase was directly added to the media in a well of a 6-well plate and cells were incubated at 37 °C until the edges of the sheet started to lift off (this could take between 5 - 45 min). Then, the sheet was carefully lifted off using a P1000 and transferred into a 1:1 mix of DMEM/F12 and Neurobasalmedium supplemented with DNase (clumps from one well of a 6-well plate would go into 4 mL of this wash media). The clumps suspension was spun at 300 RPM for 3 min and the supernatant was discarded. Two more such washes (without DNase) and spins were performed

during which careful suspension of the clumps was only performed with a 10 mL stripette to maintain the integrity of the clumps as much as possible. Finally, clumps were carefully suspended in NIM and distributed onto wells coated with 20 ng/μL laminin before incubation at 37 °C overnight.

Day 12 - 25: The day after passaging, medium was changed to NMM supplemented with 20 ng/mL FGF-2. A further full media change with NMM supplemented with FGF-2 was repeated after 48 h. Then, full media changes with pure NMM were performed every other day. Upon rosette confluency or when individual rosettes became too dense to be viable, dispase passaging in NMM onto laminin-coated wells was performed following the steps described above.

Day 25 - 35: From day 25 onwards, cells could be passaged with accutase if they reached confluency. To do so, cultures were washed with PBS once and incubated in 50 - 100 μL/cm$_2$ accutase for 8 min at 37 °C. Thereafter, cells were washed off with PBS and spun at 400 g for 5 min. After discarding the supernatant, the cell pellet was resuspended in NMM and the cell suspension was distributed onto wells coated with 20 μg/mL laminin.

Final passage: Between days 30 - 35, cells were passaged with accutase and plated in NMM as described above on wells coated with PLO and 20 μg/mL laminin at a plating density of 30,000 cells cm^2.

Afterwards, the developing neuronal cultures were kept up to day 80 with full medium changes of NMM every other day.

2.3.3 Glial differentiation

To differentiate human astrocytes from hPSCs, I used a commercial Astrocyte Differentiation and Maturation Kit from STEMCEll Technologies. This protocol requires the production of NSCs first. These neural progenitors were obtained by following all steps from the dual SMAD inhibition protocol until the emergence of neural rosettes between days 18-25. From that point onwards, cells were directed down the glial route by following the manufacturer's instructions. Days of differentiation were counted, as with all other protocols, from the pluripotency stage onwards.

Neural rosette generation: To obtain neural progenitor cells, hES were neurally differentiated by dual SMAD inhibition following all steps as mentioned above until neural rosettes appeared between day 18 - 25.

Single cell passage of NPCs: Between days 18 - 25 of dual SMAD inhibition, cells were single-cell passaged using accutase onto matrigel-coated wells. Cells were plated in NMM at a density of 15,000 cells/cm^2.

Astrocyte Differentiation: The following day, the media was changed to ADM and cells were maintained with daily full media changes with ADM for 7 days. After this initial week, full media changes with ADM were only performed every other day. Upon reaching 80-90 % confluence, the emerging astrocyte precursors were accutase-passaged onto new matrigel-coated plates. The plating density for each such passage was 15,000 cells/cm^2.

Astrocyte maturation: After three weeks in ADM, culture conditions were changed to full media changes with AMM every other day. I continued with accutase passages onto freshly

coated plates with matrigel whenever the cultures reached near confluency. The duration of accutase incubation at 37 °C had to be gradually increased throughout differentiation with astrocytes at later stages requiring 20 - 30 min incubation before loosening. Maturating astrocytes were maintained in AMM for four weeks.

Astrocyte maintenance: After four weeks maturation in AMM, astrocytes were transferred into astrocyte maintenance media with full media changes every other day and regular accutase passages onto matrigel-coated plates whenever required.

Freezing and thawing: Cells could be frozen and thawed at any point after two weeks of starting in ADM. To freeze astrocytes and their precursors, the cells were loosened with accutase, washed off with PBS and spun at 400 g for 5 min as described above. The resulting cell pellet was resuspended in ice-cold culture media of the current stage of differentiation (either ADM, AMM or astrocyte maintenance media) supplemented with 10 % DMSO. I aimed to freeze between 1 - 1.5 Million cells per vial. The respectively diluted cell suspension was then distributed onto pre-cooled cryovials which were gradually frozen down to -80 °C using a Mr. Frosty device. Cells were long-term stored in liquid nitrogen.

2.3.4 Lipofection

I used a standard lipofection protocol using Lipofectamin 3000 to transfect TSC2 -/- hES with a TSC2 overexpression plasmid (pcDNA3-Flag-TSC2). Lipofection was performed in a 12-well plate when cells had reached 80 % confluency. For each well, 2 μL Lipofectamin 3000 Reagent were mixed with 50 μL Opti-MEM Medium and vortexed for 5 sec. In a second tube, 50 μL Opti-MEM Medium was mixed with the DNA template at either 0.2, 0.5, 1, 2 or 5 μg to test the most efficient concentration. The contents of tube 1 and tube 2

were subsequently mixed and incubated at room temperature (RT) for 6 min before being directly added to the mTESR1 culture medium in the well. Cells were incubated for 24 h at RT followed by a full medium change with mTESR1.

2.3.5 Gene knockdown using an inducible CRISPR/Cas9 iPSC line

Lentiviral transduction of inducible CRISPR/Cas9 iPSCs

Cells were plated at 50,000 cells/cm^2 on matrigel and left in mTESR1 overnight. The next day, cultures were transduced in mTESR1 with a cocktail of five CRISPR-sgRNAs targeting either the mouse Rosa26 (to create human wild-type controls) or the human TSC2 gene. Lentiviral constructs were used at an multiplicity of infection (MOI) of 10 and cells were incubated for 24 h. After that, the lentivirus-containing mTESR1 media was removed and replaced with fresh mTESR1. Cells were cultured with daily media changes and frozen as per the usual protocol when 100 % confluency was reached.

CRISPR/Cas9 induction

Cells were thawed following the usual hPSC defrosting protocol and cultured in mTESR1 on matrigel with regular passages as required. Expression of Cas9 was induced using 2 μg/mL doxycycline for one week. Furthermore, successfully transduced cells were positively selected through the application of 10 μg/mL blasticidin for 24 h between day 2 and 3 of doxycycline exposure.

2.4 Molecular biology methods

2.4.1 Protein extraction

Cultures intended for protein extraction were detached using the most suitable detachment method for the respective cell type as described above. After centrifugation, the super-

natant was discarded and the resulting cell pellet was lysed in 100 μL of ice-cold RIPA buffer supplemented with 10 μL of phosphatase-proteinase inhibitor. The samples were kept on ice for 5 - 30 min. Prior to use, the lysate was further homogenised with a cell homogeniser for 1.5 mL Eppendorf tubes and spun at 13,500 RPM at 4 °C for 15 min. Samples could then be long-term stored at -80 °C. Protein concentrations were determined using a BCA assay as described in section 2.4.10.

2.4.2 DNA extraction

Cultures intended for DNA extraction were similarly detached with the most suitable method and processed accordingly until a cell pellet was yielded. DNA extraction was then carried out using the DNeasy Blood and Tissue Kit from Qiagen according to manufacturer's instruction.

Cell lysis: Cell pellets were resuspended in 200 μL PBS before the addition of 20 μL Proteinase K to produce a cell lysate. To ensure proper mixing, the cell suspension was vortexed for 10 sec and allowed a subsequent incubation at RT for 2 min. After addition of 200 μL of the kit-specific Buffer AL, samples were vortexed for 10 sec and incubated at 56 °C for 10 min using a tube heater. In a final step, 200 μL of 100 % ethanol was added and thoroughly mixed by vortexing for 10 sec.

DNA binding and washing: 650 μL of the sample preparation were transferred onto a spin column placed in a collection tube. The DNA was selectively bound to the silicia-based membrane with contaminants passing through in a 1 min spin at 8000 RPM. Two following wash steps with subsequent spins were taken to eliminate any further contaminants and ethanol remnants. First, the spin column was placed into a fresh collection tube before the addition of 500 μL Buffer AW1 onto the membrane and centrifugation at 8000 RPM for

1 min. After discarding of the flow-through, 500 μL of Buffer AW2 were added followed by a 3-min-spin at 15,000 RPM. The column was transferred into a fresh collection tube and spun an additional 1 min at 15,000 RPM to avoid any ethanol take-over into the final DNA sample.

DNA elution: I placed the spin column into a fresh 1.5 mL Eppendorf tube and added 200 μL Buffer AE carefully directly onto the membrane. Incubation for 1 min at RT ensured the elution of the DNA which was then yielded in an Eppendorf tube during a 1 min centrifugation at 15,000 RPM. Sample concentrations and purity were measured on a NanoDrop 2000 (Thermo Scientific) and DNA samples were long-term stored at -20 °C.

2.4.3 RNA extraction and complementary DNA (cDNA) preparation

To extract RNA from cellular samples, cell pellets from cultures were again obtained through a suitable detachment method depending on the cell type. Cell pellets were immediately lysed in 300 μL TrizOL Reagent (Thermo Fisher, 15596026) with thorough mixing ensured by pipetting up and down several times as well as an additional vortex step until no cell pellet was visible. Lysate could be stored at -80 °C prior to further processing.

RNA extraction: RNA was extracted using the Direct-zol RNA Mini Prep Kit according to manufacturer's protocol. At first, Trizol-lysed samples were thawed at RT and thoroughly mixed with an equal volume of 100 % ethanol. The whole mixture was then transferred onto spin column placed within a collection tube and spun at 13,500 RPM for 30 sec to enable specific binding of the RNA onto the membrane. Remaining contaminants were then washed off the membrane in three subsequent washing steps and the flow-through was discarded after each wash. First, 400 μL of Pre-Wash buffer were added followed by a

spin at 13,500 RPM for 30 sec. I repeated this step before adding 700 μL of Wash Buffer with a subsequent spin at 13,500 RPM for 2 min. To avoid take-over of any ethanol remnants, I included an additional centrifugation step at 13,500 RPM for 1 min. The RNA was eluted through incubation of the membrane in 15 μL of DNAse/RNAse-free water for 1 min. Eluted RNA could then be obtained in a 1.5 mL Eppendorf tube during a 1-min-spin at 8600 RPM. RNA concentration and purity were measured with a NanoDrop 2000 and RNA samples were long-term stored at -80 °C.

Reverse Transcription: Extracted RNA was further transformed into cDNA for future quantitative reverse transcription PCR (qRT-PCR) experiments through reverse transcription. First, the following mix was prepared for each sample:

1.3 μL	Random Decamers
1 μL	10 mM dNTP mix
50 - 150 ng	RNA sample
	$\rightarrow$ make up to 13 μL with DNAse/RNAse-free water
13 μL	

For each set of experiments, the same amount of individual sample RNA was used to ensure comparability between future qRT-PCR results. Sample mastermixes were heated at 65 °C for 5 min and left on ice for at least 1 min. Then, 7 μL of a freshly prepared buffer containing the SuperScript III enzyme to perform the reverse transcription were added to each sample.

4 μL	5x first strand buffer (Thermo Fisher, 18080044)
1 μL	0.1 M DTT (Thermo Fisher, 18080044)
1 μL	RNase OUT recombinase RNase inhibitor (Thermo Fisher, 10777019)
1 μL	SuperScript III RT (Thermo Fisher, 18080044)
7 μL	

Reverse transcription was run in a T100 Thermal Cycler (BioRad) at

$$25\ ^\circ\text{C},\ 5\ \text{min} \rightarrow 50\ ^\circ\text{C},\ 45\ \text{min} \rightarrow 70\ ^\circ\text{C},\ 15\ \text{min}.$$

Finally, the resulting cDNA was diluted 1:10 in DNAse/RNAse-free water and long-term stored at -20 °C.

2.4.4 Polymerase chain reaction (PCR)

I performed PCR tests using a standard *Taq* DNA polymerase on extracted DNA from hES and NSC to examine the correct insertion of the neomycin cassette into exon 11 of the TSC2 gene.

PCR: 200 ng DNA of each sample was used to prepare 100 μL of PCR product. I used the following primer combinations to assess the overlapping region between TSC2 exon 11 and the inserted neomycin cassette:

1. TSC2 Forward - Neomycin Reverse
2. Neomycin Forward - TSC2 Reverse
3. TSC2 Forward - TSC2 Reverse

Mastermixes for each primer combination were prepared as follows

10 μL	10X Standard Taq Reaction Buffer
2 μL	10 mM dNTPs
2 μL	10 μM Forward Primer
2 μL	10 μM Reverse Primer
0.5 μL	*Taq* DNA polymerase
16.5 μL	

Respective volumes of DNA templates were added for each sample and the whole mix was topped up to 100 μL with DNAse/RNAse-free water. The PCR was run on a RT-PCR machine using the following protocol:

⇒ Initiation at 95 °C, 30 sec

↔ Denaturation at 95 °C, 30 sec
↔ Annealing at 61 °C, 60 sec
↔ Elongation at 68 °C, 75 sec
} 35 x

→ Final elongation at 68 °C, 5 min

→ Store at 4 °C, ∞

Gel electrophoresis: To examine successful amplification, PCR products were separated on a 1 % agarose gel in 0.5X TBE buffer (*for 10X TBE Buffer: 121.1 g Tris base (1 M), 61.8 g Boric acid (1 M), 7.4 g EDTA (0.02 M) in 1 L of dH_2O, then dissolve further in dH_2O*) and visualised with a UV-sensitive in-gel staining (SYBR Safe). 15 μL of PCR product mixed with 3 μL of gel loading dye were carefully transferred into each well with the first well being loaded with 5 μL of Gene Ruler Mix DNA Ladder. DNA fragments were separated by size by applying a voltage of 180 V for 55 min to the gel.

2.4.5 Quantitative reverse transcription polymerase chain reaction (qRT-PCR)

Quantitative RT-PCR was used to examine the expression levels of NMDA and AMPA receptor subunits in differentiated neurons, glial glutamate receptors in derived astrocytes, various neural cell types markers over the course of neuronal differentiation as well as key genes of different metabolic pathways. Table D gives an overview of sequences for respective forward and reverse primers. All cDNA samples were measured in duplicates on a 02 mL 96-well PCR plate (Starlab, E1403-7700) on a StepOnePlus Real-Time PCR System (Applied Biosystems) and negative controls without the addition of cDNA template were included for all gene mastermixes.

Per sample, a gene mastermix was prepared as follows:

10 μL	SYBR green (Thermo Fisher, 4309155)
6.2 μL	DNAse/RNAse-free water
0.9 μL	Forward primer (10 μM stock)
0.9 μL	Reverse primer (10 μM stock)
18 μL	

18 μL of the gene mastermix and 2 μL of cDNA template were transferred into the respective well of the PCR plate and run with the following protocol:

$\Rightarrow$ Holding Stage at 95 °C, 10 min

$\rightarrow$ Cycling Stage

$\leftrightarrow$ 95 °C, 15 sec
$\leftrightarrow$ 60 °C, 60 sec
} 40 x

$\rightarrow$ Melting Curve Stage

$\rightarrow$ 95 °C, 15 sec
$\rightarrow$ 60 °C, 1 min
$\rightarrow$ 95 °C, 15 sec

Analysis: First, the basis level of cellular expression was determined by averaging the CT values of all duplicate measures of the two house keeping genes Actin and HRPT ($\rightarrow CT_{\text{housekeeping}}$). Then, gene and sample-specific CT values were averaged over both duplicates ($\rightarrow CT_{\text{Sample}}$) and further normalised to the level of basis expression and reported as

$$\Delta CT = 2^{-(CT_{\text{Sample}} - CT_{\text{housekeeping}})}.$$

In cases where it was feasible to assign a control sample, the gene-specific expression level of this control sample was similarly first normalised to the basic cellular expression ($\rightarrow CT_{\text{ControlSample}}$). Then, each individual sample was normalised to the control sample's expression level and was reported as

$$\Delta\Delta CT = 2^{-(CT_{\text{Sample}} - CT_{\text{Housekeeping}} - CT_{\text{ControlSample}})}.$$

2.4.6 Western Blotting

Western blotting was used to examine protein levels in various cellular samples for different scientific questions throughout my project. Beforehand, cellular samples were lysed as described above (see section 2.4.1) and protein concentrations were quantified by a standard

bicinchoninic acid (BCA) assay (see section 2.4.10).

Gel electrophoresis: Protein samples were loaded onto NuPAGE 4-12 % BisTris Gels to be separated by size in a gel electrophoresis. First, sample mixes were prepared as follows:

2.5 μL	Loading dye
1 μL	Reducing agent
x μL	Volume of protein to obtain 5 μg
	$\rightarrow$ make up to 20 μL with DNAse/RNAse-free water

Sample mixes were denaturated at 70 °C for 10 min and kept on ice until use. 18 μL of each sample mix were transferred into a well of a 12 or 15-well gel with the first well being loaded with 5 μL of SeeBlue Plus2 protein ladder. The gel electrophoresis was performed in a MiniGel tank from Invitrogen with 150 V being applied for 35-40 min. Two different running buffers were used, depending on the size of the protein of interest (MES Buffer: small to medium-sized proteins, MOPS Buffer: medium to large-sized proteins).

Transfer: After completion of the gel electrophoresis, separated proteins were transferred onto a nitrocellulose membrane using the Trans-Blot Turbo Transfer System (BioRad).

Blocking and antibody application: After transfer, the nitrocellulose membrane was placed into a clean lid of a pipette box containing 5 % bovine serum albumin (BSA) in TBS-T buffer (10 % TBS in dH_20 + 0.1 % Tween20). Membranes were kept on a shaker at 50 - 70 RPM at RT for an hour to block. Afterwards, membranes were incubated with the respective primary antibodies in 1 % BSA in TBS-T on a shaker either for 2 h at RT or at 4 °C overnight. After that, the membranes were washed with TBS-T three times for 5 min each while being kept on a shaker at RT and subsequently incubated with the secondary

antibody (Goat anti-Rb, conjugated with horseradish peroxidase (HRP)) in 1 % TBS-T at RT on a shaker for 60 min. Then, the membranes were subject to three more washes with TBS-T for 5 min each to ensure proper cleaning from all unbound antibody remnants.

ECL detection: Positively-stained proteins were detected using a standard enhanced chemiluminescence (ECL) protocol. In brief, a luminol-containing reagent A and a hydrogen peroxide-containing reagent B were equally mixed at RT directly before use. Each blot was incubated in 2 mL of ECL detection solution for 1 min on a shaker at RT. The excess liquid was removed and blots were quickly washed in TBS-T. The light emitted by the HRP-catalysed oxidation of luminol was detected with a CCD camera.

Antibody stripping: In some instances, blots were used twice for the detection of different proteins. To enable the detection of multiple proteins on the same blot, bound antibodies were stripped off the blot first. Reagent A and reagent B from the Blot Restore Kit were diluted 1:10 in sterile water directly before use. Blots were first washed in TBS-T on a shaker at RT for 5 min and subsequently incubated with the diluted reagent A and then with reagent B on a shaker at RT for 10 min each. After that, I washed the blots one more time for 5 min in TBS-T. Blots had to be blocked in 5 % BSA in TBS-T again as described above prior to the next antibody application.

2.4.7 Plasmid DNA purification

A TSC2 overexpression plasmid as well as a TSC2 short RNA (shRNA) plasmid were ordered from Addgene in a bacterial stab. To obtain highly purified plasmid DNA, bacteria were first grown on agar plates and in LB broth yielding 150 mL of bacterial culture which was then further processed with the EndoFree Plasmid Maxi Kit from Qiagen. In brief, bacterial cells were lysed under alkaline conditions releasing plasmid DNA, endotoxins, RNA,

proteins and other cellular contents. Endotoxins (= lipopolysaccharides LPS) are part of the bacterial cell wall of gram-negative bacteria. An endotoxin removal step included in the kit ensured a final endotoxin level of less than 0.056 ng LPS which is favourable as endotoxins can interfere with subsequent plasmid transfections. Further, the cellular lysate was processed over a membrane selectively binding DNA with several washing steps until the plasmid DNA was yielded via centrifugation.

Bacterial culture: Bacterial cultures grown from bacterial stabs obtained from Addgene were grown on LB agar plates and in LB broth bought from Sigma and made up according to manufacturer's instruction. Bacterial stabs were streaked onto agar plates infused with ampicillin using a sterilised bacterial loop. The bacteria were spread out widely to enable the growth of singular colonies. The agar plate was incubated at 37 °C overnight.
The next day, a singular colony was transferred from the incubated agar plate into 2 mL of LB broth supplemented with 100 μg/mL ampicillin in a 15 mL tube with round bottom using a sterile pipette tip. The broth was briefly vortexed and incubated at 37 °C for 6-8 h. Then, the incubated broth was poured into 150 mL LB broth supplemented with ampicillin in a sterile conical flask which was then further incubated at 37 °C overnight while being shacked at 225 RPM.

Plasmid DNA purification: After centrifugation at 6000 RPM for 15 min at 4 °C and removal of the supernatant, the bacterial pellet was resuspended in 10 mL of Buffer P1 of the EndoFree Plasmid Maxi Kit. The solution was mixed gently with an equal volume of Buffer P2 until the whole solution turned evenly blue. After 3 - 5 min, 10 mL of Buffer P3 were added and mixed gently until the colour had vanished to white. A filter unit was blocked with a plug before the whole mixture was poured into it and allowed to equilibrate

for 10 min. The solution was plunged into a 50 mL tube with the precipitated DNA and protein staying inside the filter unit. 25 mL of Buffer ER were added and incubated on ice for 30 min. After this, the solution was poured over the kit's specific column and allowed to travel through at its own pace. The membrane was then washed with 30 mL Buffer QC twice before the purified plasmid DNA could be eluted in 15 mL Buffer QN.

The buffer containing the eluted DNA was allowed to travel through and topped up with 10.5 mL iso-propanol before a spin at 3000 RPM for 1 h. After supernatant removal, the DNA pellet was resuspended in 10 mL 70 % ethanol followed by another spin at 3000 RPM for 30 min. The supernatant was again removed and the pellet dried on air before being finally resuspended in 200 μL TE Buffer. DNA concentration was measured using a NanoDrop 2000 and DNA samples were long-term stored at -20 °C.

2.4.8 Flow cytometry

I performed all flow cytometry experiments in the Flow Lab at the Sir William Dunn School of Pathology, University of Oxford.

Sample preparation: Depending on cellular identity and stage of differentiation, cells were detached using the most suitable detachment method and processed further until a cell pellet was yielded. The cell pellet was fixed in 100 μL 4 % PFA for 15 - 30 min at RT and washed with 200 μL FACS buffer (1 % FBS, 10 μg/mL IgG from human serum in PBS). Then, cells were permeabilised in 1 mL ice-cold 100 % methanol for 30 min at 4 °C. Such prepared samples could be long-term stored in methanol at -20 °C.

Antibody staining: For staining, methanol-preserved samples were first spun at 3,500 RPM for 5 min and the resulting cell pellet was washed twice with FACS buffer. Then, I incubated the cells with primary (for 45 min) and secondary antibodies (for 20 min) in FACS

buffer at RT with two consecutive washes in FACS buffer and a spin at 3500 RPM for 5 min after each antibody incubation. In a final step, cells were resuspended in 1 mL FACS buffer and could be stored for two weeks at 4 °C.

Flow cytometry: Stained samples were measured on a CyAn ADP flow cytometer according to the specific manufacturer's instructions.
Data analysis: Data were analysed in FlowJo according to standard analysis and gating protocols.

2.4.9 Immunofluorescence microscopy

I used immunofluorescence microscopy for qualitative and quantitative examinations of various cellular populations. Images were visualised in a microscope facility at the Department of Pharmacology, University of Oxford.

Sample preparation: Cells were plated on sterile coverslips in a 24-well plate coated as usual for the respective cell type and stage of differentiation and cultures were maintained as usual. When the desired time point was reached, cells were fixed as follows: 500 μL 4 % PFA were directly and carefully added to the media to prevent washing off of the cultures. Cultures were incubated for 10 min after which the media and PFA were removed. Then, cells were incubated in 500 μL 4 % PFA again for 10 min and carefully washed with PBS afterwards twice. Coverslips could be long-term stored in PBS at 4 °C with the plate sealed with parafilm to prevent the cultures from drying out.

Staining: After removal of PBS, cells were permeabilised in 300 μL 0.1 % Triton X-100 in PBS for 15 min at RT. Cells were then blocked for 1 h at RT in either 300 μL of 10 % goat serum or 10 % donkey serum in PBS corresponding to the host species of the

secondary antibody. Then, the cultures were incubated with the primary antibodies at their respective concentration in 300 μL of 5 % goat serum or 5 % donkey serum at 4 °C overnight. The next day, cells were carefully washed three times with 500 μL PBS and incubated with secondary antibodies in 300 μL of 5 % goat serum or 5 % donkey serum in PBS for 45 min at RT followed by another three PBS washes. Nuclei were stained with 300 μL of 600 nM DAPI in PBS for 10 min at RT. Afterwards, coverslips were mounted with cells facing downwards onto microscope slides in DAKO mounting media.

Imaging: The stained samples were imaged using an epifluorescent microscope (BX40, Olympus). The gain and exposure time was first optimised for each fluorophore and then kept consistent for all slides.

Data analysis: Subsequent image analysis was performed in FIJI/ImageJ.

Cell size: The cell size was measured in μm^2 after scaling the respective image. Cells were outlined manually and measured individually using the ROI manager. I used fluorescent images from NSCs stained with anti-GFAP antibodies and bright-field images of hES.

Rosette area: Rosettes were identified on the merged image using ZO-1 staining for the lumen and DAPI and HuC/HuD stainings to identify the extension of each individual rosette. A circle was manually drawn around each rosette and the circle area was measured in μm^2 after scaling the image appropriately.

Immunofluorescence intensity and signal: First, the image was transformed into an 8-bit image. Positive cells were then counted using the *Analyse Particles* feature of FIJI/ImageJ after the colour threshold was set appropriately. The colour

threshold was found for each experiment manually by fitting the threshold in five random images from the same experimental set and then applying this threshold to the whole set.

To determine immunofluorescence intensity, cells were measured in FIJI/ImageJ and I calculated the *corrected total cell fluorescence (CTCF)* as

CTCF = integrated density - (cell area × mean background fluorescence reading).

2.4.10 Colorimetric assays

Protein quantification – BCA assay

I performed a colourimetric assay based on the *biuret reaction*, the reduction of Cu^{2+} to Cu^{+} by protein in alkaline conditions, and BCA, which forms a purple reaction product with Cu^{+}, to determine the concentration of protein in any protein sample. The assay was performed in 96-well plates and a standard concentration was included on each individual plate as follows

Vial	Vol of PBS [μL]	Vol of BSA [μL]	Final protein conc [μg/ml]
A	0	300 (stock)	2000
B	125	375 (stock)	1500
C	325	325 (stock)	1000
D	175	175 (B)	750
E	325	325 (C)	500
F	325	325 (E)	250
G	325	325 (F)	125
H	400	100 (G)	25

For each sample, 200 μL working reaction containing a 50:1 mix of the kit's reagent A and B was mixed with 25 μL sample per well and incubated at 37 °C for 1 h. Results were read with a plate reader at 562 nm. The results were analysed in a custom-made script in R

by first fitting a standard curve and then inferring the total protein concentration for each sample.

Celltox Green assay of cell death

To measure cellular death caused by low glucose treatment in neuronal populations, I used the CellTox Green Cytotoxicity Assay from Promega according to the manufacturer's instruction (Endpoint Method). Assays were performed in 96-well plates on neurons at different stages of differentiation. Neurons were differentiated in normal 25 mM glucose media and cell death was measured 24 h after switching the media to 5 mM culture media in half of the wells. Non-cellular background controls were included on every plate. To ascertain a reasonable measure of the maximum cell death (that is the death of the whole population), I included cytotoxicity control wells in which I lysed the whole population 30 min prior to reading with the kit's lysis solution.

100 μL of CellTox Green Reagent (2X) were added to each well and mixed on an orbital shaker at RT for 1 min followed by a steady 15 min-incubation at RT in the dark. The fluorescence signal was then measured at Excitation 485 nm / Emission 520 nm. Individual results for each well are reported as

$$\frac{\text{Signal}_{\text{Sample}} - \text{Signal}_{\text{Background}}}{\text{Signal}_{\text{CytotoxicityControl}} - \text{Signal}_{\text{Background}}}$$

2.4.11 Seahorse experiments

Energy metabolism was assessed in TSC2 +/+ and TSC2 -/- Roche NSCs and NGN2 neurons on day 8 using an Agilent Seahorse Flux Analyser in Richard Wade-Martin's lab. NSCs were plated on Agilent Seahorse Cell Culture plates and cultured until confluent in their standard 25 mM glucose media. NGN2 neurons were directly differentiated on

Seahorse plates in 25 mM glucose media until day 8. Then, half of the wells were maintained in the respective low glucose media versions for 24 h prior to measurement. I supplemented Seahorse XF base medium with D-glucose, sodium pyruvate and GlutaMAX to create high (25 mM) and low (5 mM) glucose media versions for the experiment. Media were adjusted to pH 7.4 directly before usage with *NaOH* and *HCl* as required. For the Seahorse measurement, cells were adjusted in the respective Seahorse high and low glucose media for 30 min. The experiment was then performed using the Seahorse XF Glycolytic Rate Assay Kit as follows:

Four Base measurements every 6 min

→ Application of 0.5 μM rotenone / antimycin A

→ Three measurements every 6 min

→ Application of 50 mM 2-Desoxy-D-glucose

→ Four measurements every 6 min

Data were normalised to the protein content of each respective well (measured by BCA assay) and analysed using the Agilent Seahorse Wave Desktop Software 2.6.

2.4.12 Growth curves and doubling time

Growth curves were obtained from TSC2 +/+ and TSC2 -/- hES and NSCs using bright-field images taken daily over a course of four days. Prior to cell seeding, wells were marked with a cross on the bottom to ensure pictures could be taken from the same positions every day. Four pictures were taken per well every day from each inner corner of the well. Cells were counted using the *Analyse Particles* plug-in on ImageJ/FIJI. The doubling time *DT* was calculated according to

$$DT = \frac{48 * ln(2)}{ln(Cellcount_{Day4}) - ln(Cellcount_{Day2})}.$$

2.5 Multi-electrode array recordings

The Axion BioSystems MEA system was used to obtain MEA recordings from hPSC-derived glio-neuronal cultures. NSCs derived through dual SMAD inhibition were plated on clean 48-well cytoview MEA plates and differentiated and maintained according to protocol. When seeded, cells were drop-plated at approximately 100,000 cells / cm^2 in the middle of the electrode grid using a 10 μL-pipette on a 3 μL drop of coating agents to ensure a high neuronal density over the electrodes. Glio-neuronal co-cultures were established by plating rat or human astrocytes around ten days later on top of the neuronal cultures at a density of 100,000 astrocytes / cm^2.

Individual recordings from each well were taken using a Maestro system (Axion BioSystems) with associated Axis software (Axion BioSystems). During the 2 min-long recording, plates were kept at 37 °C. Recordings of neuronal activity was started after a 5 min-long settling period on the recorder and lasted for 2 minutes.

Neuronal spiking and bursting activity were analysed with a standard MEA commercial software (AxISMetricPlottingTool, Axion BioSystems; NeuralMetricTool, Axion BioSystems). The following definitions for different MEA metrics were applied:

Metric	Definition
Spike	$>$ 6 standard deviations above noise band
Active Electrode	$>$ 5 spikes/min
Burst	Maximum interspike interval: 100 ms & Minimum number of spikes: 5

2.6 Underlying biophysical model for DCM of MEA data

The underlying generative neuronal model was implemented in the SPM12 software for DCM analysis with support from Prof Rosalyn Moran. We used the canonical microcir-

cuit model (CMM) for DCM comprising three excitatory sources (marked $\epsilon 1$, $\epsilon 2$, and $\epsilon 4$) and one inhibitory source (marked $\gamma 3$) to underlay every MEA electrode but, for simplicity reasons, did not consider long-range connections between local microcircuits. This model comprises four distinct neuronal populations, each of which possesses parameters representing α-amino-3-hydroxy-5-methyl-4-isoxazolepropionic acid (AMPA), N-methyl-D-aspartate (NMDA) and γ-aminobutyric acid $(\mathrm{GABA})_{\mathrm{A}}$ receptors. Priors were informed by previous DCM analyses on EEG data [255] and by measurements performed by myself prior to model construction as outlined in chapter 5. An overview of all parameters used in the model is given by table 2.6.

In this model, inhibitory interneurons feed into all three excitatory populations with varying strength and the three excitatory populations were interconnected canonically. Further, each neuronal population possesses inhibitory feedback loops. Connectivity strengths were chosen for each connection in accordance with model posterior densities for a similar CMM previously established on human EEG data [255] as follows:

$$\mathrm{GE} = \begin{bmatrix} & \boldsymbol{\epsilon 1} & \boldsymbol{\epsilon 2} & \boldsymbol{\gamma} & \boldsymbol{\epsilon 3} \\ \boldsymbol{\epsilon 1} & 0 & 0 & 0 & 0 \\ \boldsymbol{\epsilon 2} & 4 & 0 & 0 & 0 \\ \boldsymbol{\gamma} & 4 & 0 & 0 & 2 \\ \boldsymbol{\epsilon 3} & 0 & 4 & 0 & 0 \end{bmatrix} \qquad \mathrm{GI} = \begin{bmatrix} & \boldsymbol{\epsilon 1} & \boldsymbol{\epsilon 2} & \boldsymbol{\gamma} & \boldsymbol{\epsilon 3} \\ \boldsymbol{\epsilon 1} & 8 & 0 & 2 & 0 \\ \boldsymbol{\epsilon 2} & 0 & 8 & 2 & 0 \\ \boldsymbol{\gamma} & 0 & 0 & 32 & 0 \\ \boldsymbol{\epsilon 3} & 0 & 0 & 8 & 128 \end{bmatrix}$$

$$\mathrm{S}_{AMPA} = \begin{bmatrix} & \boldsymbol{\epsilon 2} & \boldsymbol{\epsilon 3} \\ \boldsymbol{\epsilon 1} & 1 & 0 \\ \boldsymbol{\epsilon 2} & 0 & 1 \\ \boldsymbol{\gamma} & 0 & 2 \\ \boldsymbol{\epsilon 3} & 0 & 0 \end{bmatrix} /8 \quad \mathrm{S}_{NMDA} = \begin{bmatrix} & \boldsymbol{\epsilon 1} & \boldsymbol{\epsilon 3} \\ \boldsymbol{\epsilon 1} & 1 & 0 \\ \boldsymbol{\epsilon 2} & 0 & 1 \\ \boldsymbol{\gamma} & 0 & 2 \\ \boldsymbol{\epsilon 3} & 0 & 0 \end{bmatrix} /8$$

with: GE, intrinsic excitability connection strengths; GI, inhibitory connection strengths; S_{AMPA}, extrinsic AMPAR connection strengths; S_{NMDA}, extrinsic NMDAR connection strengths.

Synaptic connectivity was modelled as capacitive current flows across the membrane. Changes in membrane capacitance were implemented to be dependent on ligand-gated inhibitory (Cl^-) and excitatory ($Na^+/Ca2^+$) current flow as well as ion flow through fast $GABA_A$ and AMPA receptors and slow NMDARs. Conductance at the membrane is regulated by the number of open channels and depends on pre-synaptic input and channel time constants. These were fixed at 4 ms ($GABA_AR$), 16 ms (AMPAR) and 400 ms (NMDAR), respectively, and were implemented into the system via their inverse, the so-called channel rate constants. We choose the NMDAR time constant in accordance with the detected prenatal-like expression of the GRIN1 and GRIN2B subunits. Conductance for each channel was implemented via the following ordinary differential equations:

$$\dot{g}_{Na} = \kappa_{AMPA}(\gamma_{ex}\sigma - g_{Na}) \tag{2.1}$$

$$\dot{g}_{Cl} = \kappa_{GABA}(\gamma_{in}\sigma - g_{Cl}) \tag{2.2}$$

$$\dot{g}_{Ca} = \kappa_{NMDA}(\gamma_{ex}\sigma - g_{Ca}) \tag{2.3}$$

with: g_{Na}, AMPAR conductance; g_{Ca}, NMDAR conductance; g_{Cl}, $GABA_AR$ conductance; κ,

respective rate constants; γ_{ex}, coupling from excitatory population; γ_{in}, coupling from inhibitory population and σ, pre-synaptic firing rate.

NMDA receptors are characterised by a voltage-dependent magnesium block that ensures conductance only at coinciding pre-synaptic transmitter release and post-synaptic depolarisation [182]. We modelled this block as

$$f_{Mg} = \frac{1}{1 + 0.2e^{-0.08V}} \tag{2.4}$$

Overall, fluctuations in the membrane potential were derived from the classic Hodgin-Huxley model of single-nerve conductance [105] and implemented via the following ordinary differential equation:

$$\dot{V} = \frac{g_{Na}(V_{Na} - V) + g_{Ca}(V_{Ca} - V)f_{Mg} + g_{Cl}(V_{Cl} - V) + g_K(V_K - V)}{C} \tag{2.5}$$

with: V, membrane potential (voltage); C, membrane capacitance and f_{Mg}, non-linear NMDAR magnesium block.

We also included priors for the reversal potentials for potassium (-70 mV), sodium (60 mV), chloride (-90 mV) and calcium (via NMDAR, 10 mV) as well as a threshold potential at -40 mV. The pre-synaptic firing was modelled to be dependent on the membrane capacitance of the efferent population. Lastly, the system was characterised by parametrisation of the overall excitability, background activity and exogenous input reaching the system via the population $\epsilon 1$, mean firing rate and noise.

The final part of the model formed a sigmoidal firing rate function to transform the current

postsynaptic membrane potential of each subpopulation into an average firing rate given a specific threshold potential.

Figure 5.6 in section 5.3.2 shows a schematic of the underlying CMM.

2.7 Statistical analysis

I performed a Shapiro Test to test for normality. If not stated otherwise, I tested for statistical significance in mean values by using an ANOVA test in normally distributed data and the Kruskal Wallis Test in non-normally distributed data. To test for statistically significant differences in median values, I used the Wilcoxon rank sum test for independent samples. To avoid a type-1 error when performing multiple comparisons, I used the Bonferroni correction to adjust the p-values accordingly. A p-value of less than 0.05 was considered as a marker for a *significant* difference between groups throughout my thesis. All statistical testing was done in R with my own scripts.

Plots were generated using R ggplot2 displaying the mean μ and standard deviation SD unless otherwise stated. In cases with less than two values per group, the actual values were directly displayed together with the mean.

Acronym	Explanation
S	Overall Excitability
T(1,1)	Inhibitory Time Constant 1
T(2,1)	Inhibitory Time Constant 2
CV(1)	Capacitance in excitatory spiny stellate cells
CV(2)	Capacitance in superficial pyramidal cells
CV(3)	Capacitance in inhibitory interneurons
CV(4)	Capacitance in deep pyramidal cells
E	Background activity and exogenous input
A1(1,1)	Forward extrinsic connection
A2(2,1)	Backward extrinsic connection
A1(1,2)	Forward extrinsic connection
A2(2,2)	Backward extrinsic connection
H(1,2,1)	Excitatory spiny stellate cells to superficial pyramidal cells
H(1,3,1)	Excitatory spiny stellate cells to inhibitory interneurons
H(2,1,1)	Superficial pyramidal cells to excitatory spiny stellate cells
H(2,4,1)	Superficial pyramidal cells to deep pyramidal cells
H(3,1,1)	Inhibitory interneurons cells to excitatory spiny stellate cells
H(3,3,1)	Inhibitory interneurons self-connection
H(3,4,1)	Inhibitory interneuron cells to deep pyramidal cells
H(4,3,1)	Deep pyramidal cells to inhibitory interneurons
H(4,4,1)	Deep pyramidal cells self-connection
H(1,1,2)	Excitatory spiny stellate cells self-connection
H(1,2,2)	Excitatory spiny stellate cells to superficial pyramidal cells
H(1,3,2)	Excitatory spiny stellate cells to inhibitory interneurons
H(2,1,2)	Superficial pyramidal cells to excitatory spiny stellate cells
H(2,4,2)	Superficial pyramidal cells to deep pyramidal cells
H(3,1,2)	Inhibitory interneurons to excitatory spiny stellate cells
H(3,3,2)	Inhibitory interneurons self-connection
H(3,4,2)	Inhibitory interneurons to deep pyramidal cells
H(4,3,2)	Deep pyramidal cells to inhibitory interneurons
H(4,4,2)	Deep pyramidal cells self-connection
D(1)	Delay in signal transmission
L(1,1)	
L(1,2)	
L(1,3)	
L(1,4)	
a(1,1) - f(2,1)	Noise
VL	Reversal potential leak (K)
VE	Reversal excitatory potential (Na)
VI	Reversal inhibitory potential (Cl)
VR	Threshold potential
GL	Leak conductance
M	Mean firing rate
BE	Average background activity
Vx	Neural-mass approximation to the covariance of states

TABLE 2.6: **DCM Parameters.** Parameter acronyms and explanations of all parameters used for model construction in DCM analysis of MEA data.

3 | The impact of TSC2 on neural development

3.1 Introduction

The TSC1:TSC2-mTORC1 pathway has an important role in neurogenesis, neural circuit formation, and neuronal function [106, 144, 151, 153]. The pathway also affects the development and function of glia [144]. Much of the current knowledge on the link between this crucial pathway and neural development has been obtained from animal models. Germline knockout of either TSC1 or TSC2 is lethal in rodent models underpinning their essential relevance for normal development [132, 198]. Subsequently, different Cre-recombinase-based conditional knockout models have been established allowing the specific knockout of TSC1 or TSC2 in either neurons or glial cells at different stages during development [64, 79, 197, 269].

Due to inherent differences between rodents and humans in neurodevelopmental milestones and resulting cortical structure, there is a need for human-based models to investigate the role of the TSC1:TSC2-mTORC1 pathway in human brain development. Several stem cell-derived models using cultures harbouring mutations in either the TSC1 or TSC2 gene have provided insights on how these genes affect specific milestones, particularly in early stages of neurodevelopment [19, 44, 64, 93, 150, 162, 164, 186, 253, 304]. Most of these

studies have demonstrated that loss-of-function mutations in TSC1 and TSC2 have a relatively minor effect on differentiation to NSCs and NSC expansion but notably disturb the subsequent differentiation of the NSC pool into neurons and astrocytes.

In contrast to rodents, human brain development is characterised by a massive cellular expansion during a prolonged neural progenitor stage in the ventricular and particularly in the subventricular zone followed by a sequential differentiation of first lower and then upper-layer cortical neurons [79]. The spatial and temporal diversity of neural progenitor subtypes in the VZ and SVZ with its inner and outer regions is considered to be the fundamental basis for the resulting variety of neuronal subtypes in the human cortex [234]. The neurogenic phase is terminated by a delayed gliogenic switch around birth leading to glial cells predominantly being produced postnatally [179].

In vitro, NEC (forming the early layers of the neural tube *in vivo*) and NSC successors differentiated from hES cells have been shown to harbour mostly anterior followed by dorsal telencephalic characteristics yielding predominately cortical and excitatory neurons [148, 154]. They express anterior NSC markers such as Pax6 and FOXG1 but usually show little expression of posterior genes such as HOX genes [148]. Their ongoing development results in NSCs of a dorsal fate characterised by Pax6 expression but absent ventral forebrain markers such as NKx2.1 [149]. Therefore, most *in vitro* differentiation protocols produce excitatory glutamatergic neurons stemming from dorsal neuroprogenitors with very little production of inhibitory interneurons which stem from NKx2.1+ ventral progenitors [149].

Different approaches exist for neural differentiation *in vitro* that can broadly be divided into two major categories: neuroectoderm induction with subsequent neurogenic differentiation akin to neurodevelopmental mechanisms *in vivo* and direct neurogenic conversion through forced induction of specific genes. The former differentiation protocols exploit the

ectodermic drive inherent in hPSC leading to differentiation into neuroectodermal tissue once pluripotency clues are lifted. Dual SMAD-inhibition is a prominent example of this type of protocol which combines the liberation of hPSCs from pluripotency-maintaining media with the blockage of endodermal and mesodermal development through the application of SMAD inhibitors [30]. Ultimately, this leads to predominantly cortical neurons as corticogenesis is the default trajectory of neurodevelopment [284]. Dual SMAD-inhibition protocols mimic human neurodevelopment *in vivo* [30]. Differentiation via dual SMAD-inhibition follows embryonic milestones in real-time and thus, allows *in vitro* examination of crucial neurodevelopmental steps from different neural progenitor subtypes to lower and upper-layer neurons and finally astrocytes.

In vivo, glial cells are produced from the remaining pool of NSCs after neurogenesis has been completed [179]. Astrocytes play major roles in brain development and neuronal functioning and glio-neuronal co-culturing is often used to improve neuronal maturation *in vitro*. Due to obvious limitations in the accessibility of human brain tissue, purified murine or rat astrocytes are frequently used in *in vitro* studies. There are, however, major differences in human and rodent astrocytes including

- *a larger average cell length,*
- *increased structural complexity,*
- *the existence of at least two more glial classes in humans,*
- *five times faster speed in calcium signalling and*
- *differences in their response to various drugs.*

Due to these differences, it is favourable to use human astrocytes in neural model systems *in vitro* to increase the accuracy and translational value of such models [32]. Various protocols, either following the neurodevelopmental processes *in vitro* or via direct conversion

methods, have been proposed to allow the generation of various human glial subtypes [32]. Neuronal and glial differentiation protocols that follow *in vivo* timelines are time-consuming and do not yield mature cells with postnatal transcriptional and functional features in reasonable experimental time frames. Undirected differentiation protocols feature high intra- and interline variability with regards to neuronal and glial yield [278]. The reliance on many different growth factors and small molecules with biological batch differences further increases this variation [246].

Directed conversion of hPSCs into neural cells addresses these challenges. Directed conversion can be achieved by direct lineage transformation of fibroblasts into so-called induced neurons [6] or induced astrocytes [24], without prior reprogramming into iPSCs. However, directed conversion can also be applied to hPSCs to derive either neurons, for example through forced expression of the neurogenic transcription factor NGN2 [300], or astrocytes, through forced expression of the gliogenic transcription factor nuclear factor 1A (NF1A) [259]. Directed conversion reduces the time required to yield morphologically mature neurons markedly to one to three weeks. Variability is greatly reduced and yield is increased when using directed conversion protocols. The NGN2 protocol has been shown to produce highly standardised layer 2/3 excitatory neurons with similar transcription profiles from different hPSC lines [300]. However, the direct transformation of hPSCs into neuronal or glial cells allows no opportunity to investigate unique neurodevelopmental aspects of neurogenesis and gliogenesis as they lack features of a distinct NSC phase.

In summary, both protocol types – developmental patterning and directed conversion – have advantages and disadvantages and should be considered complementary approaches to derive neural model systems. Developmental protocols such as dual SMAD-inhibition

follow neurodevelopmental milestones and are thus, uniquely suited to investigate early neurodevelopmental stages and their impact on neuronal output and circuit formation. On the other hand, they are time-consuming and suffer from high biological variability. In contrast, direct conversion protocols derive neurons and glia by surpassing early developmental stages. Directed conversion differentiation methods achieve a uniform population of the desired neuronal or glial type in shorter time periods but without the opportunity to examine early neurodevelopment.

3.2 Aims

To perform mechanistic investigations into the role of TSC2 in neural development and neuronal connectivity, I first aimed to reliably derive neurons and astrocytes from TSC2-mutated hES and their isogenic wild-type controls. I sought to take advantage of both methods of differentiation by first, using dual SMAD-inhibition to investigate the effects of TSC2 on the neurogenic period and second, quickly generating networks of NGN2 neurons to examine the role of TSC2 in neuronal connectivity. I aimed to generate human astrocytes from both genotypic lines to enable investigations on the impact of astrocytic function on neural circuit development. In general, this chapter makes the following contributions:

1. Characterise TSC2 +/+ and TSC2 -/- hES and NSC cell lines with regards to their transcriptional and translational TSC2 status, mTORC1 activation levels, and general cellular properties such as morphology, cell type, and proliferation characteristics.

2. Establish pharmacological and genetic methods to specifically upregulate and downregulate the TSC1:TSC2-mTORC1 pathway *in vitro*.

3. Establish neuronal differentiation protocols from these TSC2 +/+ and TSC2 -/- hES

lines. First, establish a developmental differentiation method to allow investigations into early neurodevelopmental phases. Second, implement a direct conversion neuronal differentiation protocol to allow the quick and reliable derivation of a uniform neuronal population.

4. Derive TSC2 +/+ and TSC2 -/- astrocytes using a commercially available glial differentiation method based on a developmental patterning protocol.

5. By using the developmental patterning protocol, investigate the impact of TSC2 gene knockout on neural cell fate *in vitro* through characterisation of the derived NSCs and neurons with regards to their morphology, proliferation, and transcriptional and translational maturity marker expression.

3.3 Results

3.3.1 TSC2 +/+ and TSC2 -/- hES and NSC lines.

I used a set of genetically engineered TSC2 +/+ and TSC2 -/- hES cell lines from Roche Hoffmann AG [44]. These lines were originally created at Roche Hoffmann AG using a zinc-finger nuclease-mediated targeted gene disruption. Hereby, a loxP-flanked phosphoglycerate kinase promoter (PGK)-driven neomycin phosphotransferase cassette (loxP-PGK-neo-loxP) was inserted into the AAVS1 safe harbour locus or into both alleles of exon 11 of the TSC2 gene of the well-characterised hES line SA-001 to create isogenic TSC2 +/+ and TSC2 -/- lines, respectively. Subsequently, TSC2 +/+ and TSC2 -/- lines of stable, self-renewing NSCs were differentiated at Roche Hoffmann AG using a modified dual SMAD-inhibition protocol [30]. The correct neomycin resistance cassette insertion into the AAVS1 locus in TSC2 +/+ lines and lack of off-target effects have previously been demonstrated (see [44]).

To confirm the correct insertion into the TSC2 gene exon 11, I generated two PCR products that span the overlapping regions between the TSC2 gene and the neomycin resistance cassette, one at the 3'-end of neomycin resistance cassette (labelled *TC* in figure 3.1 (B)) and one at the end of 5'-end of neomycin resistance cassette (labelled *CT* in figure 3.1 (B)). Both primer pairs span the zinc-finger nuclease-cutting site within the TSC2 gene as well as the adjacent parts of the neomycin resistance cassette. In TSC2 -/- hES and NSCs, I successfully amplified the 1 kbp PCR product *TC* and the 800 bp PCR product *CT* confirming the correct insertion of the neomycin resistance cassette into the TSC2 locus. No amplification of the cassette insertion sites was detected in TSC2 +/+ hES and NSCs.

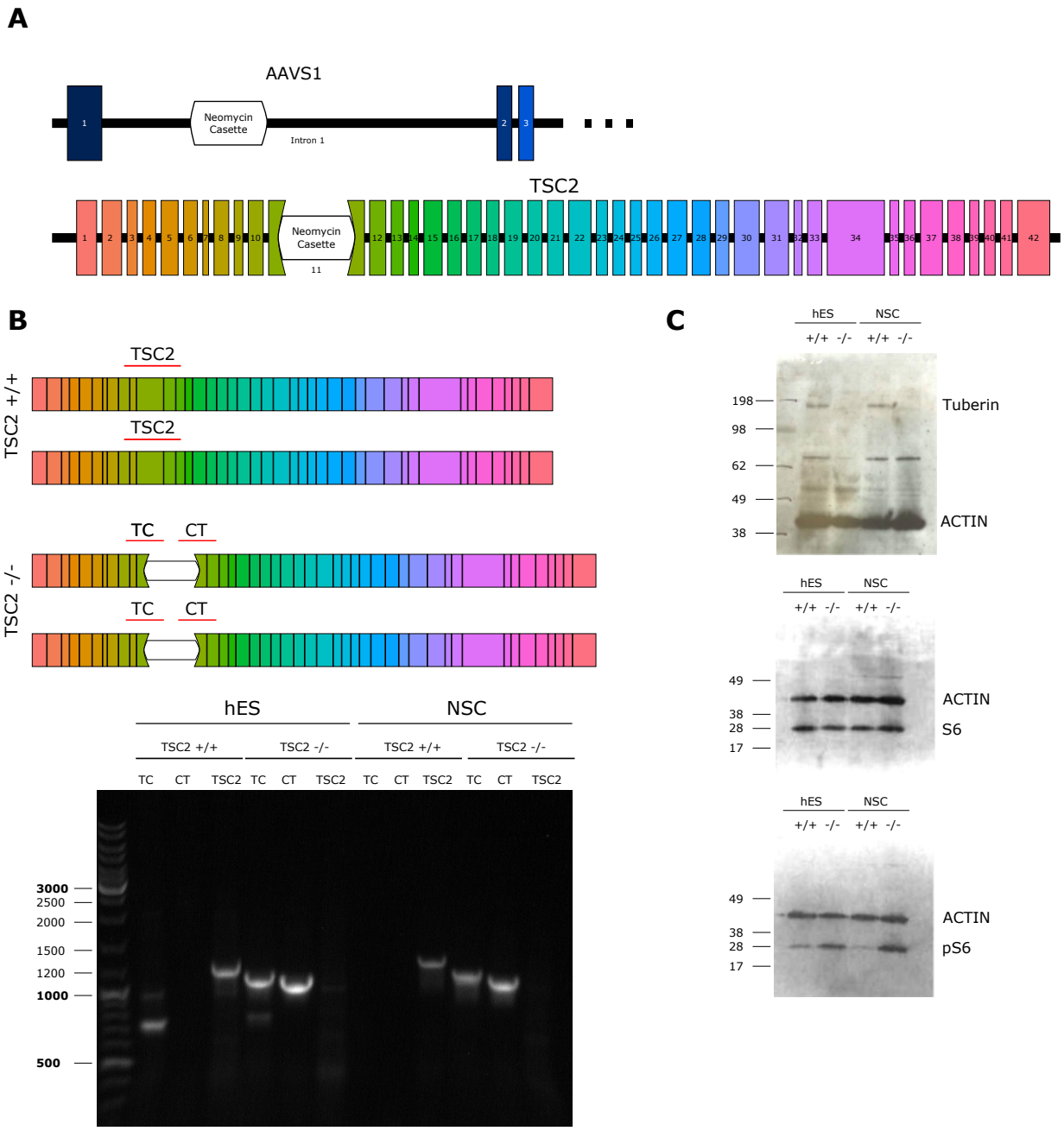


FIGURE 3.1: **Characterisation of TSC2 +/+ and TSC2 -/- hES and NSC lines** (A) Schematic of the neomycin resistance cassette insertion into either the AAVS1 intron 1 (for TSC2 +/+) or into both alleles of exon 11 of the TSC2 gene (for TSC2 -/-). (B) Primer binding sites to amplify the integration sites of the neomycin resistance cassette in exon 11 of the TSC2 gene. The gene products labelled *TC* and *CT* refer to the overlapping sites between the TSC2 gene and the cassette. Visualisation of the PCR products confirmed the correct insertion of the neomycin resistance cassette in TSC2 -/- hES and NSC but an absent insertion in TSC2 +/+ lines. Exon 11 of the TSC2 gene was amplified in TSC2 +/+ lines but not in TSC2 -/- lines (gene product labelled *TSC2*). (C) Western blotting confirmed the lack of TSC2 gene product tuberin resulting in mTORC1 hyperactivation (measured by an increase in pS6 expression with no increase in S6 expression) in the TSC2 -/- hES and NSC lines.

A 1.2 kbp PCR product could be generated using a primer pair spanning the Zinc-finger nuclease cutting site in the TSC2 exon 11 confirming no insertion of the 1.7 kbp big neomycin resistance cassette into this exon. The disruption of the TSC2 gene in exon 11 led to changes on the translational level, namely a complete lack of the TSC2 gene product tuberin (see figure 3.1 (C)). The lack of tuberin resulted in increased phosphorylation of the ribosomal protein S6, presumably due to a dis-inhibition of mTORC1.

There were no morphological differences in TSC2 +/+ and TSC2 -/- hES on bright-field imaging (see figure 3.2). Both hES cultures showed the characteristic appearance of feeder-free cultured hES, namely tightly packed mostly round cells with a high nucleus-to-cytoplasm ratio and a variable number of nucleoli [45]. Both cell lines produced similarly-sized cells with a mean area surface of $345.27 \pm 108.03\,\mu m^2$ (TSC2 +/+) and $380.60 \pm 121.51\,\mu m^2$ (TSC2 -/-) ($p = 0.736$). However, TSC2 deficiency shifted the range in cell size towards larger cells with a significant increase in cell size median in hES ($p = 0.03$).

In stable Roche NSCs, TSC2 +/+ and TSC2 -/- cells exhibited similar morphological features characteristic of NSCs in culture. Cells were elongated with multiple short processes, a reduced nucleus-to-cytoplasm ratio and tended to grow in star-like structures containing multiple cells. No differences could be found in the mean cellular surface area (Mean surface area TSC2 +/+: $5916.96 \pm 2108.02\,\mu m^2$, TSC2 -/-: $9447.24 \pm 4499.36\,\mu m^2$, $p = 0.411$). However, TSC2 -/- NSCs displayed a much wider range of cell surface areas with the largest TSC2 -/- cell being 1.6-fold as large as the largest TSC2 +/+ cell. This was apparent when statistically comparing the median of both groups as TSC2 deficiency caused a significant increase in the cell size median in NSCs ($p = 2.394 \times 10^{-9}$).

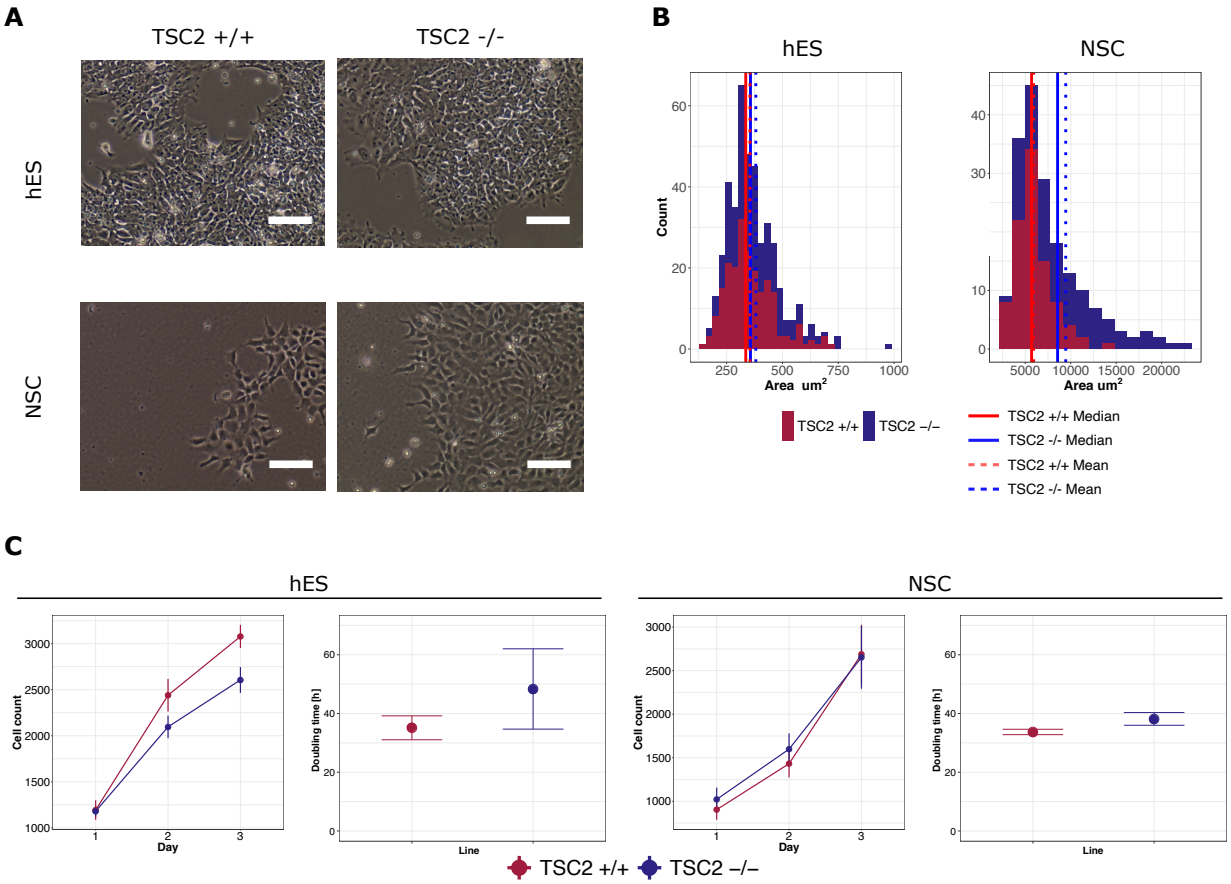


FIGURE 3.2: **Morphological characterisation of TSC2 +/+ and TSC2 -/- hES and NSCs.** (A) Brightfield images of TSC2 +/+ and TSC2 -/- hES (upper row) and NSCs (lower row). TSC2 +/+ and TSC2 -/- hES and NSCs showed similar cellular morphologies, respectively. (B) Grouped cell size histograms for TSC2 +/+ (red) and TSC2 -/- (blue) hES (upper row) and NSCs (lower row). No difference in area size was observed in TSC2 +/+ and TSC2 -/- hES ($p = 0.736$) or NSCs ($p = 0.411$) (Area bins in table E). (C) Growth curves and doubling times for TSC2 +/+ (red) and TSC2 -/- (blue) hES (left) and NSCs (right) over three days. No significant difference in doubling times was found between TSC2 +/+ and TSC2 -/- hES or NSCs (hES, $p = 0.406$; NSC, $p = 0.131$). *Scale bar* $= 100\mu m$. *Replicates: Cell size: hES, 2 differentiations,* $\sim$ *210 cells per line; NSC, 1 differentiation,* $\sim$ *90 cells per line; Growth curve: hES, 1 differentiation, 3 technical replicates; NSC, 4 differentiations, 3 technical replicates.*

In hES and NSCs, both cell lines proliferated at similar rates. Confluent cultures were usually split in a one-to-three or one-to-four ratio into new wells and it took around three to four days for the cultures to grow confluent again. I found no significant differences in doubling times between TSC2 +/+ and TSC2 -/- hES or NSCs (hES, $p = 0.406$; NSC, $p = 0.131$). Cell characteristics for TSC2 +/+ and TSC2 -/- hES and NSCs including brightfield microscopy, cell size, and proliferation rates are displayed in figure 3.2).

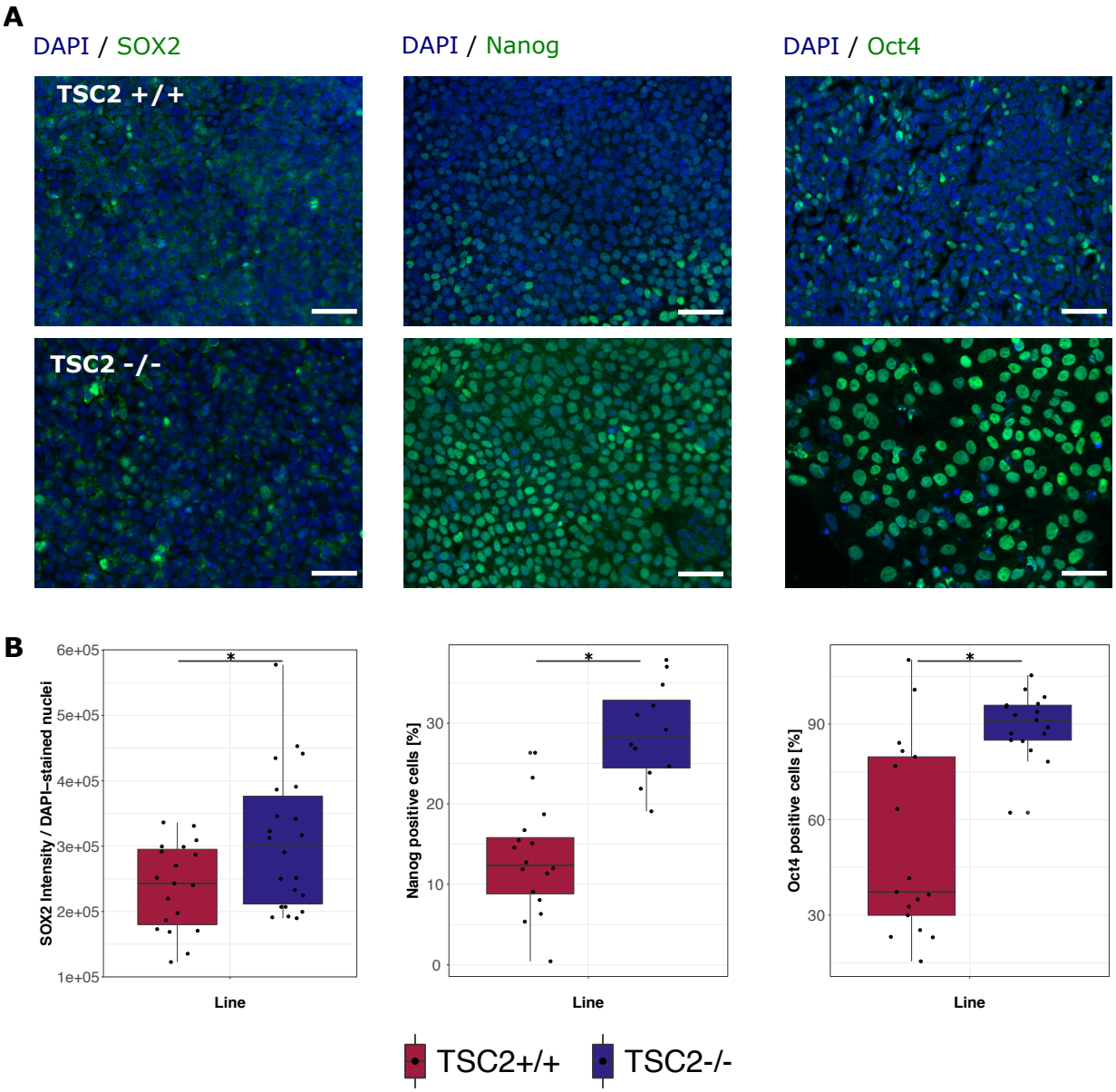


FIGURE 3.3: **Cellular identity of TSC2 +/+ and TSC2 -/- hES.** (A) TSC2 +/+ (upper row) and TSC2 -/- (lower row) hES expressed the pluripotency markers SRY-Box transcription factor 2 (SOX2), NK2-family homeobox transcription factor (Nanog) and octamer-binding transcription factor 4 (Oct4). (B) Quantification of SOX2 intensity and the percentage of Nanog and Oct4 positive cells on DAPI-stained nuclei in both cultures. TSC2 -/- hES presented with a significantly higher SOX2 signal intensity as well as percentage of Nanog and Oct4 stained cells (SOX2, $p = 0.019$; Nanog, $p = 6.00 \times 10^{-7}$; Oct4, $p = 3.65 \times 10^{-5}$). *Scale bar* $= 100\mu m$. *Replicates: SOX2,* $\sim$ *20 images per line; Nanog,* $\sim$ *15 images per line; Oct4,* $\sim$ *17 images per line.*

Next, I sought to confirm the cellular identity in each TSC2 +/+ and TSC2 -/- hES and NSC line by examining the expression of characteristic cellular identity markers: SOX2, Nanog and Oct4 as hPSC markers as well as SOX2, Nestin, Pax6, Vimentin and glial fib-

rillary acidic protein (GFAP) as markers for NSCs (see figures 3.3 & 3.4).

Both hES lines stained positive for the pluripotency markers SOX2, Nanog and Oct4 but expression levels differed significantly depending on genotype. In both, TSC2 +/+ and TSC2 -/- hES, Oct4 and Nanog were located intranuclear, but SOX2 was mainly present in the cytoplasm. It was therefore quantified as the overall expression intensity of SOX2 rather than the percentage of SOX2 positive nuclei.

As displayed in figure 3.3, TSC2 -/- hES cultures demonstrated a significantly higher expression of all three pluripotency markers (SOX2 expression intensity / DAPI-stained nuclei, $p = 0.019$; Nanog-positive nuclei / DAPI-stained nuclei, $p = 6.00 \times 10^{-7}$; Oct4-positive nuclei / DAPI-stained nuclei, $p = 3.65 \times 10^{-5}$).

In stable Roche NSCs, both genotypic lines showed positive staining for the NSC markers SOX2, Nestin, Pax6, Vimentin and GFAP with similar levels of expression intensity as can be seen in figure 3.4. I also assessed the expression of NF1A in NSCs as NF1A expression is a hallmark in neural development that marks the switch from neurogenesis towards gliogenesis [55]. TSC2 -/- Roche NSCs showed a significantly increased NF1A expression signal measured in immunostainings compared to their TSC2 +/+ counterparts (NF1A signal intensity / DAPI-stained nuclei, $p = 0.0098$).

The here characterised TSC2 +/+ and TSC2 -/- hES and NSCs formed the basis of my DPhil project. The next sections will provide an overview of different neuronal and glial differentiation protocols for experiments presented in the subsequent results chapters.

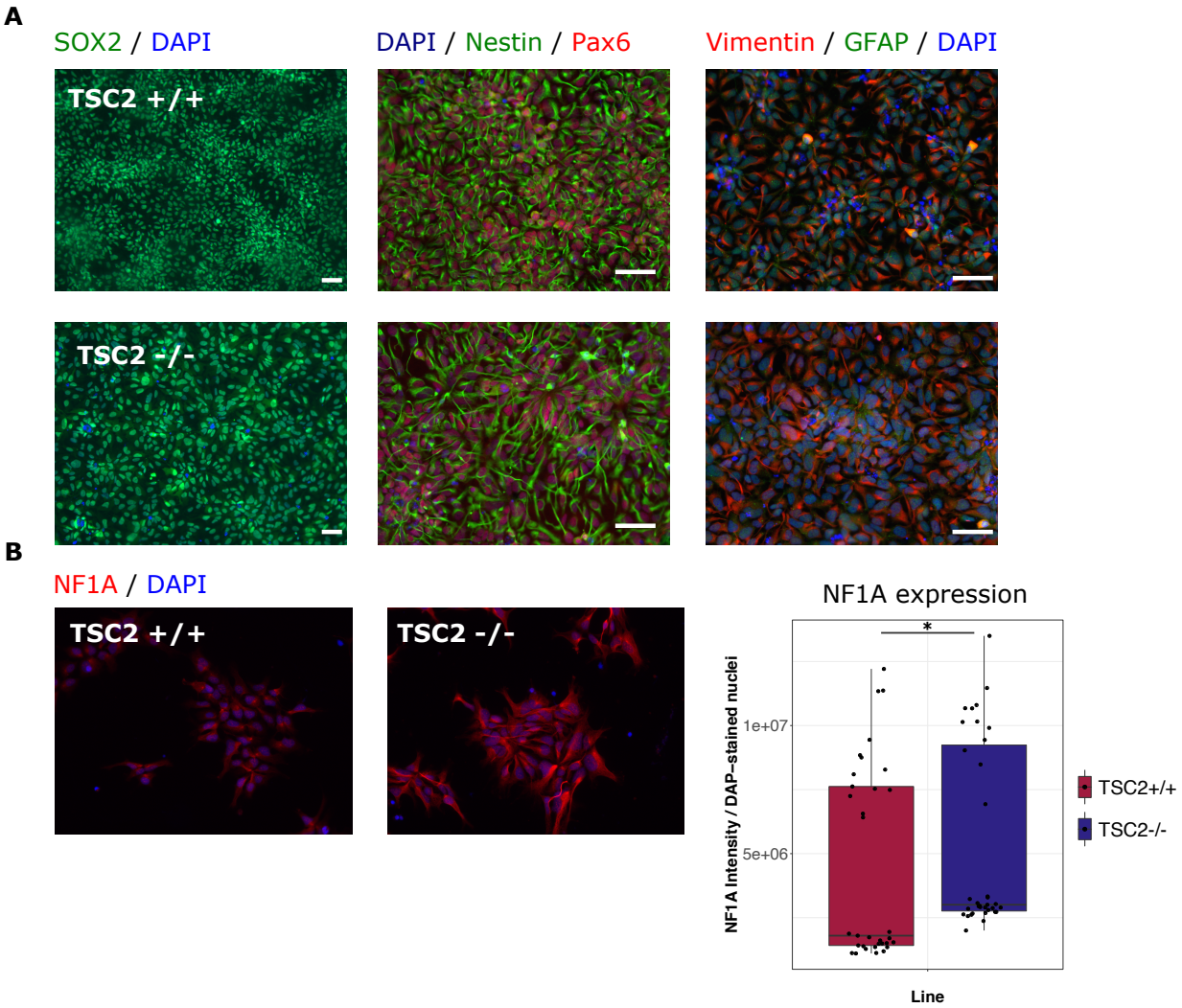


FIGURE 3.4: **Cellular identity of TSC2 +/+ and TSC2 -/- Roche NSCs.** (A) TSC2 +/+ (upper row) and TSC2 -/- (lower row) NSCs expressed specific NSC identity markers, namely SOX2, Nestin, Pax6 , Vimentin and GFAP. (B) Example images of TSC2 +/+ and TSC2 -/- Roche NSCs stained against NF1A. TSC2 -/- Roche NSCs demonstrated a significantly increased expression of NF1A compared to TSC2 +/+ cells ($p = 0.0098$). *Scale bar* $= 100\mu m$. *Replicates: NF1A,* $\sim$ *30 images per line.*

3.3.2 Cortical neuronal differentiation.

To examine the impact of TSC2 on cortical differentiation, I derived cortical neurons from TSC2 +/+ and TSC2 -/- hES using two different protocols. This section will outline both protocols in more detail and compare the cellular output at different stages between TSC2 +/+ and TSC2 -/- cultures. First, I differentiated both lines of hES using the dual SMAD-inhibition protocol from Shi et al. [238] into neural progenitors followed by

spontaneous differentiation and maturation into cortical neurons (see figure 3.5). This protocol has been extensively validated, including by the Cader lab [98, 278], to produce predominantly forebrain glutamatergic cortical projection neurons. Second, I used the forced NGN2 protocol from Zhang et al. [300] to directly differentiate hES into cortical neurons without passing through a well-defined neural progenitor stage.

Dual SMAD-inhibition

Dual SMAD-inhibition promotes ectoderm development while blocking the development of mesoderm and endoderm tissue [30]. In the original protocol, the development of different types of cortical progenitors (RGCs, IPCs and outer RGCs) is reported followed by the derivation of cortical inner-to-outer layer neurons in a sequential manner. Beyond 90 days of differentiations, the authors further reported that cultures can undergo a gliogenic switch to subsequently produce astrocytes.

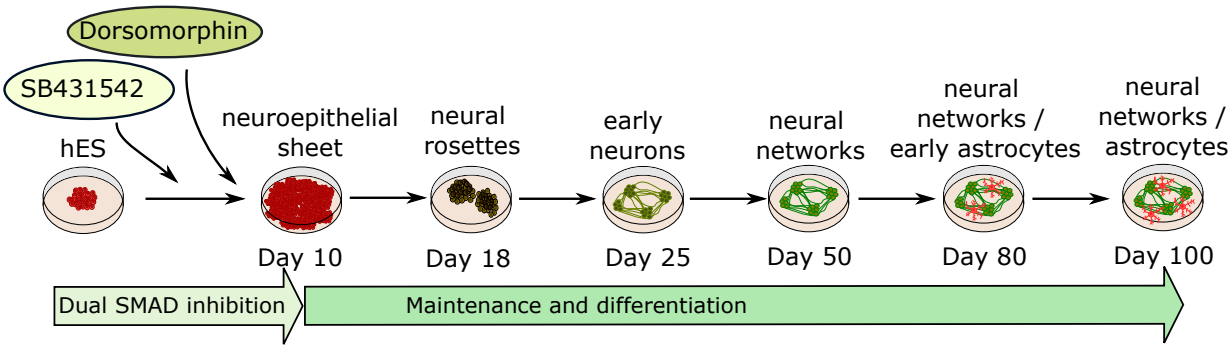


FIGURE 3.5: **Neuronal cortical differentiation via dual SMAD-inhibition.** Schematic of differentiation milestones during the dual SMAD-inhibition protocol. After 10 days of dual SMAD inhibition, the confluent hES sheet has transformed into the neuroepithelial sheet. Breaking up the sheet in clumps leads to the formation of neural rosettes and the subsequent production of early lower-layer cortical neurons. Without further passaging, upper-layer cortical neurons as well as early astrocytes are differentiated later in the protocol.

I examined key developmental markers at different time points during differentiation using immunostaining and qRT-PCR.

Rosettes: As a first step, I characterised TSC2 +/+ and TSC2 -/- rosettes between day 18 – 25. The appropriate apical-basal polarity of rosettes was confirmed by apical expression of the tight junction protein zona occludens 1 (ZO-1) and the basal emergence of migrating post-mitotic neurons (see figure 3.6 (B)). TSC2-deficient rosettes displayed a wider range of rosette surface area with TSC2 -/- rosettes occasionally growing 1.6-fold larger than the maximum TSC2 +/+ rosette (Range of rosette surface area: TSC2 +/+, $8,217 - 174,757\,\mu m^2$; TSC2 -/-, $8,528 - 275,415\,\mu m^2$).

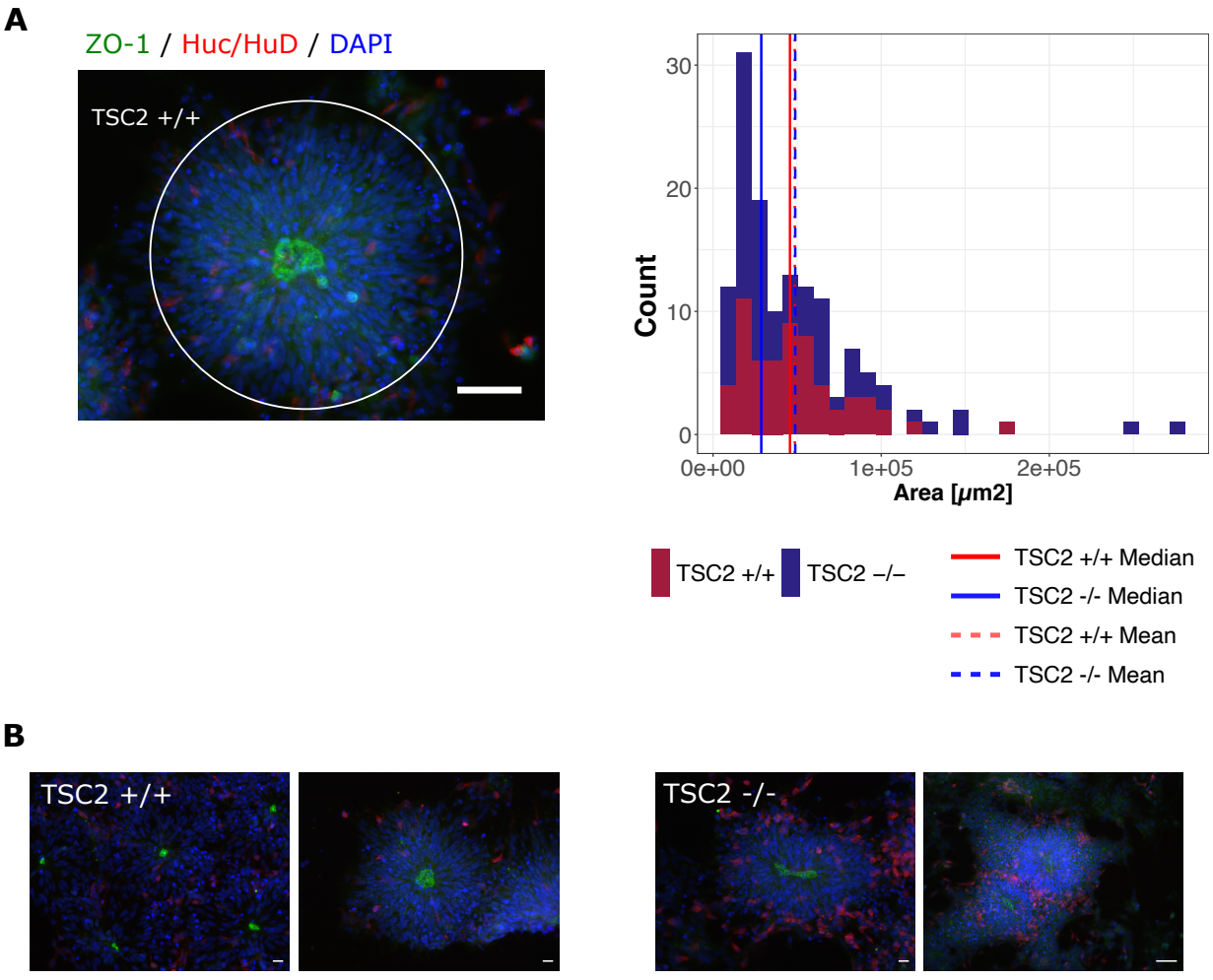


FIGURE 3.6: **Rosette formation in neuronal cortical differentiation.** (A) Rosette surface area was measured manually in images stained for the luminal markers ZO-1 and the post-mitotic marker HuC/HuD between days 18 - 25. TSC2 +/+ and TSC2 -/- cultures produced equally sized rosettes (p = 0.18). However, TSC2 -/- rosettes grew occasionally 1.6x as large as TSC2 +/+ rosettes. (B) Example images for TSC2 +/+ and TSC2 -/- rosettes stained with antibodies against ZO-1 and HuC/HuD illustrating that apical-basal polarity was maintained in rosettes from both cultures. *Scale bar* = $100\mu m$. *Replicates: TSC2 +/+, 1 differentiation, 60 rosettes; TSC2 -/-, 1 differentiation, 75 rosettes*

Despite the occasional occurrence of such large rosettes, TSC deficiency did not cause a significant shift in rosette size as I found no difference in the mean or median rosette size (Mean surface area, p = 0.18; median surface area, p = 0.18). This phenomenon is displayed in figure 3.6.

Neural progenitors: In a second step, I examined the neural progenitor or NSC stage as the production and maintenance of different types of NSCs are crucial in cortical development (see figure 3.7).

Expression of the RGC markers Pax6 and FOXG1, measured by qRT-PCR at different time points during dual SMAD-inhibition, was slightly increased in TSC2 +/+ cultures during the neuroepithelial and neural rosettes stage. After day 18, TSC2 +/+ cultures showed a marked decrease in NSC marker expression. At day 80, expression of FOXG1 rose again in TSC2 +/+ cultures as expected due to its function in cortical layer formation [27]. TSC2 deficiency led to upregulated Pax6 expression between day 30 to day 50 followed by a notable greater increase in FOXG1 expression at the end of differentiation.

Next, I characterised the NSC stage using immunostaining to investigate the expression levels of the radial glial marker Pax6 and the IPC marker T-box brain protein 2 (Tbr2) [70] at early neurodevelopmental stages. At the neuroepithelial stage, TSC2 -/- cultures showed a significantly reduced expression of Pax6 throughout the sheet (Pax6 signal intensity / DAPI area at day 10, p = 0.023). No difference in Pax6 intensity could be observed at day 18 and day 30 as TSC2 -/- cultures increased their Pax6 expression respectively (Pax6 intensity at day 18, p = 1.0; Day 30, p = 1.0).

Both genotypes also gave rise to Tbr2-positive IPCs. No significant differences were found in the intensity of Tbr2 immunofluorescence signal between TSC2 +/+ and TSC2 -/- cultures at day 18. TSC2 -/- cultures exhibited a significantly higher Tbr2 expression at day 25 (Tbr2 expression intensity / DAPI area at day 18, p = 1.00; day 25, p = 0.001).

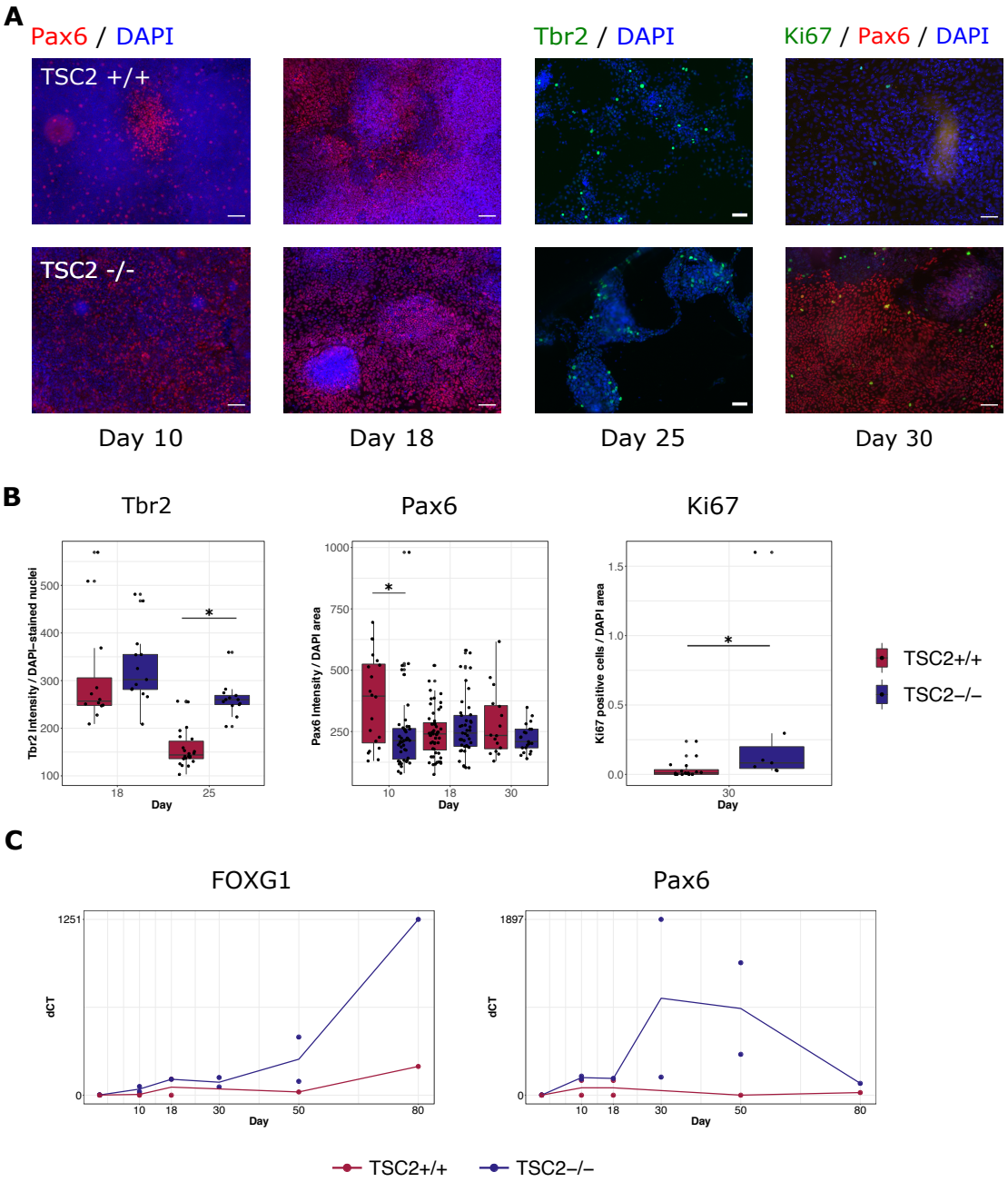


FIGURE 3.7: **Neural stem cell pool in neuronal cortical differentiation via dual SMAD-inhibition.** (A) Example images of TSC2 +/+ (upper row) and TSC2 -/- (lower row) NSCs stained for Pax6 (at day 10, 18 and 30), Tbr2 (at day 25) and Ki67 (at day 30). (B) Expression of the NSC markers Pax6 and Tbr2, and the mitotic marker Ki67 in TSC2 +/+ (red) and TSC2 -/- (blue) cultures on different days during dual SMAD-inhibition. No significant difference in Tbr2 expression was observed on day 18 but TSC2 -/- cultures showed significantly increased Tbr2 staining on day 25 (Day 18, p = 1.0; day 25, p = 0.001). No significant difference in Pax6 expression was detected on days 18 and 30 but TSC2 -/- cultures showed a significantly lower Pax6 expression at day 10 (Day 10, p = 0.0023; day 18, p = 1.0; day 30, p = 1.0). The number of Ki67-positive mitotic cells was significantly increased in TSC2 -/- compared to TSC2 +/+ cultures on day 30 (p = 0.0072). (C) QRT-PCR data of NSC markers FOXG1 and Pax6 on days 10, 18, 30, 50, and 80 during dual SMAD inhibition in TSC2 +/+ (red) and TSC2 -/- (blue) cultures. TSC2 +/+ cultures saw a moderate increase in NSC marker expression between days 10 and 30 with a second increase of FOXG1 towards the end of neuronal maturation. In TSC2 -/- cells, Pax6 was markedly increased on days 30 and 50 and FOXG1 increased on days 50 and 80. *Scale bar* = $100\mu m$. *Replicates: (B) 1 differentiation, 3 technical replicates per line; (C) number of replicates differs at different time points, 1-2 differentiations, 2 technical replicates.*

TSC2 -/- cultures showed a prolonged period of NSC proliferation, measured by the number of antigen KI-67 (Ki67)-expressing cells per DAPI area at day 30 of dual SMAD inhibition (Ki67-positive cells / DAPI area at day 30, p = 0.0072).

In brief, these results suggest that both cultures produced at least two different types of neural progenitors (radial glial cells and intermediate progenitors) and TSC2 deficiency led to an increased NSC production and prolonged NSC renewal.

Neuronal output: Lastly, I examined the neuronal output after several weeks of neuronal differentiation in both cultures (see figure 3.8). TSC2 +/+ cultures steadily increased the expression of the post-mitotic pan-neuronal marker microtubule-associated protein 2 (Map2) whereas only a small increase in Map2 gene expression between day 0 and day 80 could be observed in TSC2 -/- cultures. No significant difference was found in post-mitotic neuronal output, examined by the HuC/HuD expression at day 80, between both genotypes (HuC/HuD signal intensity / DAPI area at day 80, p = 0.589). I measured HuC/HuD immunofluorescence signal rather than the number of HuC/HuD-positive cells as the neuronal cell bodies tended to cluster in big clumps which did not allow the identification of single cells.

The dual SMAD-inhibition protocol is reported to follow the trajectory of embryonic neural development and thus, to produce six cortical neuronal layers in an inside-out manner. I, therefore, measured the expression of different cortical layer markers by qRT-PCR during the whole course of 80 days. Lower layer markers such as the transcription factor T-box brain protein 1 (Tbr1), a marker for layer VI, and COUP-TF-interacting protein 2 (CTIP-2), which labels layer V, were upregulated in TSC2 -/- cultures from day 50 onwards, but both markers only slightly increased in TSC2 +/+ cultures. Both cell lines showed a similar pattern of expression for the upper-layer marker special AT-rich sequence-binding protein 2 (Sat2b) whose expression levels increased from around day 30 onwards.

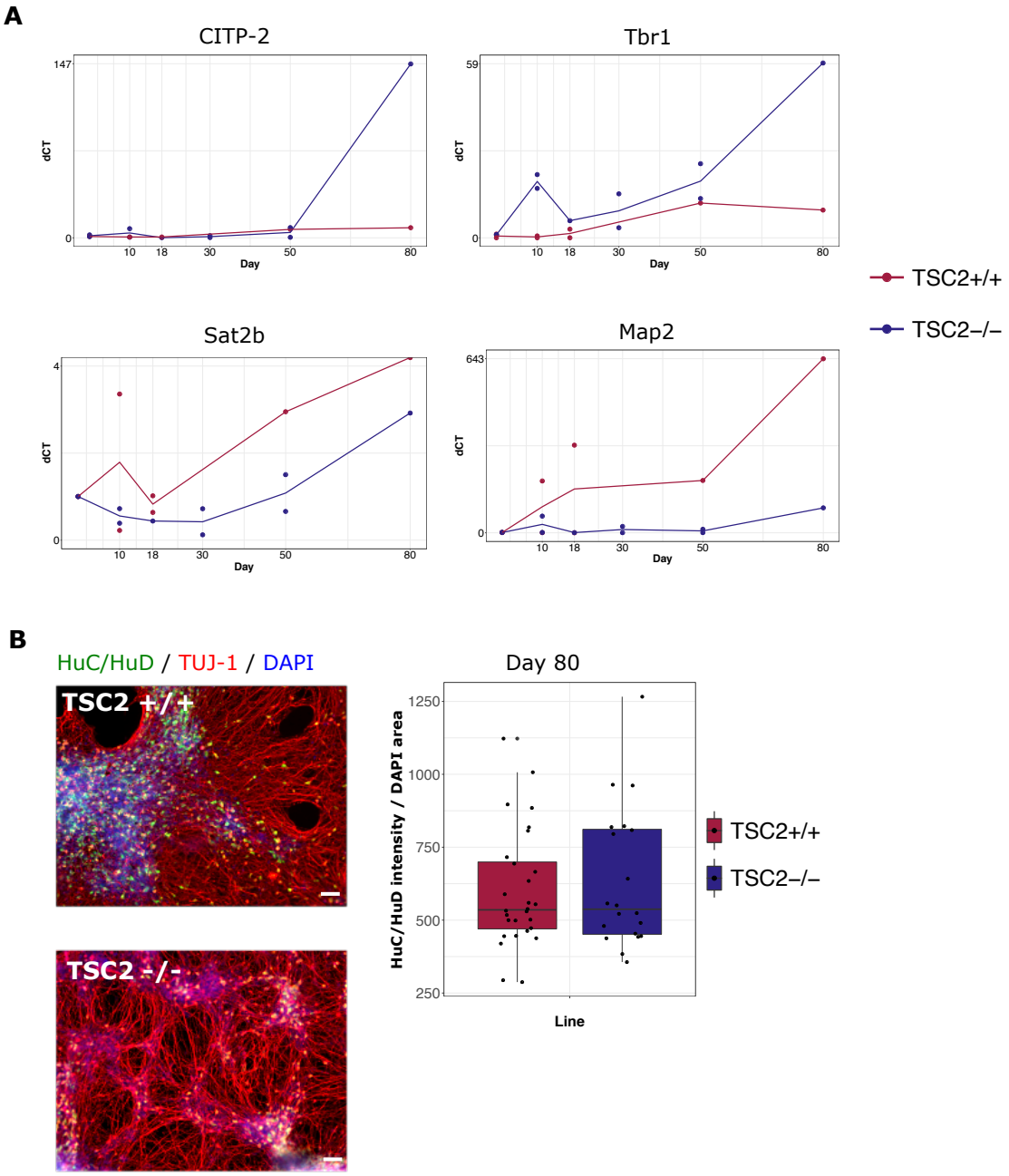


FIGURE 3.8: **Neuronal output in cortical differentiation via dual SMAD-inhibition.** (A) QRT-PCR data showing expression of Map2 (right), CTIP-2, Tbr1 (left), and Sat2b (middle) at days 10, 18, 30, 50, and 80 during dual SMAD inhibition in TSC2 +/+ (upper plots) and TSC2 -/- (lower plots) cultures. TSC2 +/+ cultures increased expression of the mature neuronal marker Map2 throughout the course of differentiation which was not seen in TSC2 -/- cultures. Both cell lines presented an increase in Sat2b expression from day 30 onwards. TSC2 +/+ cultures only showed little expression of CTIP-2 and Tbr1 whereas TSC2 -/- cultures demonstrated high expression levels of these early neuronal markers towards day 80. (B) Example images of TSC2 +/+ (upper row) and TSC2 -/- (lower row) day 80 neurons stained for HuC/HuD. Quantified expression of the post-mitotic neuronal marker HuC/HuD at day 80 (HuC/HuD) in both cultures (red, TSC2 +/+; blue, TSC2 -/-) did not show any differences of post-mitotic neuronal output between both cultures ($p = 0.589$). *Scale bar* $= 100\mu m$. *Replicates: (A) number of replicates differs at different time points, 1-2 differentiations, 2 technical replicates; (B) 2 differentiations, 3 technical replicates per line.*

Glio-neuronal composition: To evaluate the glio-neuronal composition (see figure 3.9), I first measured the expression levels of the glial marker GFAP as well as the astrocyte precursor marker NF1A using qRT-PCR in TSC2 +/+ and TSC2 -/- samples. In TSC2 +/+ cultures, no significant increase in the expression of glial markers was seen whereas TSC2 deficiency led to a substantial increase in both glial markers by day 80.

I next investigated the proportion of β-tubulin (TUJ-1) (neuronal) and GFAP (glial) positive cells using flow cytometry. Samples were collected on days 10, 18, 30, 50, and 80 and measured using a standardised gating protocol that was specified on a control sample stained only with secondary antibodies. Both cultures showed the same pattern of TUJ-1 and GFAP dynamics over the whole course of the differentiation and no significant differences in the expression for either marker could be observed at any time point. TUJ-1 expression was consistently high between 90 - 99 % from day 18 onwards in both culture types. Similarly, no differences in the proportion of GFAP-positive cells was observed between TSC2 +/+ and TSC2 -/- cultures at any time point. On average, around 60 % of both cultures stained GFAP-positive at early stages of the differentiation. This percentage considerably decreased towards later time points in both cultures to below 5 %. The variation in GFAP expression was remarkably high between individual samples from different differentiations in both genotypes at day 10 and 18 with GFAP positivity ranging from 0.71 % to 94.5 % in TSC2 +/+ samples and from 1.39 % to 96.5 % in TSC2 -/- samples, respectively.

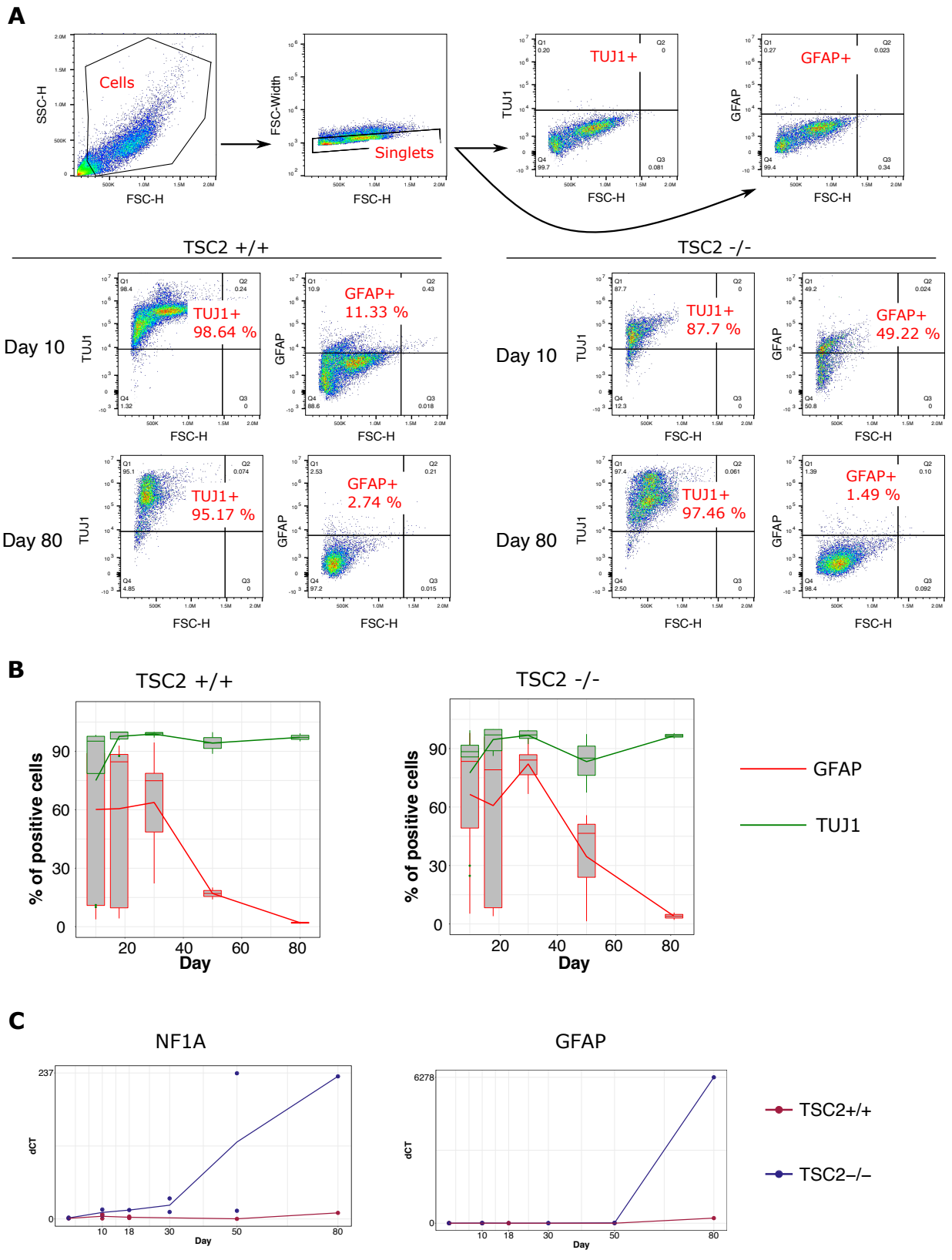

A
Cells
SSC-H
FSC-H
Singlets
FSC-Width
TUJ1+
TUJ1
GFAP+
GFAP
TSC2 +/+
TSC2 -/-
Day 10
Day 80
TUJ1+
98.64 %
GFAP+
11.33 %
TUJ1+
87.7 %
GFAP+
49.22 %
TUJ1+
95.17 %
GFAP+
2.74 %
TUJ1+
97.46 %
GFAP+
1.49 %
B
TSC2 +/+
TSC2 -/-
% of positive cells
Day
GFAP
TUJ1
C
NF1A
GFAP
dCT
Day
TSC2+/+
TSC2–/–

FIGURE 3.9: **Glio-neuronal balance during cortical differentiation via dual SMAD-inhibition.** (A) Flow cytometry data of GFAP and TUJ-1 expression in TSC2 +/+ and TSC2 -/- cultures at day 10, 18, 30, 50, and 80. Upper row: Gating pathway in a control sample stained with secondary antibodies only to obtain the thresholds for positive TUJ-1 and GFAP signals. Lower row: Example flow cytometry windows for gated samples of TSC2 +/+ and TSC2 -/- cultures stained for TUJ-1 and GFAP illustrating the high percentage of TUJ-1-positive cells at the beginning and end of the differentiation in contrast to the dynamic percentage of GFAP-positive cells during differentiation. (B) Quantified dynamics of TUJ-1 (green) and GFAP (red) expression in TSC2 +/+ (left) and TSC2 -/- (right) cultures. Both cultures showed a similar pattern with persistent TUJ-1 expression in around 95 % of the culture throughout the whole differentiation. The proportion of GFAP positive cells was more dynamic in both cultures increasing early during differentiation followed by a considerable decrease at later time points. No significant differences between TSC2 +/+ and TSC2 -/- cultures in both markers at any time point were observed. (C) GFAP and NF1A gene expression measured by qRT-PCR in TSC2 +/+ (red) and TSC2 -/- (blue) cultures during cortical differentiation. TSC2 +/+ cultures showed no increase in either GFAP or NF1A expression during the whole course of 80 days. In contrast, TSC2 -/- cultures exhibited a considerable increase in the expression of both markers during the second half of differentiation. *Replicates: (B) number of replicates differs at different time points, 2-3 differentiations, 2 technical replicates per line; (C) number of replicates differs at different time points, 1-2 differentiations, 2 technical replicates..*

In summary, I found that dual SMAD-inhibition-based differentiation was suitable to derive cortical neurons from TSC2 +/+ and TSC2 -/- hES lines with significant differences in cortical development between genotypes. At early stages of differentiation, TSC2 -/- cultures showed an enhanced production and prolonged maintenance of NSCs. Furthermore, TSC2 -/- cultures showed the tendency to produce more immature neurons at the end of differentiation. No differences in the proportions of glial and neuronal cells were found at any time point between both cultures.

In the next section, I will apply a second cortical differentiation protocol, the NGN2 protocol, which can produce cortical neurons in a much shorter period of time by directly converting hPSC into neurons.

Neurogenin 2 protocol

The *NGN2 protocol* (schematic protocol displayed in figure 3.10) allows the direct lineage conversion of hPSC into induced neurons through forced expression of the single transcription factor NGN2 [300]. This directed conversion yields a very high percentage of cortical layer 2/3 neurons within one to three weeks.

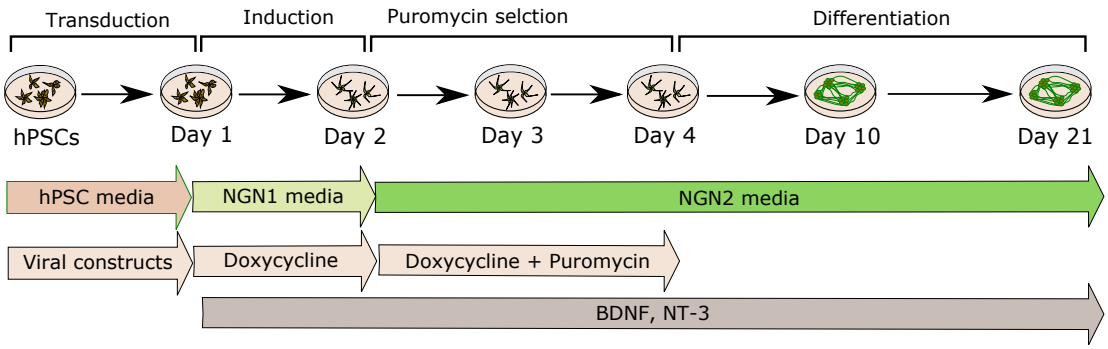


FIGURE 3.10: **Neuronal cortical differentiation via forced NGN2 expression.** Schematic illustration of different milestones during the Neurogenin 2 protocol. Human pluripotent cells are transduced with an Ubi-rtTA3 and a Tet-ON-NGN2 -puromycin construct. Neurogenin 2 expression is then induced by doxycycline exposure over three days and successfully transduced cells are selected for with puromycin. Neuronal cells are further matured in neuronal media containing BDNF and neurotrophin 3 (NT-3) for up to 21 days. (B) Schematic structure of the Ubi-rtTA3 and Tet-ON-NGN2 -puromycin constructs.

Human TSC2 +/+ and TSC2 -/- ES cells were transduced with two lentiviral vectors allowing sustained expression of rtTA3 driven by a ubiquitous promoter as well as doxycycline-inducible expression of NGN2 and a puromycin resistance gene. As early as 24 h after doxycycline induction, cells started to undergo neuronal conversion and demonstrated neuronal phenotypes with elongated processes and a reduced nucleus-to-cytoplasm ratio. The induced puromycin resistance further allowed for positive selection of successfully transduced cells 24 h after the start of doxycycline. Doxycycline was withdrawn after 72 h and neuronal cells were matured in a Neurobasal-based media supplemented with BDNF and NT-3 until day 21.

Morphology: No obvious differences were observed in brightfield images between TSC2 +/+ and TSC2 -/- cultures over the whole course of 20 days. Both cell lines yielded predominately upper-layer neurons of layers 2 and 3 confirmed by positive staining for Sat2b and the brain-specific homeobox / POU domain protein 3a (Brn3a) shown in figure 3.11. Neurons derived by the NGN2 protocol (NGN2 neurons) from both genotypes showed a similar proliferation behaviour with the production of similarly dense cultures over time. This impression from brightfield microscopy was confirmed by quantifying the cell count per field view in DAPI-stained cultures in immunostainings. No significant differences in cell number at any time point were seen between TSC2 +/+ and TSC2 -/- NGN2 neurons, however, both cell lines showed a significant decrease in cell number between day 10 to day 20 (Cell count per field view in TSC2 +/+ and TSC2 -/- cultures: Day 7, $p = 1.00$; Day 10, $p = 1.00$; Day 20, $p = 0.24$; Day 7 - day 10: TSC2 +/+, $p = 0.17$, TSC2 -/-, $p = 0.34$; Day 10 - day 20, TSC2 +/+, $p = 1.08 \times 10^{-23}$, TSC2 -/-, $p = 2.48 \times 10^{-15}$).

Cell type characterisation: I next characterised TSC2 +/+ and TSC2 -/- NGN2 neurons through immunostainings for different neural markers (see figure 3.12). Both cultures produced neurons positive for TUJ-1, Map2 and HuC/HuD from day 7 onwards. TSC2 +/+ and TSC2 -/- cultures showed similar levels in HuC/HuD expression at early time points of the protocol and after 20 days with a significant drop in HuC/HuD staining in TSC2 -/- cultures at day 10 (HuC/HuD expression intensity / DAPI area: Day 7, $p = 1.0$; Day 10, $p = 0.009$; Day 20: TSC2 +/+, $p = 1.0$).

Due to the directly induced lineage conversion, no notable period of NSC production and maintenance can be expected during the NGN2 protocol. To confirm the lack of a neural progenitor pool, I measured the expression of Pax6 in both cell lines and found a consistently low expression of Pax6 in TSC2 +/+ cultures. TSC2 -/- cultures produced localised patches of Pax6-positive neural progenitors that grew in cell number over time.

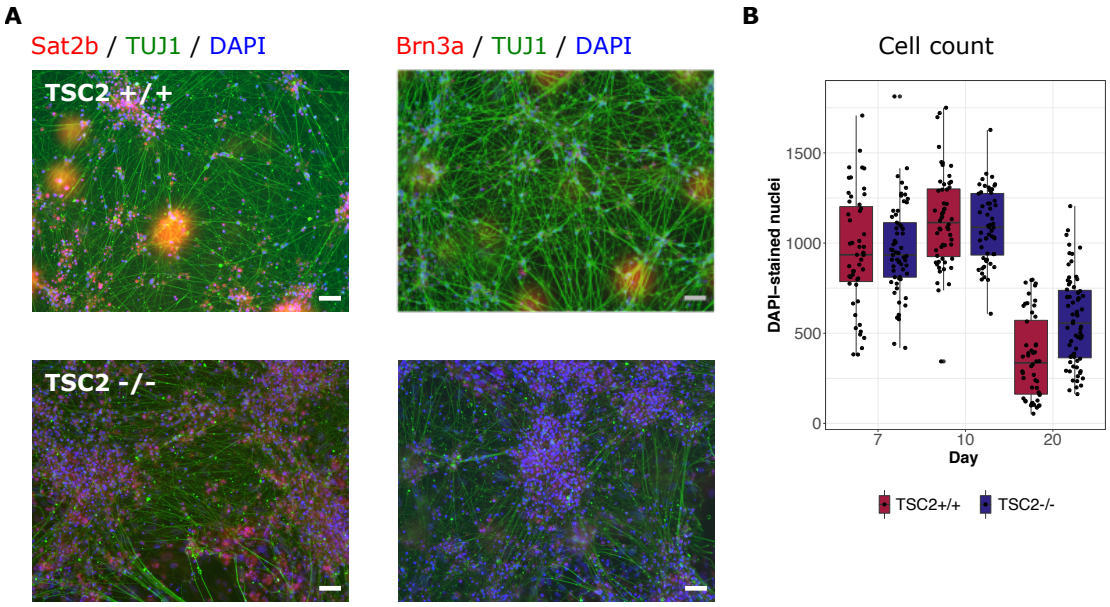


FIGURE 3.11: **Neuronal output of the NGN2 differentiation protocol.** (A) TSC2 +/+ (upper row) and TSC2 -/- (lower row) cultures produced upper-layer neurons after 12 days of NGN2 differentiation detected by positive staining for the pan-neuronal marker TUJ-1 (green) and the layer 2/3 markers Sat2b (red, left) and Brn3a (red, right). (B) No difference in proliferation was observed between TSC2 +/+ and TSC2 -/- cultures during 20 days of NGN2 differentiation as both lines yielded a similar cell number after 7, 10, or 20 days as measured by the number of DAPI-stained nuclei (Day 7, p = 1.0; day 10, p = 1.0, day 20; p = 0.24). *Scale bar* = 100μm. *Replicates: 1 differentiation, 3 technical replicates per line.*

Both, TSC2 +/+ and TSC2 -/- NGN2 cultures, lacked specific GFAP staining and overall, GFAP expression was low with no significant temporal changes in both cultures over the whole course of the differentiation (GFAP expression intensity: Day 7, p = 0.718; Day 10, p = 0.1; Day 20, p = 0.473).

In summary, the NGN2 protocol yielded a high percentage of directly converted TSC2 +/+ and TSC2 -/- neurons within 7 days that could be maintained and matured for at least 21 days in total. No differences in the final yield of glial or neuronal cells were found between TSC2 +/+ and TSC2 -/- cultures although TSC2 -/- cultures showed an increased production of Pax6-positive neural progenitors during the differentiation.

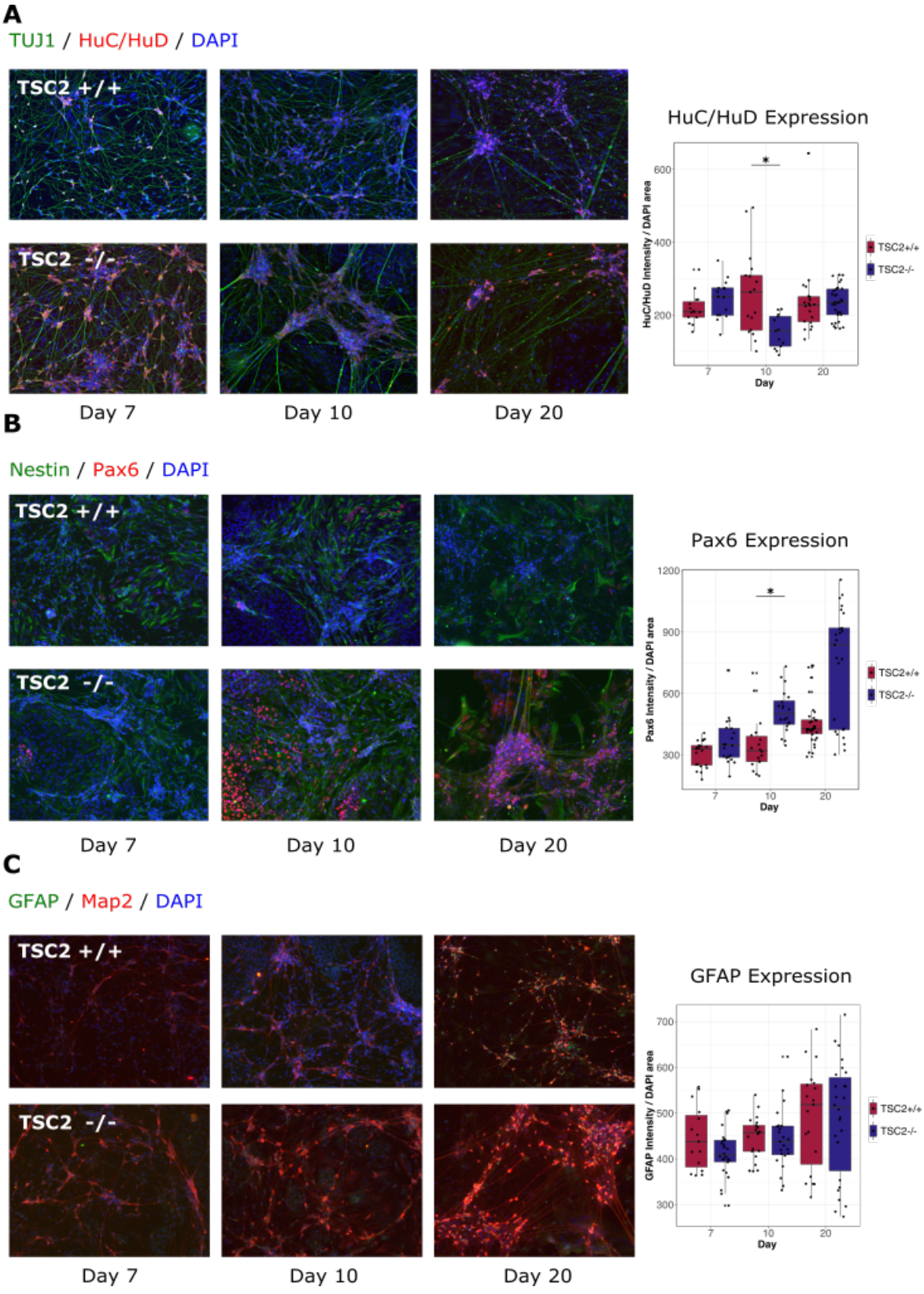

A
TUJ1 / HuC/HuD / DAPI
TSC2 +/+
TSC2 -/-
Day 7
Day 10
Day 20
HuC/HuD Expression
HuC/HuD Intensity / DAPI area
600
400
200
7
10
20
Day
TSC2+/+
TSC2-/-
B
Nestin / Pax6 / DAPI
TSC2 +/+
TSC2 -/-
Day 7
Day 10
Day 20
Pax6 Expression
Pax6 Intensity / DAPI area
1200
900
600
300
7
10
20
Day
TSC2+/+
TSC2-/-
C
GFAP / Map2 / DAPI
TSC2 +/+
TSC2 -/-
Day 7
Day 10
Day 20
GFAP Expression
GFAP Intensity / DAPI area
700
600
500
400
300
7
10
20
Day
TSC2+/+
TSC2-/-

FIGURE 3.12: **Characterisation of NGN2 differentiation in TSC2 +/+ and TSC2 -/- cultures.** Example immunostainings of TSC2 +/+ (upper row) and TSC2 -/- (lower row) cortical neurons differentiated via the NGN2 protocol on days 7, 10 and 20. (A) Stainings for the neuronal markers TUJ-1 (green) and HuC/HuD (red) against DAPI (blue), (B) Stainings for the NSC markers Nestin (green) and Pax6 (red) against DAPI (blue). (C) Stainings for the glial marker GFAP (green) and the neuronal marker Map2 (red) against DAPI (blue). Quantified expression of different markers in NGN2 neurons differentiated from TSC2 +/+ (red) and TSC2 -/- (blue) hES on days 7, 10, and 20. (A) HuC/HuD expression. No significant differences could be observed between TSC2 +/+ and TSC2 -/- cultures on day 7 or day 10 but significantly lower HuC/HuD expression was seen on day 10 in TSC2 -/- compared to TSC2 +/+ cultures (Day 7, p = 1.0; day 10, p = 0.009, day 20, p = 1.0). (B) Pax6 expression. TSC2 -/- cultures showed a significantly higher Pax6 expression than TSC2 +/+ cultures on day 10 only (Day 7, p = 1.00; day 10, p = 0.0006; day 20, p = 0.14). (C) GFAP expression. GFAP expression was diffuse and unspecific in both cultures during the whole course of 20 days with no significant differences in intensity between both cultures (Day 7, p = 0.718; day 10, p = 0.1; day 20, p = 0.473). *Scale bar* = 100μ*m. Replicates: 1 differentiation, 3 technical replicates per line.*

3.3.3 Glial differentiation.

Astrocytes were differentiated from TSC2 +/+ and TSC2 -/- neural progenitors (derived via dual SMAD-inhibition) using commercially available astrocyte differentiation and maturation kits from STEMCELL Technologies. After a single-cell passage, neural progenitors were kept in astrocyte differentiation media for 2-3 weeks to induce gliogenesis. Thereafter, cells were matured in astrocyte maturation media for another 2 -3 weeks. Astrocytes could be maintained indefinitely in a self-made astrocyte maintenance media with regular passages and freeze/thaw cycles as required.

Cell type characterisation: Both, TSC2 +/+ and TSC2 -/- lines, produced a wide variety of different astrocyte morphologies ranging from elongated neuronal-like cells to large flat cells as well as star-shape stereotypical astrocytes (example images in figure 3.14 (E)). I stained cultures with antibodies against the glial marker GFAP and the neuronal marker TUJ-1 between days 40 and 50 and between days 60 and 70.

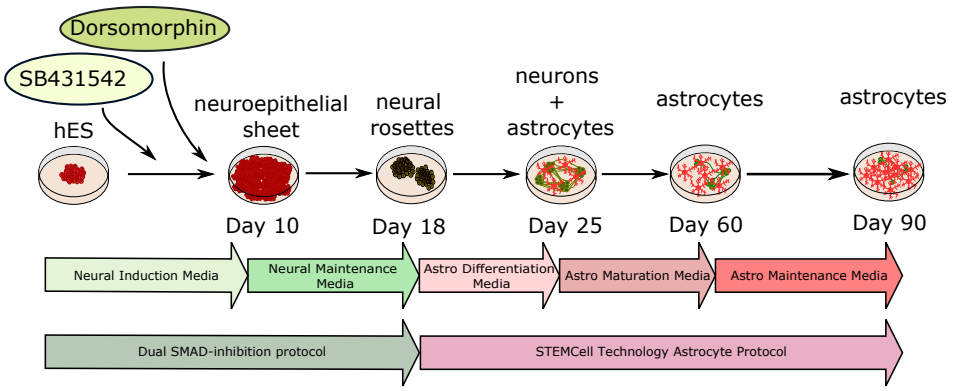


FIGURE 3.13: **STEMCELL Technologies astrocyte differentiation.** Astrocytes were differentiated from rosette progenitors derived via dual SMAD inhibition. Neural progenitors were single-celled and differentiated into astrocyte progenitors from which they further maturated using STEMCELL Technologies Kits. From day 60 onwards, astrocytes were maintained in a custom-made media indefinitely.

The percentage of GFAP-positive cells was similarly low in both lines at the earlier time point. TSC2 deficiency led to a sharp rise in GFAP expression after day 50, a 9.7-fold increase in the percentage of GFAP-positive cells to nearly 80 %, which was not mirrored in their TSC2 +/+ counterparts. At the end of glial differentiation, there was a significant difference in the GFAP-positive proportion between TSC2 -/- and TSC2 +/+ cultures (percentage of GFAP-positive cells: Day 40-50, $p = 0.14$; Day 60-70, $p = 2.34 \times 10^{-15}$).

In a next step, I examined the expression of glial glutamine synthetase (GS) between day 60 and 70 as well as key glial genes on day 40 (as illustrated in figure 3.14 (C) and (D)). I observed a significantly reduced expression of GS in TSC2 -/- compared to TSC2 +/+ cells (GS signal intensity / DAPI area, $p = 0.0009$). TSC2 -/- astrocytes showed downregulated levels of genes transcribing for key glial function proteins including GFAP, excitatory amino acid transporter 1 (EAAT1), and connexin 43 (Cx43) (a connexin protein facilitating glial gap junctions), however, no statistical significance was detected (only two TSC2 +/+ samples for each gene).

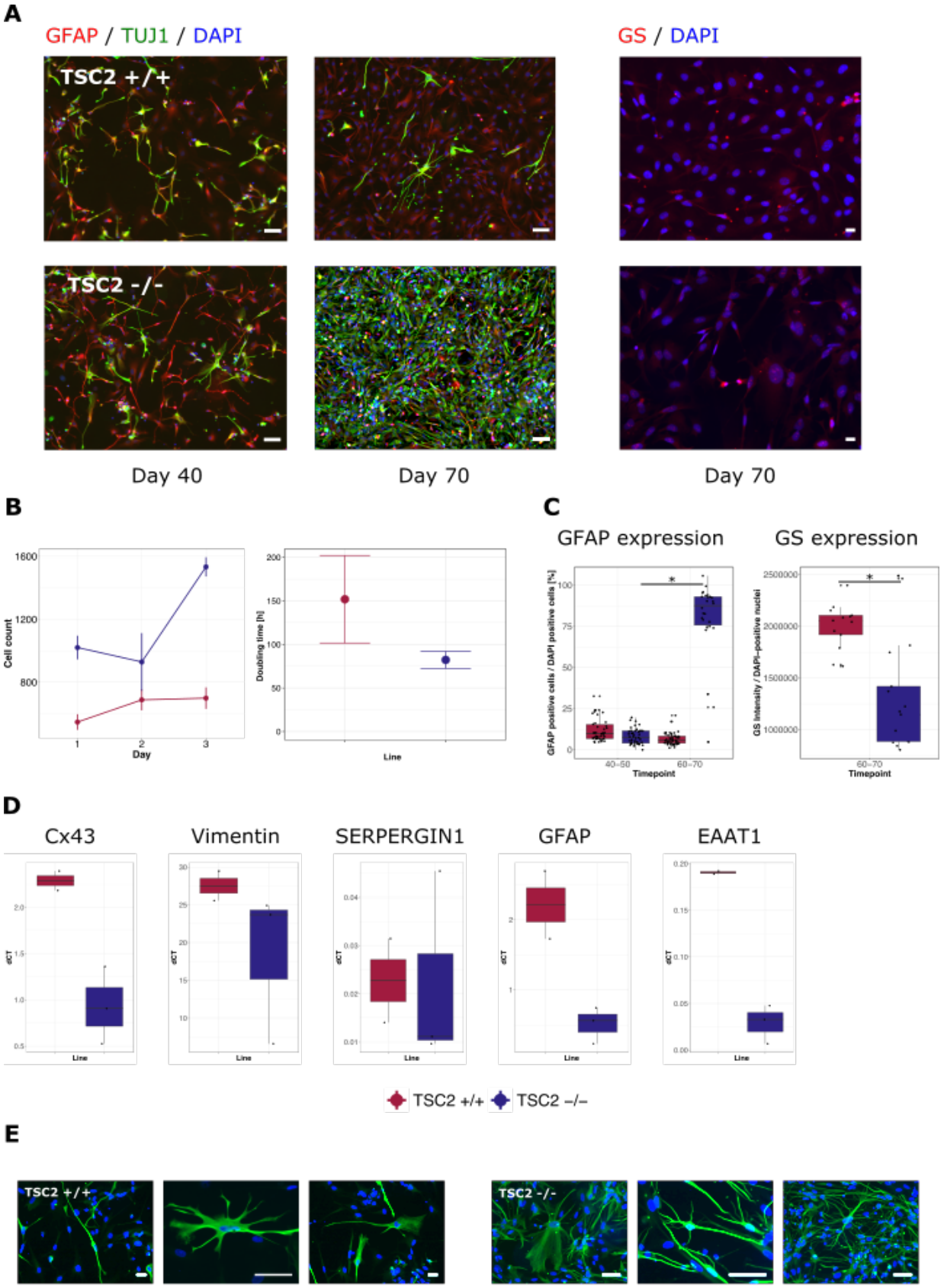

A
GFAP / TUJ1 / DAPI
GS / DAPI
TSC2 +/+
TSC2 -/-
Day 40
Day 70
Day 70
B
Cell count
Day
Doubling time [h]
Line
C
GFAP expression
GS expression
GFAP positive cells / DAPI positive cells [%]
GS intensity / DAPI−positive nuclei
Timepoint
D
Cx43
Vimentin
SERPERGIN1
GFAP
EAAT1
dCT
Line
TSC2 +/+
TSC2 −/−
E
TSC2 +/+
TSC2 -/-

FIGURE 3.14: **Derivation of TSC2 +/+ and TSC2 -/- astrocytes.** (A) TSC2 +/+ (upper row) and TSC2 -/- (lower row) astrocytes stained for the glial marker GFAP (red) and neuronal marker TUJ-1 (green) on day 40 and day 70, and for glutamine synthetase (GS, red) on day 70. (B) Growth curve and doubling times for TSC2 +/+ (red) and TSC2 -/- (blue) astrocytes aged 70 days. There was no significant difference in the doubling time between both lines ($p = 0.121$). (C) Percentage of GFAP-positive cells in both cultures between the days 40 - 50 and days 60 - 70. TSC2 -/- cultures showed a nearly 10-fold increase in GFAP-positive cells from day 60 onwards with no such increase in GFAP expression seen in TSC2 +/+ cells. TSC2 -/- cells presented with a significantly lower expression of GS between days 60-70 compared to TSC2 +/+ cultures ($p = 0.0009$). (D) Expression of key glial genes in TSC2 +/+ (red) and TSC2 -/- (blue) astrocytes on day 40. TSC2 -/- astrocytes showed notably decreased expression of GFAP, EAAT1 and CX43. (E) Example images of GFAP-positive TSC2 +/+ (left) and TSC2 -/- (right) astrocytes between days 60 - 70. *Scale bar* $= 100\mu m$. *Replicates: (B) 1 differentiation, 2 technical replicates per line ; (C) 2 differentiations, 3 technical replicates per line; (D) 1 differentiation, 3 technical replicates per line.*

Proliferation: Both cultures slowed down their turnover rate with ageing and passaging was less often required towards the end of the protocol. TSC2 -/- astrocytes were, overall, more proliferative than their TSC2 +/+ counterparts requiring more frequent passages and producing more cells as a result. However, no significant difference in doubling times of TSC2 +/+ and TSC2 -/- astrocytes was found when assessed around day 70 (Doubling times [h]: TSC2 +/+, 151.9 ± 71.1; TSC2 -/-, 82.3 ± 13.6; $p = 0.121$).

3.3.4 Transient mTORC1 modification.

Inhibiting and activating modifications of the TSC1:TSC2-mTORC1 pathway can either target the TSC1:TSC2 complex or mTORC1 directly. Pharmacological agents are available to alter mTORC1 function such as the mTORC1 inhibitor rapamycin or its activating counterpart MHY1485. Since a similarly established pharmacological modification is not readily available for the TSC1:TSC2 complex, its targeting requires genetic modification. I trialled the introduction of ectopic TSC2 expression to increase TSC2 activity in TSC2 -/- cultures as well as shRNA-mediated knockdown of TSC2 translation in TSC2 +/+ cells

(see figure 3.15).

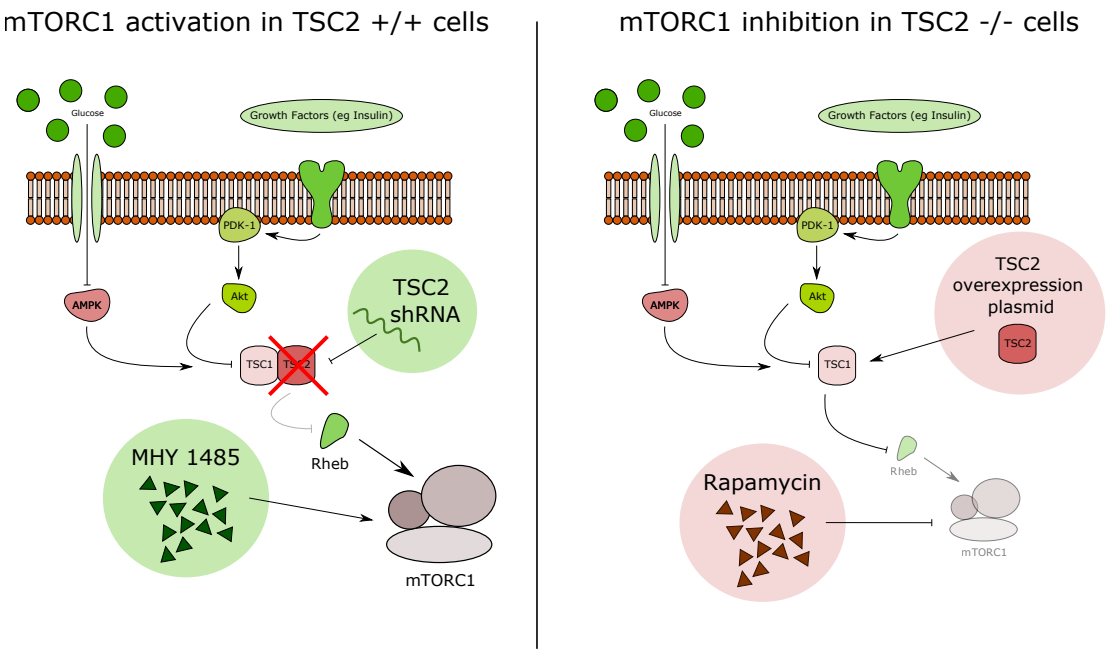


FIGURE 3.15: **Modifications of mTORC1 activity.** Low mTORC1 activity can theoretically be increased pharmacologically by the mTORC1 activator MHY 1485 or via the introduction of an TSC2 shRNA blocking TSC2 expression with subsequent dis-inhibition of mTORC1. In contrast, high mTORC1 activity can either be inhibited pharmacologically by rapamycin or via ectopic TSC2 gene expression to increase TSC2-mediated inhibition of mTORC1.

Pharmacological modification of mTORC1. I exposed TSC2 +/+ and TSC2 -/- NSCs to two different pharmacological agents, rapamycin and MHZ1485, to either directly inhibit or activate mTORC1, respectively. Different concentrations of both chemicals were tested in both cell lines and mTORC1 activity was measured by the ratio of phosphorylated to total S6 (pS6/S6) using western blotting (see figure 3.16 (A)). Rapamycin, a mTORC1 inhibitor, was applied at either 0.2, 0.5, 1, 2 or 5 nM for 24 h and tested against a DMSO control. Phosphorylation of S6 was notably decreased in TSC2 +/+ and TSC2 -/- NSCs at in a dose-dependent manner is illustrated in figure 3.16 (C).

In a fresh culture, I also applied either 0.2, 0.5, 1, 2 or 5 μM of MHY1485, a mTORC1 activator, for 24 h to both cell lines and tested its effect against a DMSO control. None of these tested concentrations led to a further increase in S6 phosphorylation compared to

the control sample in TSC2 +/+ or TSC2 -/- NSCs.

Genetic modifications of TSC1:TSC2 activity. I next sought to test genetic modifications of the TSC2-mTORC1 axis in either TSC2 +/+ or TSC2 -/- hES. To knock-down TSC2 expression in TSC2 +/+ hES, a TSC2 shRNA (pLKO.1-TSC2, Do-Hyung Kim via Addgene), was cloned into a lentiviral construct and transduced into TSC2 +/+ hES. I used different volumes of the untitered viral construct solution, namely 0.2, 0.5, 1, 2 and 5 μL per 1 ml of mTESR1 media in a well of a 12-well plate. An empty pLKO.1 backbone served as control. None of the tested viral plasmid concentrations produced a notable effect on tuberin levels nor on mTORC1 activity levels compared to control samples as can be seen in figure 3.16 (C). When analysing mTORC1 activation in the control samples, I noted a reduced mTORC1 activation in TSC2 +/+ hES compared to their NSC counterparts.

I further introduced ectopic TSC2 expression into TSC2 -/- hES. The purified DNA could not reliably be cloned into a lentiviral vector due to its size and thus, was directly transduced into the cells via lipofection using either 0.2, 0.5, 1, 2 or 5 μg plasmid DNA or without plasmid DNA as control. Ectopic TSC2 expression led to a slight increase in tuberin expression as well as a decrease in mTORC1 activation in TSC2 -/- hES compared to control samples (see figure 3.16 (C)). In contrast to TSC2 +/+ cells, non-transduced TSC2 -/- hES did not show a reduction in mTORC1 activation compared to their NSC counterparts.

The results of these pilot experiments suggested that mTORC1 activity can be inhibited using either rapamycin or by introducing an ectopic TSC2 expression. In contrast, pharmacological efforts and the introduction of a TSC2 shRNA were not sufficient to increase mTORC1 activity.

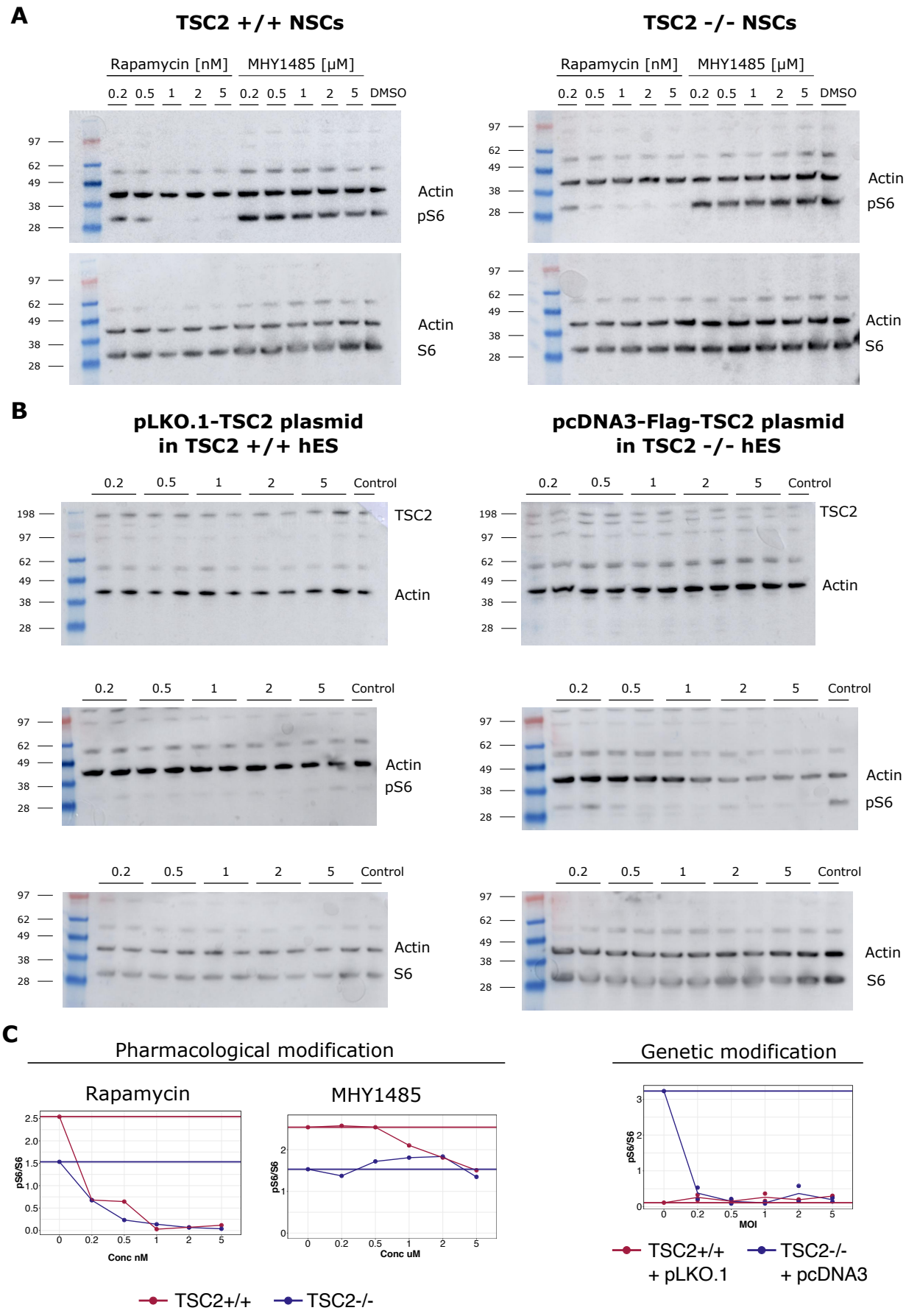

A
TSC2 +/+ NSCs
TSC2 -/- NSCs
Rapamycin [nM]
MHY1485 [μM]
0.2 0.5 1 2 5 0.2 0.5 1 2 5 DMSO
97
62
49
38
28
Actin
pS6
Actin
S6
B
pLKO.1-TSC2 plasmid
in TSC2 +/+ hES
pcDNA3-Flag-TSC2 plasmid
in TSC2 -/- hES
0.2 0.5 1 2 5 Control
198
TSC2
Actin
pS6
S6
C
Pharmacological modification
Genetic modification
Rapamycin
MHY1485
pS6/S6
Conc nM
Conc uM
MOI
TSC2+/+
TSC2-/-
+ pLKO.1
+ pcDNA3

FIGURE 3.16: **Transient mTORC1 modification.** (A) Pharmacological modification of mTORC1 activity was performed in TSC2 +/+ (left) and TSC2 -/- (right) NSCs using different concentrations of either the mTORC1 inhibitor rapamycin (0.2, 0.5, 1, 2, 5 nM) or the mTORC1 activator MHY1485 (0.2, 0.5, 1, 2, 5 μM). DMSO served as vehicle control. The activity of mTORC1 was measured as the ratio of phosphorylated to total S6. (B) Genetic TSC2 modifications were trialled in TSC2 +/+ (left) and TSC2 -/- (right) hES. In TSC2 +/+ hES, a TSC2 shRNA (pLKO.1-TSC2) was introduced via a lentiviral plasmid at different MOI (0.2, 0.5, 1, 2, 5) to post-transcriptionally knock-down TSC2. In TSC2 -/- hES, ectopic TSC2 gene expression was introduced via lipofection at different MOI. (C) Quantification of the pS6/S6 ratio after pharmacological or genetic TSC2-mTORC1 modifications. Rapamycin significantly decreased mTORC1 activity in both NSC in a dose-dependent manner. No effect on mTORC1 activity was observed for all MHY1485 concentrations. Introduction of ectopic TSC2 expression downregulated mTORC1 activity in TSC2 -/- hES. In TSC2 +/+ hES, knockdown of TSC2 did not affect mTORC1 activity.

3.3.5 Creation of additional TSC2-mutated stem cell lines.

I planned to use a second set of wild-type and TSC2 knockdown lines for repeat experiments on neurodevelopment in TSC. I aimed to create these cell lines from an inducible CRISPR/Cas9 iPSC for which I had TSC2 sgRNAs available. In this CRISPR/Cas9 iPSC line, Cas9 expression was induced by doxycycline.

Cas9 activation. I first tested different doxycycline concentrations and their ability to induce Cas9 expression at the iPSC stage as well as in NGN2 neurons at day 10 derived from this CRISPR/Cas9 iPSC line. Either 0.1, 0.5, 1, 2, or 5 μg/ml doxycycline was added to the respective cellular cultures for 24 h and Cas9 expression was subsequently measured using western blotting (see figure 3.17). All doxycycline concentrations tested induced a notable Cas9 expression compared to control samples exposed to a vehicle control after 24 h in iPSCs. In neurons, doxycycline-induced Cas9 expression was much lower compared to iPSCs. Following these pilot observations, I used 2 μg/ml of doxycycline as recommended by the line-producing lab and performed the CRISPR-mediated gene editing at the iPSC stage.

Gene editing. Five different strands of CRISPR-single-guide RNA (sgRNA) targeting either the mouse gene Rosa26 or the human TSC2 gene were cloned into lentiviral systems by the WIMM Genome Engineering facility. A cocktail of all five CRISPR-sgRNAs was each transduced into cultures of the inducible CRISPR/Cas9 iPSC line to create CRISPR/Cas9^{wt} and CRISPR/Cas9^{TSC2} lines. I performed this transduction in two consecutive rounds with two and four samples per line, respectively. After one week of doxycycline exposure and positive selection for successfully transduced cells with blasticidin, TSC2 gene expression was measured by qRT-PCR (see figure 3.17). No difference was found between the CRISPR/Cas9^{wt} and CRISPR/Cas9^{TSC2} samples (TSC2 gene expression ddCT: First round, p = 1.0; Second round, p = 1.0).

I then measured tuberin protein levels by western blotting in samples produced during the first round of transduction. One of the two CRISPR/Cas9^{TSC2} samples showed a slight reduction in TSC2 protein expression. However, the decreased amount of tuberin did not translate into an increased mTORC1 activation level measured by the pS6/S6 ratio.

Since the results of the qRT-PCR experiments on samples from the second round also did not show any significant knockdown of TSC2, I did not progress with these samples to measure tuberin levels by western blotting.

No further efforts to create an isogenic set of wild-type and TSC2 knockdown lines could be made due to limited time in light of the coronavirus-associated disease 2019 (COVID-19) pandemic restrictions. I thus continued to use the TSC2 +/+ and TSC2 -/- hES and NSC lines characterised above for the experiments presented in the subsequent chapters.

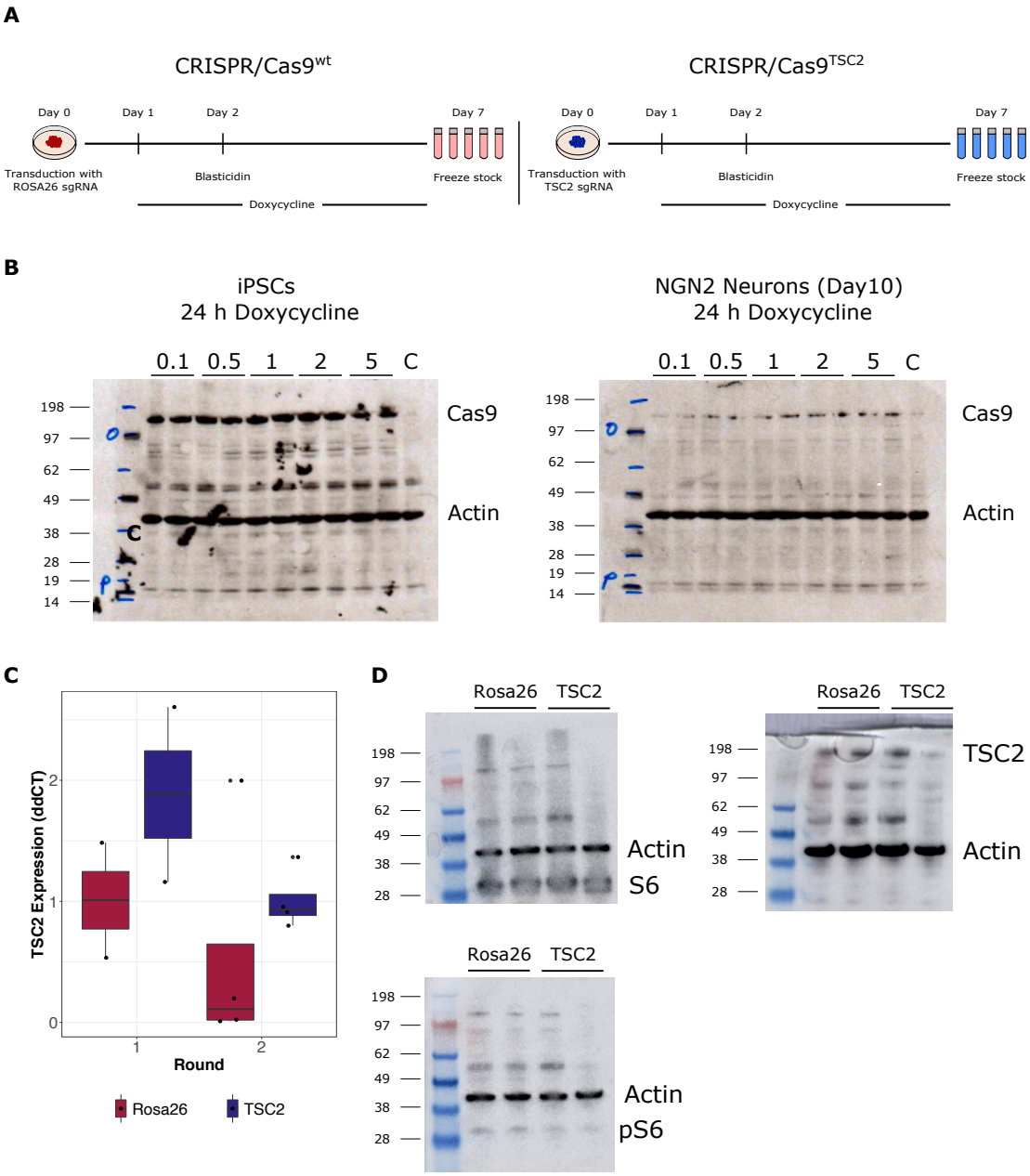


FIGURE 3.17: **Creation of a TSC2 KO line using an inducible CRISPR/Cas9 system.** (A) Cells were either transduced with CRISPR-sgRNAs targeting the mouse gene ROSA26 (for control) or the human TSC2 gene (for TSC2 KO). Cas9 expression was induced for one week through doxycycline exposure and transduced cells were positively selected with blasticidin. (B) The minimal concentration of doxycycline needed to induce Cas9 expression was trialled using 0.1, 0.5, 1, 2, and 5 μg/ml doxycycline for 24 h in iPSCs and NGN2 neurons on day 10. All doxycycline concentrations tested were sufficient to induce Cas9 expression after 24 h in iPSCs but Cas9 expression was notably lower in NGN2 neurons. (C) TSC2 gene expression in two attempted transductions to create CRISPR/Cas9^{wt} and CRISPR/Cas9^{TSC2} lines. No significant difference in TSC2 expression was observed between both lines in both attempts (First round, $p = 1.0$; second round, $p = 1.0$). (D) TSC2, pS6, and S6 protein expression for two samples of each, CRISPR/Cas9^{wt} and CRISPR/Cas9^{TSC2} lines, obtained from the first transduction attempt after one week of doxycycline and blasticidin-selection. A slightly lowered expression of TSC2 could be observed in one of the CRISPR/Cas9^{TSC2} samples. However, this probable knockdown of TSC2 did not translate into an increase in mTORC1 activity.

3.4 Discussion

Neuronal differentiation in TSC2 +/+ and TSC2 -/- cultures. TSC2 knockout hES and isogenic wild-type control lines are the foundation of my thesis. These lines were genetically manufactured at Roche Hoffmann AG from a well-characterised hES line [44] and tested for their genotype and associated phenotype twice, at Roche and by myself. Full deletion of TSC2 was confirmed in TSC2 -/- hES as well as their derived NSC counterparts. TSC2 knockout resulted in a complete loss of the TSC2 transcript tuberin and caused increased activity of the TSC1:TSC2 downstream target mTORC1. This is in line with the underlying molecular biology and mTORC1 hyperactivation in TSC2-deficient lines has previously detected elsewhere [19, 150].

In my study, I used two conceptually different neuronal differentiation protocols to examine neurodevelopment in TSC, namely spontaneous differentiation through dual SMAD inhibition as well as guided differentiation through forced expression of NGN2.

Neuronal differentiation from TSC2 +/+ and TSC2 -/- hES through dual SMAD inhibition recapitulated key milestones of human neurodevelopment such as

- the production of multiple neuroprogenitor types,
- the formation of a 2D equivalent of the polarised neural tube,
- differentiation into migrating neurons and
- partial neuronal maturation and cortical layer formation.

Immunostainings and qRT-PCR experiments demonstrated that dual SMAD-inhibition produces typical *in vitro* neuronal networks characterised by clumps of neuronal somata

interconnected through axonal processes. I confirmed dorsal telencephalic characteristics in these neurons. In contrast to my human cultures, mouse ES cells have previously been found to spontaneously differentiate mostly into ventral neural progenitors [89] emphasising the importance of establishing human systems when modelling neurodevelopmental disorders *in vitro*.

Immunostainings further confirmed that cultures after 18 to 25 days produced at least two different dorsal neural progenitor types, Pax6-positive RGCs as well as Tbr2-positive IPCs. The presence of both NSC markers is further consistent with the formation of a ventricular (comprising Pax6+ve cells) and a subventricular (comprising Tbr2+ve cells) zone as seen *in vivo* [165]. No clear structural division into two different zones could be detected in neural rosettes, however, rosettes appeared clearly polarised into a ZO-1 positive inner lumen and outer neurogenic zone, as seen previously elsewhere [201]. Rosette neural progenitors underwent neurogenic divisions producing TUJ-1+ve neurons that migrated out of the rosette structure. In both genotypes, cortical layering was only partially detected transcriptomically through the expression of lower layer markers such as CTIP-2 and Tbr1 as well as the upper layer marker Sat2b. No temporal succession was seen, however, other studies have previously demonstrated early expression of lower layer markers followed by upper layer markers in dual SMAD-inhibition protocols [239].

Direct conversion through forced expression of NGN2 converted hPSC into neurons within a few days as previously seen elsewhere [300]. Other studies demonstrated that NGN2 conversion is also sufficient to directly differentiate non-neuronal somatic cells into neurons as shown from mouse astrocytes and fibroblasts [8, 9, 36, 101, 167] as well as from human primary astrocytes [9, 298]. Due to that strong neurogenic conversion drive, the NGN2 protocol lacks a distinctive progenitor stage with TUJ-1+ve and HuC/HuD+ve

post-mitotic neurons appearing from the early stages of the protocol onwards. I confirmed the dorsal telencephalic nature of these neurons through the positive expression of the cortical layer 2/3 markers Sat2b and Brn3a. This is in accordance with the original protocol published by Zhang et al. who found that, when applied directly to hPSC, NGN2 upregulation produces uniform cortical layer 2/3 neuronal cultures [300].

The final milestone of human cortical development is the gliogenic switch when neurogenesis ceases and gliogenesis from the remaining neuroprogenitor pool intensifies. As this glial switch happens *in vivo* after three to four months of gestation, the production of a sufficient number of astrocytes *in vitro* is a long-term effort [243]. Thus, the here used neuronal protocols were not suitable for deriving sufficient numbers of astrocytes. In line with that, I did not detect significant glial marker expression after 80 days in my dual SMAD-inhibition cultures. Direct neuronal conversion through NGN2 expression does not lead to astrogenesis due to the lacking formation of a pool of neural progenitors.

I used a commercially available glial differentiation kit that starts from a neural progenitor pool created through dual SMAD inhibition. In contrast to the neuronal route, neural progenitors were not kept tightly packed in structured rosettes but instead, were sparsely plated out destroying the rosette structure and lifting cell adhesion clues which triggers gliogenesis [134]. As a result, both lines yielded star-shaped astrocytic cells with varying GFAP expression without reaching a post-mitotic state within the lifespan of the cultures which allowed continuous expansion.

Cortical identity as well as regional affiliations are difficult to assess in astrocytes, predominately due to the lack of specific markers [224]. Location and regional pattern of astrocytes *in vivo* are primed at the neuroepithelial and NSC stage. NSCs first differentiate into neurons and then into astrocytes of the same regional identity [154]. Likewise, reprogrammed neurons derived from cerebral or cerebellar astrocytes have been

shown to inherit the regional properties of their glial originators suggesting that regional characteristics are robustly primed into the differentiated cell at the progenitor level [36]. As astrocytes from TSC2 +/+ and TSC2 -/- hES have been produced from the same dorsal telencephalic neuroprogenitor pool found to produce cortical neurons, they are thus likely to carry a dorsal cortical glial fate as well.

No direct glial conversion protocol could be established within the reach of this thesis. Such protocols were recently published, for example by using forced expression of the gliogenic transcription factor NF1A [259]. However, the respective plasmid could not be made available in time to perform necessary optimisation and quality control experiments on the resulting glial cells.

In summary, I was able to differentiate TSC2 +/+ and TSC2 -/- hES into cortical neurons and astrocytes using conceptually different approaches which is a unique basis for my thesis. The availability of a neuronal protocol that recapitulates neurodevelopment allows me to study the effects of TSC2 deficiency in combination with non-genetic factors on different hallmarks of cortical development. On the other hand, the NGN2 protocol enables me to produce neurons more efficiently facilitating a greater number of experiments. At the start of my project, I was not aware of any study using human TSC2-deficient astrocytes for *in vitro* investigations on neurodevelopment in TSC. Since then, only a small number of such studies have been published. My experiments are, thus, uniquely placed to answer questions regarding the neurodevelopmental basis of cortical tubers and disturbed neuronal networks in TSC.

Stem cell-derived cell lines show high biological variability, detected even in experiments using similar or the same cell lines but performed in different laboratories or at

different times. This high variability can lead to false-positive results when biological variability correlates randomly with genetic phenotypes without a causal connection. In my study, I had only one set of TSC2 +/+ and TSC2 -/- hES and NSC lines available hampering the interpretability of my experiments. Therefore, I attempted to generate additional TSC2 knockout and control cell lines using an inducible CRISPR/Cas9 system which turned out to be unsuccessful. The CRISPR/Cas9 system was a revolutionary milestone in molecular biology as it allows much simpler genetic engineering. However, target-dependent variations in the efficiency of delivery methods [297] and site-dependent variations in sgRNA specificity and sensitivity [188] can hamper its efficiency and efficacy and can lead to extensive optimisation requirements. Due to constraints imposed by the COVID-19 pandemic and limited laboratory resources, such optimisation efforts were not possible to be performed within the scope of my project.

I also tested pharmacological and genetic modifications of the TSC1:TSC2-mTORC1 pathway *in vitro*. Ectopic TSC2 expression in TSC2 -/- cells or TSC2 knock-down in TSC2 +/+ cultures proved unreliable in their ability to modify tuberin expression and mTORC1 activation. Similarly, pharmacological activation of mTORC1 was unsuccessful in both genotypic NSC lines. Only the pharmacological inhibition of mTORC1 with rapamycin was found to be effective in TSC2 +/+ as well as TSC2 -/- NSCs. This is in line with rapamycin being an established and widely used agent that has been shown to reverse various mTORC1-mediated effects on cellular metabolism, growth and differentiation potential in models of TSC *in vitro* [19, 44, 93, 150, 253] as well as similar cellular phenotypes, seizure generation, and tumoural growth *in vivo* [64, 125, 145, 295].

I had planned to characterise TSC2+/+ and TSC2-/- neurons, either derived via

dual SMAD-inhibition or via the NGN2 protocol, functionally as well, for example by performing electrophysiological measurements or molecular investigations of their synaptic composition. Such investigations would have included immunofluorescence staining for common synaptic markers such as the pre-synaptic markers synaptophysin or SNAP25 and the post-synaptic protein Homer-1. However, these experiments were not possible due to limitations to resources and time, predominantly inflicted on my project by the COVID-19 pandemic and related restrictions.

Impact of TSC2 knockout on neural development *in vitro*. Lastly, I examined the impact of TSC2 on neuronal and glial differentiation *in vitro*. Overall, knockout of TSC2 affected NSC size and proliferation as well as cell fate decisions during neural differentiation.

Prolonged self-renewal and enlarged NSCs

After dual SMAD inhibition, TSC2 -/- cultures generated cytomegalic NSCs and large rosettes but this was not a consistent feature of all TSC2 -/- cells. In previous studies, homozygous TSC2 knockout cell lines were found to produce enlarged NSCs [19, 44] as seen here. However, my TSC2 -/- NSCs also demonstrated a tendency for increased proliferation during the neurogenic phase. When kept in stable, non-neurogenic conditions, TSC2 +/+ and TSC2 -/- NSCs showed no differences in growth rate and doubling time. This is in accordance with previous studies on TSC1 and TSC2-mutated hPSC [44, 150, 253, 304]. However, other studies on heterozygous or homozygous TSC2 loss-of-function NSCs have demonstrated increased proliferation rates [150, 164]. A possible explanation for this difference might be that NSCs with increased turnover in previous studies were undergoing active neurogenesis whereas the NSCs used in this study were kept stable at the NSC stage. Their ability to progress with neurogenic cell divisions was suppressed by the addition of NSC-mitogenic growth factors epidermal growth factor (EGF) and basic fibroblast growth

factor (bFGF) [232]. In contrast, NSC self-renewal was prolonged during the dual SMAD-inhibition protocol in TSC2 -/- cultures compared to TSC2 +/+ cultures suggesting that TSC2 impacts selectively on the proliferation of NSCs undergoing neurogenic cell divisions.

Increased propensity for gliogenesis and neural immaturity

In this study, TSC2 -/- neural cultures showed an increased tendency towards glial differentiation which was seen in cells derived by various differentiation approaches. Stable TSC2 -/- Roche NSCs presented with a higher expression of the gliogenic transcription factor NF1A compared to TSC2 +/+ controls. After dual SMAD inhibition, loss of TSC2 further led to disturbances in neuronal maturation and cortical layering and upregulated levels of the glial markers NF1A and GFAP. These transcriptional changes did not affect protein content and cellular fate as the overall proportions of produced neurons and glia up to day 80 were unaffected by TSC2 knockout. However, in a dedicated glial differentiation protocol, gliogenesis was strikingly enhanced by the loss of TSC2. At day 40, TSC2 -/- astrocytes showed a reduction in GFAP transcription, however, associated with no changes to the expression of the GFAP protein. This underlines the mismatch between transcriptional and translational changes that I have been seeing in neurons with a disturbed TSC1:TSC2-mTORC1 axis as well. In contrast, TSC2 deficiency led to a significant elevation in GFAP protein expression between days 60 to 70 suggesting that loss of TSC2 favours glial development and potentially activation of glia into a more reactive state. Previous studies similarly found increased glial tendency in neural differentiations on TSC2-mutated cultures [93, 150]. TSC1/TSC2-deficient stem cell-derived cultures have been reported to produce elevated glial cell numbers during neuronal differentiation, but in contrast to my study, these observations were made after 100 days of differentiation in a 3D neural model system [19]. Here, transcriptional changes

induced by TSC2 deficiency did not translate into a full cortical malformation-like picture as the ratio between neurons and glia remained normal throughout the differentiation.

Conclusions. In this chapter, I established that stem cell-derived neuronal and glial cultures are suitable to examine neurodevelopmental milestones using conceptually different hPSC differentiation methods in the context of TSC. I confirmed that the here used TSC2 -/- hES and NSCs lack TSC2 on the transcriptional as well as translational level causing changes in cell size, NSC self-renewal, and neural cell fate tendencies. I further demonstrated that dual SMAD-inhibition is suitable to induce cortical neurons from both genotypic cell lines, TSC2 +/+ and TSC2 -/-, with no differences in glio-neuronal composition after 80 days of differentiation. TSC2 knockout impacted on early as well as later stages in neuronal development with a tendency to produce larger neural rosettes, prolonged NSC maintenance, and transcriptional changes towards glial cell fate. Lastly, TSC2 knockout enhanced glial differentiation in a dedicated glial protocol.

Taken together, these results indicate that the here used *in vitro* stem cell-based neural modelling systems are suitable to elicit the effect of TSC2 on early neurodevelopment. TSC2 deficiency caused changes on the transcriptional level throughout neural differentiation and affected the NSC stage, but these changes did not manifest in a disturbed glio-neuronal ratio at later neuronal stages. Thus, I hypothesise, that a combination of TSC2 deficiency and additional external perturbations, for example, the deprivation of the important energy-delivering nutrient *glucose*, is required for features of cortical tubers to manifest.

People with germline TSC1 or TSC2 mutations present with localised disturbances in glio-neuronal development leading to regional cortical tubers while leaving the remaining

brain tissue relatively unaffected. The germline character of TSC1/TSC2 mutations in patients with TSC as well as detected heterozygosity in cortical tubers suggests that a TSC2 mutation alone is insufficient to induce tuber formation. So far, it is unclear which additional external stimuli are necessary or sufficient to trigger tubergenesis in patients with TSC. As the TSC1:TSC2-mTORC1 pathway is involved in the transformations of nutrients to cellular energy, I will next examine the potential of external glucose supply to be such a trigger of cortical malformation in TSC.

4 | The impact of glucose/energy metabolism on neural development in TSC

4.1 Introduction

In most model systems, stem cells and their cellular derivatives are maintained at non-physiologically high glucose levels. Standard human cell culture media has glucose concentrations of up to 25 mM which is significantly higher than normal blood glucose (5 mM) or brain glucose (1 - 2.5 mM) levels [218]. However, human and mouse stem cells alter their genetic and epigenetic landscape and differentiation propensity significantly when cultured in lower glucose concentrations [177, 178]. For example, high glucose supply promotes differentiation of mouse embryonic stem cells (ES) into primordial germ cells [177] whereas lower glucose levels have been found to support neuronal differentiation from mouse embryoblasts *in vitro* [178]. In mouse trophoblasts, glucose deprivation leads to perturbations in stemness-related transcription factors that significantly affect marker genes after differentiation [189]. TSC-related tumours show increased growth when maintained in *carbohydrate-free* conditions suggesting a tight link between glucose metabolism and tuberigenesis in TSC [119].

As will be shown below, the metabolic state of neural cells is tightly linked to neurodevelopment. TSC2-deficient cells are characterised by a significant disruption in their ability to regulate their metabolic balance with respect to nutrient supply.

The mTORC1 is a main regulator of the cellular anabolic-catabolic balance. mTORC1 stimulates cell growth, proliferation, and development by increasing the production of important elementary cell units such as proteins, nucleotides and lipids in response to the cellular supply of energy and nutrients. Catabolic processes such as autophagy are inhibited through mTORC1-mediated pathways.

mTORC1 is mainly controlled by four extra- and intracellular signals: nutrients, energy, oxygen and stress, for example, DNA damage [76]. These signals regulate mTORC1 activation via various signalling cascades, from which the phosphoinositide 3-kinase (PI3K)/Akt/TSC1:TSC2/Rheb route takes a prominent role. The pathway is an important connection between extracellular growth factors such as insulin and insulin-like growth factor and mTORC1 [43]. TSC1:TSC2-independent mechanisms of mTORC1 control also exist, for example through the Rag family of GTPases and lysosomal translocation of mTORC1 [161].

Downstream targets of mTORC1 are displayed in figure 4.1. They include important cellular processes such as transcription and protein translation as well as nucleotide synthesis, or lipid and glucose metabolism [242]. Through increased ribosome biogenesis and enhanced mRNA translation, mTORC1 drives mRNA translation as a whole. It upregulates a distinct set of mRNAs characterised by a 5'-terminal oligopyrimidine tract (5'-TOP-mRNAs) which increases the ribosomal pool of the cell leading to increased translational rates [213].

The synthesis of other important cellular building blocks such as nucleotides is also

dependent on mTORC1 activation [231]. Nucleotides serve as the elementary units of DNA and RNA but also have an important energy-storing and supplying function so that their synthesis stimulates both, cell growth as well as cell division.

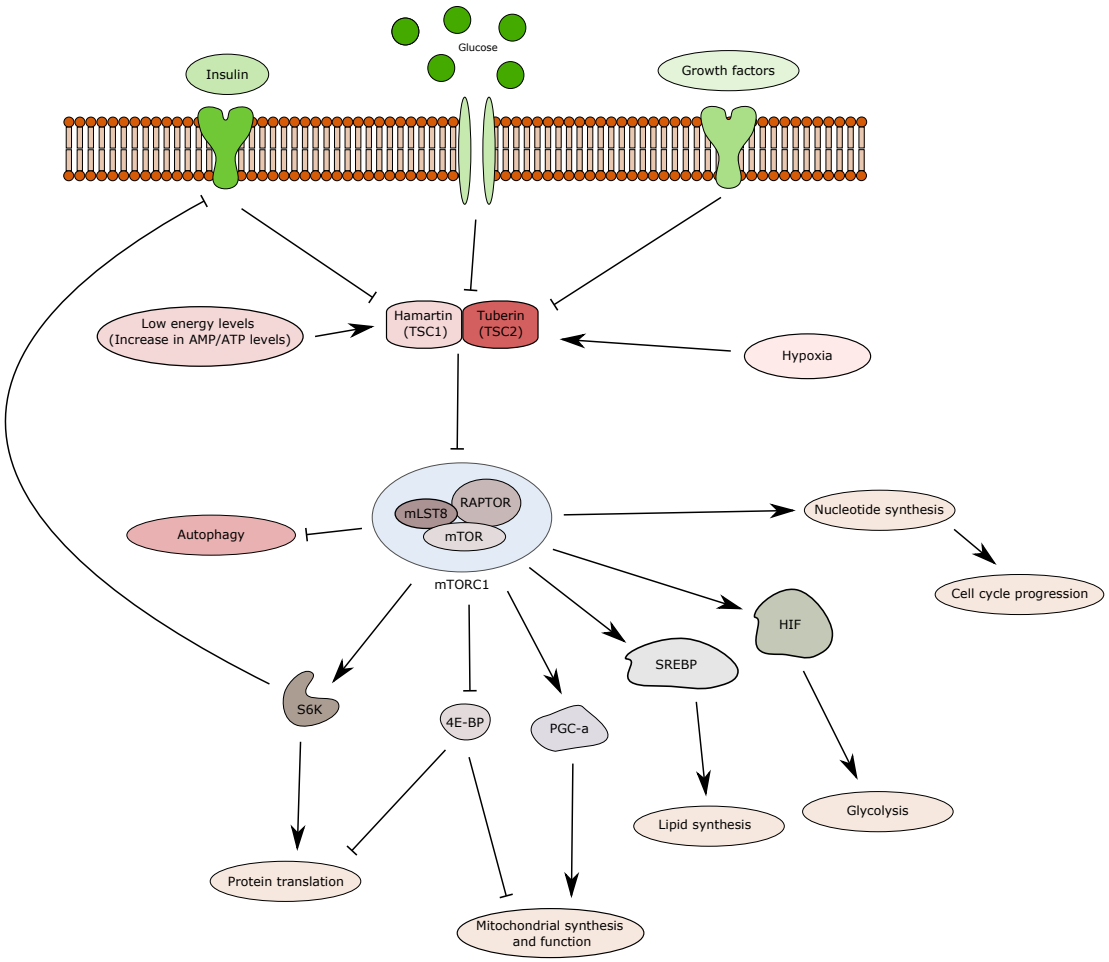


FIGURE 4.1: **Downstream targets of mTORC1.** The mTORC1 controls important cellular pathways to regulate the balance between anabolism and catabolism, including protein translation, metabolic pathways, cell cycle progression, mitochondrial homeostasis, and autophagy. It does so via its downstream targets, the protein kinases S6K, 4E-BPs, or the transcription factors hypoxia-induced factor (HIF), and SREBPs. S6K exerts negative feedback onto mTORC1 via inhibition of the activating insulin receptor substrate-1.

Many metabolic pathways, including glycolytic activity, are also controlled and stimulated by mTORC1. The complex indirectly upregulates genes encoding for enzymes involved in nearly every step of glycolysis leading to increased glucose uptake and lactate production in TSC2 -/- cells [62]. The increased expression of glycolytic genes might be mediated by mTORC1-regulated activity of the transcription factor HIF, the active dimer formed

of its subunits HIF-α and HIF-β. HIF upregulates multiple metabolic genes including glycolytic enzymes. The activity of the transcriptionally active HIF-α/HIF-β complex is increased by mTORC1, likely due to increased HIF-α synthesis [140].

Other metabolic pathways are also stimulated through mTORC1 such as the pentose phosphate pathway or *de novo* synthesis of lipids and steroids [62]. Similar to its action on HIF, mTORC1 promotes the transcriptional activity of a range of transcription factors, for example, the family of SREBPs. SREBPs impact on metabolic gene expression which links cellular metabolic activity with the availability of key nutrients and energy [233].

As a main regulator of cellular energy homeostasis, mTORC1 is further involved in mitochondrial metabolism. Mitochondrial homeostasis is critical in neurodevelopment and healthy neurons due to their high energy demands and tight regulation intracellular of Ca^{2+} flow [100]. Neurons constantly shift mitochondria between their various compartments including the soma, axons, and dendrites and disturbances in mitochondrial transport can lead to severe neurological presentations [236]. Through upregulation of nuclear-encoded mitochondrial proteins via 4E-BPs, mTORC1 increases mitochondrial biosynthesis and further stimulates the mitochondrial oxidative function through the master regulator of mitochondrial synthesis peroxisome-proliferator-activated γ co-activator-1α (PGC-1α) [100].

Two main cellular pathways have been identified to mediate the effects of mTORC1 on cellular growth, namely via the family of ribosomal protein S6 kinases (S6K) and via 4E-BPs. In contrast to S6K, 4E-BPs inhibit translation by preventing the eukaryotic translation initiation factor 4E (eIF4E) to assemble into its functioning complex. Phosphorylation of 4E-BPs by mTORC1 blocks the binding to eIF4E allowing eIF4E-mediated translation [231]. Various studies in Drosophila and mice have demonstrated that knock-out of S6Ks

inhibits cellular growth but not proliferation leading to smaller and developmentally delayed animals [181, 240]. S6Ks are a major controller of ribosome biogenesis and protein translation [240]. More than 75 % of all ribosome biogenesis factors are downregulated in S6K-deficient mice tissue [33]. S6Ks further phosphorylate and activate the multi-modal enzyme CAD which executes rate-limiting steps of pyrimidine synthesis [220]. However, S6Ks also implement an important negative feedback loop on mTORC1 activation. S6Ks inhibit the insulin receptor substrate 1, an upstream signal of PI3K, which decreases mTORC1 activation [174]. The phosphorylation of the S6K downstream target ribosomal protein S6 is therefore a widely-used measure of cellular mTORC1 activity.

Role of mTORC1 in neurodevelopment. Neurogenesis is a very well-orchestrated and fine-tuned process. The synthesis of elementary cellular units and maintenance of cellular homeostasis is essential to enable controlled cell growth and proliferation during development and mTOR signalling also exerts a profound role in many aspects of neurogenesis [151].

Reduced protein translation is a critical feature in embryonic stem cells. The start of differentiation from ES is associated with a massive anabolic switch characterised by an overall increase in protein synthesis [228]. Hyperactivation of S6K-mediated protein synthesis induces differentiation and reduces the expression of pluripotency markers in ES [63]. The intrinsic mTOR inhibitor DEPTOR plays a crucial role in maintaining pluripotency in mouse ES and its levels are dramatically reduced upon differentiation suggesting that mTOR can serve as a main initiator of differentiation [3].

In NSCs, mTORC1 impacts the delicate balance of stem cell renewal and differentiation. RAPTOR-deficient mice present with much smaller brains during embryonic development and at birth as a result of decreased cell number and increased neuronal cell death at later stages during development [41]. RAPTOR-deficient NSCs are characterised by a length-

ening in their cell cycle duration which reduces NSC proliferation and induces neuronal differentiation leading to an overall reduction in neuronal output [41]. In neonatal NSCs, mTORC1-mediated cap-dependent translation is critical for their differentiation into intermediate progenitors and subsequent neuronal differentiation [99]. The mTORC1 pathway promotes the progression of Pax6-positive RGCs towards Tbr2-positive basal progenitors. The timing of this transition is crucial for the maintenance of the RGC pool and the expansion of neuronal cell numbers [57]. The mTORC1-induced push towards neuronal differentiation is mainly translated through the inhibition of 4E-BP2 whereas S6Ks play a pivotal role in regulating NSC soma size [99]. Various growth factors enhance neuronal development, amongst which insulin and insulin-like growth factor (IGF) are prominent examples. Exposure of NSCs to insulin and IGF increases neuronal differentiation and neuronal output. This effect is mediated by Akt-dependent mTORC1 phosphorylation and activation and demonstrates the direct role of mTORC1 in integrating extracellular nutrition signals with cellular differentiation [97]. Overall, mTORC1 is critical for the build-up of the NSC pool to allow subsequent neuronal differentiation and mTORC1 inhibition leads to a significant disruption of neurodevelopment from early NSC stages onwards.

Following its central role in NSC renewal and differentiation, mTORC1 also exerts various effects on the migration and maturation of newly-born neurons. Cortical tubers show aberrant lamination and disrupted neuronal organisation suggesting that loss of TSC1:TSC2 and mTORC1 hyperactivation disturbs neuronal migration and integration [110, 157]. Also, mTORC1 signalling is essential for dendritic branching, axonal sprouting, synaptogenesis, and cortical connectivity [151].

Lastly, mTORC1 signalling is strongly involved in gliogenesis, although its effect on glial maturation is less well studied. Increased mTORC1 activity enhances glial output from NSC differentiation due to hyperactivation of the mTOR-Stat3 axis [280]. RAPTOR-

deficient mice also demonstrate a significantly reduced production of glial cells which highlights that sustained mTORC1 signalling is critical for gliogenesis [41].

Metabolic reprogramming during neural development. During neurogenesis, differentiating cells shift their energy generation from glycolysis in NSCs to oxidative phosphorylation in post-mitotic neurons [301]. Glycolysis generates only two ATP molecules per glucose molecule, in contrast to 32 ATP molecules produced during mitochondrial respiration. However, glycolysis also generates pyruvate and lactate, starting molecules for many anabolic pathways. Glycolysis, thus, enables proliferating and expanding cells, such as NSCs or cancer cells, to balance their energy needs with their metabolic demands in order to generate the required biomass for further cell growth and division [302]. Also, glycolysis is a very rapid source of ATP allowing fast-rate cell proliferation [270]. In contrast, mitochondrial respiration is a slow but very efficient energy-generating process enabling post-mitotic neurons to meet their high energy demands, for example, to maintain the energy-costly membrane potential [114].

Changes in metabolic gene expression during neurogenesis facilitate the metabolic switch in a distinct way. The balance between glycolysis and oxidative phosphorylation is mainly controlled via the differential expression of key glycolytic enzymes whereas the expression levels of mitochondrial genes are mostly unchanged during neural development [301]. Neuronal differentiation is associated with the downregulation of enzymes facilitating high glycolytic flux such as the cellular glucose transporters GLUT1 and GLUT3 or the glycolysis rate-controlling enzyme Hexokinase 2. Lactate dehydrogenase A is also repressed during neurogenesis which withdraws pyruvate from anabolic activity but frees it for metabolic respiration [124].

The metabolic switch is not a pure by-product of neurogenesis but one of its active drivers. The balance between glycolysis and oxidative phosphorylation, as well as related mitochondrial dynamics, actively influences cell fate decisions. Mitochondrial dynamics after mitosis in NSCs affect cell fate decisions in the daughter cells and thus, are an important mechanism to regulate the balance between stem cell renewal and differentiation [114]. Mitochondrial dynamics are linked to cell cycle progress with mitochondrial fusion mainly happening during G1/S and mitochondrial fission during G2/M. Disruption of these mitochondrial dynamics can change cell fate decisions in NSC daughter cells. Induced fission tilts the cell towards neurogenesis whereas induced mitochondrial fusion promotes ongoing NSC self-renewal [113].

Metabolites produced during mitochondrial respiration also impact cell fate decisions but the exact effects depend on the stage of neurogenesis the cell is at. In proliferating NSCs, disruption of oxidative phosphorylation lowers their capacity for self-renewal, ultimately leading to a decrease in the neurogenic stem cell pool and decreased neurogenesis [15, 127, 271]. At the end of NSC differentiation, oxidative phosphorylation is necessary to drive NSCs out of the cell cycle and into a post-mitotic state [108]. Products of mitochondrial respiration such as reactive oxygen species or NAD^+/NADH are responsible for these effects through their actions as activating factors for transcription factors or enzymes [126, 142].

Glycolysis by-products can likewise influence NSC proliferation and neurogenesis. Methylglyoxal is an intermediate metabolite derived from glyceraldehyde-3-phosphate which impacts the expression of the Notch1 receptor through its effect on glycerinaldehyd-3-phosphat-Dehydrogenase (GAPDH). GAPDH plays an important role within glycolysis but has an additional, non-enzymatic function as a ribosome binding protein which decreases translation of the Notch1 receptor. Methylglyoxal decreases GAPDH enzymatic

properties but enhances its ribosomal affinity linking enhanced glycolysis to the induction of neurogenesis [222].

These interactions demonstrate the vast cross-talk between metabolism and the cellular protein landscape that determines neural cell fate, and vice versa. Such interactions occur on the transcriptional level through changes in chromatin and epigenetic structures [215] as well as on the translational level as highlighted above or even post-translational through protein modifications [258].

Glucose addiction in TSC2 deficiency. Deprivation of the cell from nutrients and energy leads to mTORC1 repression. Glucose deprivation impacts indirectly on mTORC1 by lowering cellular ATP levels. This promotes the 5' AMP-activated protein kinase (AMPK) which then activates TSC2 and thus, indirectly inhibits mTORC1. This connection provides the cell with the crucial ability to appropriately respond to low nutrient levels with a decrease in catabolic metabolism and is vital for cellular survival in periods of deprivation [233].

The appropriate adaptation of cellular metabolism according to supply levels is severely disrupted in TSC2-deficient cells causing an abnormal glucose addiction. TSC2-deficient cells mainly meet their energy needs via aerobic glycolysis and are unable to adjust their metabolic activity to a limited glucose supply. Dis-inhibited mTORC1 causes increased levels of cell death in glucose deprivation due to a mismatch between nutrient supply and metabolic consumption [35]. Increased vulnerability to glucose deprivation in TSC2-deficient cells has also been linked to mTORC1-driven accumulation of p53 [143]. The inhibition of mTORC1 is sufficient to protect TSC2 -/- cultures from glucose deprivation-induced cell death. This protection is not only p53-dependent but is mainly facilitated through a decrease in metabolic consumption which allows the cells to maintain viable ADP/ATP ratios [35]. Although glycolysis appears to be the dominant energy-producing

pathway in TSC2 -/- cells, their mitochondrial activity is sufficient to meet their ATP needs and prevent glucose deprivation-induced cell death, but only if their metabolic demand is decreased by mTORC1 inhibition.

4.2 Aims

Results from chapter 3 suggested that TSC2 deficiency leads to developmental alterations at the NSC stage as well as to transcriptomic changes in neurons affecting their maturity but leaves the glio-neuronal balance in derived cultures unchanged. Patients with TSC present with local cortical malformations despite the germline character of the underlying TSC1:TSC2 mutation. Therefore, I speculate that a TSC1:TSC2 knockout is not sufficient to cause cortical malformation per se but that additional triggers are needed to induce these severe disruptions in cortical development. Due to the central position of the TSC1:TSC2-mTORC1 pathway within energy metabolism and neurodevelopment, I hypothesise that deprivation of the energy supplier *glucose* could act as such a trigger.

The aims of this chapter are:

1. Examine the effect of glucose deprivation during neural differentiation in TSC2-deficient cells with regards to glio-neuronal balance and overall neuronal output.

2. Measure mTORC1 activation in response to glucose supply at different developmental stages in TSC2 +/+ and TSC2 -/- hES, NSCs, and neurons.

3. Investigate the impact of solitary or combined glucose deprivation and TSC2 deficiency on energy metabolism in NSCs and neurons via transcriptomic and functional screens.

4. Examine whether changes in energy metabolism are causatively linked to disturbed

neural differentiation in glucose-deprived TSC2 -/- cultures.

I addressed these aims in two stages and figure 4.2 gives an overview of the different experimental blocks I used in this chapter.

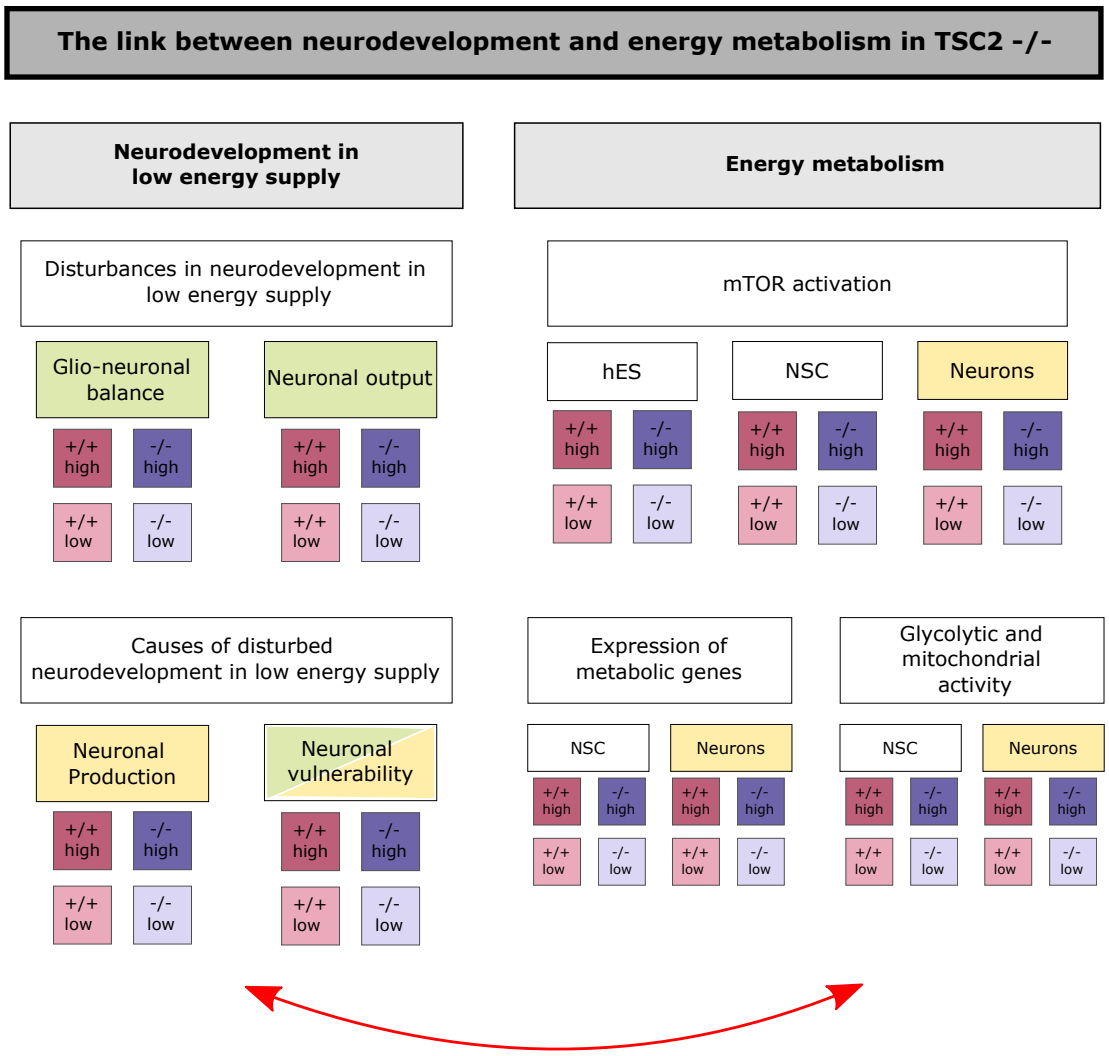


FIGURE 4.2: **Investigations into the effect of combined glucose deprivation and TSC deficiency on the link between disturbed neurodevelopment and energy metabolism.** Overview of the experiments I used to address the effect of combined TSC2 deficiency with glucose deprivation on neurodevelopment and energy metabolism. I measured the glio-neuronal composition in glucose-loaded and glucose-deprived TSC2 +/+ and TSC2 -/- cultures. I also measured neuronal production and neuronal vulnerability in response to glucose supply in both genotypic cultures. Green, cells derived via dual SMAD inhibition; yellow, cells derived by NGN2 protocol.

First, I examined the impact of combined glucose deprivation and TSC2 deficiency on (i) neurodevelopment and (ii) energy metabolism separately. To examine neurodevel-

opment, I measured the glio-neuronal ratio and overall neuronal output during dual SMAD-inhibition in glucose-loaded vs glucose-deprived TSC2 +/+ and TSC2 -/- cultures to detect the effect of low glucose supply on the development of cortical malformations in TSC. To investigate energy metabolism, I quantified mTORC1 activation in response to glucose supply at different neurodevelopmental stages in TSC. I then quantified the effect of combined glucose deprivation and TSC2 knockout on energy metabolism by measuring the expression of key glycolytic and mitochondrial genes as well as quantifying glycolytic and mitochondrial activity using a Seahorse analyser.

Second, I aimed to examine the link between disturbed energy metabolism and neurodevelopment in glucose-deprived TSC2-deficient cultures. My ability to do so was severely limited by the COVID-19 pandemic and related restrictions.

4.3 Results

4.3.1 Glucose concentrations of different media

I differentiated TSC2 +/+ and TSC2 -/- neurons in either standard cell culture media at approximately 22 mM glucose (referred to as *high glucose media*) or in a *low glucose media* at 5 mM glucose. Media containing different glucose concentrations were prepared as described in section 2.2.2.

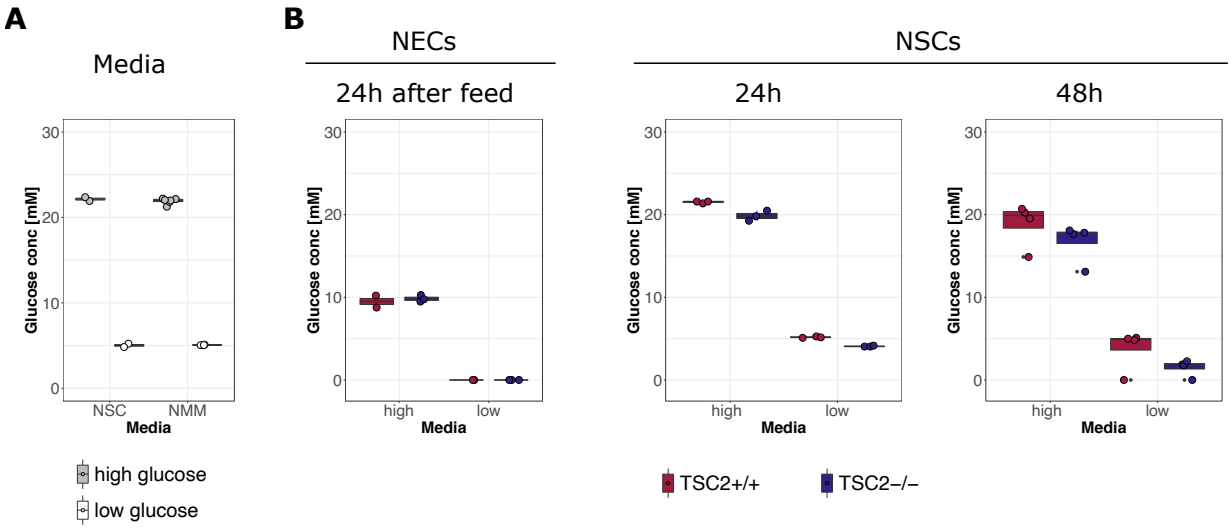


FIGURE 4.3: **Glucose concentrations of different media.** (A) High and low glucose NSC and NMM media had reproducible glucose concentrations of 22 mM and 5 mM, respectively. (B) After 24 h, high glucose NIM media on NECs only had half its original glucose concentration left. All glucose was consumed in 24 h by NECs maintained in low glucose NIM. Stable NSCs consumed much less glucose causing glucose concentrations of roughly 18-20 mM and 3-5 mM in high and low glucose NSC media after 48 h. *Replicates: (A) NMM, 6 technical replicates; NSC, 2 technical replicates; (B) NECs, 4 technical replicates per line and media; NSCs, 3-5 technical replicates per line and media.*

The low glucose version was prepared by supplementing no glucose basal media with key media components such as L-glutamate or sodium pyruvate to match the concentrations of the respective standard culture media. Glucose was then added to reach a concentration of 5 mM. Such high and low-glucose versions of the same culture media were used for culturing and differentiating different neural cell types throughout this chapter. The glu-

cose concentrations of high and low glucose media were tested regularly with a commercial glucometer to confirm the desired concentrations of 22 mM and 5 mM, respectively (see figure 4.3 (A)).

Glucose consumption. I tested media glucose concentrations at 24 or 48 h after a full media change to examine the glucose consumption of different cultures. The respective results are displayed in figure 4.3 (B). TSC2 +/+ and TSC2 -/- cultures at the NEC stage of dual SMAD-inhibition demonstrated the highest glucose turnover compared to other cell and culture types. When cultured in high glucose media, the neuroepithelial sheet of both genotypes consumed more than half of the glucose in the media leading to glucose concentrations of around 10 mM after 24 h. Cell cultures in the low glucose media had no glucose left in the media at 24 hours. In contrast, media from Roche NSCs showed remaining glucose concentrations of around 20 mM (high glucose version) or 3 mM (low glucose version) after a feeding interval of 48 h.

4.3.2 Glucose deprivation does not affect NSC proliferation

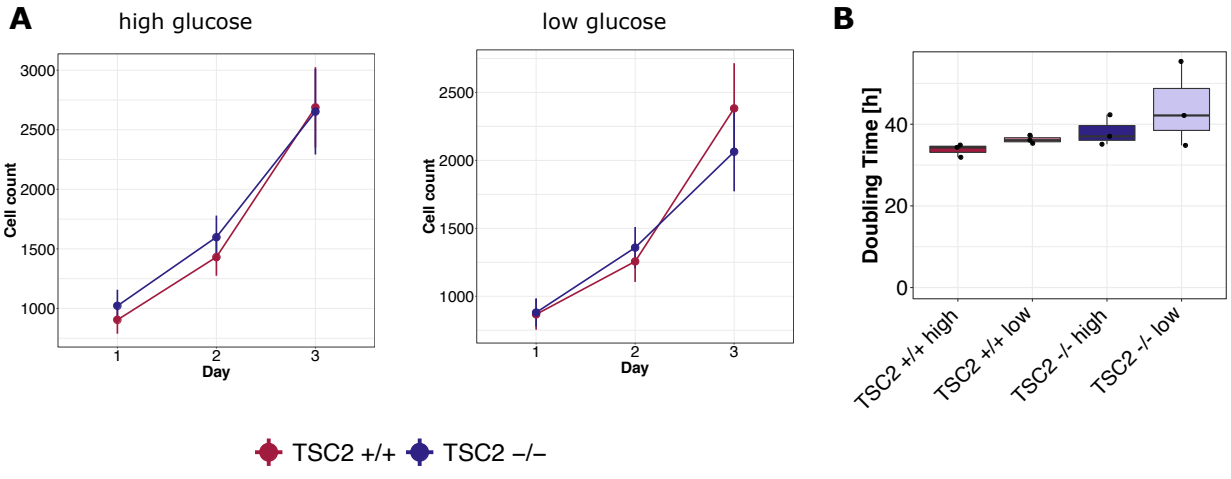


FIGURE 4.4: **Proliferation of stable NSCs in low glucose media.** (A) No differences in the growth curves of stable TSC2 +/+ (red) and TSC2 -/- (blue) NSCs were seen when maintained in high (left) or low (right) glucose media. (B) Doubling times of TSC2 +/+ and TSC2 -/- NSCs were similar when grown in either high or low glucose media. *Replicates: 3 differentiations, 3 technical replicates per line and media.*

The growth of non-neurogenic TSC2 +/+ and TSC2 -/- Roche NSCs was not affected by glucose deprivation. NSC cultures were grown in either high or low glucose media for three days and cells were counted in brightfield microscopic images taken from the same four well positions each day. No significant differences in the doubling rate of TSC2 +/+ and TSC2 -/- NSCs in either high or low glucose media could be observed (see figure 4.4).

4.3.3 Impact of glucose deprivation on neuronal and glial development in TSC2-deficiency

Neural differentiation in glucose deprivation.

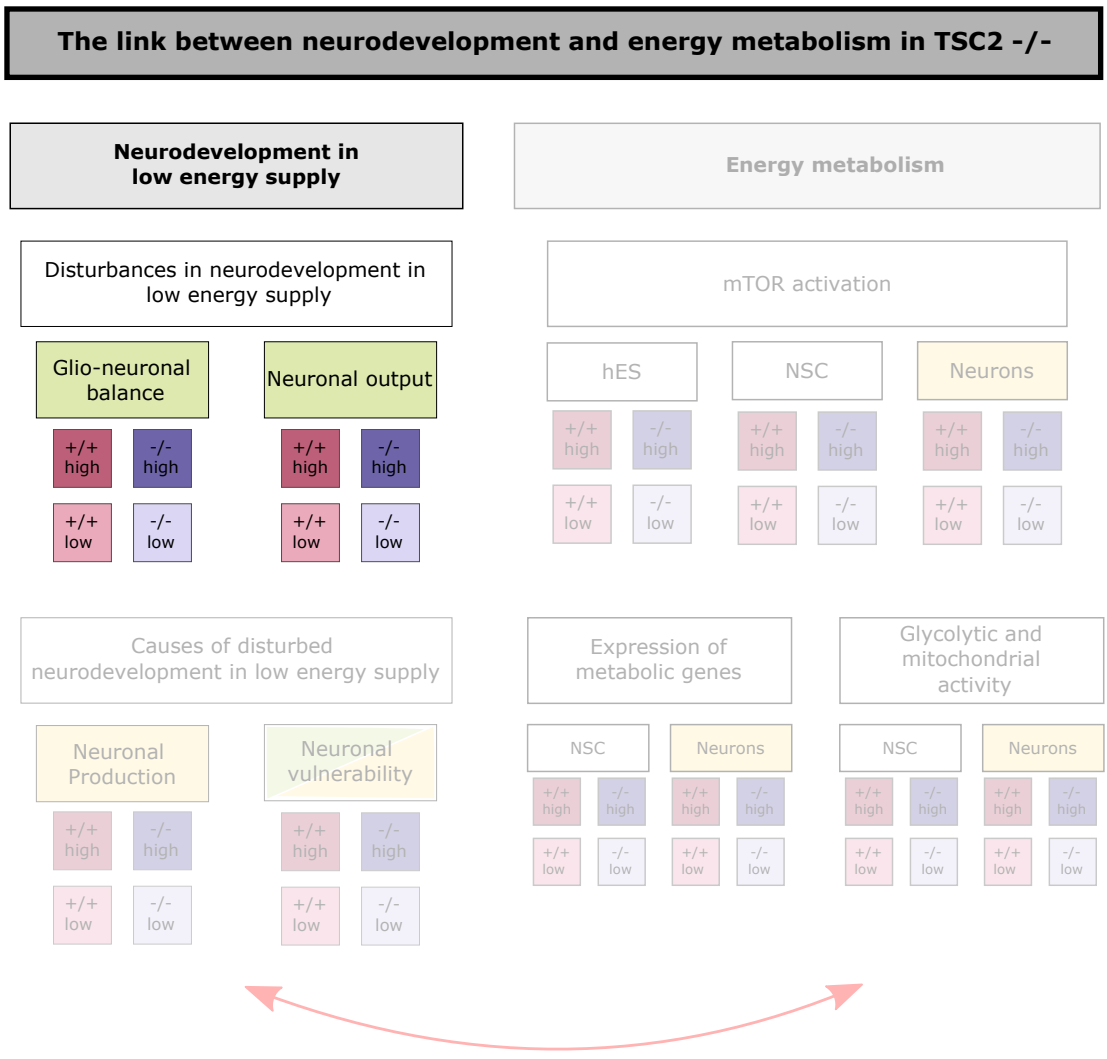


FIGURE 4.5: **Investigations into the effect of glucose deprivation combined with TSC deficiency on the link between disturbed neurodevelopment and energy metabolism.** Green, cells derived via dual SMAD inhibition; yellow, cells derived by NGN2 protocol.

In the previous chapter, I examined the neural differentiation behaviour of TSC2 +/+ and TSC2 -/- cultures in glucose-loaded conditions. The results reveal clear transcriptional differences but, based on protein content, do not show significant differences in glio-neuronal balance or neuronal output between TSC2 +/+ and TSC2 -/- cultures. Here, I examined how the neural differentiation potential changes in glucose-deprived conditions by differentiating TSC2 +/+ and TSC2 -/- hES via dual SMAD-inhibition in either high or low glucose media (see figure 4.5 and 4.6).

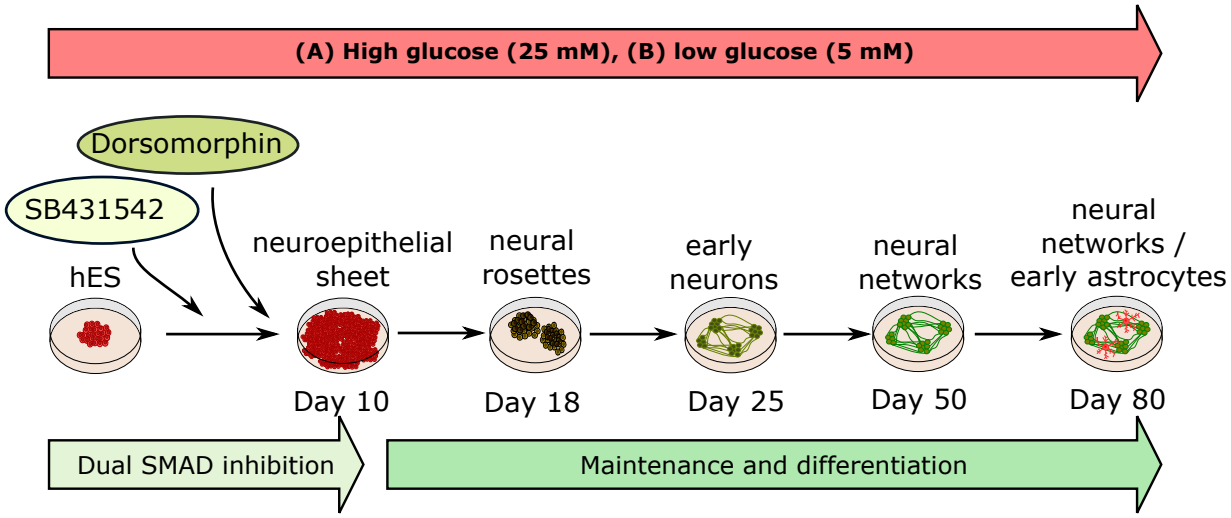


FIGURE 4.6: **Neuronal cortical differentiation in different glucose media.** Dual SMAD-inhibition was performed on TSC2 +/+ and TSC2 -/- hES as described in the previous chapter. To test the effect of glucose supply on neuronal differentiation, cultures were either differentiated in high glucose media or in low glucose media for the entire protocol duration.

Glucose deprivation led to disturbances in neural differentiation in TSC2 -/- cultures. Human ES from both genotypes were differentiated into cortical neurons via dual SMAD inhibition with half of the cultures being differentiated and matured in the low glucose version of the respective media throughout the whole differentiation (see figure 4.6). The differentiation characteristics were measured in two ways: (1) TUJ-1 and GFAP expression served as a measure for the glio-neuronal composition throughout the differentiation and (2) the proportion of HuC/HuD-positive neurons on day 80 was used as a measure of neuronal output.

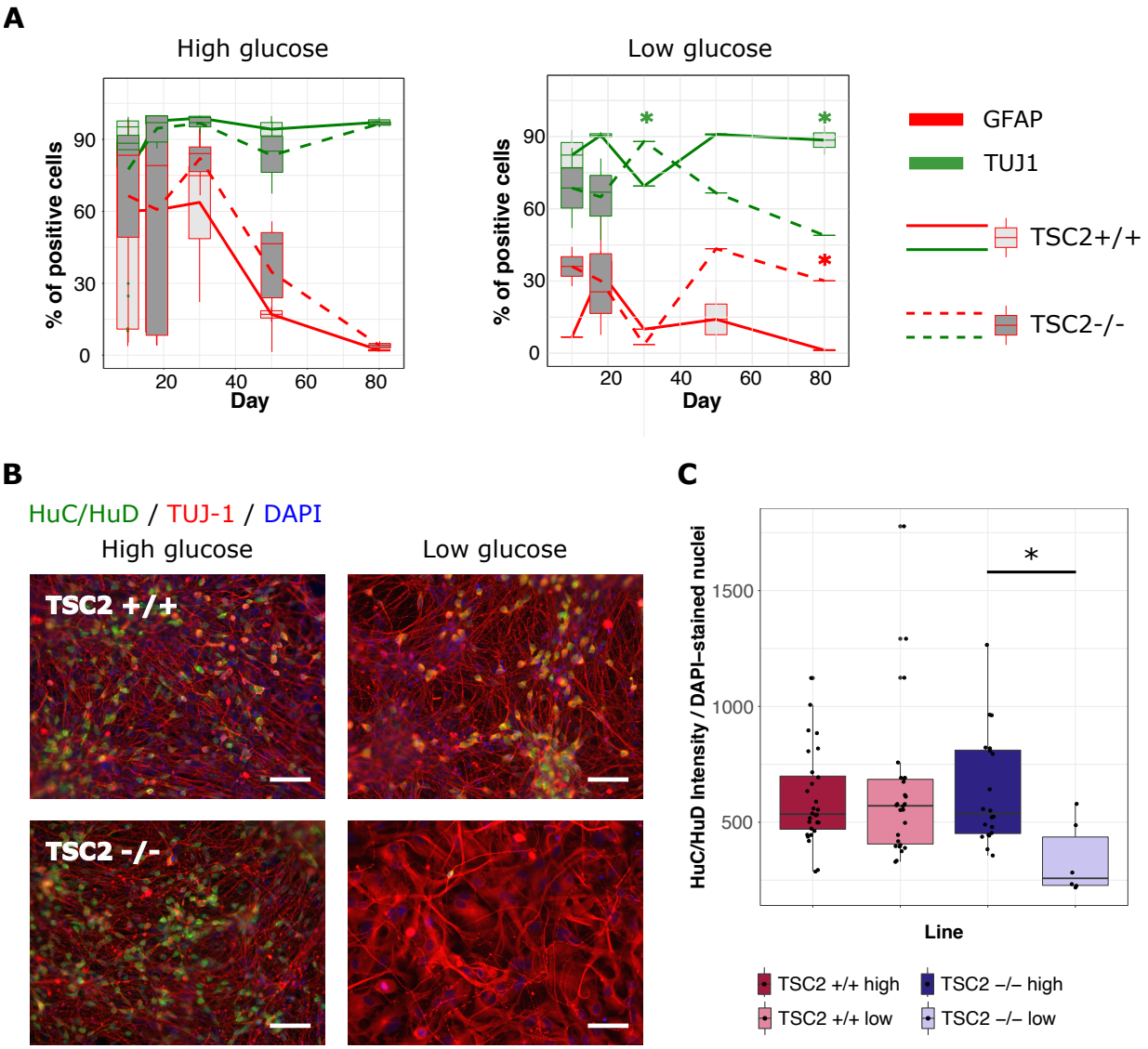


FIGURE 4.7: **Impact of glucose deprivation on neuronal output in dual SMAD-inhibition.** (A) Proportion of TUJ1 (green) and GFAP (red) positive cells in TSC2 +/+ (continuous line) and TSC2 -/- (dashed line) cultures during dual SMAD-inhibition over 80 days in either high glucose (left) or low glucose media (right). In high glucose media, TSC2 deficiency did not cause significant differences in glio-neuronal composition. In low glucose media, TSC2 deficiency led to a significant reduction in TUJ1-positive neurons from day 30 onwards (Day 30, p = 0.0002; day 80, p = 0.003) as well as a significant increase in GFAP-positive glia on day 80 (p = 0.0002). Coloured stars indicate a significant difference between TSC2 +/+ and TSC2 -/- cultures in TUJ1 (green) or GFAP (red) positivity on the respective day. (B) Example images of glucose-loaded and glucose-deprived TSC2 +/+ and TSC2 -/- cultures at day 80 stained against HuC/HuD (green), TUJ-1 (red) and DAPI (blue). Scale bar = 100 μM. (C) Quantification of HuC/HuD-positive cells in TSC2 +/+ and TSC2 -/- cultures differentiated in high and low glucose media at day 80 revealed a significant reduction in HuC/HuD intensity in glucose-deprived TSC2 -/- cultures. *Scale bar* = $100\mu m$. *Replicates: Number of replicates varies per time point between 1-3 differentiations with 3 technical replicates per line and media.*

Glio-neuronal composition. In high glucose media, TSC2 +/+ and TSC2 -/- cultures exhibited a similar pattern of glio-neuronal composition during differentiation as described in the previous chapter. In brief, they presented with high TUJ-1 positivity at ∼90 % from day 10 onwards. GFAP expression was high initially, further peaked at the NSC stage (day 18) at ∼70 % and then declined to less than ∼5 %.

In low glucose media, TSC2 deficiency led to a significant decrease in TUJ1-positive cells (TUJ1 positivity in TSC2 +/+ and TSC2 -/- cultures, day 30, $p = 0.0002$; day 80, $p = 0.003$) as well as a significant increase in GFAP signal (GFAP positivity in TSC2 +/+ and TSC2 -/- cultures, day 80, $p = 0.0002$) at later stages during the differentiation (see figure 4.7 (A)). TSC2 -/- cells showed a generally lower TUJ-1 signal that decreased to ∼55 % on day 80. In both genotypic cultures, glucose deprivation caused lower GFAP expression of around 30 % at the NSC stage. In TSC2 +/+ cultures, GFAP expression then declined to less than 5 % as was seen in glucose-loaded conditions whereas TSC2 -/- cultures saw high GFAP expression levels of ∼30 % at day 80 (see figure 4.7 (A)).

Neuronal output. Glucose deprivation led to impaired neuronal output in TSC2 -/- cultures. In high glucose media, TSC2 +/+ as well as TSC2 -/- cells produced clumps of HuC/HuD-stained neuronal bodies connected by TUJ-1 positive axons. TSC2 +/+ cultures differentiated in low glucose media presented with a similar characteristic neuronal picture. In contrast, TSC2 -/- cultures differentiated in low glucose media were characterised by a very low number of HuC/HuD positive cells, a high degree of variation in cell size and structure as well as a disorganised cellular network without clear axonal connections (figure 4.7 (B)).

In TSC2 +/+ neurons, glucose deprivation did not lead to any significant differences in the HuC/HuD intensity at day 80. In contrast, TSC2 -/- cultures expressed significantly less HuC/HuD when derived in low glucose media 4.7 (C)).

Potential causes for glucose-dependent disturbances in neural differentiation in TSC deficiency

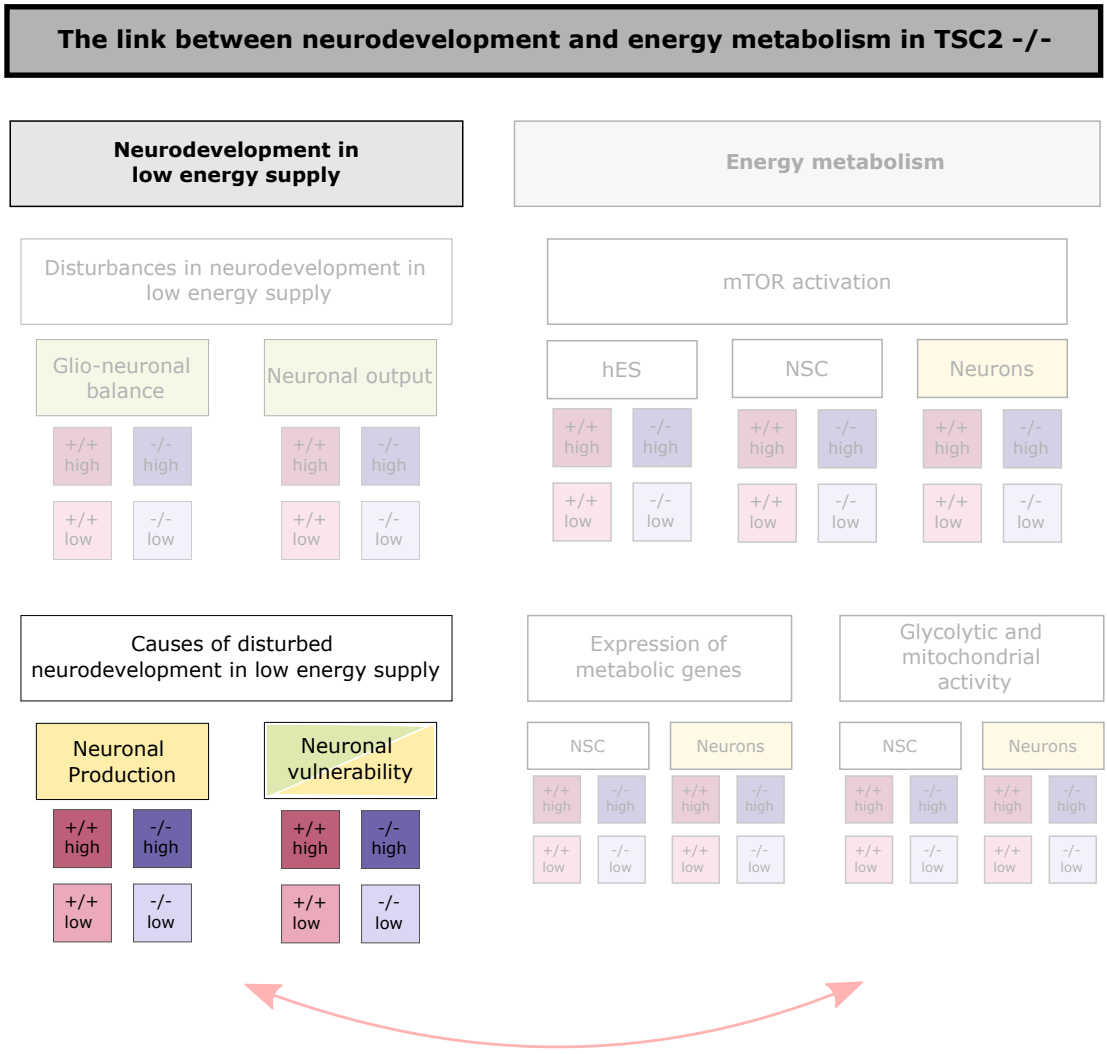


FIGURE 4.8: **Investigations into the effect of glucose deprivation combined with TSC deficiency on the link between disturbed neurodevelopment and energy metabolism.** Green, cells derived via dual SMAD inhibition; yellow, cells derived by NGN2 protocol.

In general, the decreased output of mature neurons in TSC2 -/- cultures in low glucose can either be attributable to decreased production of neurons during the neurogenic NSC phase, increased neuronal cell death at later stages of differentiation, or potentially both. With the following experiments, I investigated the impact of glucose deprivation on neuronal production and vulnerability in TSC2 deficiency.

Effect of early glucose deprivation on neuronal production. Neuronal production is disturbed in glucose-deprived TSC2-deficient cultures. I examined the impact of glucose deprivation on neuronal production in the NGN2 protocol where the neurogenic transformation is driven by the doxycycline-controlled expression of NGN2 during the very first days of the differentiation. TSC2 +/+ and TSC2 -/- hES were differentiated in either high or low glucose media for the first four days and then matured in high glucose media for a further eight days. HuC/HuD expression, measured by immunostainings, was used as a measure for neuronal output on day 12. (see figure 4.9 (A)).

In TSC2 +/+ cultures, no differences in neuronal output were seen for samples differentiated in either high or low glucose media. In contrast, TSC2 -/- cultures generated significantly fewer HuC/HuC-positive neurons when the differentiation was started in low glucose media compared to cultures derived in high glucose media (HuC/HuD intensity per DAPI-positive nuclei: TSC2 +/+ in high and low glucose media: $p = 1.0$, TSC2 -/- in high and low glucose media: $p = 0.0025$) (see figure 4.9 (B)). Example images of all sample groups at day 12 are shown in figure 4.9 (C).

In a similar experimental set-up, I measured the expression levels of two key neuronal differentiation genes at day 12, namely NGN2 and NeuroD1, which are markers of amplifying progenitors and neuroblasts [225]. In the NGN2 protocol, NGN2 is only forcibly expressed for the first three days so that this doxycycline-driven NGN2 gene does not interfere with the innate NGN2 expression at day 12. (see figure 4.10 (A)).

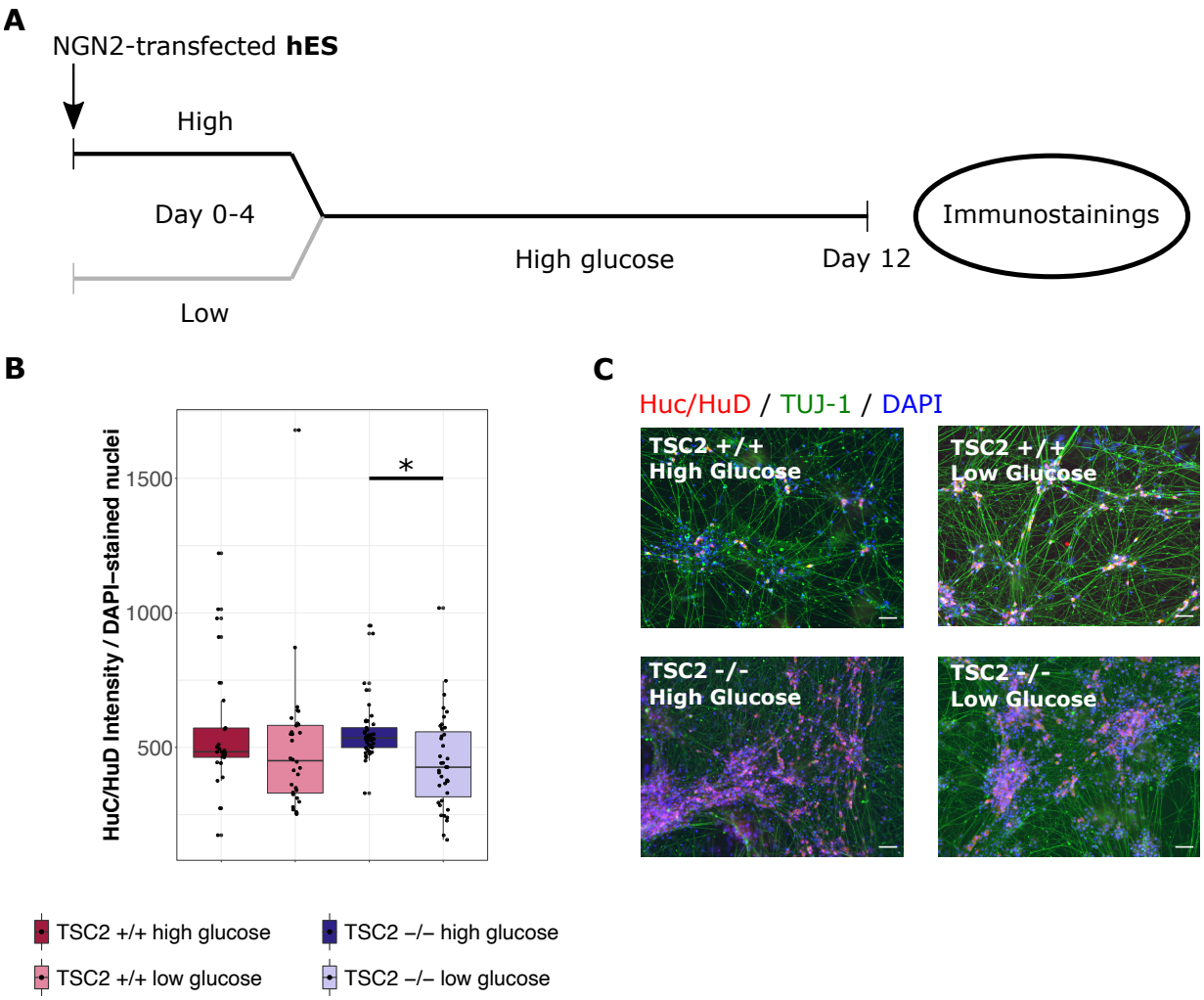


FIGURE 4.9: **Effect of early glucose deprivation on neuronal output in NGN2 differentiation.** (A) NGN2-transfected TSC2 +/+ and TSC2 -/- NGN2 neurons were derived in either high or low glucose media for four days and then maintained in high glucose media until day 12 when cultures were assessed for HuC/HuD expression. (B) Quantification of HuC/HuD expression in TSC2 +/+ (red) and TSC2 -/- (blue) NGN2 neurons. Early glucose deprivation did not affect HuC/HuD intensity in TSC2 +/+ cultures but led to a significant reduction in HuC/HuD expression in TSC2-deficient cultures (hES: TSC2 +/+ in different media: $p = 1.0$, TSC2 -/- in different media: $p = 0.0025$). (C) Example images of NGN2 neurons on day 12 obtained from TSC2 +/+ (upper row) and TSC2 -/- (lower row) hES derived in high or low glucose media and stained against HuC/HuD (red), TUJ-1 (green) and DAPI (blue). *Scale bar* $= 100\mu m$. *Replicates: 1 differentiation, 3 technical replicates with* $\sim$ *40 images per line and media.*

Glucose deprivation did not affect the expression of both genes in TSC2 +/+ cultures. TSC2 -/- cells derived in low glucose media demonstrated elevated expression levels of NGN2 and NeuroD1 whereas their high glucose counterparts showed similar low expression levels to TSC2 +/+ cultures. Probably due to the low number of samples per group and the

high variability in the low glucose TSC2 -/- group, the difference did not reach significance.

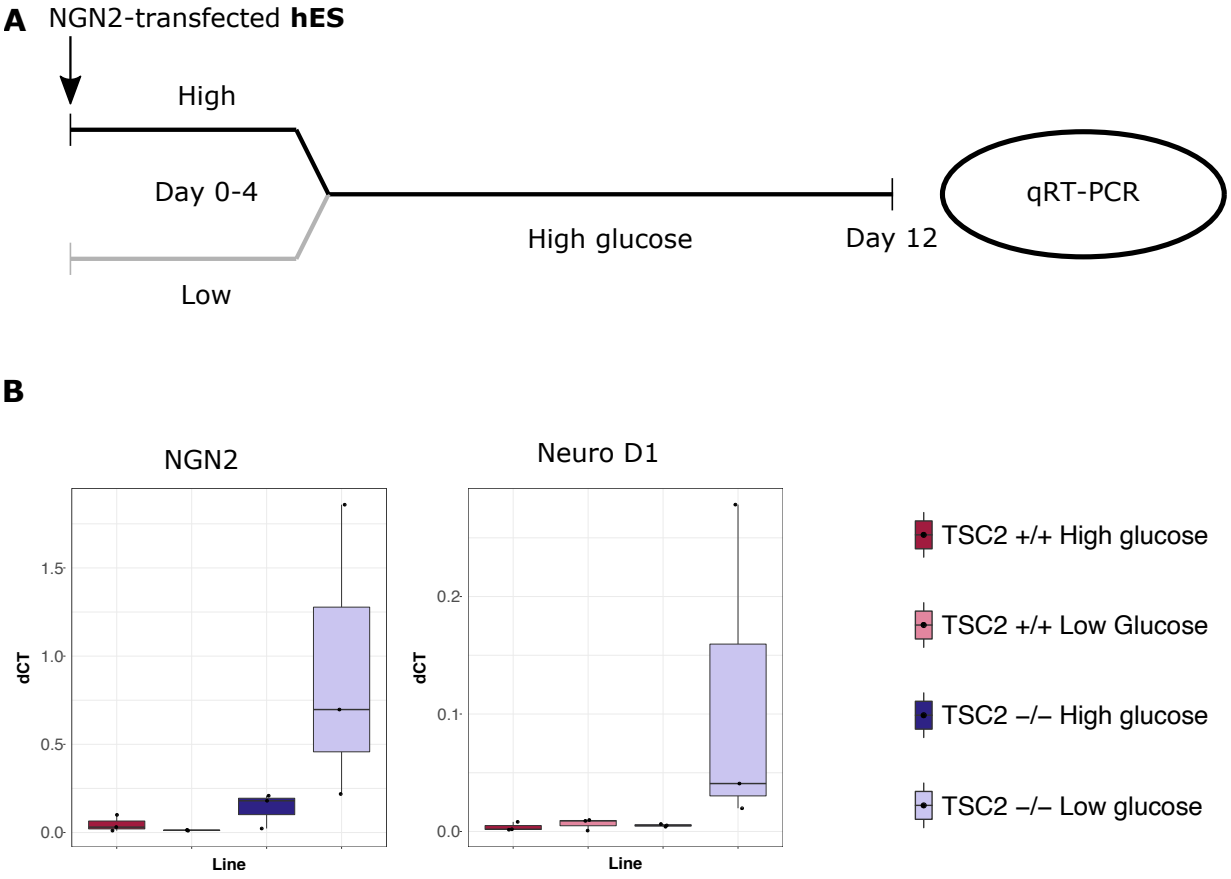


FIGURE 4.10: **Effect of early glucose deprivation on expression of neuronal progenitor genes.** (A) Expression of NGN2 and NeuroD1 was measured in TSC2 +/+ and TSC2 -/- NGN2 neurons derived in either high or low glucose media for the first four days and maintained in high glucose media until day 12. (B) Glucose deprivation did not affect NGN2 or NeuroD1 expression in TSC2 +/+ (red) cultures. In contrast, TSC2 -/- (blue) neurons derived in low glucose showed a notable, yet not significant, elevation in NGN2 and NeuroD1 expression on day 12 (NGN2: TSC2 +/+ high vs low, p = 0.999; TSC2 -/- high vs low, p = 0.185. NeuroD1: TSC2 +/+ high vs low, p = 0.999; TSC2 -/- high vs low, p = 0.324.). *Replicates: 1 differentiation with 3 technical replicates per line and media.*

Neuronal vulnerability to glucose deprivation. Neuronal vulnerability was increased in some TSC2-deficient cultures but not affected by glucose supply. To test neuronal vulnerability, I used the CellTox Green assay to measure cell death in TSC2 +/+ and TSC2 -/- neurons, derived either via dual-SMAD inhibition or via the NGN2 protocol. I used neurons from both protocols to increase comparability with other experiments that had either been performed with dual SMAD-inhibition-derived neurons or NGN2 neurons,

due to disruptions caused by the COVID-19 pandemic. Glucose deprivation was limited to 24 h at the end of neuronal differentiation in TSC2 +/+ and TSC2 -/- neuronal cultures (derived via either NGN2 differentiation or dual SMAD-inhibition) to only test its impact on neuronal vulnerability and avoid interference with neuronal production earlier during the differentiation (see figure 4.11 (A)).

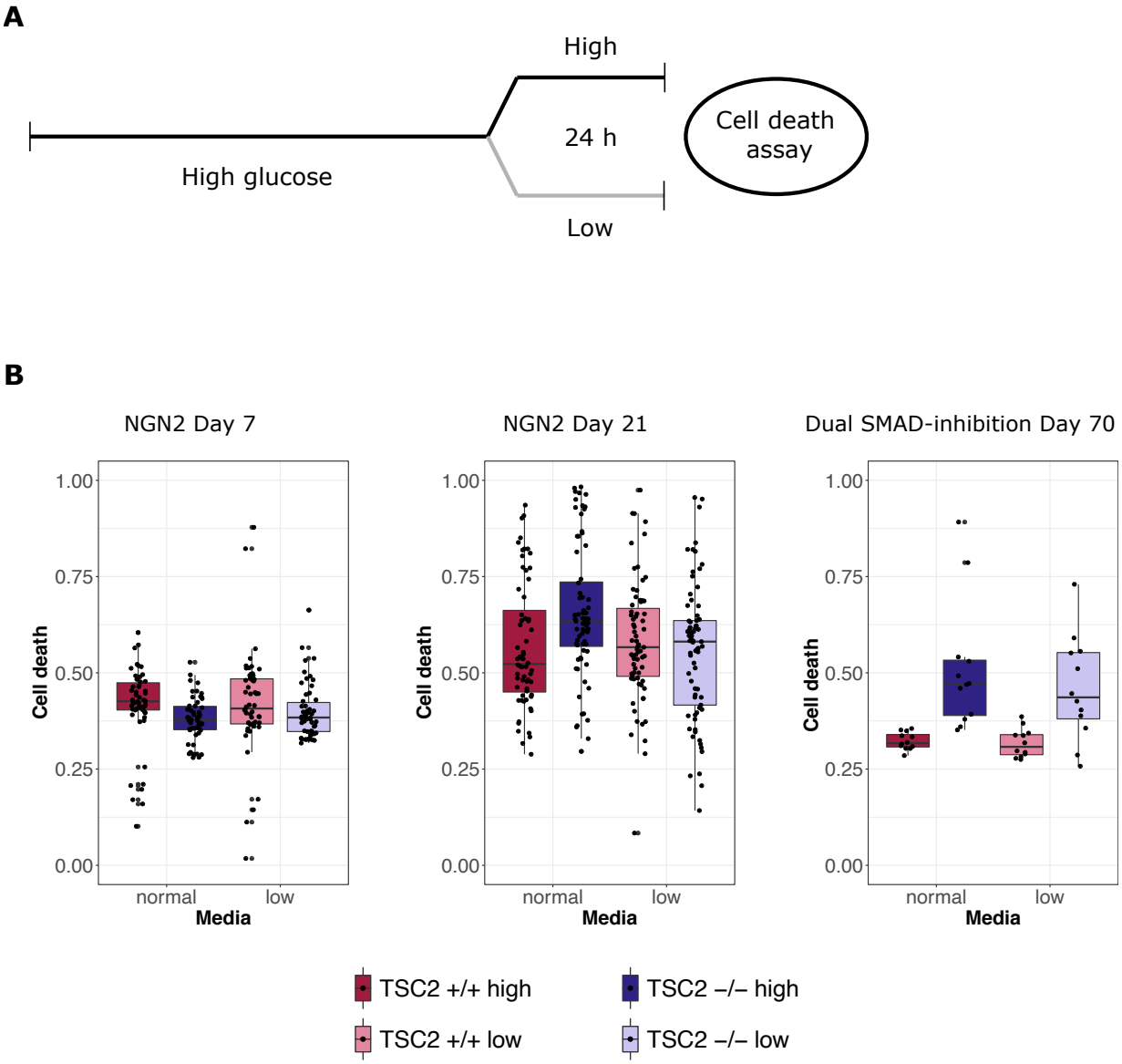


FIGURE 4.11: **Effect of glucose deprivation on neuronal death.** (A) TSC2 +/+ and TSC2 -/- neurons, derived in high glucose media, were cultured in either high or low glucose media for 24 h cells before cell death was assessed with a colourimetric assay. (B) Neither TSC2 deficiency nor glucose deprivation impacted neuronal death in NGN2 neurons on day 7 and day 21. In dual SMAD-inhibition neurons, TSC2 -/- cultures presented with a higher proportion of dying neurons irrespective of glucose supply. *Replicates: NGN2, 2 differentiations with 2 technical replicates comprising 23 wells each per line and media; Dual SMAD-inhibition, 1 differentiation with 1 technical replicate comprising 12 wells each per line and media.*

In the NGN2 protocol, TSC2 +/+ and TSC2 -/- cultures in high glucose media showed equal levels of cell death of around 40 % at day 7 and significantly elevated levels of cell death of approximately 55 % at day 21. In low glucose media, similar levels of cell death were seen in both genotypes.

A different picture was present in neurons derived via dual SMAD inhibition on day 70. TSC2 -/- cells showed significantly elevated levels of cell death compared to TSC2 +/+ cultures but the neuronal vulnerability was not affected by glucose deprivation (see figure 4.11 (B)).

In summary, neither TSC2 +/+ nor TSC2 -/- neurons showed an increased vulnerability to 24 h of glucose deprivation. TSC2 deficiency led to an increase in cell death in day 70 neurons differentiated via dual SMAD-inhibition but not in NGN2 neuronal cultures of day 7 and day 21.

4.3.4 Dependency of mTORC1 activity on cell type, glucose supply, and TSC2 genotype

The TSC1:TSC2-mTORC1 pathway is tightly linked to extracellular glucose supply but activation of mTORC1 varies notably at different stages in neuronal development. Here, I examined mTORC1 activation in TSC2 +/+ and TSC2 -/- hES, NSCs and neurons, representing different stages of neuronal development, and tested whether mTORC1 activation was reactive to glucose supply (see figure 4.12). Cells were kept in high glucose media until 24 h before sampling when half the cultures were changed into low glucose media. Activity of mTORC1 was determined by western blotting measuring the phosphorylated S6 to total S6 ratio (see figure 4.13 A).

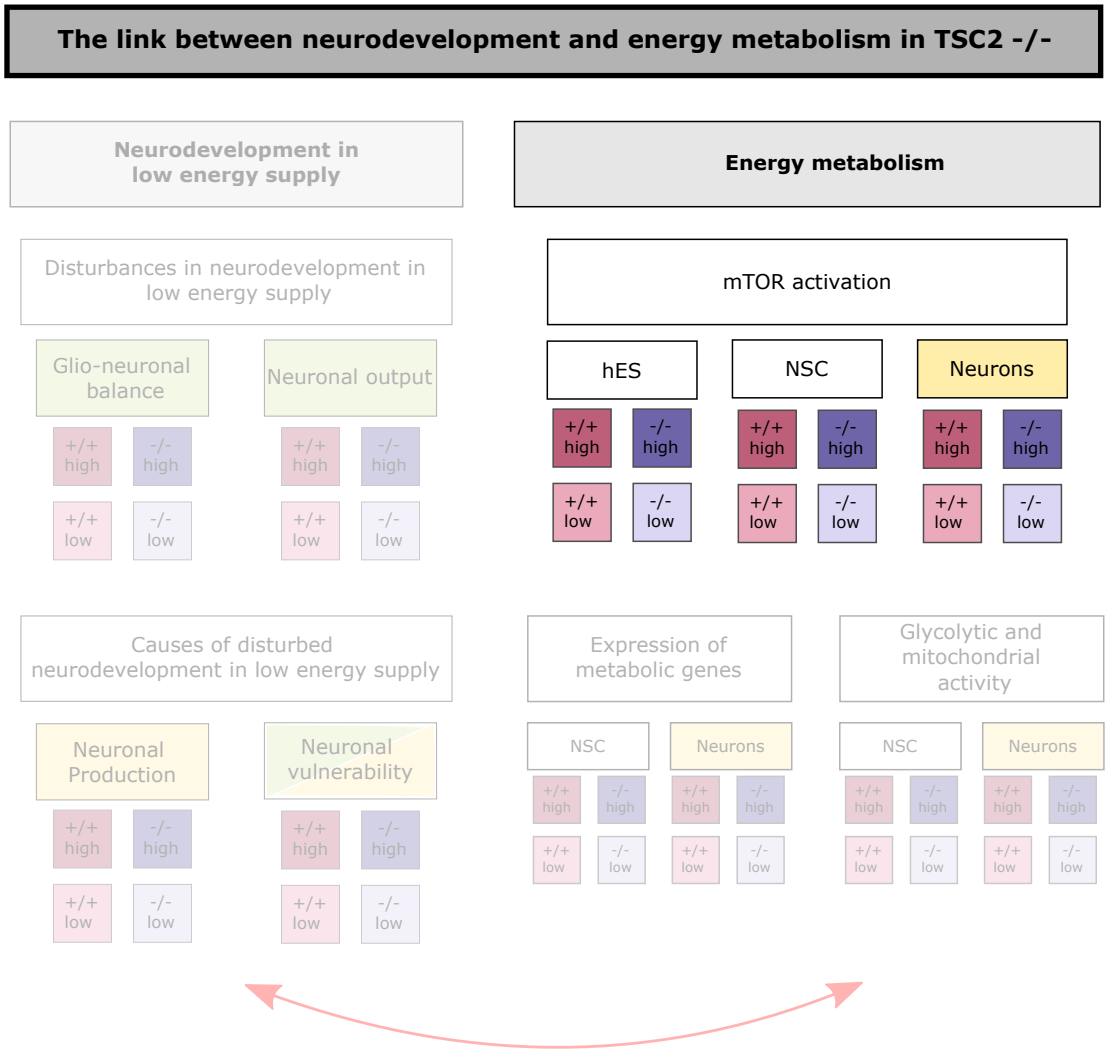


FIGURE 4.12: **Investigations into the effect of glucose deprivation combined with TSC deficiency on the link between disturbed neurodevelopment and energy metabolism.** Green, cells derived via dual SMAD inhibition; yellow, cells derived by NGN2 protocol.

In brief, TSC2 deficiency led to significantly higher mTORC1 activity levels in hES but not in NSCs or neurons. Low glucose supply reversed these effects in hES.

Human ES: In high glucose media, mTORC1 activation was significantly elevated in TSC2 -/- hES compared to their TSC2 +/+ counterparts ($p = 0.008$). Low glucose media led to a significant reduction of mTORC1 activity in TSC2 -/- cells so that hES from both genotypes showed equally low levels of mTORC1 activity in low glucose media (TSC2 -/- hES in high vs low glucose media, $p = 0.00005$).

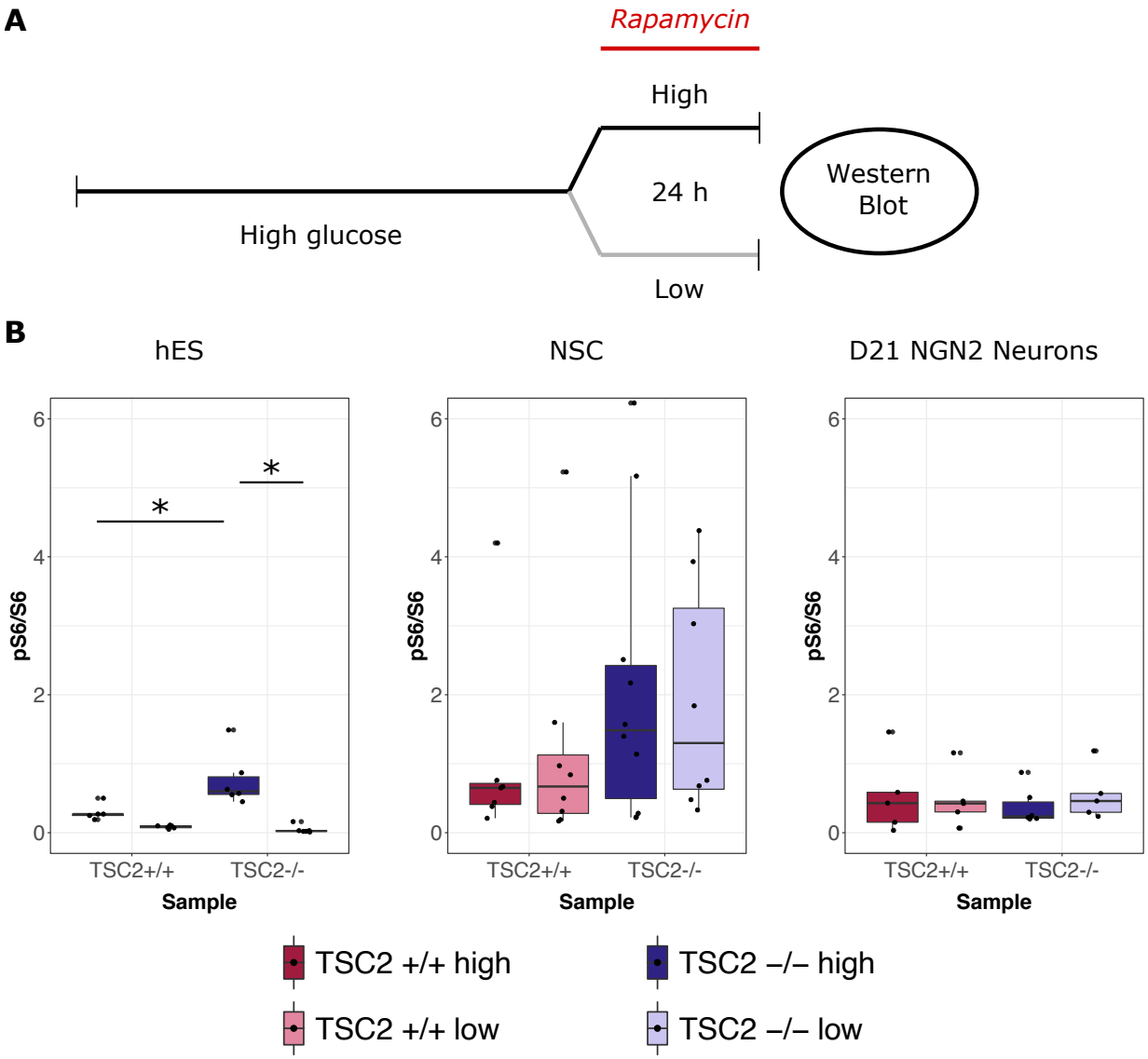


FIGURE 4.13: **mTORC1 activity in different cell types depending on glucose supply.** (A) Activation of mTORC1 was measured using the pS6/S6 ratio in TSC2 +/+ and TSC2 -/- hES, NSCs and NGN2 neurons on day 21 cultured for 24 h in either high or low glucose media. (B) TSC2 -/- hES in high glucose media showed significantly elevated mTORC1 activation which was abolished by glucose deprivation. TSC2 -/- NSCs in high and low glucose media showed increased mTORC1 levels compared to their respective TSC2 +/+ counterparts, although these differences did not reach significance. No impact of TSC2 deficiency or glucose deprivation on mTORC1 activity was seen in neurons. An original example western blot for this data is presented in figure 4.14. *Replicates: hES, 1 differentiation with 6 technical replicates per line and media; NSCs, 5 differentiations with 2-3 technical replicates per line and media; NGN2 neurons, 1 differentiation with 5 technical replicates per line and media.*

NSCs: NSCs demonstrated a different picture. As in hES, mTORC1 was notably more active in TSC2 -/- NSCs compared to TSC2 +/+ samples, although this difference did not reach significance. Glucose deprivation did not reduce mTORC1 activity in TSC2 +/+ or

in TSC2 -/- NSCs.

Day 21 NGN2 neurons: Lastly, mTORC1 activity was found to be similarly low in TSC2 +/+ and TSC2 -/- neurons, regardless of the glucose media (see figure 4.13 (B)).

Impact of low glucose supply on rapamycin efficiency. In TSC2 +/+ and TSC2 -/- NSCs, I also tested the impact of glucose deprivation on the efficiency of the established mTORC1 inhibitor rapamycin. In high glucose media, rapamycin completely abolished mTORC1 activity in TSC2 +/+ and TSC2 -/- NSCs. The difference to cells treated with a vehicle control reached significance in TSC2 -/- but not in TSC2 +/+ NSCs (TSC2 +/+ control vs rapamycin, $p = 0.582$; TSC2 -/- control vs rapamycin, $p = 0.003$). Glucose deprivation partially blocked the rapamycin-driven mTORC1 inhibition in both genotypes. Rapamycin was still able to decrease mTORC1 activity notably but the decrease did not reach significance in TSC2 -/- NSCs (see figure 4.14).

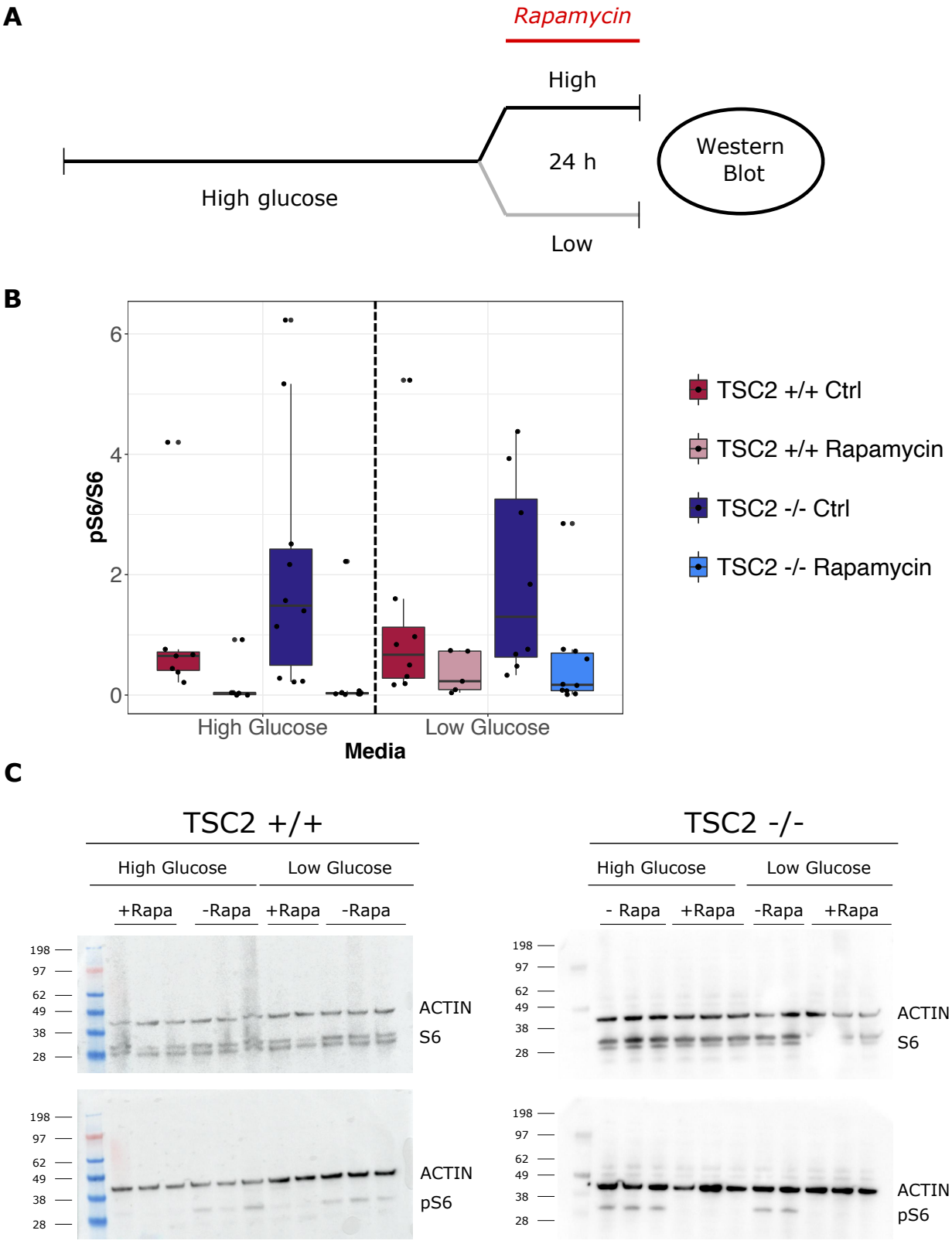


FIGURE 4.14: **Effect of rapamycin on mTORC1 activity in glucose-loaded and glucose-deprived NSCs.** (A) The effect of rapamycin on mTORC1 activation was measured using the pS6/S6 ratio in glucose-deprived and glucose-loaded TSC2 +/+ and TSC2 -/- NSC. (B) Rapamycin incubation for 24 h completely abolished mTORC1 activity in glucose-loaded TSC2 +/+ and TSC2 -/- NSCs. Rapamycin efficiency was lowered by glucose deprivation in TSC2 +/+ and TSC2 -/- NSCs equally. (C) Example western blots investigating pS6 and S6 levels in TSC2 +/+ and TSC2 -/- NSCs cultured on high and low glucose media, with and without the addition of rapamycin. *Replicates: 5 differentiations with 2-3 technical replicates per line, media, and treatment.*

4.3.5 Impact of glucose deprivation on energy metabolism in TSC2 +/+ and TSC2 -/- cultures

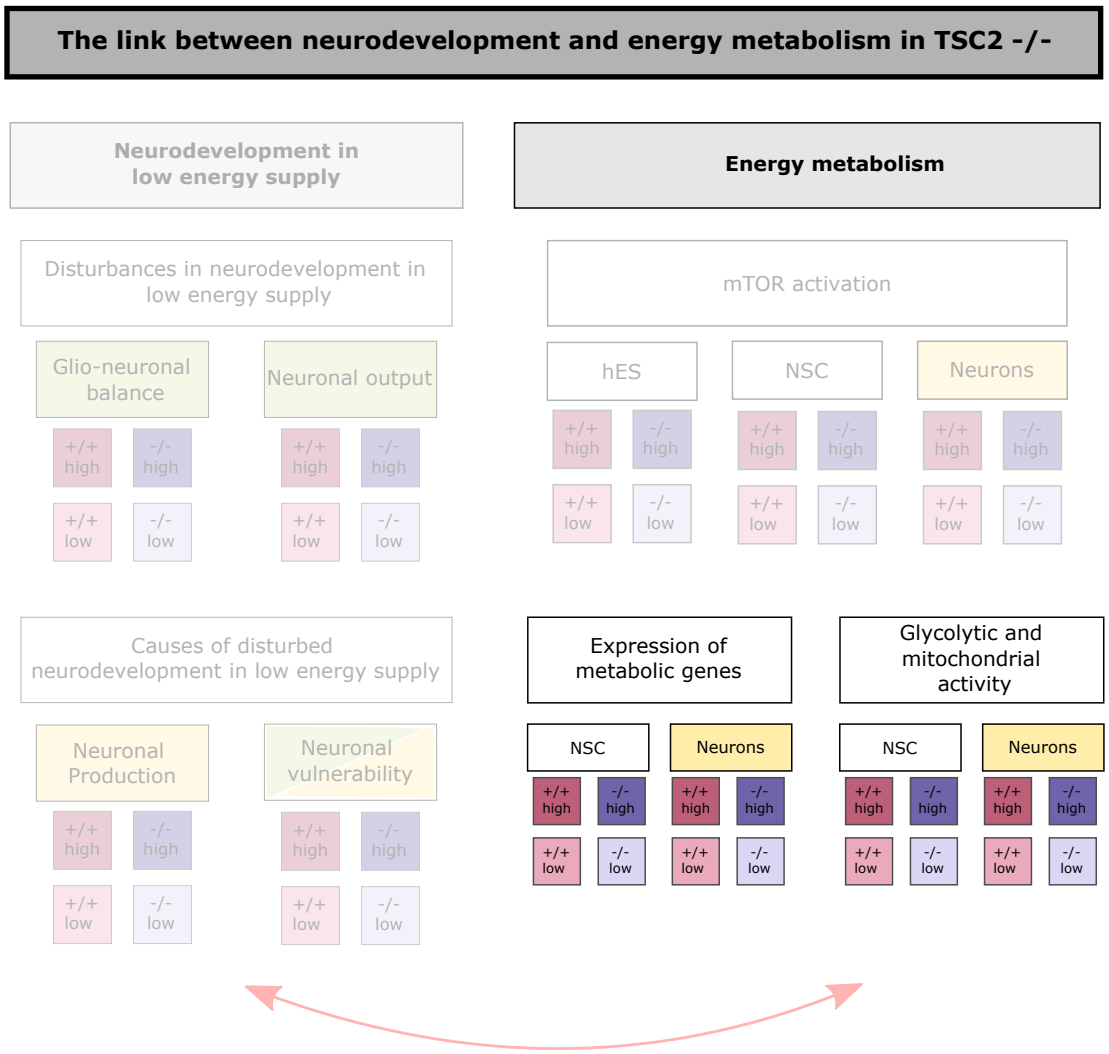


FIGURE 4.15: **Investigations into the effect of glucose deprivation combined with TSC deficiency on the link between disturbed neurodevelopment and energy metabolism.** Green, cells derived via dual SMAD inhibition; yellow, cells derived by NGN2 protocol.

In the last section, I assessed the effects of glucose deprivation and TSC2 deficiency on the activity of energy-producing pathways at different neurodevelopmental stages. I first measured expression levels for key genes involved in the three main energy-producing pathways: glycolysis, Krebs cycle (TCA) and oxidative phosphorylation (mitochondrial respiration). I then proceeded by quantifying the metabolic rates of glycolysis and mitochondrial respi-

ration using Seahorse facilities. I performed these experiments in TSC2 +/+ and TSC2 -/- NSCs and NGN2 neurons subjected to high or low glucose media for 24 h.

Metabolic gene expression

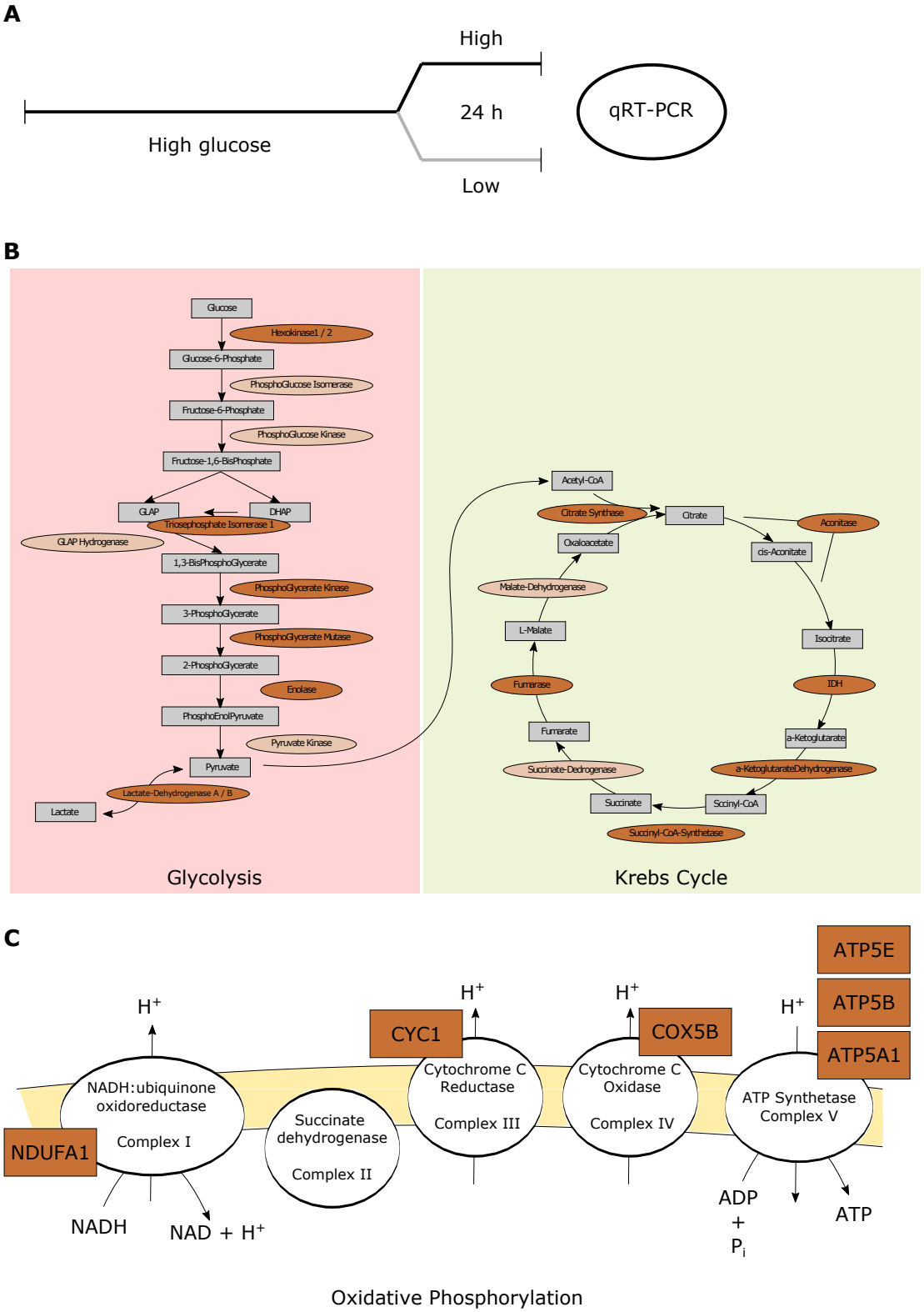


FIGURE 4.16: **Transcriptomic experiments on genes involved in metabolic pathways.** (A) Stable NSCs and NGN2 neurons were subjected to either high or low glucose media for 24 h before harvesting the cells for RNA extraction. (B) Gene expression levels of key metabolic enzymes from the three energy-producing pathways *glycolysis*, *Krebs cycle (TCA)* and *oxidative phosphorylation* were measured by qRT-PCR. Enzymes included in these measurements are coloured in dark orange.

I first measured expression levels of key genes facilitating energy production in NSCs and day 21 NGN2 neurons, focusing on three main energy-producing pathways: glycolysis, the Krebs cycle and oxidative phosphorylation. Gene expression was measured by qRT-PCR and the ddCT value was calculated by using the TSC2 +/+ NSCs in high glucose media as reference. Figure 4.16 shows an overview of all three pathways with their respective enzymatically-mediated steps. The enzymes measured in this experiment are coloured dark orange.

As illustrated in figure 4.17, the most prominent changes in gene expression were present in glycolysis whereas oxidative phosphorylation was least affected.

In NSCs, TSC2 deficiency or glucose deprivation alone led to similar changes, namely an upregulation of nearly all **glycolytic genes** except for HK1/2 and LDHB. LDHB and HK2 were, in contrast, downregulated by both conditions. The combination of TSC2 deficiency and glucose deprivation caused not only the upregulation of the glycolytic genes as seen in both conditions separately but also of HK2 and LDHB.

Neurons, irrespective of their TSC2 status or glucose supply, demonstrated a uniform upregulation of nearly all glycolytic genes except for LDHB and HK2, which were uniformly downregulated in all neuronal groups.

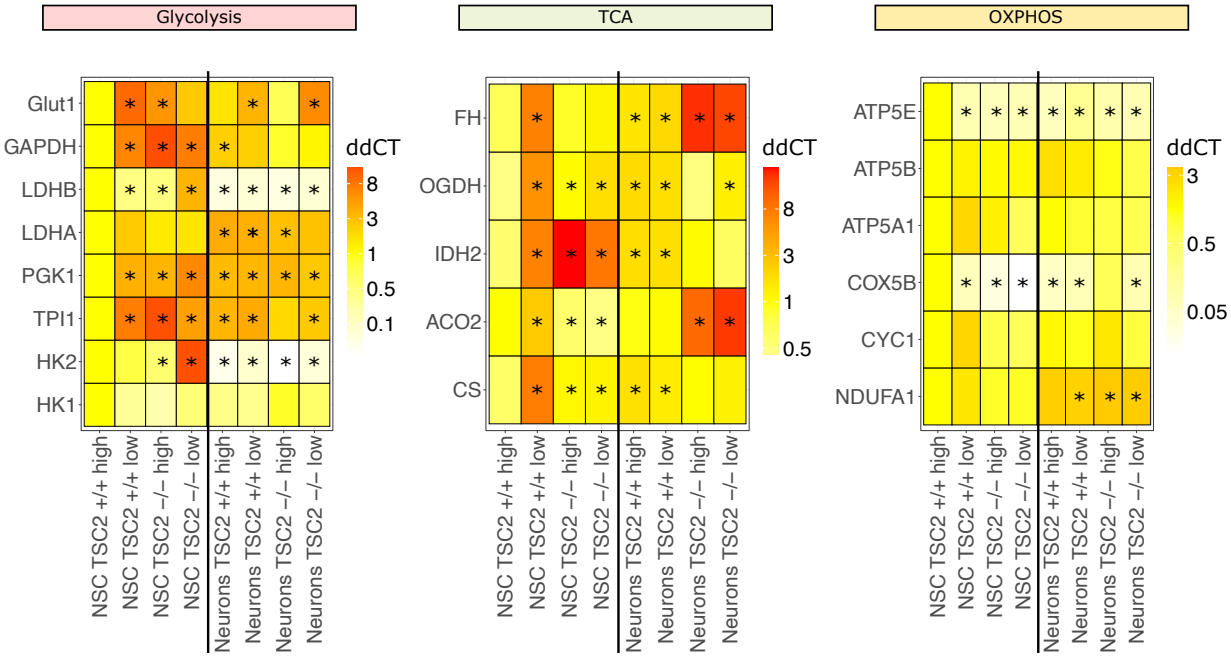


FIGURE 4.17: **Differently expressed metabolic genes in NSCs and NGN2 neurons.** Each heatmap displays the ddCT values of key genes involved in glycolysis, the Krebs cycle (TCA) or oxidative phosphorylation (OXPHOS) in TSC2 +/+ and TSC2 -/- NSCs (first four columns) and NGN2 neurons (second four columns). Significant differences in ddCT between the sample group and the reference group (TSC2 +/+ NSCs in high glucose) are marked with a star. In brief, glycolysis was most affected by glucose deprivation and TSc2 deficiency whereas OXPHOS genes were least impacted. In NSCs, TSC2 deficiency or glucose deprivation alone caused an upregulation of glycolytic genes associated with downregulated HK2 and LDHB. Combination of TSC2 deficiency and glucose deprivation increased HK2 and LDHB together with all other glycolytic genes. Glucose deprivation further upregulated TCA genes markedly in TSC2 +/+ but not in TSC2 -/- NSCs. *Replicates: 1 differentiation, 5 technical replicates per line and media.*

Wild type NSCs reacted to glucose deprivation with marked upregulation of all **TCA genes** whereas TSC2-deficient NSCs were much less responsive to glucose deprivation with regards to TCA gene expression levels. Although significant, TSC2 deficiency-induced changes in TCA gene expression occurred at a different magnitude compared to glucose deprived TSC2 +/+ NSCs as illustrated in figure 4.17.

TSC2 +/+ neurons presented with mild upregulation of nearly all TCA genes. TSC2 -/- neurons, in contrast, only enhanced the expression of fumarase and aconitase. Both genotypic neurons were unresponsive to glucose deprivation with regards to TCA gene expression.

Neither TSC2 deficiency nor glucose deprivation caused notable changes in **OXPHOS gene** expression in NSCs except for a uniform downregulation of ATP5E and cytochrome c oxidase subunit 5B (COX5B) across all NSC sample groups.

This ATP5E and COX5B downregulation is persistent in neurons. Further, neuronal differentiation led to a significant upregulation in the complex I subunit NDUFA1 irrespective of TSC2 status or glucose supply but left all other OXPHOS genes unchanged.

Functional assessment of energy metabolism

Gene expression on its own is not sufficient to investigate the functional state of a cell as the resulting enzymatic activity depends not only on the transcriptional rate, but also on translational activity, post-translational changes, and the interaction with other intra- and extracellular components, for example pH, activity of other signalling pathways or availability of required consumables. I measured the rate of glycolysis and mitochondrial respiration in NSCs and day 8 NGN2 neurons to explore how TSC2 deficiency and glucose deprivation affect the activity of different energy-generating pathways during neurodevelopment. Seahorse measurements included the extracellular acidification rate (ECAR) and proton efflux rate (PER) to measure glycolytic rate and the oxygen consumption rate (OCR) to estimate mitochondrial respiration. These measurements were calculated from media oxygen and proton measurements at baseline and under exposure to rotenone, a potent blocker of mitochondria, and 2-desoxyglucose (2DG), a glycolysis inhibitor. A detailed description of the Seahorse system can be found in appendix F.

I examined TSC2 +/+ and TSC2 -/- Roche NSCs as well as NGN2 neurons on day 8 with the Seahorse Analyser Glycolysis Kit. All cells had been derived and maintained in high

glucose media up to 24 h before the experiment when half of the cultures were transferred into the respective low glucose media version. Results were extracted from the Agilent Seahorse Analyser Software. Figure 4.19 displays mitochondrial activity and figure 4.18 shows glycolytic activity at different stages of the experiment. All measurements were normalised to the protein content of each well to account for differences in cell numbers.

Metabolic activity in NSCs. By far the highest glycolytic and mitochondrial activity was seen in glucose-loaded wild-type NSCs.

Glucose deprivation led to a reduction in metabolic activity with reduced glycolysis and OXPHOS in TSC2 +/+ as well as in TSC2 -/- NSCs. The magnitude of reduction varied with TSC2 status. In TSC2 +/+ NSCs, glucose deprivation led to a significant, approximately 5-fold reduction in glycolytic as well as mitochondrial activity whereas, in TSC2 -/- NSCs, glucose deprivation only caused a non-significant 2-fold decline in glycolytic and mitochondrial activity.

The mitochondrial blocker rotenone caused reduced mitochondrial activity but did not lead to a significant increase in compensatory glycolytic activity in NSCs. The application of 2DG blocked glycolytic activity in TSC2 +/+ and TSC2 -/- NSCs.

In glucose-loaded as well as glucose-deprived TSC2 +/+ NSCs, over 99 % of proton efflux was due to glycolytic activity. TSC2 deficiency significantly decreased the share of glycolysis on the total proton efflux (glycoPER), although glycoPER levels remained high at approximately 98 % in TSC2 -/- cultures.

Metabolic activity in neurons. Metabolic activity was overall five-to-ten times lower in neurons than in NSCs. Contrary to NSCs, neuronal metabolic activity was increased by glucose deprivation with significant enhancement of basal and compensatory glycolysis in TSC2 +/+ and TSC2 -/- neurons. Glycolytic activity was overall reduced in TSC2-

deficient cultured compared to their wild-type counterparts whereas the opposite was true for mitochondrial activity.

Rotenone exposure led to a slight elevation of glycolytic activity in neurons. The addition of 2DG abolished extracellular acidification.

In TSC2 +/+ neurons, glycolysis was responsible for approximately 97 % of the total proton efflux. This share was significantly reduced by TSC2 deficiency in high and low glucose media to glycoPER levels as low as 91 and 94 %, respectively.

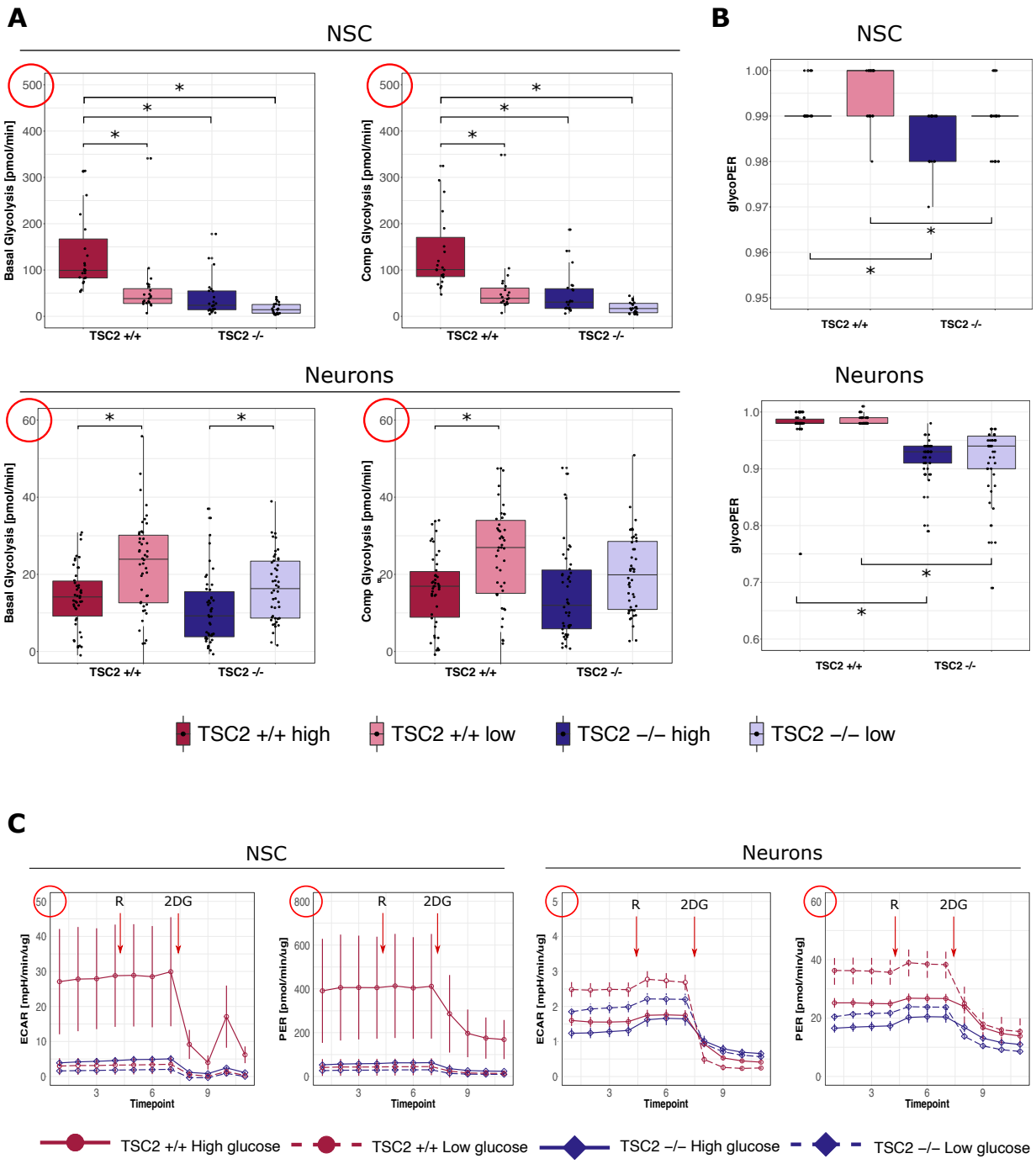


FIGURE 4.18: **Glycolytic activity in TSC2 +/+ and TSC2 -/- neuronal cells.** (A) Basal (left) and compensatory (right) glycolysis in TSC2 +/+ and TSC2 -/- NSCs (upper row) and neurons (lower row) challenged in either high or low glucose media. Glucose-loaded TSC2 +/+ NSCs demonstrated by far the highest glycolytic rates. TSC2 deficiency as well as glucose deprivation reduced glycolysis in NSCs. In neurons, glucose deprivation increased glycolytic activity whereas TSC2 deficiency did not impact glycolytic rates. (B) In NSCs (upper) and neurons (lower plot), glycolysis contributed nearly 100 % to the total proton efflux. In both cell types, TSC2 deficiency but not glucose deprivation reduced the glycolytic share on the total proton efflux. (C) Dynamics of the extracellular acidification rate (ECAR) and proton efflux rate (PER) which served as measures for glycolytic activity in NSCs (left) and neurons (right). R, rotenone; 2DG, 2-desoxyglucose. *Replicates: NSCs, 1 differentiation with 23 wells per line and media; Neurons, 2 differentiations with 23 wells per line and media each.*

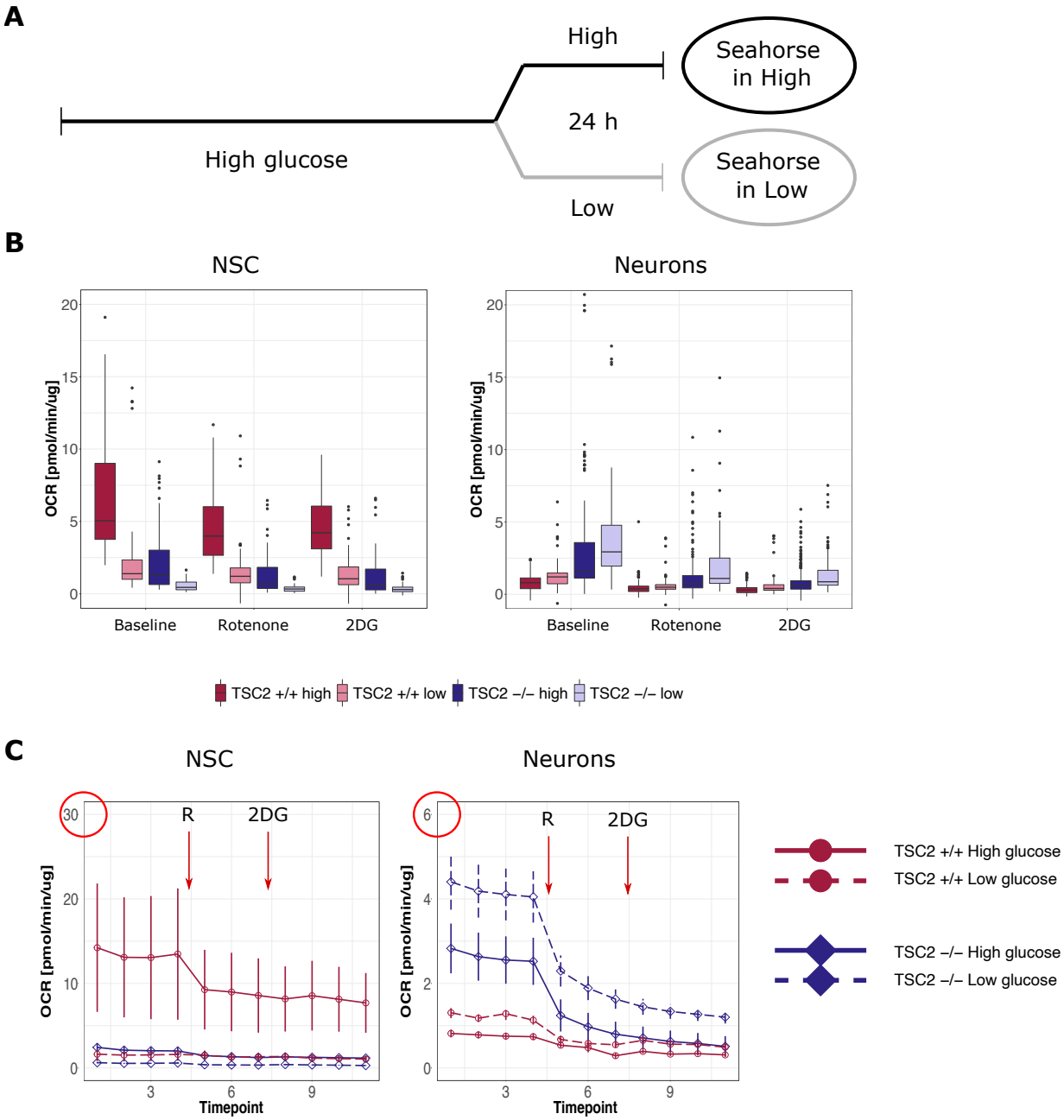


FIGURE 4.19: **Mitochondrial respiration in TSC2 +/+ and TSC2 -/- neuronal cells.** (A) TSC2 +/+ and TSC2 -/- NSCs and day 8 NGN2 neurons were challenged in either high or low glucose media for 24 h before being examined in a Seahorse analyser for their mitochondrial and glycolytic activity. (B) Total media oxygen consumption (OCR) served to estimate mitochondrial respiration at baseline and after rotenone (mitochondrial inhibitor) and 2-DG (glycolysis inhibitor) application. In NSCs, glucose deprivation, as well as TSC2 deficiency, reduced mitochondrial activity with the lowest OXPHOS activity measured in glucose-deprived TSC2 -/- cells. The opposite was true in neurons where TSC2 deficiency and glucose deprivation separately, and in combination increased mitochondrial respiration at all time points. (C) Dynamics of oxidative phosphorylation (estimated through oxygen consumption rate (OCR)) over time in NSCs and neurons demonstrated a marked decrease in respiration after rotenone application. R, rotenone; 2DG, 2-desoxyglucose. *Replicates: NSCs, 1 differentiation with 23 wells per line and media; Neurons, 2 differentiations with 23 wells per line and media each.*

4.4 Discussion

I explored the effect of combined glucose deprivation and TSC2 deficiency on energy metabolism and neurodevelopment. Neurodevelopment and energy metabolism are closely linked and the TSC1:TSC2-mTORC1 pathway plays a crucial role in integrating external energy supply with internal metabolism and neural differentiation. Thus, I hypothesised that energy deprivation impacts cortical development via disturbances in the cellular energy metabolism causing tuberigenesis in TSC2 deficiency.

Modelling glucose deprivation. Choosing appropriate media glucose concentrations is challenging in cell culture experiments. Stem cell culture is usually performed in glucose concentrations ∼5-times higher than physiological levels, mostly to allow longer intervals between media changes and to keep the cells generally well. In previous studies [54, 77, 91, 92, 109, 169, 263, 290], glucose concentrations of ∼ 25-30 mM were considered to be *high glucose levels*, concentrations between 5-10 mM were labelled as *normal* whereas concentrations below 5 mM were used to mimic *glucose deprivation*.

Glucose deprivation of *in vitro* cultures is used in stroke experiments, to examine glucose starvation as a potential treatment for cancer, or to determine survival rates in engineered tissue with physiologically low or variable supply levels [54, 77]. *In vitro* cancer therapy studies have used media with reduced glucose concentrations between 3-6 mM [91, 169, 290]. Lowering media glucose to 3 mM decreased cancer cell survival rates by one-third after only 4 h [169]. *In vitro* ischemia experiments are mainly performed at zero glucose concentrations for a maximum of 72 h or less [92, 109, 263]. Likely, culturing cells for longer periods up to several weeks of differentiation in very low to no glucose would lead to considerable cell death. Therefore, the experimental system with a minimum of 5 mM glucose seems best suited to model glucose deprivation in long-term cell cultures. This approach occa-

sionally led to glucose starvation, especially in very densely populated cultures such as the neuroepithelial sheet, as media was only replaced every 24 h at maximum. Media glucose concentrations were not tested at shorter time intervals so it is unclear for how long these cultures were starved of glucose. If I were to do similar experiments again, I would add additional time points for glucose testing to explore the dynamics of glucose consumption in more detail.

Glucose deprivation disturbs neural development in TSC2 deficiency. Glucose-loaded TSC2-deficient neuronal cultures demonstrated increased glial tendency and neuronal immaturity on the transcriptomic level, but these transcriptomic changes did not manifest translationally. Glucose deprivation triggered the translational manifestation causing a disturbed ratio between neurons and glia and reduced neuronal maturity in TSC2 knockout neuronal cultures.

Results presented in this chapter suggest that this manifestation is caused by the combination of two separate mechanisms:

1. Increased vulnerability of TSC2-deficient neurons independent of glucose supply.

2. Reduced neurogenic potential of the NSC pool in glucose deprivation due to altered energy metabolism.

TSC2-deficient neurons displayed increased vulnerability irrespective of glucose supply. This vulnerability became only apparent in neurons derived via dual SMAD inhibition, not in NGN2 neurons. In NGN2 neurons, neurons were similarly labile with high levels of cell death seen in both cultures. However, TSC2-deficient neurons derived via dual SMAD inhibition showed higher levels of cell death on day 70 than their wild-type counterparts, an effect that was observed irrespective of glucose supply. I would speculate that this difference between protocols was caused by a combination of factors. For

example, differences in neuronal maturity could affect neuronal viability, given that dual SMAD inhibition-derived neurons were tested at day 70 compared to day 21 NGN2 neurons. Also, the lower baseline levels in vulnerability seen after dual SMAD inhibition could allow the effect of TSC2 deficiency to manifest whereas high baseline vulnerability levels in NGN2 neurons might mask the TSC2 deficiency-induced neuronal instability.

Glucose deprivation during the early stages of the NGN2 protocol significantly lowered the neuronal output in TSC2 -/- cultures at later stages suggesting that neuronal production was severely affected by glucose deprivation in TSC2 -/- cultures. Also, early glucose deprivation led to the prolonged expression of neuronal progenitor markers Neurogenin 2 and NeuroD1 in TSC2-deficient cultures indicating that the reduced neuronal output might be caused by a delayed or reduced neurogenic transformation of progenitors into post-mitotic neurons. Glucose deprivation might reduce the number, or functioning, of RGCs in both cultures, however, this did not lead to disturbed neuronal numbers at the end of differentiation in TSC2 +/+ cultures. This means that TSC2-sufficient cultures benefit from a compensation mechanism that can rescue neuronal production from the diminished NSC pool. Oxygen/glucose deprivation triggers neurogenesis from injured NSCs and, in turn, causes a reduction in the remaining stem cell pool [281] which might explain the reduction of RGCs but normal neuronal levels in TSC2 +/+ cultures. TSC2 -/- cultures might lack the capability to upregulate neurogenesis in glucose-deprived conditions sufficiently as neurogenesis after ischemia is mediated by mTORC1-regulated pathways [88].

Activation of mTORC1 is crucial to induce neurogenic differentiation from neural progenitors [151]. The elevated mTORC1 levels in glucose-loaded TSC2 -/- pluripotent stem cells likely cause the expansion of an NSC pool with functioning neurogenic potential

as observed in chapter 3. In glucose-deprived conditions, TSC2 -/- hES showed reduced mTORC1 levels impacting their ability to expand NSC numbers sufficiently to compensate for their increased neuronal vulnerability. Subsequent experiments are needed to explore the exact mechanism of the glucose deprivation-induced reduction in neuronal production in TSC2-deficient cultures.

Glucose deprivation and TSC2 deficiency drives a metabolic compensation response in NSCs. The metabolic response to TSC2 deficiency and glucose deprivation differed with the neurodevelopmental stage and was most profound on the NSC level. As illustrated in figure 4.20, the activity of the energy-producing pathways glycolysis and mitochondrial respiration decreased in TSC2 deficiency and under low glucose supply. Glycolytic activity and OXPHOS rate were profoundly high in glucose-loaded TSC2 +/+ NSCs with very little reserve capacity for further upregulation of these pathways. Lowering glucose in the media deprived NSCs to continue performing glycolysis and OXPHOS at their previously high rates as it withdrew the starting metabolite from these pathways. Interestingly, TSC2 deficiency on its own also led to a reduction in metabolic activity which was further amplified by glucose withdrawal. This was surprising as TSC2 -/- NSCs demonstrated elevated mTORC1 levels indicating the propensity for increased metabolism.

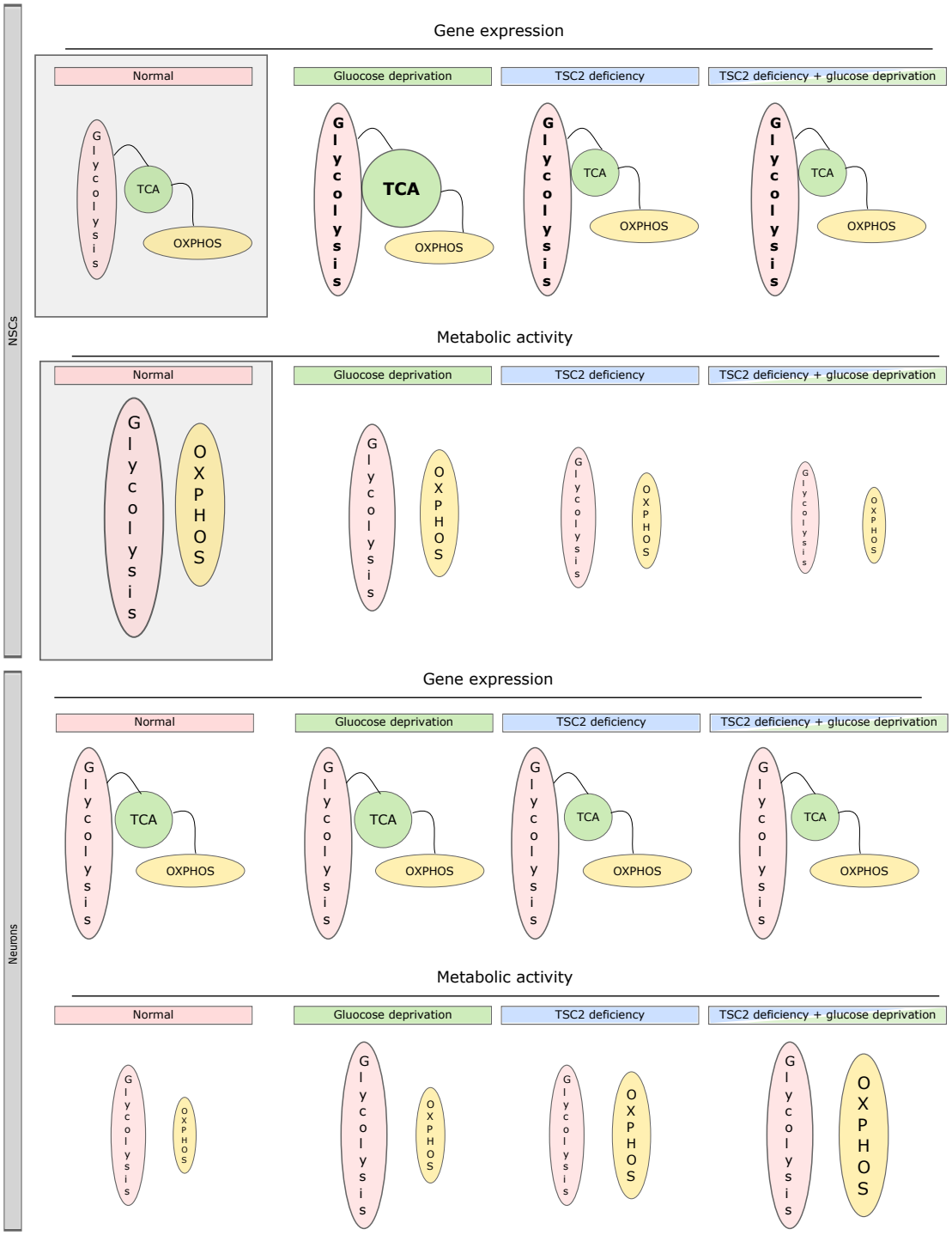


FIGURE 4.20: **Schematic overview of the metabolic response to glucose deprivation and TSC2 deficiency in NSCs and neurons.** Graphic illustration of gene expression levels and metabolic activity in NSCs (upper rows) and neurons (lower rows) when subjected to glucose deprivation (green), TSC2 deficiency (blue) or a combination thereof. Glucose-loaded TSC2 wild-type NSCs ('normal', pink) were used as reference samples.

Gene expression for glycolytic genes was significantly upregulated by TSC2 deficiency and glucose deprivation as well as their combination. This can be interpreted as the

cellular attempt to compensate for decreased glycolytic activity imposed by glucose deprivation and TSC2 knockout. The isoforms HK2 and LDHB were exempt from the general upregulation of glycolytic genes in wild-type and glucose-loaded TSC2-deficient NSCs. This is in line with the fact that in healthy individuals, HK2 and LDHB are highly expressed in muscle and adipose tissues but show little expression in neuronal tissue [267, 268]. However, combined TSC2 knockout with glucose deprivation triggered additional upregulation of HK2 and LDHB, potentially as a response to the combined stress imposed on these cells. Hexokinase and Lactate Dehydrogenase are important players in regulating metabolic plasticity and survival in various cancer cells as they serve as important moderators of glycolysis entry and exit. Hexokinase 2 can enhance tumour cell resistance to apoptotic processes and facilitate high glycolytic activity and lactate production [287]. HK2 and LDHB upregulation leads to increased cell survival and tumour growth, even under nutrient-deprived conditions. The expression of both enzymes is regulated by mTORC1-dependent pathways [219, 296]. Here I showed that the combination of TSC2 deficiency and glucose deprivation drives upregulated HK2 and LDHB levels in NSCs which might tip NSCs into a more 'cancer-like' metabolic state promoting NSC self-renewal and subsequently decreasing their neurogenic potential.
Wild-type NSCs further upregulated Krebs cycle genes which, however, did not manifest in higher mitochondrial respiration rates, likely due to missing glucose molecules to fuel mitochondrial activity. This genetic switch from glycolysis towards TCA/OXPHOS in response to glucose deprivation was not seen in TSC2 -/- NSCs.

Neurons demonstrated overall lower metabolic rates for both, glycolysis and mitochondrial respiration. Functionally, glucose deprivation-induced upregulation of both pathways in TSC2 +/+ and TSC2 -/- neurons suggests that they harbour some com-

pensatory capacity to respond to nutrient deprivation with increased metabolism. This compensation capacity appeared even greater in TSC2-deficient neurons as they upregulated mitochondrial respiration further than their wild-type counterparts. Neurons only mildly increased glycolytic and TCA genes reflecting that glucose deprivation did not drive them towards a state of *over-compensation* as seen in NSCs.

The link between metabolic response and neurodevelopmental disturbances. As a final step, I aimed to explore the link between the metabolic response to combined TSC2 deficiency plus glucose deprivation and neurodevelopmental disturbances during cortical development. I hypothesize that the compensatory upregulation of all glycolytic genes including the crucial players HK2 and LDHB in glucose-deprived TSC2 -/- NSCs prevents neurogenic progression. High glycolytic activity is associated with stemness rather than neuronal phenotypes. HK2 and LDHB are enzymatic drivers of glycolysis [296] preventing the cell from switching to other energy-producing pathways such as OXPHOS. The reduced neurogenic potential of glucose-deprived TSC2 -/- NSCs might impact their ability to produce sufficient numbers of neurons in glucose-deprived conditions and could further favour their transformation to glia at later stages during development. However, due to COVID-19-related restrictions, I was not able to pursue this hypothesis further.
An overview of the hypothesised mechanism underlying the reduced neuronal output in glucose-deprived TSC2-deficient cultures is shown in figure 4.21.

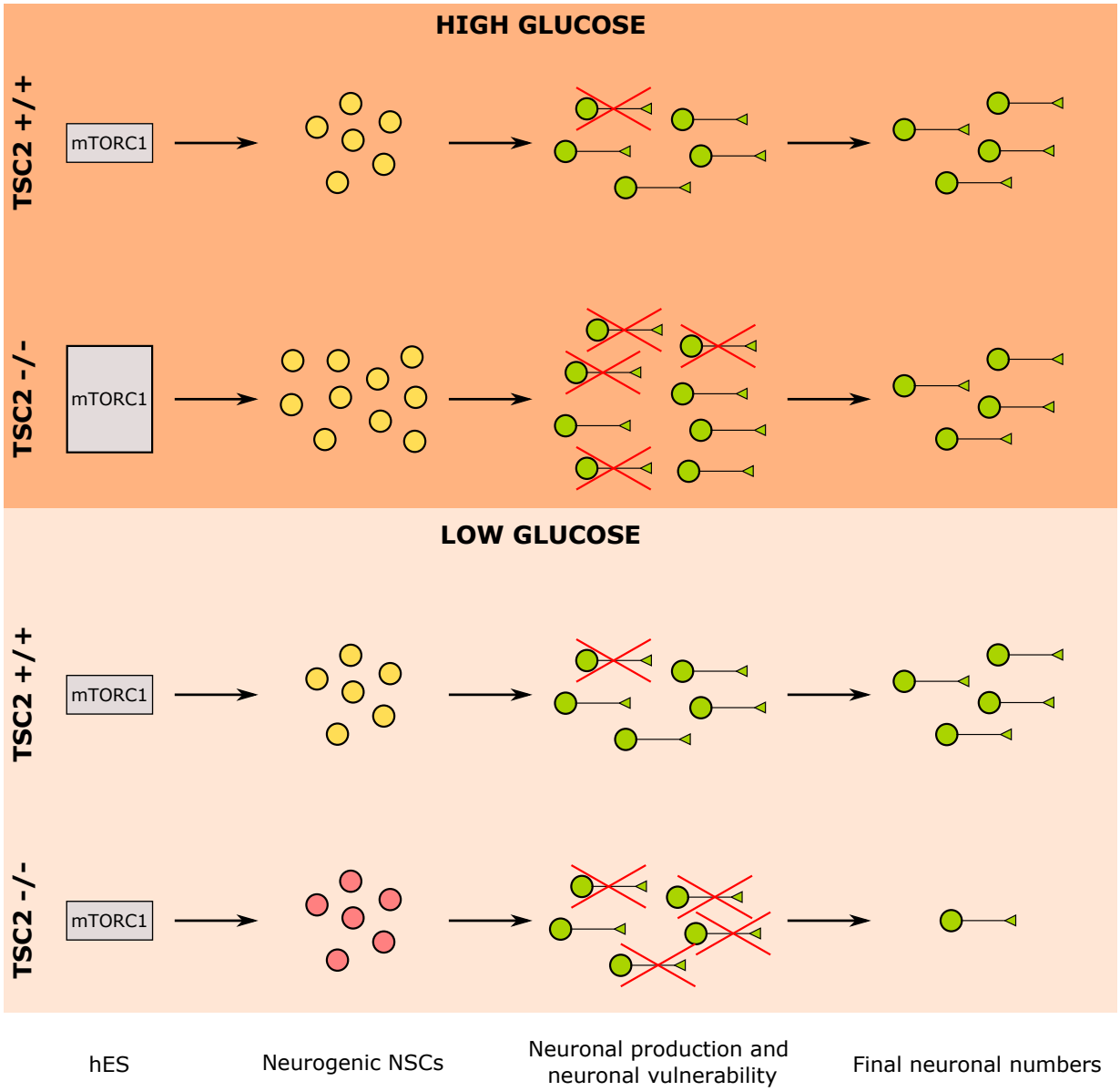


FIGURE 4.21: **Simplified hypothesised mechanism for reduced neuronal output in glucose-deprived TSC2 -/- cultures.** In high glucose media, TSC2 -/- cultures show increased mTORC1 activity at the hES level which might induce the expansion of the neurogenic NSC pool. This expanded NSC pool could then compensate for the increased cellular vulnerability inherent in TSC2-deficient neurons leading to a similar neuronal output compared to TSC2 +/+ cultures. In contrast, glucose deprivation reduced mTORC1 activity in TSC2 -/- hES. In turn, this could reduce the number and functioning of neurogenic NSCs, directly reducing their ability to compensate for the increased neuronal vulnerability.

Limitations and future experiments. The combination of TSC2 deficiency and glucose deprivation caused a shift in the glio-neuronal balance combined with a reduction in mature neurons and axonal connections that partially resembled the microscopic picture observed in cortical tubers. However, a **comprehensive microscopic characterisation**

of the derived neuronal cultures was not performed so I was unable to confirm the presence or absence of other tuber-like hallmarks, such as aberrant neuronal branching or giant balloon cells. In future experiments, I would characterise these cultures with regards to such hallmarks to determine whether glucose deprivation induces a full tuber-like picture in *in vitro* TSC2-deficient cultures.

Due to time and resource constraints due to the COVID-19 pandemic and related restrictions, I only performed a **limited number of experimental repeats**. In the future, the number of samples from independent differentiations and experimental rounds should be increased to enhance statistical confidence.

Additional experiments would also be needed to examine the **link between energy metabolism and neuronal differentiation** in TSC in more detail.
Glucose deprivation potentially exerts different effects on neural differentiation output depending on timings during neurodevelopment. One could apply transient glucose deprivation during dual SMAD inhibition, for example during the neuroepithelial phase (day 1-10), the radial glial phase (approx. day 12-20), the expansion and transition phase to intermediate progenitors (approx. day 20 - 30) and neuronal maturation phase (after day 30).
Also, I would examine whether and how survival and proliferation of TSC2 -/- neurogenic NSCs are impaired by glucose deprivation. The number of Ki67-positive and thus, proliferating cells at the NSC stage could be measured during glucose-deprived dual SMAD inhibition. Time-lapse imaging of dividing TSC2 +/+ and TSC2 -/- neurogenic NSC cultures could reveal NSC division patterns in different glucose conditions in more detail [187]. The expression levels of HK2 and LDHB could be manipulated in TSC2 +/+ and

TSC2 -/- NSCs to examine their impact on NSC self-renewal and neurogenic potential.
I would further investigate the role that HK2 and LDHB play in glucose-deprived TSC2 -/- cultures regarding their glycolytic activity and neurogenic potential. Modifications of HK2 and LDHB levels in both, TSC2 +/+ and TSC2 -/- cells at different stages during neurodevelopment could yield insights into their effect on energy metabolism, NSC renewal, neuronal production, and astrogenesis. I was unable to examine the effect of additional metabolic changes on the transcriptional and functional levels in TSC2-deficient NSCs on neural differentiation. Such experiments are needed to determine whether changes in gene expression levels and energy production ability are causative or consequential to disturbances in neural development.

The transcriptomic and functional experiments presented in this study were entirely performed in stable NSCs and similar investigations on neurogenic NSCs are warranted. Also, I used NGN2 neurons on day 21 for investigations on mTOR activity and metabolic gene expression levels, however, day 8 neurons to examine metabolic activity rates. This discrepancy was caused by time restrictions I faced due to the COVID-19 pandemic and related restrictions on laboratory opening times.
As described, additional experiments are needed to advance our understanding of the molecular mechanisms of tuberigenesis in TSC which might help find potential targets for curative treatment.

In summary, I found evidence that glucose deprivation during neural differentiation significantly alters the glio-neuronal composition and decreases neuronal maturity in TSC2-deficient cultures. These changes seem mostly due to alterations in the balance between self-renewal and neurogenesis on the NSC stage. Notably, combined TSC2 deficiency and glucose deprivation reduced glycolytic and mitochondrial activity with a, likely compen-

satory, upregulation of mostly glycolytic genes, including the gatekeeper genes HK2 and LDHB. Increased glycolytic gene expression might tip these cells into a more stem-like and less neurogenic state. Further experiments are needed to determine whether the observed transcriptional changes might impact the neuronal differentiation potential in TSC2-deficient NSCs and to investigate whether these changes are mTORC1-dependently or mTORC1-independently mediated.

Glucose deprivation as a potential trigger of tuberigenesis could open up new therapeutic targets in patients with TSC. During neurodevelopment, expansion of the brain is met with matching expansion in vascularisation to ensure sufficient nutrient and oxygen supply to the developing tissue [279]. Cortical tubers exhibit impaired vascularisation with evidence of hyper- and hypo-vascularised tubers found in different studies and TSC1:TSC2 deficiency can affect the regulation of vascularisation. I would speculate that a transient mismatch in vascularisation and brain expansion could lead to a transient deprivation of glucose and other nutrients in the affected developing area, potentially triggering tuberigenesis *in vivo* as seen in my study *in vitro*. However, further research into this hypothesis is warranted to determine the clinical relevance of the detected mechanism for aberrant neurodevelopment in TSC.

5 | The impact of astrocytes on effective connectivity in TSC

5.1 Introduction

The previous chapter explored whether and how changes in nutrient supply in TSC2 deficiency might contribute to cortical malformation in TSC. Next, I was interested in examining changes in the cellular, specifically glial, environment as a factor to induce tuber-like neuronal networks in TSC.

The origin of epileptic activity in patients with TSC is unclear, but evidence points towards cortical tubers and the perituberal tissue as the potential epileptogenic source [95, 158, 247]. Within cortical tubers, glial architecture and function are significantly disturbed [71, 184, 226, 265]. Astrocytes play a crucial role in guiding the development and maintaining the architecture of neuronal circuits [209]. Thus, I was interested in the impact of astrocytes on neuronal connectivity and the development of epileptiform neuronal activity against the background of TSC.

In vitro, neuronal activity and connectivity can be investigated via patch clamp analysis or through recordings from MEAs. Both methods allow, to varying extents,

insights into neuronal activity on a single cell or population level. Patch clamp analysis usually examines single neurons but can be used to investigate neuronal connections when applied to two neurons simultaneously (dual neuron clamping) [200]. MEA analysis, on the other hand, records neuronal population activity data allowing investigations into connectivity and population behaviour [209]. MEAs record local field potential (LFP) data as well as neuronal spiking and bursting activity. Most MEA-based studies analyse the latter as they are produced by neuronal action potential firing and thus, are considered measures of neuronal and network function. LFPs, in contrast, depend on the dendritic and somatic activity of neurons adjacent to electrodes and as such, provide a unique data set to examine the molecular basics of synaptic connections within an *in vitro* neuronal network [21].

Connectivity in neural networks can be examined at three different levels [249]:

> **Anatomical connectivity**: The structural connectivity that describes the direct anatomical layout of axons and synapses and provides the basis for any connectivity between different neuronal structures.
>
> **Functional connectivity**: Describes the statistical dependencies seen in time series recordings between multiple neuronal units.
>
> **Effective connectivity**: Expresses the direct impact neural units have on each other and thus, describes causal effects between different neuronal elements.

In vitro, anatomical connectivity can be assessed through immunohistochemistry, for example via pre- and post-synaptic synaptic markers such as SNAP-25, synaptophysin or SAP-102. Functional connectivity might be examined in MEA recordings, for example by looking at the synchronous bursting activity in different areas of a neuronal culture. How-

ever, to gain a deeper understanding of the mechanistic basis of neuronal connectivity, it is paramount to assess the effective connectivity of a neuronal population. *In vivo*, this can be done by applying a computational modelling approach – *DCM* – to neuronal activity data such as fMRI or EEG recordings [86]. Similar to EEG recordings, MEA-recorded data are the population-wide summation of single neuronal activity comprising LFP and axonal activity. In this study, I applied DCM to MEA recordings of stem cell-derived neuronal cultures for the first time to gain a better understanding of synaptic connectivity *in vitro*.

DCM is a statistical reasoning method used here to infer the states of molecular markers underlying network connectivity from extracellular LFP recordings. The method is based on the principles of Bayes' Theorem and probabilistic inference which are briefly summarised in appendix G.

5.1.1 Assessing synaptic connectivity using DCM

DCM is a Bayesian-based modelling approach to unravel experimentally induced changes in the effective connectivity of a neural network. It is based on a Bayesian model comparison that evaluates different dynamic system state models in their ability to predict which neurophysiological architecture might underlay real-world electrophysiological data [163]. DCM was introduced by Friston and colleagues in 2003 [86] and is usually applied to EEG/MEG or fMRI recordings *in vivo*. Most DCM studies analyse the response in brain activity to an external intervention and typically examine changes in the synaptic coupling that are generated by either changes in membrane excitability or connection strength [250].

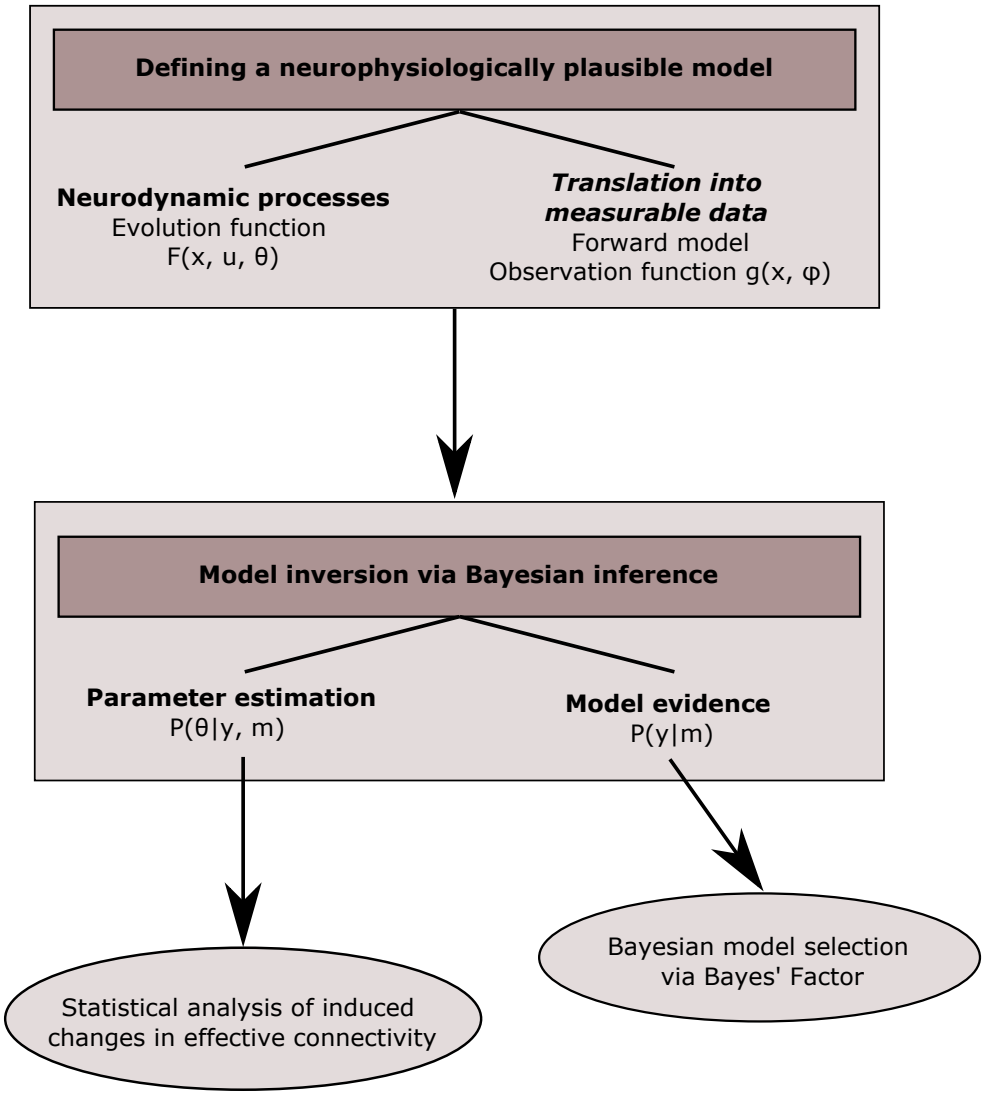


FIGURE 5.1: **Key steps in DCM analysis.** First, a neurophysiological model, recapitulating the underlying neurodynamic processes as well as the translation of neuronal activity into a measurable signal, is implemented together with reasonable estimates of the model parameter values. Second, parameter values are tuned so that the generated data fits the original data adequately which results in a posterior estimation of model parameters as well as an estimate of the model evidence. Lastly, statistical analysis detects changes in model parameters and allows model comparison. In this study, the neurophysiological model is based on a cortical canonical microcircuit model with parameter estimates drawn from previous electrophysiological studies on human cortical tissue. The model inversion via DCM yielded posterior parameter estimates used for further statistical analysis via a logistic regression.

Every DCM analysis comprises two key components as displayed in figure 5.1: (1) a plausible and interpretable biophysical model of the neuronal network of concern and (2) probabilistic statistical analysis for parameter estimation as well as model comparison [52]. I will describe the core principles of DCM in the next section. A more comprehensive

overview of its mathematical foundations can be found in appendix H.

First step: Defining the model. DCM analysis allows inference on experimentally-induced changes in hidden states of a neuronal model that are otherwise not accessible to experimental measurements. DCMs are dynamic by using differential equations to describe the changes in a neuronal network and are causal by looking into how one neuronal population affects the activity of another neuronal population and how these interactions can be modified by external stimuli [250]. We first define a system of variables (referring to different system elements such as neurons, neuronal units, etc) where specific properties of these system elements (membrane potential, ion channel status, etc) interact with one another in a distinct way. These interactions are described by a set of ordinary differential equations which builds the first part of our model, the so-called *evolution function*.

The second part of the model comprises the *forward/observation/transfer function* describing how the neuronal activity is translated into the measured signal. Consider fMRI which measures haemodynamic signals generated by the underlying neuronal activity. The forward model for DCM analysis of fMRI data describes the transformation of neuronal activity into haemodynamic signals. The forward model is, thus, dependent on the data acquisition method. Together, the evolution function and the forward function build the core modelling component of every DCM analysis [163, 251].

Different types of underlying neuronal biophysical models have been applied to DCM analysis so far. Conceptually, they all treat the brain as a multi-input-multi-output system with causal interactions within the system that mediate between the input and output state [183]. Models of brain activity provide a simplified, coarse-grained expression

of neuronal population behaviour via a set of mean-field neuronal activity equations. A simplifying mean-field approach is required as modelling the interaction of hundreds of thousands of single neurons to generate population behaviour would be computationally inaccessible. Mean-field models replace this multi-player problem with a single-body system that reduces the behaviour of all interacting subunits to the relevant mean activity [37]. In the 1940s, McCulloch and Pitts assembled a deterministic network of binary neurons that transform a threshold-exceeding input signal into firing activity and proved the existence of computational power in such network [173]. However, these networks lacked robustness and often plausibility. Efforts were then focused on developing statistical tools governing firing probabilities in neuronal populations rather than implementing logical deterministic connectivity networks [37, 241]. These works eventually led to the development of various activity equations [115, 282] that underpin different probabilistic neuronal mass and neuronal field models to generate oscillatory brain activity. Neural mass models and neural field models have been used extensively as generative models for DCM [183].

Neural mass models treat population neuronal activity as a point source and population dynamics are modelled with first-order differential equations that express the interaction between population means only. Neural field models consider spatial dimensions of the modelled neuronal population and thus, allow inference on not only temporal but also spatial parameters. Here, the complete activity density of one population is impacted by the mean activity of another population which is mathematically implemented using higher-order differential equations [183].

Biologically, neuronal models in DCM can also be distinguished into *convolution-based* vs *conductance-based* models. Convolution-based models arise from the idea of a cortical mesocolumn as the comprehensive neuronal unit [84] whereas conductance-based models

[105] centre around a single neuronal cell and its electrophysiological properties [183]. In convolution-based models, different cortical populations are lumped together as point sources that are interconnected via extrinsic connections but lack intra-population connections. Here, the population membrane potential is transformed into population spiking activity via a sigmoid transformation function. On the other hand, conductance-based models start with single neurons so that cells with different characteristics can be coupled together within and between regions to create a population behaviour.

In theory, all these different models of neuronal activity can be combined with a transfer function appropriate for the experimental data. The model should be chosen with regard to the research question. It should provide a relevant level of complexity, eg include the structures and parameters of interest, but needs to be simple enough to allow sufficient degrees of freedom for efficient parameter estimation [183].

Second step: Inferring on parameter densities. After defining a reasonable model, the model is fitted to the real-world data aiming to reduce the discrepancy between the predictive model outcome and the actual data to a minimum (*model inversion*). By doing so, DCM analysis offers an explanation for the mechanisms underlying real-world data by trying to generate something that looks like the real-world data on the basis of a plausible neurophysiological model [128]. To ensure the plausibility of this method, reasonable prior values as well as an expected range of parameter variance need to be defined for each model parameter before model inversion [250].

The classic Bayesian theorem allows the calculation of two statistical conclusions: (1) an estimate of the posterior mean value of the model parameters as well as their confidence interval via the posterior probability density function and (2) the so-called model evidence

which is a measure for how plausible the model is able to explain the data [208]. This process is illustrated in figure 5.2.

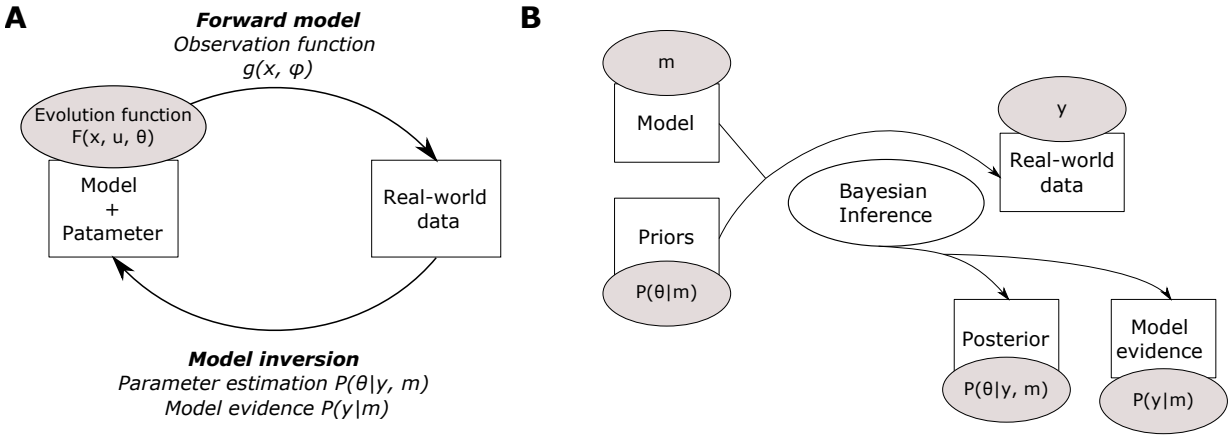


FIGURE 5.2: **Principles of Bayesian inference in DCM analysis.** (A) The neurobiological model, represented by the evolution function F and the observation function g, generates data that is mapped onto the real-world data through forward modelling. Model fit, the extent to which the generated data recapitulates the real-world data, is improved by feeding real-world data back into the model data generation (*model inversion*). (B) Overview of how mathematical terms in DCM analysis translate to modelling terms.

Both model components, the evolution function and the forward model, are fitted simultaneously in multiple repetitive fitting rounds. The resulting parameter posterior mean and distribution are constrained to the *a priori* specified prior density – an informed expression of the range that the parameter is most likely to lie within [208]. DCM analysis should always avoid underfitting (high discrepancy between real-world data and predicted model output) as well as overfitting (near-perfect match between data and model output). Underfitted models might lead to poor explanatory value due to high bias and little accuracy. Overfitted models are characterised by very low bias and extreme accuracy but lack the capacity for generalisation [250].

Third step: Bayesian model selection. Model inversion also allows the comparison of different models with regard to their ability to explain the real-world data. The model

providing the best balance between accuracy and complexity should be chosen for further analysis.

The model evidence can be calculated using *Bayesian model selection* (BMS) tools that allow finding the neurophysiological model that is most likely to generate the data. The required integration is often only achievable using computational approximation mechanisms such as the *Akaike information criterion (AIC)*, *Bayesian information criterion (BIC)* or variants thereof [163]. These comparison tools provide an accuracy term (so-called log-evidence which describes *how well the generated outcome fits the real-world data*) and a complexity term. When comparing different models, a lower AIC indicates a better suitability of the model to explain the real-world data. To measure complexity, AIC and BIC take the number of parameters into account, but not their interdependencies nor the prior density functions. Therefore, most DCM analyses use a different but more complex model comparison method, the so-called *free energy F*. Free energy tools also provide a measure for model complexity that accurately validates parameter dependencies [163].

Fourth step: Statistical analysis on parameter posterior densities. Choosing the most suitable model allows completing the DCM analysis using parameter posterior densities from only a single model. The statistical comparison of the posterior densities before and after an experimental intervention detects changes in effective connectivity induced by an experimental stimulus.

In summary, DCM is powerful in inferring causal mechanisms underlying effective connectivity dynamics in neuronal networks that are not directly accessible to experimental observations. It requires the careful construction of a model of the neuronal network

activity and its translation into the measured data, completed with an informed decision on the likely range of each model parameter distribution. These prior parameter densities are then combined with the real-world data during model inversion to fit the model output to the initial data. This model inversion yields an estimate of each parameter mean and distribution (posterior densities) as well as a measure of the plausibility of the model itself (model evidence).

5.2 Aims

I applied DCM as a means to examine synaptic connections within a stem cell-derived cortical glio-neuronal co-culture. The first step was to validate the method on a control culture so that it could then be used in a second step to reveal potential changes in effective neuronal connectivity induced by TSC2-deficient astrocytes.

Specifically, the aims of this chapter were

1. Perform a proof-of-concept study to evaluate the suitability of DCM analysis for analysis of effective connectivity in neuronal networks *in vitro* using MEA recordings. This will be done by detecting GABA-induced changes in effective connectivity through DCM analysis in iPSC-derived neuronal networks over individual MEA electrodes.

2. Investigate the effects of TSC2-deficient astrocytes on neuronal network formation and neuronal network activity using MEA recordings and DCM analysis on TSC glio-neuronal co-cultures.

In the proof-of-concept study, I aimed to detect GABA-induced effects on effective connectivity in iPSC-derived neuronal networks using DCM analysis on MEA recordings from individual electrodes. The specific code for this implementation was adapted from the academic freeware SPM12 (http://www.fil.ion.ucl.ac.uk/spm/toolbox/DCMMEEG) and can be found on github (https://github.com/PaulaRock/DCM-MEA).

5.3 Proof-of-concept study: Establishing DCM on stem cell-derived glio-neuronal co-cultures

To check whether DCM analysis can pick up network changes *in vitro*, we exposed a stem cell-derived glio-neuronal co-culture to the neurotransmitter GABA whose inhibitory effects on neuronal networks are well-documented [210]. The tissue culture work for this part of the study was kindly done by Dr Liting Tina Wei. The LFP recordings were processed by cross-spectral analysis before the data was fitted through DCM to establish a set of distinct posterior parameter values for the GABA and control wells, respectively. In the last steps, these posterior values were analysed using standard logistic regression analysis to reveal potential significant differences between both sets (see figure 5.3).

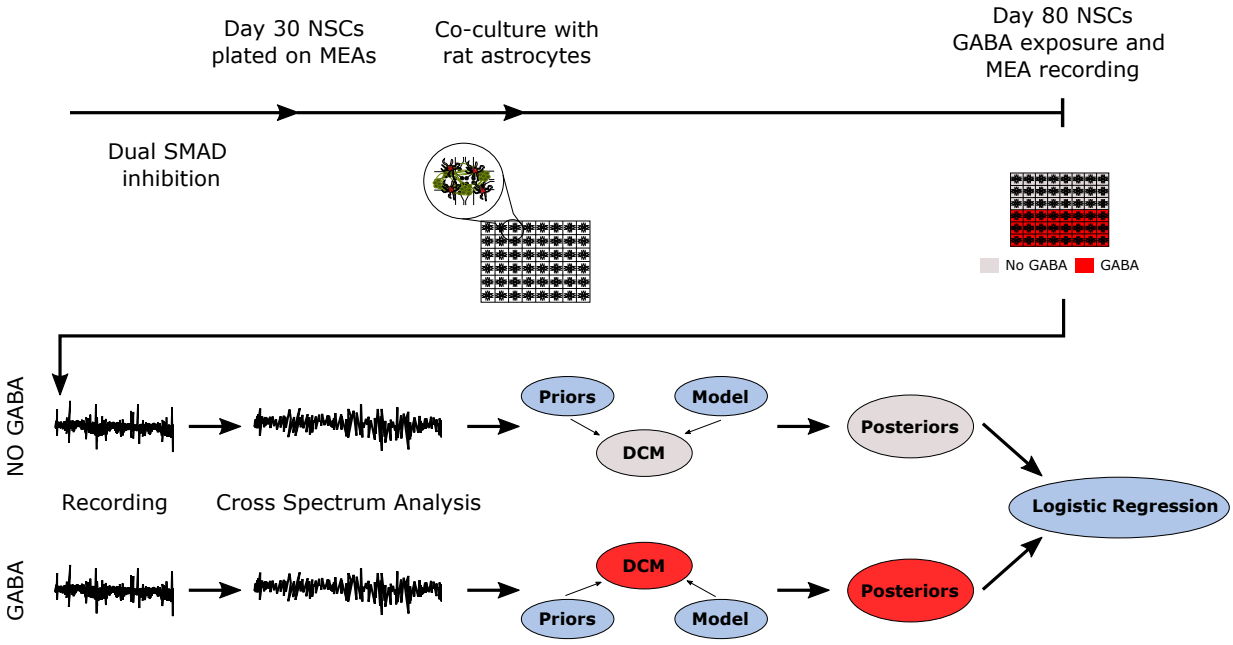


FIGURE 5.3: **Establishing DCM on iPSC-derived glio-neuronal cultures.** In the proof-of-concept study, control iPSCs were differentiated into cortical neurons and co-cultured with rat astrocytes on MEAs from day 40 onwards. Cultures were briefly exposed to GABA or PBS as a control vehicle on day 81. Their recorded response in firing activity and LFP was processed via a cross-spectrum analysis and analysed with DCM followed by a logistic regression to detect significant effects that GABA application exerted on the network connectivity.

5.3.1 MEA recordings of a stem cell-derived cortical glio-neuronal co-culture.

A well-established control iPSC culture (SBAD-03-01) derived during the STEMBANCC project was used to generate NSCs via dual SMAD inhibition. NSCs were drop-plated onto MEA cell culture plates on day 30 at a high density of 100,000 cells / cm^2 to ensure good neuronal covering of the electrodes later on. Neuronal cultures were co-plated with rat astrocytes on day 35 at a ratio of 1:1. The response in spiking and LFP activity to the application of either 50 μM GABA or PBS was recorded on NSC day 80. For future reference, figure 5.4 B shows an outline of the used 48-well MEA plate in an 8x6 format. The wells are named A1-F8 with each well containing a 4x4 grid of electrodes, named 11-44, respectively.

To inform the prior model parameters later on, the iPSC-derived neuronal cultures were characterised with regards to molecular markers of key synaptic features. The cultures used for these a priori tests were differentiated and maintained without glial co-culture. Flow cytometry data revealed that the vast majority of the culture on day 80 was composed of excitatory neurons expressing VGlut1, a protein responsible for their ability to release the excitatory neurotransmitter glutamate [85]. Less than 1 % of the culture appeared to be inhibitory neurons expressing GAD67, a CNS-specific isoform of the glutamate decarboxylase which transforms glutamate to GABA [245]. Around 12 % of the neuronal culture did not express either marker (see figure 5.4 C).

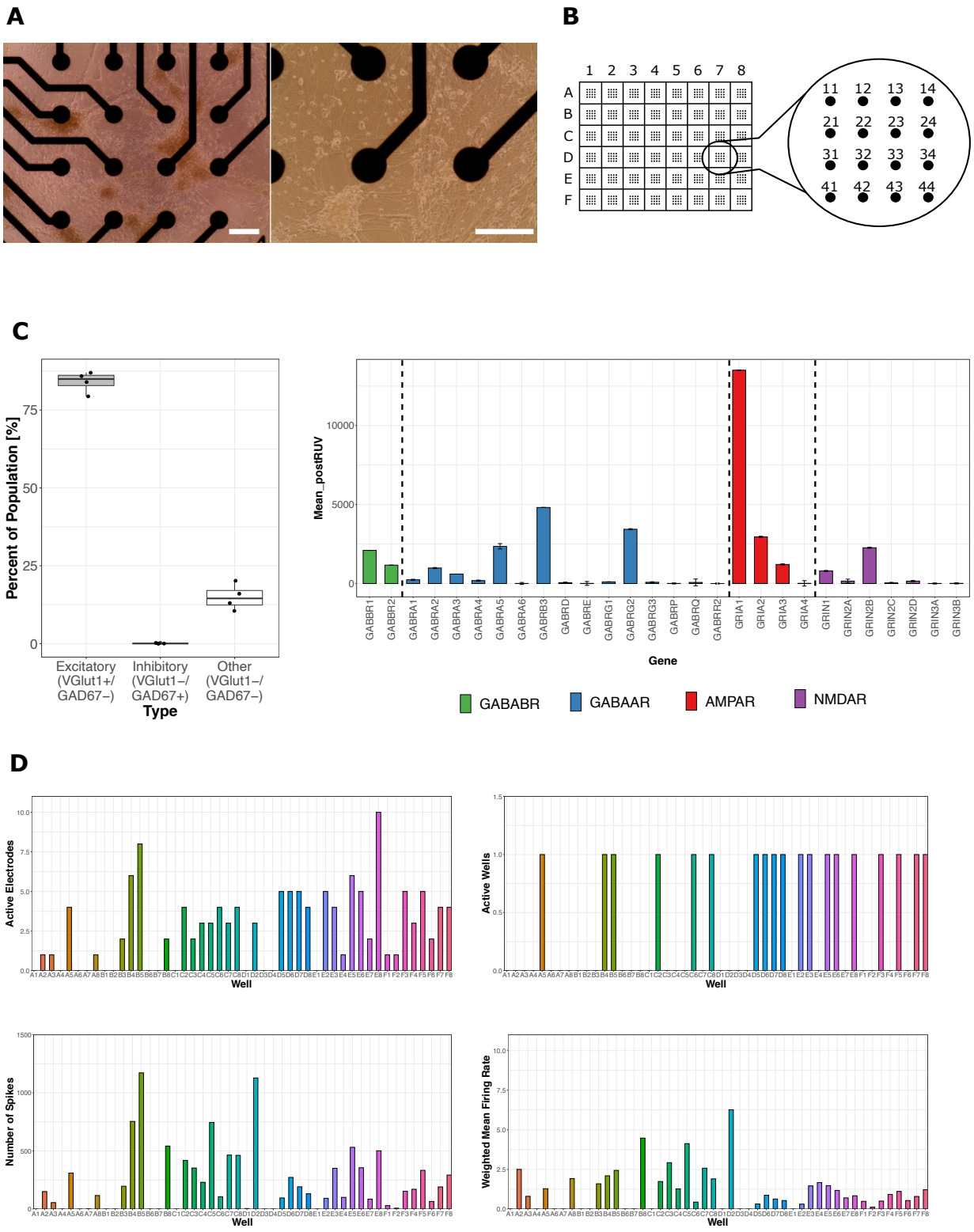


FIGURE 5.4: **Characteristics of iPSC-derived neuronal cultures.** (A) Exemplary image of glio-neuronal co-cultures grown on MEA plates with the MEA electrodes visible as black dots. (B) Schematic of a 48-well MEA plate with the respective labels for wells and electrodes. (C) Flow cytometry of iPSC-derived neuronal cultures on day 80 revealed that the vast majority of the culture comprised excitatory neurons labelled positive for VGlut1. Bulk transcriptomic data detected different neuronal receptor subunits typical for pre-natal neurons such as the NMDAR subunit GRIN2B. (D) Baseline MEA recordings at day 81 showed a uniform pattern of neuronal activity across all wells for the main four conventional MEA parameters *active electrodes*, *active wells*, *number of spikes* and *weighted mean firing rate*. *Replicates: (C) 1 differentiation; (D) 1 differentiation in 48 wells.*

Bulk transcriptomic data on SBAD-03-01 neuronal cultures at day 80 after dual SMAD-inhibition showed a distinct expression of key receptor subunits for the $GABA_A$, $GABA_B$, NMDA and AMPA receptors. These data revealed a rather immature expression pattern of key receptor subunits, as can best be seen on the NMDA and AMPA receptors (see figure 5.4 C). The NMDA receptor is usually formed as a dimer from the subunit GRIN1 together with one of the four GRIN2 subunits A, B, C or D. The tested neuronal cultures around day 80 almost exclusively expressed the subunit GRIN2B in addition to GRIN1, a pattern which is normally found in pre-natal neurons [202].

MEA recordings from the glio-neuronal co-culture were taken over 2 min at baseline, 5 min after GABA application and 30 min after GABA wash-out. Baseline recordings demonstrated a random distribution of the key spiking parameters *weighted mean firing rate*, *active wells*, *active electrodes*, and *number of spikes* over all MEA wells (see figure 5.4 D). There were no significant differences between the wells which would later become GABA or control wells for any of these parameters.

Analysis of conventional MEA parameters on neuronal firing revealed an overall inhibitory impact of GABA on neuronal spiking. There was a significant decrease in active electrodes and active wells in the treatment group five minutes after GABA application which was not seen in the control wells (Active wells Baseline vs 5min GABA, $p = 0.0081$; Active electrodes Baseline vs 5 min GABA, $p = 0.0124$). Cultures reacted with a five-fold decrease in the number of spikes per well to GABA application, however, this difference did not reach significance ($p = 0.2690$). No such response was seen in the control group where the number of spikes was steady after the application of the control vehicle PBS. After washout, GABA wells showed a significant increase in the number of spikes ($p = 0.0101$). No significant difference in the weighted mean firing rate between the different

groups and time points was seen (Baseline vs 5 min GABA, p = 0.3001; 5 min GABA vs GABA washout, p = 0.2297). However, the GABA group saw a respective trend with a three-fold decrease after GABA application and a three-fold increase after washout; a pattern that was not present in the control group (see figure 5.5).

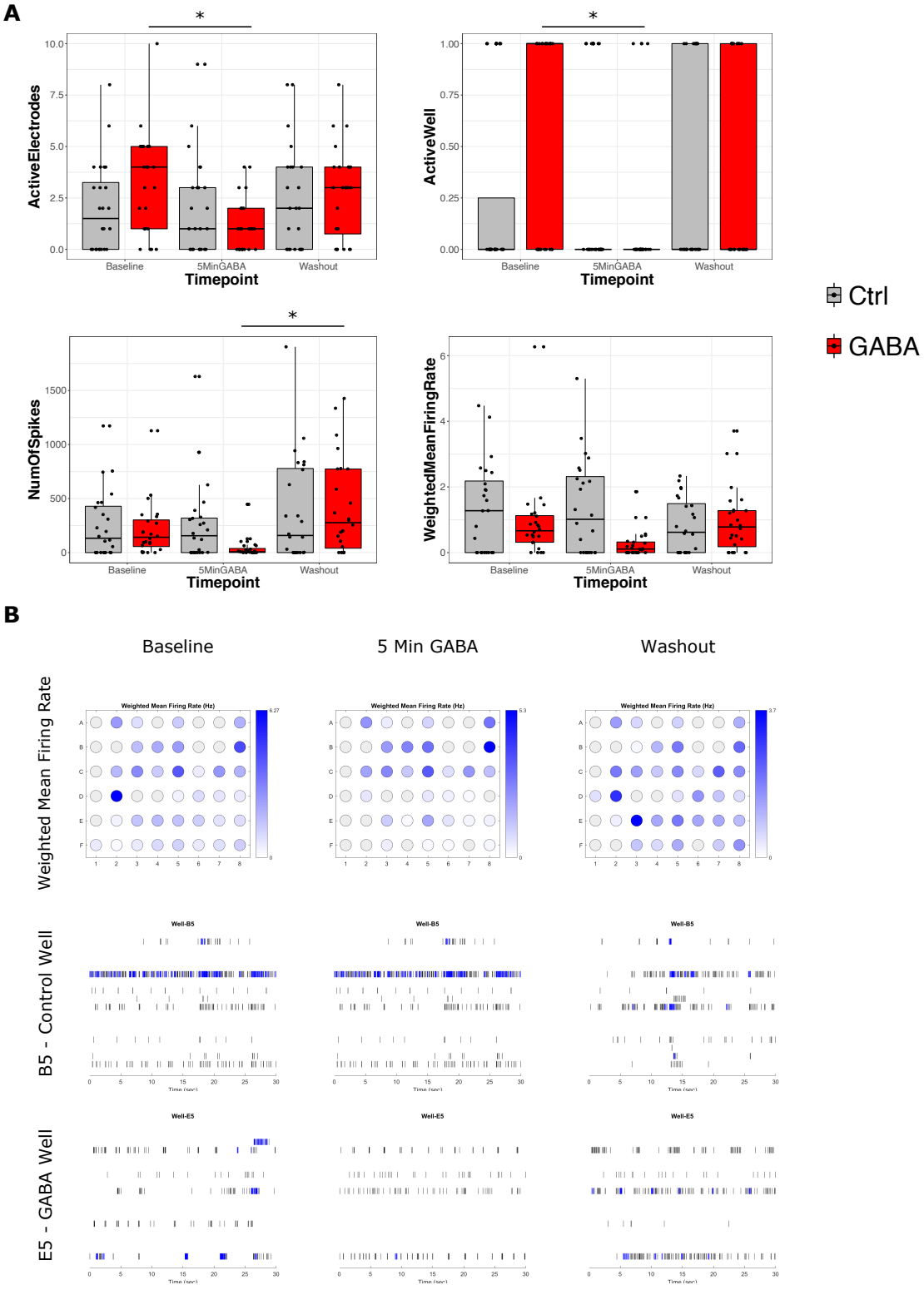


FIGURE 5.5: **Influence of GABA on neuronal firing.** (A) The four MEA parameters *active electrodes*, *active wells*, *number of spikes* and *weighted mean firing rate* were analysed on day 81 at baseline, five minutes after GABA application and 30 min after washout of GABA in wells receiving PBS as a control vehicle (grey) or 50 μM GABA (red). GABA caused a significant decrease in the number of active electrodes and active wells but no significant changes in the number of spikes or weighted mean firing rate compared to baseline recordings. However, GABA sources reacted with a significant increase in the number of spikes to GABA washout. (B) Plots showing the weighted mean firing rate per well as well as example raster plots for a control well (B5) or GABA well (E5) at baseline, 5 min after GABA application, and 30 min after washout. *Replicates: 1 differentiation in 24 wells per treatment.*

5.3.2 Model construction.

The underlying biophysical neuronal model was implemented in the SPM12 software for DCM analysis with support from Prof Rosalyn Moran. A detailed model description can be found in section 2.6. Figure 5.6 shows a schematic of the used canonical microcircuit model (CMM) comprising three excitatory and one inhibitory neuronal population, all equipped with parameterised AMPA, NMDA, and $GABA_A$ receptors.

We used the CMM for DCM, a conductance-based model that has been developed based on extensive knowledge of cortical anatomy and physiology. Our model was based on a previously published CMMs of cortical macrocolumns in accordance with the cortical nature of the iPSC-derived neuronal network [255]. In contrast to convolution-based models that consider whole cortical mesocolumns as the main electrophysiological unit, conductance-based models represent the electrophysiological properties of single cells. Since the neuronal organisation of my hPSC-derived cultures did not resemble cortical mesocolumns, conductance-based models were deemed more suitable in the context of my study. The model comprised three excitatory sources (labelled $\epsilon 1$, $\epsilon 2$, and $\epsilon 4$,) and one inhibitory source (labelled $\gamma 3$) that were interconnected as shown in figure 5.6. In the original model developed to analyse human EEG data, characteristics of these individual cell populations were modelled to represent different cortical cell types such as

superficial and deep pyramidal cells or spiny stellate cells [255]. However, hPSC-derived cortical networks do not mimic the layered organisation of cortical macrocolumns. Thus, I did not distinguish between different excitatory cell types but instead, assumed similar characteristics for all neuronal sources in my neuronal cultures. Priors were chosen in accordance with previous DCM analyses on EEG data [255] as well as in line with standard characteristics for receptor properties such as receptor opening potentials. We also applied specific priors for NMDA and AMPA receptor properties to match the immature and slower receptor functions of iPSC-derived neurons as outlined in section 2.6.

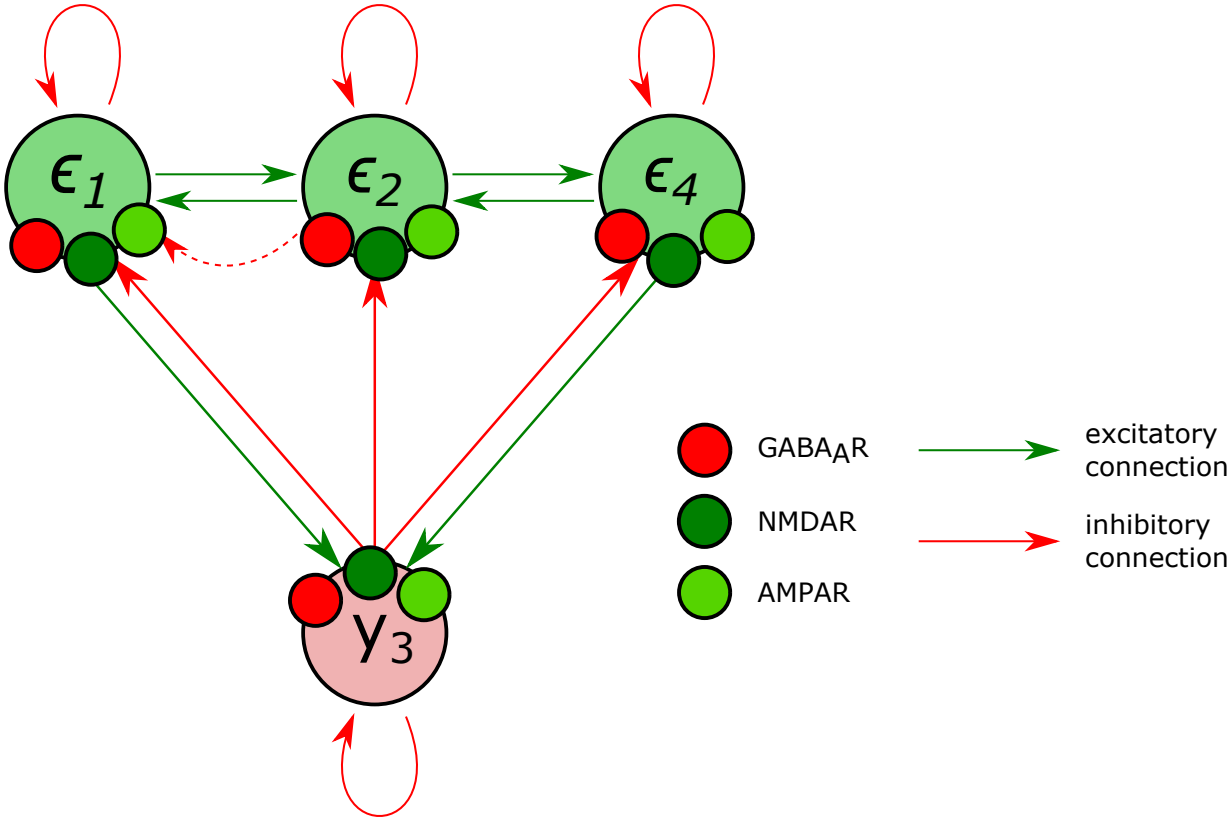


FIGURE 5.6: **Canonical microcircuit model.** The CMM was constructed of three excitatory populations $\epsilon 1$, $\epsilon 2$ and $\epsilon 4$ and one inhibitory source $\gamma 3$ with excitatory (green) and inhibitory (red) connections as well as inhibitory self-feedback loops. Each population received inputs via three receptors: GABA$_A$R (red), NMDAR (dark green) and AMPAR (light green).

5.3.3 Bayesian model inversion.

Recordings were made at a sampling rate of 12.5 kHz from the 4x4 electrode grid of each of the 48 wells. For DCM analysis, we used the first minute of each two-minute recording. Pre-processing involved the downsampling of the data to 312.5 Hz which yielded sufficient bandwidth to capture gamma band activity (between 30 to 200 Hz). For each well, the electrode with the highest LFP activity over the whole time series was identified as *anchor electrode* and paired with the remaining electrodes to form 15 electrode pairs over each 4x4 electrode grid. To transform the data into a more accessible format, Prof Rosalyn Moran decompressed this paired sensor data into two spatial modes using an autoregressive cross-spectral analysis method which was originally developed for spectral DCMs. This method provided a $15x2$ matrix of complex cross-spectra where we focused on LFP activity in the gamma band between 0 - 60 Hz at 1 Hz resolution (60 frequency points). This approach yielded $15x2x61 = 1860$ real and complex data points which formed the features used for model fitting for each well.

During model inversion, we generated data using the CMM framework explained above according to a Variational Bayes scheme.

To quantify the model fit, I calculated the percentage of the variance explained (VE) by the model as

$$VE = r^2(M, R) \tag{5.1}$$

where r is the correlation factor between the cross-spectra of the real data R and the respective cross-spectra of the modelled data M (implemented using Matlab's *corr()* function). There was no significant difference between VE for control and GABA sources

with VE being around 99 % for both groups. Figure 5.7 shows the mean cross-spectra for control and GABA sources with their respective model fit.

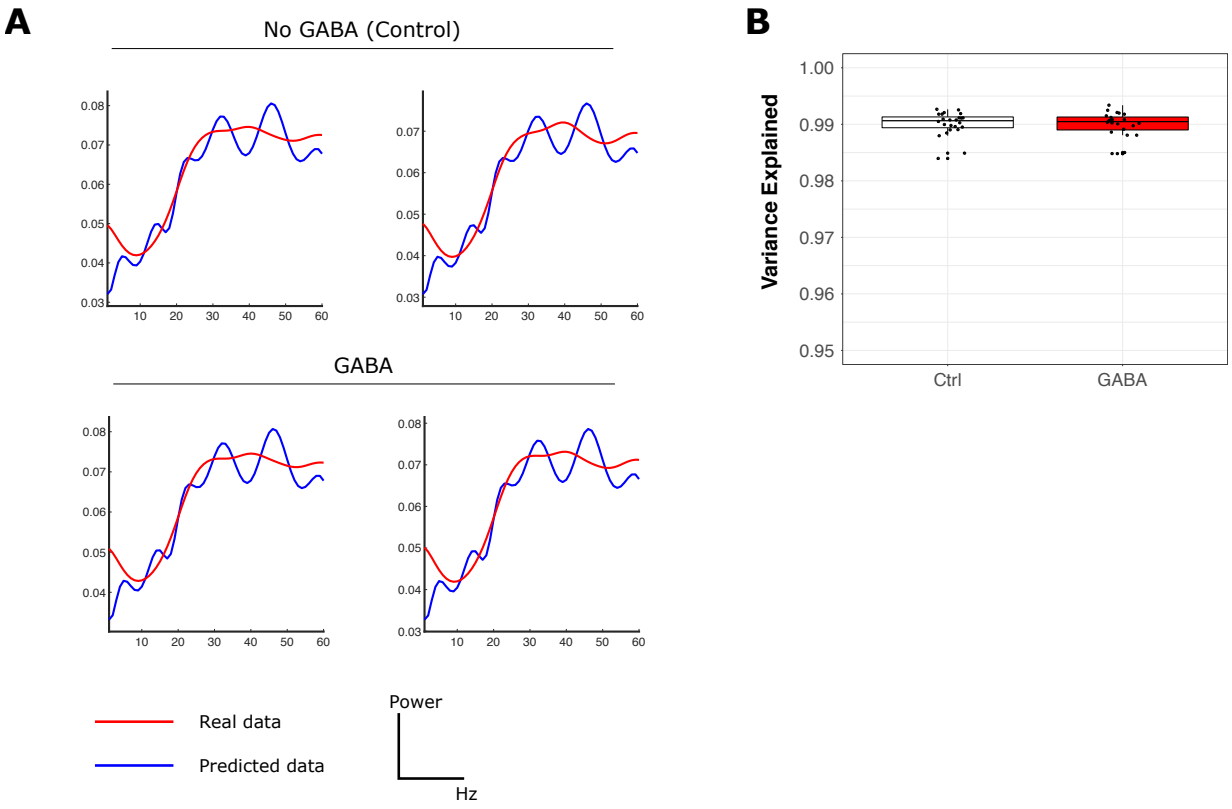


FIGURE 5.7: **Model fit for GABA and control sources.** (A) The mean cross-spectra spanning 0-60 Hz for the original data (red) and the predicted data (blue) showed adequate model fit for control (upper row) and GABA electrodes (lower row) in both modes (left and right plot). (B) There was no group effect of model fit as the percentage of variance explained was around 99 % for both groups.

5.3.4 Generalised linear regression as statistical analysis.

To test for consistent GABA effects, I applied a generalised linear model (GLM) with the posterior parameter set from each electrode-pair as independent (predictor, X) and the drug status (GABA or no GABA) of the well as dependent (response, Y) variable.

$$E(Y|X) = g(X\beta)$$

Here, the likelihood of a well being a GABA or no GABA well ($E(Y|X)$) was computed

dependent on the posterior parameter set X with g being the link function that establishes a linear relationship between Y and X.

I implemented GLM using Matlab's inbuilt function *glmfit()*. To build the response variable Y, each well was assigned either GABA (1) or vehicle (0). The predictor variable X comprised the maximum á posterior values for each posterior parameter normalised to the mean of each parameter over all control wells.

The β-coefficient and p-value for each posterior parameter were obtained to identify the parameters that significantly predicted the 1/0 drug effect and thus, significantly correlated with the application of GABA to the neuronal network. Significance was assumed when $p < 0.05$ after Bonferroni correction.

This approach identified two significantly different model parameters associated with the application of GABA. Specifically, these comprised an increase in the GABA receptor conductance at $\epsilon 1$ (parameter H(3,1,1), the input from inhibitory source $\gamma 3$ to excitatory source $\epsilon 1$) and a decrease in the excitatory drive from $\epsilon 2$ to $\epsilon 1$ (parameter A1(1,1), the input from excitatory source $\epsilon 2$ to $\epsilon 1$). The change in a third parameter, associated with background noise, just reached significance. Figure 5.8 recapitulates the resulting network, summarising the decrease in the excitatory and increase in the inhibitory drive towards population E1, which is consistent with GABA's inhibitory properties.

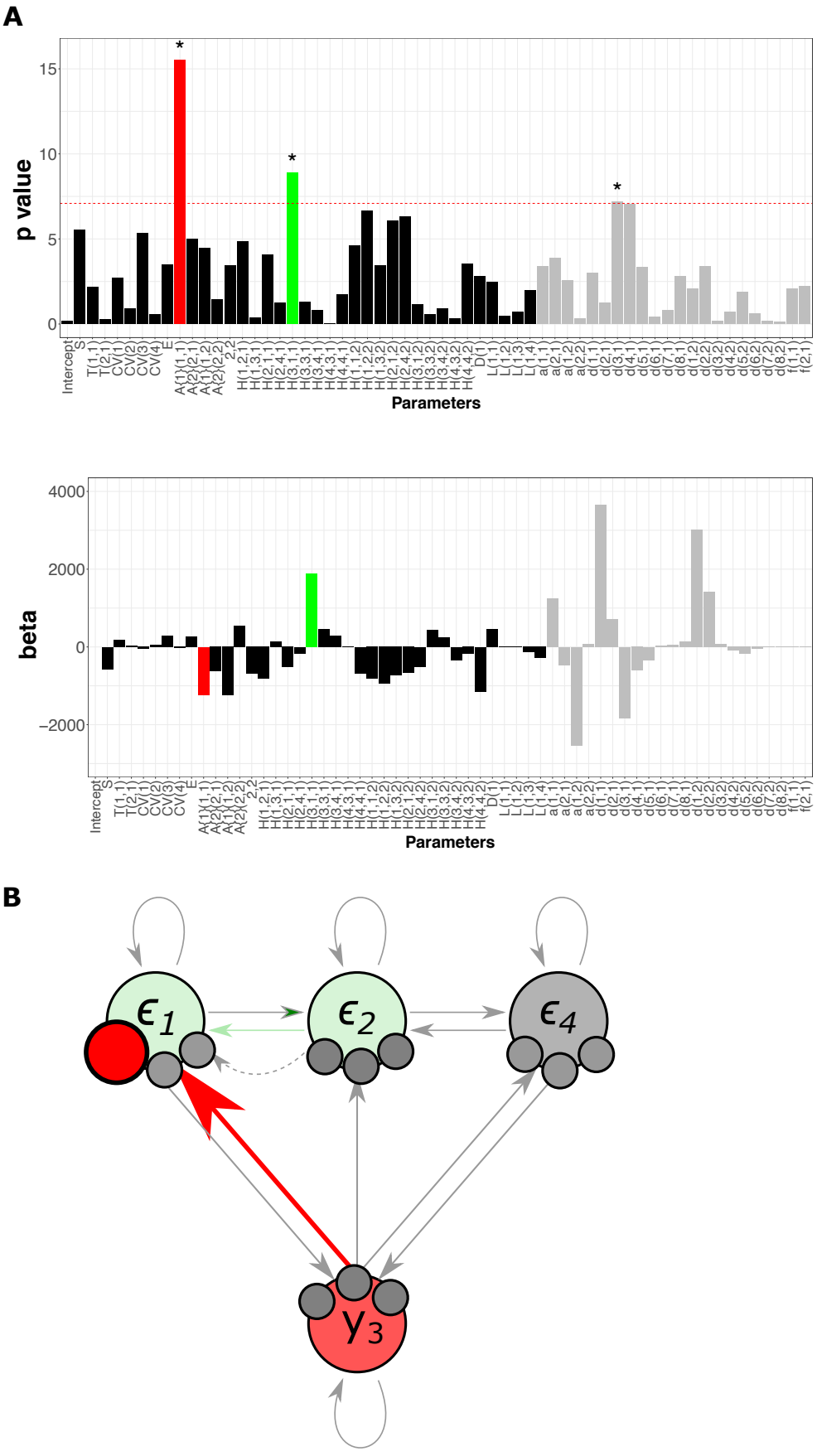


FIGURE 5.8: **Results of the DCM proof-of-concept analysis.** (A) P-values and β-coefficients from the logistic regression on the control and GABA posterior sets showing two significant changes in parameters (indicated by a star): an increase in H(3,1,1), the $GABA_A$ R conductance on $\epsilon 1$ (red), and a decrease in A1(1,1), the excitatory connection between $\epsilon 2$ and $\epsilon 1$ (green). The change in a noise parameter just reached significance. (B) Resulting model for neuronal cultures that received GABA according to the DCM analysis: The inhibition-excitation ratio was increased with a strengthened inhibitory connection between $\gamma 3$ to $\epsilon 1$ and a weakened excitatory connection between $\epsilon 2$ and $\epsilon 1$.

5.3.5 DCM on LFP data reveals network changes independent of spiking activity.

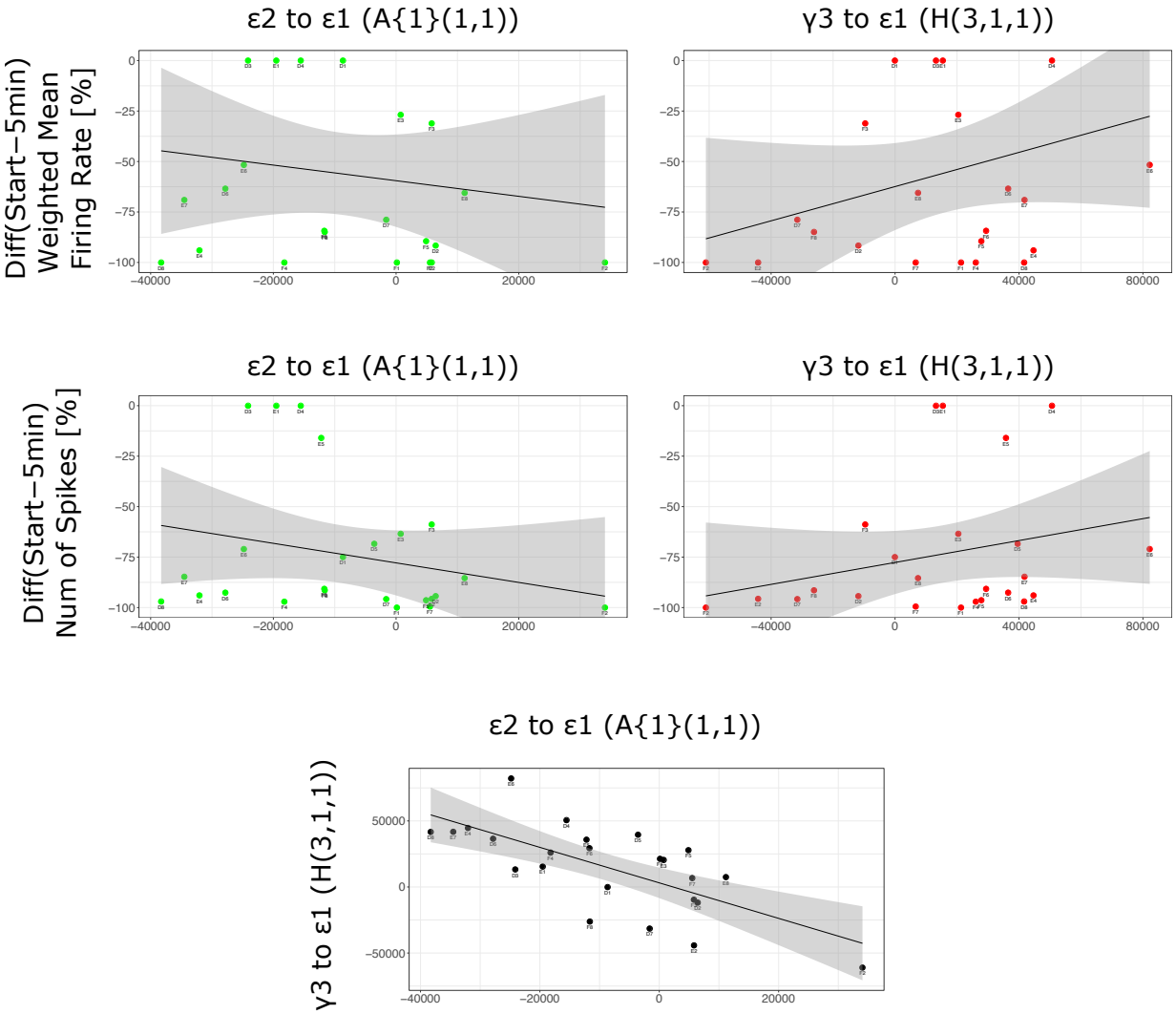


FIGURE 5.9: **Correlation between spiking parameters and DCM posteriors.** Well-based comparison between the conventional MEA measurements *Weighted mean firing rate* (upper row) and *number of spikes* (middle row) and the significant DCM parameters *A1(1,1)* (left) and *H(3,1,1)* (right) showed no correlation between the results of the MEA and DCM analysis. Each dot represents a well of the whole MEA plate including all control and GABA sources. However, the significantly changed DCM parameters *A1(1,1)* and *H(3,1,1)* were inversely correlated with each other (bottom plot).

On a well-specific basis, no correlation could be observed between GABA-induced changes in spiking and the extent of the GABA conductance increase (Difference in number of spikes – H(3,1,1): Pearson correlation coefficient (PCC) = 0.26: Difference in weighted mean firing rate – H(3,1,1): PCC = -0.29) nor between the spiking changes and the extent

of the excitatory drive's decrease (Difference in number of spikes – A1(1,1): PCC = 0.24: Difference in weighted mean firing rate – A1(1,1): PCC = 0.14). Changes in both synaptic parameters, however, were inversely correlated to each other (PCC = –0.7) (please refer to figure 5.9).

5.3.6 Model validation.

The validity of the presented CMM model was evaluated by comparing its AIC with 5000 surrogate group models generated through randomised drug label assignments. The AIC for the correctly assigned drug model (the here used CMM) was significantly lower than the AIC for all surrogate models (see figure 5.10 (B)).

I further evaluated the performance of the model by inferring the drug condition (GABA vs control) from the source-specific β-coefficients generated through the logistic regression analysis for each active electrode, active well, or all wells.

This method yielded a predicted drug status for each well between 0 (control) to 1 (GABA). The drug status was considered to be correctly assigned when $0.5 \leq \text{prediction} \leq 1$ for a GABA source and $0 \geq \text{prediction} < 0.5$ for a control source. The probability of the model correctly identifying the drug status of a source (P_{val}) was then calculated as

$$P_{val} = \frac{\text{number of correctly assigned sources}}{\text{total number of drug-specific sources}}.$$

The method robustly identified the drug status of a specific source with a probability of over 0.8 (see figure 5.10 (A) and table 5.1).

	GABA source	Control source
Active electrodes	0.80	0.88
Active well	0.81	0.83
All wells	0.82	0.8

TABLE 5.1: **Probability of correct drug assignment.** Drug labels (GABA vs control) were correctly inferred from the source-specific β-coefficients generated through GLM for different sources (active electrodes, active wells, all wells) with a probability of more than 80 %.

As will be discussed in section 5.5, DCM was suitable to analyse MEA data from glio-neuronal co-cultures and thus, I moved on to apply DCM analysis to glio-neuronal co-cultures with a TSC background in order to reveal the impact of astrocytes on neuronal circuit formation in TSC *in vitro*.

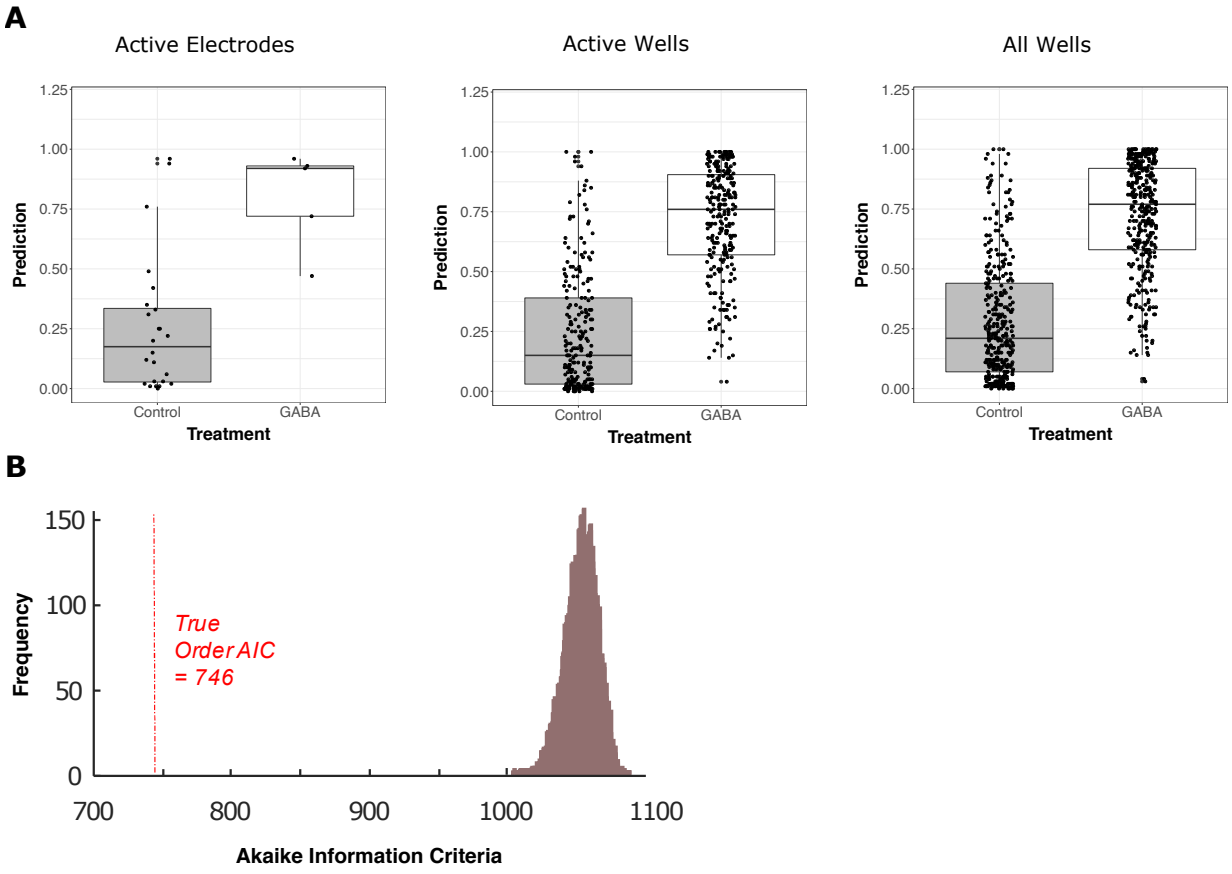


FIGURE 5.10: **Evaluation of model validity.** (A) The drug state (Control, 0 or GABA, 1) could be correctly identified from the source-specific β-coefficient set to over 80 % for the sources *active electrodes*, *active wells*, and *all wells*. (B) Comparing the Akaike Information Criterion (AIC) of the CMM to 5000 surrogate models demonstrated the significantly better performance of the here used model.

5.4 The impact of astrocytes on neuronal connectivity in TSC

DCM analysis using a canonical circuit model correctly identified inhibitory effects of GABA on the molecular level in a stem cell-derived neuronal network. Due to these encouraging findings in the proof-of-concept study, I took this analysis method forward to examine the impact of astrocytes on circuit development in a TSC *in vitro* model.

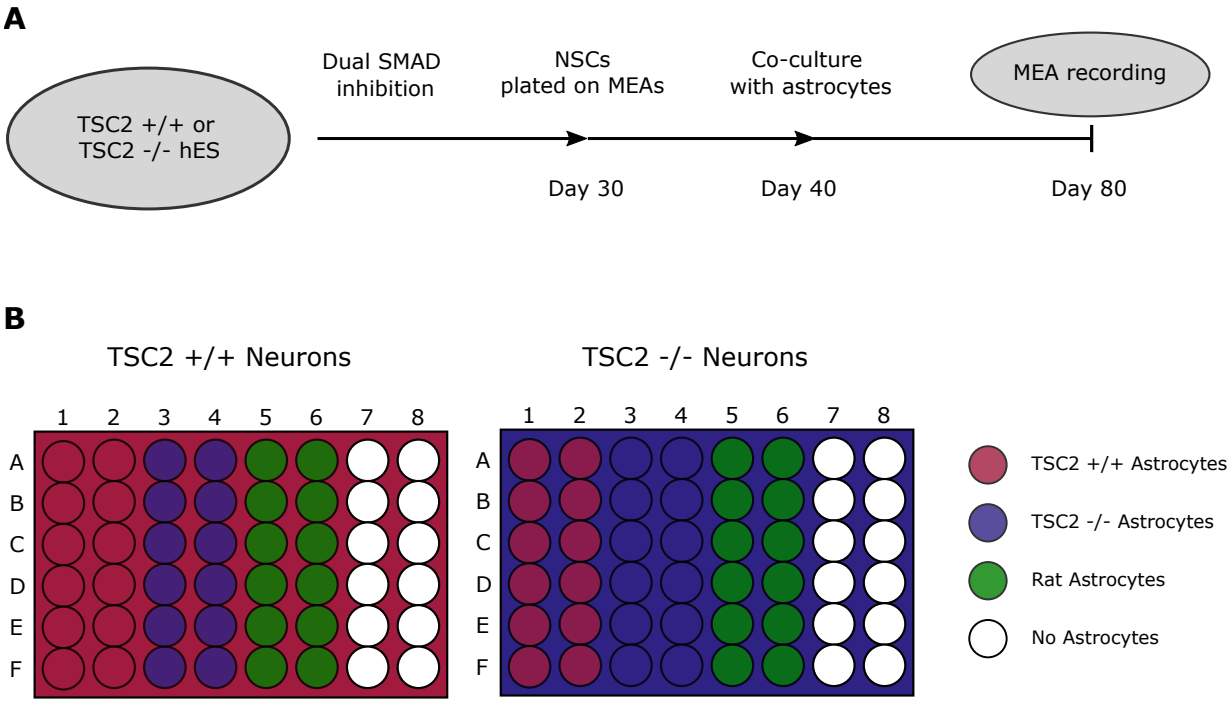


FIGURE 5.11: **Experimental layout for TSC2 glio-neuronal co-culture on MEA.** (A) Rough experimental timeline to examine the impact of astrocytes on neuronal connectivity in TSC using DCM analysis of MEA data. (B) Experimental layout of the two 48-well MEA plates to co-culture TSC2 +/+ (left) and TSC2 -/- (right) neurons with different astrocytes (TSC2 +/+ (red), TSC2 -/- (blue), rat (green) and none (white).

TSC2 +/+ and TSC2 -/- neurons derived by dual SMAD-inhibition were co-plated with different groups of astrocytes on MEA plates and maintained in high glucose media until neuronal day 80 with regular recordings of neuronal activity from day 54 onwards. NSCs were transferred onto the MEA plate on neuronal day 30 and astrocytes of four different types were added 10 days later: (i) day 37 TSC2 +/+ astrocytes, (ii) day 42 TSC2 -/- astrocytes, (iii) rat astrocytes and (iv) one group without astrocytes (see figure 5.11).

Conventional MEA analysis. Regular MEA recordings showed little neuronal spiking activity throughout the observation period for all sample groups. In TSC2 +/+ neurons, only a few electrodes reached the threshold to classify the electrode as *active* and activity was below the defined threshold for *active well* in all wells. Weighted mean firing rate was overall low in TSC2 +/+ neurons at all time points regardless of the glial partner. Similarly, TSC2 -/- neurons only showed very little neuronal activity with few active electrodes and no active wells. Co-culture of TSC2 -/- neurons with TSC2 -/- astrocytes increased the number of active electrodes and the weighted mean firing rate on days 76 and 81 (see figure 5.12), although this increase did not reach significance.

Construction of DCM analysis. The MEA recording from day 81 was taken forward for DCM analysis using the model and priors from the proof-of-concept study described above. One 48-well plate was used for each, TSC2 +/+ and TSC2 -/- neurons. Each neuronal genotype was paired with either TSC2 +/+, TSC2 -/-, rat, or no astrocytes in 12 wells comprising 15 electrode pairs each which yielded 180 DCMs per glio-neuronal co-culture, $4 \times 180 = 720$ DCMs per neuronal genotype and $2 \times 720 = 1440$ DCMs with respective posterior densities in total. Cross-spectral analysis decompressed the downsampled data into three spatial modes and DCM analysis focused on the gamma band between 0 - 80 Hz.

To determine significant changes in parameters, I used a multinomial logistic regression (MNR) to statistically compare the DCM posterior densities with the *TSC2 +/+ neurons – TSC2 +/+ astrocytes* as the reference group. The MNR was implemented in Matlab using the *mnrfit()* function which provides corrected p-values and β-coefficients for each comparison between sample groups and the reference group.

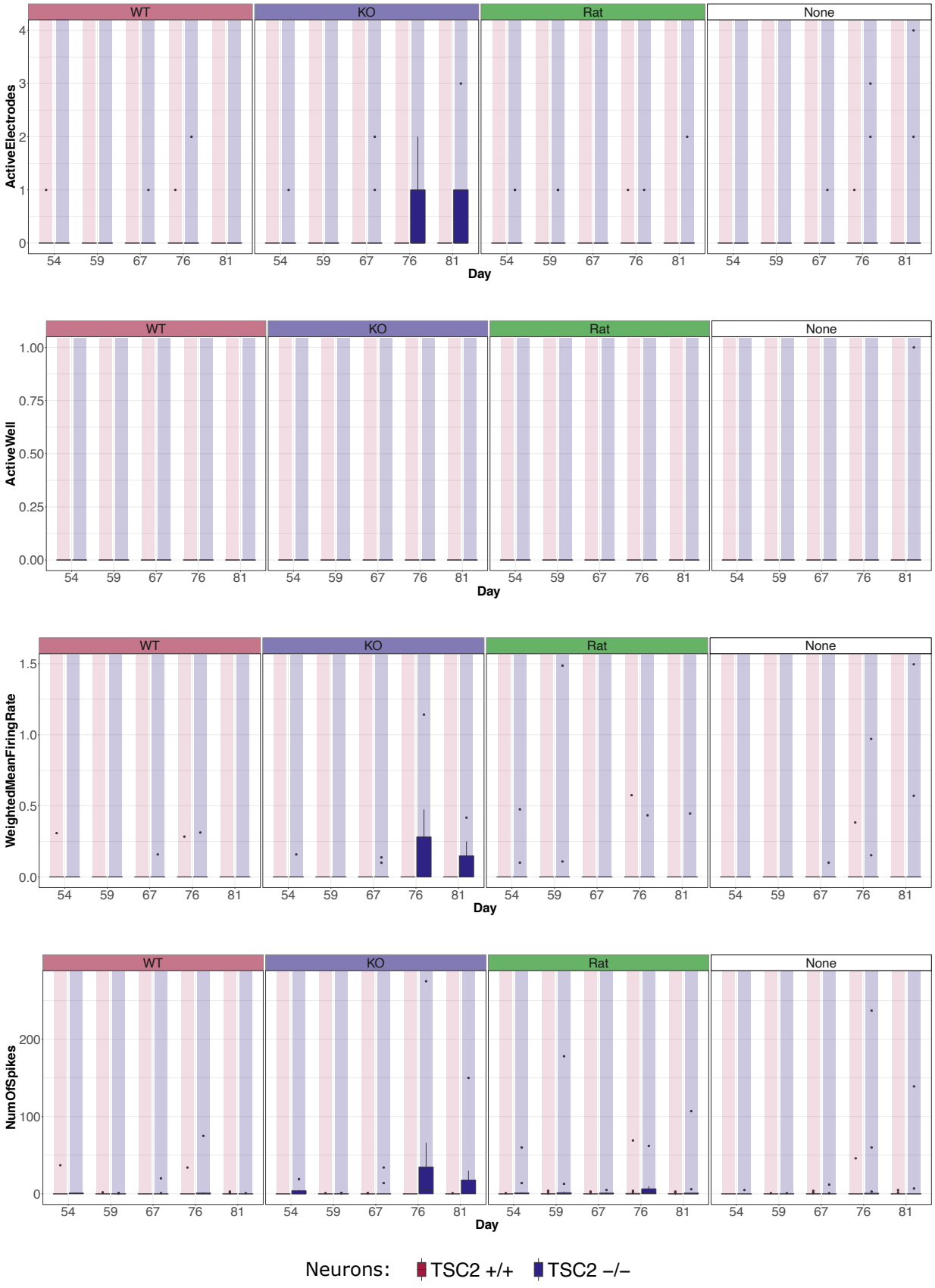


FIGURE 5.12: **MEA analysis of TSC glio-neuronal co-culture.** Overview of MEA conventional spiking parameters in TSC glio-neuronal co-cultures. The four boxes per plot represent the glial groups (TSC2 +/+, TSC2 -/-, rat, none) with the development of neuronal activity displayed for each parameter from day 54 to day 80 for TSC2 +/+ neurons (red transparent background) and TSC2 -/- neurons (blue transparent background). Overall, TSC glio-neuronal co-cultures remained mostly inactive over the recording period from day 54 to day 81. The combination of TSC2-deficient neurons and astrocytes showed a mild increase in neuronal activity on days 76 and 81. *Replicates: 1 differentiation with 12 wells per glio-neuronal condition.*

Results of DCM analysis. The highest number of connectivity parameters was effected in TSC2 -/- neurons co-cultured with TSC2 -/- astrocytes as illustrated in figure 5.14 which displays the p-values (A) and the direction of change (B) for all significantly changed parameters in all sample groups.

Most strikingly, co-culture with TSC2 -/- astrocytes led to opposite effects in TSC2 +/+ and TSC2 -/- neurons (see figure 5.14 and 5.13). In TSC2 +/+ neurons, TSC2-deficient astrocytes induced an overall increase in inhibition, mostly mediated by an increase in the strength of connections from the inhibitory population $\gamma 3$ to $\epsilon 1$ and $\epsilon 4$. In contrast, the inhibitory drive was significantly decreased and excitation increased in TSC2 -/- neurons when co-cultured with TSC2-deficient astrocytes. This change was mostly driven by a reduction in the excitatory input from $\epsilon 1$ and $\epsilon 4$ to the inhibitory population $\gamma 3$ as well as a further decrease in inhibitory self-feedback loops on $\epsilon 1$ and $\epsilon 4$.

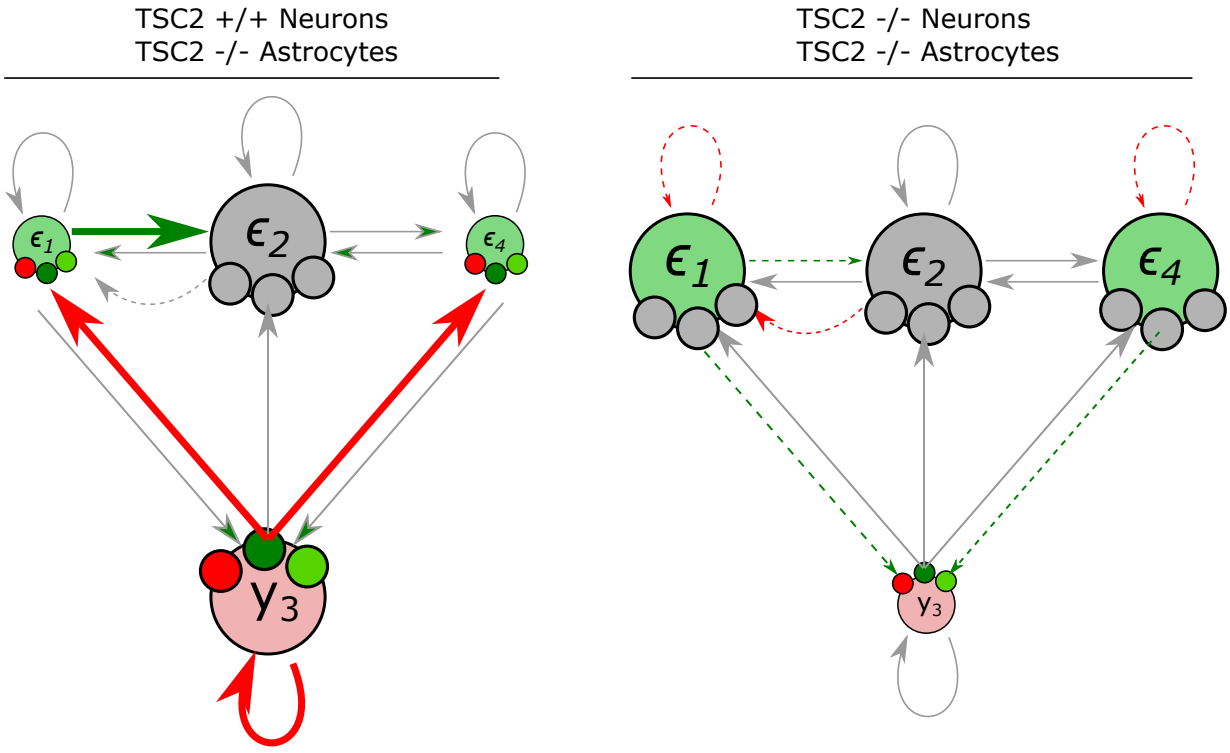
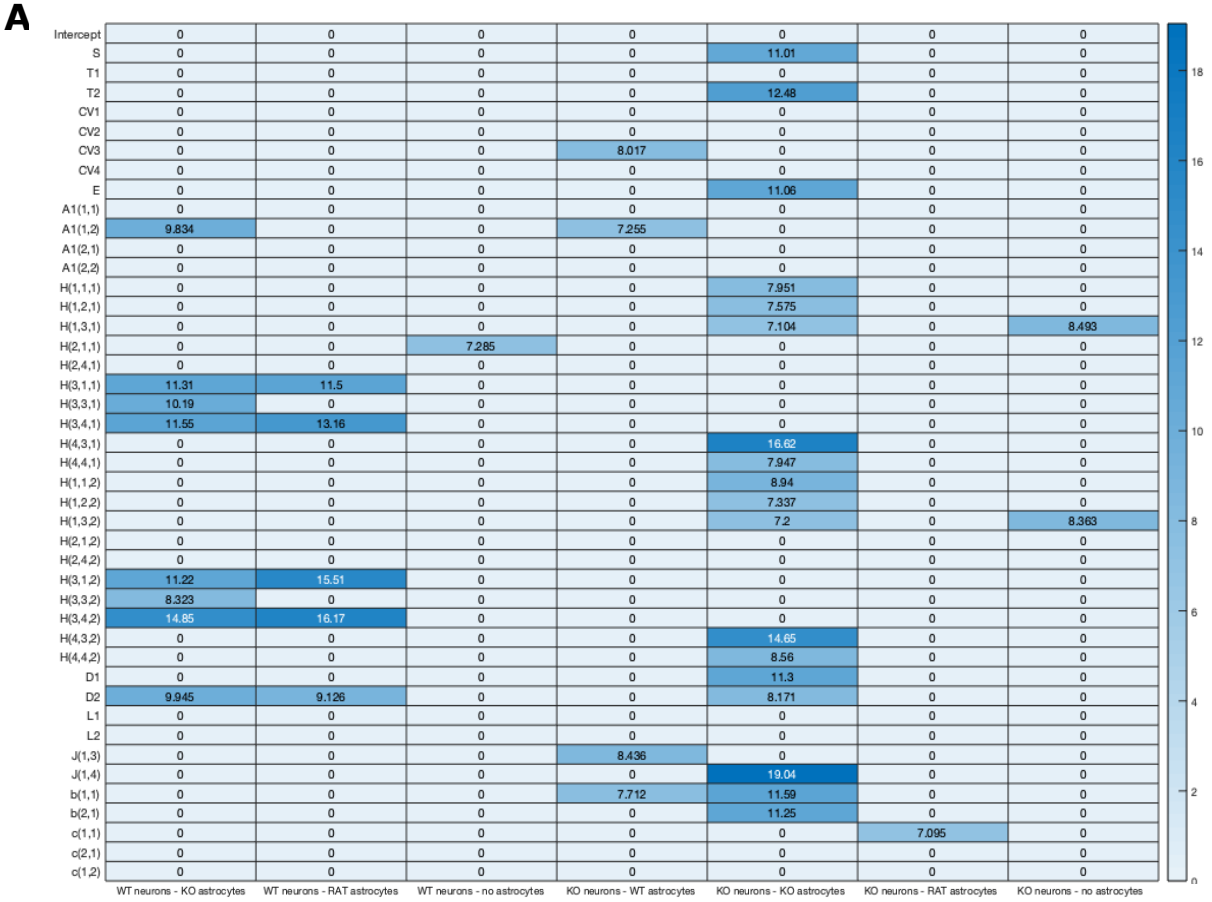


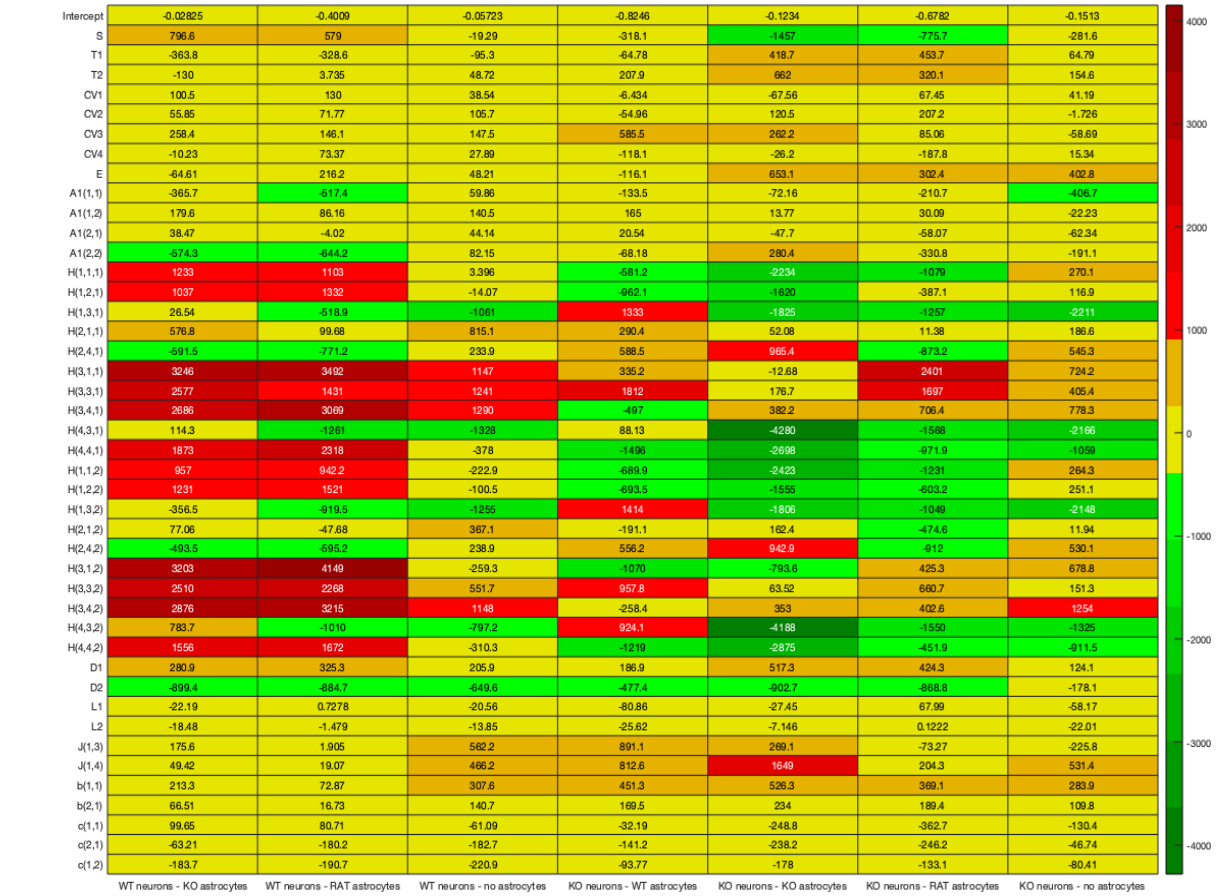
FIGURE 5.13: **Modelled effect of TSC2 -/- astrocytes on neuronal connectivity.** Exemplary schematic of the contrary effect that TSC2 -/- astrocytes exert on connectivity in TSC2 +/+ (left) and TSC2 -/- (right) neurons as per DCM analysis.

A



	WT neurons - KO astrocytes	WT neurons - RAT astrocytes	WT neurons - no astrocytes	KO neurons - WT astrocytes	KO neurons - KO astrocytes	KO neurons - RAT astrocytes	KO neurons - no astrocytes
Intercept	0	0	0	0	0	0	0
S	0	0	0	0	11.01	0	0
T1	0	0	0	0	0	0	0
T2	0	0	0	0	12.48	0	0
CV1	0	0	0	0	0	0	0
CV2	0	0	0	0	0	0	0
CV3	0	0	0	8.017	0	0	0
CV4	0	0	0	0	0	0	0
E	0	0	0	0	11.06	0	0
A1(1,1)	0	0	0	0	0	0	0
A1(1,2)	9.834	0	0	7.255	0	0	0
A1(2,1)	0	0	0	0	0	0	0
A1(2,2)	0	0	0	0	0	0	0
H(1,1,1)	0	0	0	0	7.951	0	0
H(1,2,1)	0	0	0	0	7.575	0	0
H(1,3,1)	0	0	0	0	7.104	0	8.493
H(2,1,1)	0	0	7.285	0	0	0	0
H(2,4,1)	0	0	0	0	0	0	0
H(3,1,1)	11.31	11.5	0	0	0	0	0
H(3,3,1)	10.19	0	0	0	0	0	0
H(3,4,1)	11.55	13.16	0	0	0	0	0
H(4,3,1)	0	0	0	0	16.62	0	0
H(4,4,1)	0	0	0	0	7.947	0	0
H(1,1,2)	0	0	0	0	8.94	0	0
H(1,2,2)	0	0	0	0	7.337	0	0
H(1,3,2)	0	0	0	0	7.2	0	8.363
H(2,1,2)	0	0	0	0	0	0	0
H(2,4,2)	0	0	0	0	0	0	0
H(3,1,2)	11.22	15.51	0	0	0	0	0
H(3,3,2)	8.323	0	0	0	0	0	0
H(3,4,2)	14.85	16.17	0	0	0	0	0
H(4,3,2)	0	0	0	0	14.65	0	0
H(4,4,2)	0	0	0	0	8.56	0	0
D1	0	0	0	0	11.3	0	0
D2	9.945	9.126	0	0	8.171	0	0
L1	0	0	0	0	0	0	0
L2	0	0	0	0	0	0	0
J(1,3)	0	0	0	8.436	0	0	0
J(1,4)	0	0	0	0	19.04	0	0
b(1,1)	0	0	0	7.712	11.59	0	0
b(2,1)	0	0	0	0	11.25	0	0
c(1,1)	0	0	0	0	0	7.095	0
c(2,1)	0	0	0	0	0	0	0
c(1,2)	0	0	0	0	0	0	0

B



	WT neurons - KO astrocytes	WT neurons - RAT astrocytes	WT neurons - no astrocytes	KO neurons - WT astrocytes	KO neurons - KO astrocytes	KO neurons - RAT astrocytes	KO neurons - no astrocytes
Intercept	-0.02825	-0.4009	-0.05723	-0.8246	-0.1234	-0.6782	-0.1513
S	796.6	579	-19.29	-318.1	-1457	-775.7	-281.6
T1	-363.8	-328.6	-95.3	-64.78	418.7	453.7	64.79
T2	-130	3.735	48.72	207.9	662	320.1	154.6
CV1	100.5	130	38.54	-6.434	-67.56	67.45	41.19
CV2	55.85	71.77	105.7	-54.96	120.5	207.2	-1.726
CV3	258.4	146.1	147.5	585.5	262.2	85.06	-58.69
CV4	-10.23	73.37	27.89	-118.1	-26.2	-187.8	15.34
E	-64.61	216.2	48.21	-116.1	653.1	302.4	402.8
A1(1,1)	-365.7	-517.4	59.86	-133.5	-72.16	-210.7	-406.7
A1(1,2)	179.6	86.16	140.5	165	13.77	30.09	-22.23
A1(2,1)	38.47	-4.02	44.14	20.54	-47.7	-58.07	-62.34
A1(2,2)	-574.3	-644.2	82.15	-68.18	280.4	-330.8	-191.1
H(1,1,1)	1233	1103	3.396	-581.2	-2234	-1079	270.1
H(1,2,1)	1037	1332	-14.07	-962.1	-1620	-387.1	116.9
H(1,3,1)	26.54	-518.9	-1061	1333	-1825	-1257	-2211
H(2,1,1)	576.8	99.68	815.1	290.4	52.08	11.38	186.6
H(2,4,1)	-591.5	-771.2	233.9	588.5	965.4	-873.2	545.3
H(3,1,1)	3246	3492	1147	335.2	-12.68	2401	724.2
H(3,3,1)	2577	1431	1241	1812	176.7	1697	405.4
H(3,4,1)	2686	3069	1290	-497	382.2	706.4	778.3
H(4,3,1)	114.3	-1261	-1328	88.13	-4280	-1568	-2166
H(4,4,1)	1873	2318	-378	-1496	-2698	-971.9	-1059
H(1,1,2)	957	942.2	-222.9	-689.9	-2423	-1231	264.3
H(1,2,2)	1231	1521	-100.5	-693.5	-1555	-603.2	251.1
H(1,3,2)	-356.5	-919.5	-1255	1414	-1806	-1049	-2148
H(2,1,2)	77.06	-47.68	367.1	-191.1	162.4	-474.6	11.94
H(2,4,2)	-493.5	-595.2	238.9	556.2	942.9	-912	530.1
H(3,1,2)	3203	4149	-259.3	-1070	-793.6	425.3	678.8
H(3,3,2)	2510	2268	551.7	957.8	63.52	660.7	151.3
H(3,4,2)	2876	3215	1148	-258.4	353	402.6	1254
H(4,3,2)	783.7	-1010	-797.2	924.1	-4188	-1550	-1325
H(4,4,2)	1556	1672	-310.3	-1219	-2875	-451.9	-911.5
D1	280.9	325.3	205.9	186.9	517.3	424.3	124.1
D2	-899.4	-884.7	-649.6	-477.4	-902.7	-868.8	-178.1
L1	-22.19	0.7278	-20.56	-80.86	-27.45	67.99	-58.17
L2	-18.48	-1.479	-13.85	-25.62	-7.146	0.1222	-22.01
J(1,3)	175.6	1.905	562.2	891.1	269.1	-73.27	-225.8
J(1,4)	49.42	19.07	466.2	812.6	1649	204.3	531.4
b(1,1)	213.3	72.87	307.6	451.3	526.3	369.1	283.9
b(2,1)	66.51	16.73	140.7	169.5	234	189.4	109.8
c(1,1)	99.65	80.71	-61.09	-32.19	-248.8	-362.7	-130.4
c(2,1)	-63.21	-180.2	-182.7	-141.2	-238.2	-246.2	-46.74
c(1,2)	-183.7	-190.7	-220.9	-93.77	-178	-133.1	-80.41

FIGURE 5.14: **Results of DCM analysis in TSC2 glio-neuronal co-cultures.** (A) P-values from the MNR comparing the posterior sets of TSC2 +/+ and TSC2 -/- glio-neuronal co-cultures to the TSC2-sufficient reference group (WT neurons - WT astrocytes). Y axis, DCM parameters; x-axis, sample groups. P-values below the significance level are coloured in darker blue. (B) β-coefficients from the MNR comparing the posterior sets of TSC2 +/+ and TSC2 -/- glio-neuronal co-cultures to the TSC2-sufficient reference group (WT meurons - WT astrocytes). Y-axis, DCM parameters; x-axis, sample groups. Positive *beta*-coefficients, red; negative *beta*-coefficients, green.

Evaluation. Model fit was analysed using the percentage of variance explained VE calculated as in equation 5.3.3. The mean VE was just under 90 % in all groups with no significant difference between neuronal TSC2 +/+ and TSC2 -/- wells. Figure 5.15 displays the mean cross-spectra for all neuronal TSC2 +/+ and TSC2 -/- groups as well as their group-wise VE.

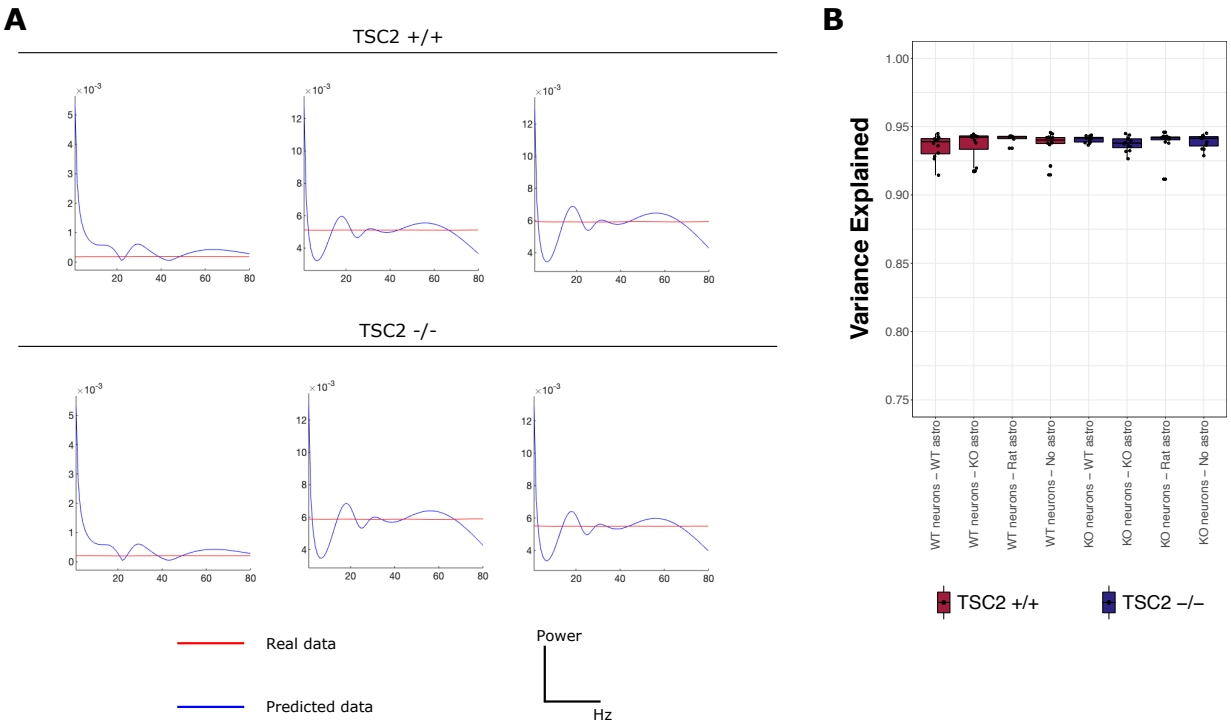


FIGURE 5.15: **Model fit in TSC glio-neuronal co-cultures.** (A) Exemplary plots for the mean cross-spectra spanning 0-80 Hz from pooled data of TSC2 +/+ and TSC2 -/- (lower row) neuronal activity (each pooled over all glial co-cultures, respectively). Comparison between the original data (red) and the predicted data (blue) showed adequate model fit in both groups. However, the original neuronal activity resembled a near-flat line in all groups. (B) There was no group effect of model fit as the percentage of variance explained was around 95 % in all groups.

5.5 Discussion

Overall, I aimed to establish a computational Bayesian method to assess the synaptic basics of effective connectivity in stem cell-derived neuronal cultures. I then applied this tool to TSC glio-neuronal co-cultures to examine the impact of astrocytes on the development of ill-formed and potentially epileptogenic neuronal networks in the context of TSC.

In MEA recordings, neuronal spiking activity near the electrode is detected as high-frequency activity whose analysis can help investigate neuronal population activity. However, analysis of spiking activity alone does not allow conclusions on the synaptic landscape within the neuronal network nor on molecular mechanisms underlying changes in neuronal firing caused by network modifications. In contrast, synaptic transmembrane currents in dendrites and somata of electrode-near neurons lead to low-frequency LFPs whose analysis could inform about synaptic connectivity [21]. I developed a DCM approach to analyse such LFP data recorded from *in vitro* neuronal cultures to detect synaptic-level changes in neuronal circuits. In a proof-of-concept study, I determined whether this DCM approach picks up distinct effects of the well-characterised neuroinhibitor GABA on stem cell-derived cortical networks.

The proof-of-concept study showed that DCM analysis of neuronal connectivity *in vitro* is feasible but not as straightforward as previously hoped.

I used a cortex-inspired CMM comprising three excitatory and one inhibitory sources with distinct receptor properties tailored to the immature nature of the stem cell-derived neurons. The suitability of this model was assumed firstly due to the cortical nature of the derived neurons. Secondly, this model was used previously to answer similar questions regarding the synaptic basis of effective connectivity in human EEG data [255]. Model

inversion produced cross-spectrum data which adequately recapitulated the original data while avoiding over-fitting. I did not observe a group effect of model fit between GABA and control sources indicating that the model was equally applicable to all data.

Model comparison is a main part of DCM analysis to evaluate the dominance of one model over others with regard to model fit, external validity, and model complexity. Here, a model comparison amongst different neurophysiological models was not performed as I only implemented one biological model. To evaluate model validity, I compared the performance of the CMM to 5000 surrogate models generated through randomisation of parameter allocation. The CMM model was significantly better suited to explain the original data than all 5000 surrogate models. I further evaluated the model by inferring the drug condition from the β-coefficients obtained through statistical analysis which correctly identified the drug state of a specific source in over 80 %. Taken together with its biological plausibility, these results indicate the suitability of the CMM model in the particular context of this study.

Bayesian inverse modelling with this canonical microcircuit model at its core and subsequent statistical analysis with a logistic regression revealed a distinct pair of parameters that were significantly changed by GABA. These changes included a decrease in the excitatory connection from population $\epsilon 2$ to $\epsilon 1$. Further, I detected a significant increase in the conductance of the GABA receptor in one of the three excitatory populations although the two remaining excitatory populations were left unchanged. This was somewhat surprising as GABA is a potent neuroinhibitor and no differences in the receptor characteristics were implemented between the three excitatory populations a priori. It can, therefore, be speculated that the model inversion did not pick up the effects of GABA on the whole network. The dual SMAD-inhibition protocol has been shown to mostly

generate a uniform population of excitatory glutamatergic neurons with only a small proportion of inhibitory interneurons [239], owing to the dorsal telencephalic character of their progenitors. Thus, a simpler underlying model with only one excitatory and one inhibitory population might have been better suited to model the stem cell-derived cortical network which, in contrast to a full cortical microcolumn, does not comprise layered connections between different excitatory neuronal subtypes.

I did not observe a correlation between spiking activity and changes in model parameters. This suggests that the analysis of LFP data from MEA recordings can reveal underlying network changes independent of spiking activity. DCM analysis of MEA data offers information focusing on receptor activity which can be complementary to conventional MEA analyses. This is particularly important given that often only low spiking frequencies are achieved in stem cell-derived neuronal cultures which can confound meaningful results in spiking-dependent analyses [195].

Overall, I demonstrated that DCM analysis is suitable to characterise iPSC-derived neuronal networks regarding their synaptic connectivity when applied to LFP data recorded from MEAs but further improvements to the underlying model are needed to ensure a comprehensive analysis. GABA application resulted in increases in the model-based ratio between inhibition and excitation but did not affect all parameterised GABA-specific connections equally.

The effects of astrocytes on neuronal connectivity in the context of TSC were investigated in the second part of this study. In patients with TSC, strong evidence points towards cortical tubers as the epileptogenic source [117]. As cortical tubers are characterised by an increased glia-to-neuron ratio as well as ill-formed and dysfunctional

astrocytes, I aimed to explore the impact that TSC astrocytes exert on neuronal network formation and behaviour. This study was significantly affected by the COVID-19 pandemic and related restrictions on laboratory work and I was, therefore, only able to tackle this question sketchily.

TSC2 +/+ and TSC2 -/- neurons were differentiated and matured in co-culture with human TSC2 +/+ and TSC2 -/- as well as wild-type rat astrocytes. Neuronal spiking and LFP data were recorded regularly on MEAs. Overall, all glio-neuronal co-cultures showed very little neuronal spiking activity up to day 81 when recordings had to be stopped. Only cultures comprising both, TSC2-deficient astrocytes and neurons, displayed a mild increase in activity towards the end of the recording period indicating that these cultures were slightly more active than all their counterparts. Ideally, recordings would have been taken at later time points assuming a gradual increase in neuronal activity in all groups with further maturation. Derived cortical neurons have been shown to form functional AMPA receptor-mediated synapses suggesting they can mature beyond an early NMDA receptor-mediated state *in vitro* [239, 300]. Several studies have shown an increase in neuronal activity with developing maturation [16, 16, 152, 172, 239]. However, differentiated neurons often display more immature passive membrane properties than their *in vivo* counterparts [152, 152, 217, 227, 227]. Neuronal immaturity manifests with low spontaneous firing frequency in early cultures [152] and long-term culturing of up to 20 weeks and beyond is required to achieve firing rates comparable to those seen in *in vivo* cortical neurons [195]. Here, neurons have only matured for slightly more than ten weeks in comparison.

Bayesian analysis revealed a contrary effect of TSC2 -/- astrocytes on neurons depending on the neuronal TSC2 status. In TSC2-sufficient neurons, TSC2 -/- glia caused

an increase in the parameterised inhibition-to-excitation ratio. In contrast, TSC2-deficient neurons reacted with an overall increase in excitation caused by less excitatory stimulation of the inhibitory population. No such changes in the parameterised balance between inhibition and excitation were seen in TSC2 -/- neurons co-cultured with TSC2-sufficient astrocytes. These preliminary results emphasise the important role that astrocytes play in the development of stable and functioning neuronal networks. Further, they suggest that, in the context of TSC, astrocytes play a strong role in pushing developing neuronal networks towards a state of higher excitation.

Model fit was equally adequate between all groups. However, in line with the low neuronal activity seen on the MEA recordings, the original cross-spectrum data resembled mostly a flat line rather than characteristic wave-like spectra. Every result obtained through a generating modelling approach can only be as valid as the original data allows. Thus, results obtained from this study are to be interpreted with caution as it is likely that the neuronal activity was recorded at a state of glio-neuronal immaturity when neuronal networks were still only sparsely formed, if at all. Further work would concentrate on repeating the wet lab experiments allowing more maturation time. Taking the maturation period to later time points would hopefully see a substantial increase in neuronal network activity so that data recorded from these networks is better suited to investigate their synaptic connectivity.

In summary, this study successfully applied a Bayesian computational modelling tool to stem cell-derived neuronal networks to assess their effective connectivity. Further, I used this method to tackle pressing and difficult-to-assess biological questions in the context of TSC. More broadly, having elicited GABA-specific changes in the network phenotype, this method is promising to help characterise novel target compounds and disease-related circuit phenotypes. Outside of this specific TSC-based question asked here, the method could be

immediately applied to many existing MEA datasets that may have been discarded from the conventional spiking analysis because the spontaneous firing was low. Analysis with DCM could also complement high-frequency analysis to conclude on the molecular basis of the underlying network connections. The here demonstrated DCM analysis uses MEA recordings from stable neuronal cultures which can be maintained and matured for long periods of time. In the context of neurodevelopmental diseases such as TSC, this method, therefore, provides a route to help identify pathogenic tipping points from early embryonic to more mature stages of brain circuit development.

6 | Discussion

6.1 Summary of experimental findings

In **chapter 3**, I confirmed that the TSC2 +/+ and TSC2 -/- hES and NSCs harbour their expected TSC2 genotype, namely a functioning TSC2 gene in the TSC2 +/+ cells and a total loss of the TSC2 gene in the TSC2 -/- counterparts leading to a lack of the TSC2 gene product tuberin in TSC2 -/- hES and NSCs. TSC2 deficiency was not sufficient to induce cortical malformation-like characteristics after 80 days of cortical neuronal differentiation. However, TSC-deficient neurons showed immature and glial-like features on the transcriptional level. TSC2 deficiency further caused various changes at the NSC stage including increased NSC production, prolonged NSC maintenance, and larger rosettes. TSC2 knockout further enhanced glial differentiation in a specific astrocyte differentiation protocol.

In **chapter 4**, I examined the effect of glucose deprivation on neuronal differentiation and energy metabolism in TSC2 +/+ and TSC2 -/- neural cells. Glucose deprivation triggered molecular and cellular hallmarks of cortical tubers in TSC2 -/- neuronal cultures after 80 days of cortical differentiation with a significant increase in the glio-neuronal ratio. My results indicate that this was mainly due to impairments at the NSC stage resulting in a decreased production of neurons.

The difference in mTORC1 activation between TSC2 +/+ and TSC2 -/- cells varied with cell type and was highest in hES and lowest in neurons. Activation of mTORC1 was only responsive to glucose deprivation in hES but not in NSCs or in neurons.

TSC2 deficiency and glucose deprivation separately reduced glycolytic and mitochondrial activity in NSCs causing compensatory upregulation in mostly glycolytic genes, however, TSC2 +/+ NSCs also upregulated TCA genes. Combined glucose deprivation and TSC2 deficiency also reduced metabolic activity leading to compensatory upregulation of glycolytic genes, including the gatekeeper genes HK2 and LDHB. Neurons did not upregulate glycolytic or TCA genes in response to glucose deprivation.

In **chapter 5**, I examined the impact of astrocytes on neuronal connectivity in TSC. I first showed that the Bayesian computational modelling tool *Dynamic Causal Modelling* (DCM) is suitable to examine effective connectivity in stem cell-derived neuronal cultures. Then, DCM analysis revealed that TSC2 -/- astrocytes significantly impact neuronal connectivity. They demonstrated opposite effects on TSC2 +/+ and TSC2 -/- neuronal cultures with decreasing overall excitability in TSC2-sufficient but increasing excitability in TSC2-deficient cultures.

6.2 Is TSC2 knockout sufficient to induce cortical malformation?

In my study, TSC2 knockout was insufficient to cause a full cortical malformation-like picture *in vitro*. Although TSC2 deficiency induced transcriptional changes favouring neuronal immaturity and glial cell fate, the translational manifestation of these features was lacking. Previous studies reported recapitulating cortical malformations in hPSC-based models of TSC including increased glio-neuronal ratio [19, 44, 93, 253], dysmorphic neurons [44, 150, 253] and glial-like giant cells [19]. In these studies, neuronal dysmorphology

comprised increased dendritic arborisation and reduced synaptogenesis [19, 44, 150]. It is likely that the TSC2 -/- neurons derived in my study displayed similar characteristics which, however, I could not confirm in targeted microscopy due to limited time and laboratory resources. Most TSC stem cell studies reported a shift in the glio-neuronal balance on the transcriptional level [44, 93, 253] or detected increased glial protein expression at late stages of differentiation only [19, 44]. Giant cells were only detected in one *in vitro* 3D model and have not been observed in 2D stem cell-derived neuronal cultures [19] which further highlights that genetic factors alone are insufficient to trigger cortical malformation.

The TSC1:TSC2 complex and mTORC1 exert specific effects on each neurodevelopmental stage. In pluripotent stem cells, mTORC1 activation initiates differentiation and reduces the pluripotent potential. **In my TSC2-deficient hES**, however, I observed increased pluripotency as indicated by enhanced expression of various pluripotency markers. This is contrary to previous reports that found normal stem cell properties in hPSC with a TSC background [186]. The exact mechanism behind increased pluripotency marker expression in my cultures remains to be elucidated.

In NSCs, mTORC1 is a main orchestrator of the balance between NSC self-renewal and differentiation and is responsible for the organised build-up of an NSC pool with subsequent initiation of neurogenesis, as discussed in the introduction of this thesis. I observed the most prominent effects of the impaired TSC1:TSC2-mTORC1 pathway at the NSC stage, namely occasional hypertrophy, increased proliferation, and abnormal marker expression suggesting prolonged NSC renewal. TSC2 deficiency favoured the build-up of an NSC population that, however, in glucose-loaded conditions continued to be capable of neurogenesis. In a forced conversion neuronal differentiation protocol where an

NSC stage is normally absent, TSC2 -/- cultures produced patches of Pax6-positive cells. Observations on NSC proliferation were somewhat conflicting, with no effect of TSC2 knockout on NSC growth rate in a stable population but increased NSC proliferation during active neurogenesis. Other studies have reported similar conflicting results as some authors found increased NSC proliferation rates in TSC1/TSC2 insufficient NSCs [19, 44, 150, 164, 253] and others did not [304]. Expression of Pax6 was not increased but prolonged in TSC NSCs which suggests that TSC2 deficiency does not affect differentiation into NSCs but ongoing neurogenesis afterwards. Pax6 is an important transcription factor in neurodevelopment as it is involved in neuronal migration, patterning, and circuit formation [50]. Its expression is modulated by mTOR [68] and prolonged Pax6 expression might be a cause for disturbances of neurogenesis from TSC NSCs.

In general, other studies have noted an equally high impact of TSC1/TSC2 knockout and mTORC1 activity on early neurodevelopment. For example, TSC1-haploinsufficient NSCs show mTORC1-independent alterations to proliferation and neurite outgrowth [164]. TSC2-haploinsufficient NSCs are further transiently delayed in neurogenesis but later catch up and produce similarly high neuronal numbers as TSC1/TSC2 sufficient controls [304].

The TSC1:TSC2-mTORC1 pathway impacts **neuronal migration, maturation, and connectivity**. Here, I observed a tendency towards immaturity in TSC2-deficient neurons, highlighted by the upregulation of immature neuronal markers and failed expression of mature neuronal genes. A previous transcriptomics study on TSC2 knockout neuronal cultures similarly found impaired neural differentiation *in vitro* [93]. *In vivo*, cortical tubers comprise dysmorphic neurons featuring high expression levels of early neuronal markers suggesting that TSC causes abnormal maturation *in vivo* as well [48].

Neuronal function is also affected by TSC1/TSC2 insufficiency indicative of reduced neuronal maturation [44, 186, 253]. Here, no investigations on the single cell level into the firing behaviour and synaptic composition have been performed that would reveal whether the observed transcriptional immaturity translates into greater functional immaturity as well.

Lastly, mTORC1 activation favours **glial development** as evident from previous *in vitro* studies [19, 44, 93, 253] and histological examinations on cortical tubers [248]. In line with that, I observed a propensity towards glial cell fate during neuronal differentiation and notably enhanced glial differentiation when differentiating NSCs specifically towards astrocytes. This tendency did not result in cellular consequences as the proportions of glia and neurons were not affected by TSC2 deficiency in cortical differentiation. My investigations indicated a reduced maturity in TSC2-deficient astrocytes, as evident by reduced expression of glutamate synthetase and the glutamate receptor EAAT1. In combination with my observations in neurons, these results suggest that TSC2 knockout hinders maturation in various neural cell types.

Taken together, TSC2-deficient cultures demonstrated disturbances on all levels of neurodevelopment, however, these impairments were not sufficient enough to produce a full cortical malformation-like picture. The observed transcriptional changes did not manifest in changes on the protein or cell fate level which is in line with findings from other stem cell-derived TSC models.

Study	**Cell lines**	**Protocol**	Ref
Costa et al. 2016	hES	2D, cortical neurons	[44]
Grabole et al. 2016	hES	2D, cortical neurons	[93]
Ebrahimi-Fakhari et al 2016	iPSCs	2D, cortical neurons	[64]
Rocktäschel, started in 2016	hES	2D, NSCs, cortical neurons, astrocytes	[221]
Li et al. 2017	iPSCs	2D, cortical neurons, astrocytes	[150]
Marinowic et al 2017	iPSCs	Reprogramming	[162]
Sundberg et al. 2018	iPSCs	2D, Purkinje neurons	[253]
Blair et al. 2018	hES	3D, cortical spheroids	[19]
Zucco et al 2018	iPSCs	2D, NSCs, cortical neurons	[304]
Nadadhur et al. 2019	iPSCs	2D, cortical neurons, oligodendrocytes	[186]
Winden et al., 2019	iPSCs	2D, neurons	[285]
Dooves et al., 2019	iPSCs	2D, neurons, oligodendrocytes	[58]
Martin et al, 2020	iPSCs	2D, NSCs	[164]
Alsaqati et al., 2020	iPSCs	2D, neurons, MEA study	[4]
Hisatsune et al., 2021	iPSCs	2D, neurons	[104]
Catlett et al., 2021	iPSC	2D, neurons	[29]
Dooves et al., 2021	iPSCs	2D, neurons, organoids, astrocytes	[59]
Miller et al., 2022	iPSCs	2D, astrocytes	[175]
Hernandez et al., 2021	iPSCs	3D, organoids	[102]
Eichmüller et al., 2022	iPSCs	3D, organoids	[65]

TABLE 6.1: **Stem cell studies on TSC.** Overview of the starting cell lines as well as the differentiation outcome of stem cell studies on TSC.

Since I started my project, several groups differentiated genetically engineered hES or patient-derived iPSCs with a TSC background into 2D neuronal cultures to study the effect of TSC1/TSC2 deficiency on neural development and neuronal function. At the

beginning of my project, we were only aware of three other studies published on stem cell models of TSC. By the end of it, the number of publications increased to 20 (see table 6.1) with a significant number of reviews published on the subject as well [2, 18, 190, 252]. This confirms the importance of stem cell models for research into neurodevelopmental diseases such as TSC.

These studies confirmed mTORC1 hyperactivation in TSC1/TSC2 deficient cells in a gene dose-dependent manner [18]. They also provided evidence that alterations in TSC1/TSC2 impact mostly on the second part of neuronal development, namely on neurogenic processes after the NSC stage, whereas the early development of NSCs was mostly unaffected [18]. Cellular features of TSC1/TSC2 mutations manifest in a gene dose-dependent manner, too. In general, differentiated TSC2 -/- NSCs and neurons were characterised by increased cell size [44, 150, 253] and enhanced dendritic arborisation [44, 253] together with increased NSC proliferation [150, 253], features that were less apparent in TSC2 +/- cells [19, 44]. Most studies worked on cortical excitatory neurons, likely because these differentiation protocols are well-established and TSC affects cortical development. As patients with TSC develop cerebellar tubers as well, Sundberg and colleagues derived cerebellar Purkinje cells from TSC iPSCs that presented with many of the neuronal phenotypes found in their cerebral counterparts [253]. The activity of single neurons and neuronal networks was differently affected by TSC1/TSC2 deficiency. Single neurons presented with overall decreased spontaneous firing and intrinsic excitability [44, 253] whereas TSC neuronal networks demonstrated increased network activity [186]. Blair and colleagues presented a 3D model derived from TSC2+/- and TSC2 -/- hES and their findings mirrored results seen in 2D studies with TSC2 -/- cells showing greater tendencies towards glial cell fate, larger cell sizes, and mTORC1 hyperactivation [19]. Several studies have now also attempted to differentiate glial cells including oligodendrocytes [58, 186] and astrocytes [59, 150, 175].

Such studies have shown that TSC astrocytes behave less mature with decreased glutamate uptake [175] which is in line with my transcriptomical analyses.

6.3 Does glucose deprivation drive neuronal differentiation towards cortical malformation in TSC?

Glucose is one of the main providers of energy for cells in the brain [299]. As discussed in the introduction to chapter 4, TSC2-deficient cultures are dependent on glucose for their energy supply. As metabolic activity, particularly energy metabolism, and neurodevelopment are tightly linked on the cellular level, I wanted to explore whether glucose deprivation could trigger disturbed corticogenesis in TSC2 -/- cultures. TSC2-deficient cells have previously been examined towards their increased vulnerability to glucose deprivation but, to my knowledge, no distinct investigations on neural differentiation in glucose-limited conditions against a TSC background have been undertaken. Based on the tight interaction of metabolism and neurodevelopment, I hypothesised that not only cell survival but also neural cell fate choices of TSC2-deficient cultures are affected by extracellular glucose supply.

TSC2-deficient cultures subjected to glucose deprivation during neuronal differentiation developed into dysmorphic cultures characterised by low neuronal and high glial cellular features, ill-morphed cellular networks with few axonal connections, few post-mitotic neurons, and non-uniform cells of various sizes and shapes. As I did not perform detailed microscopic examinations of these cultures, I could not determine the exact cellular character of the derived cells. A *full* cortical malformation-like picture would have required the derivation of giant balloon cells, dysmorphic neurons, a high glio-neuronal ratio, and disturbed cortical lamination. I detected dysmorphic TUJ-1-positive neurons and a high glio-neuronal cellular ratio in glucose-deprived TSC2 -/- cultures. The derived

cultures further harboured multiple large, flat, and glial-shaped cells which stained positive for TUJ-1 suggesting the existence of giant balloon cells in my cultures as well. Cortical dyslamination is difficult to model in a 2D neuronal system but could be inferred from transcriptional data. However, such experiments were not performed due to time constraints.

My results suggest that the timing of glucose deprivation during neurodevelopment is crucial to either allow normal neuronal differentiation or induce malformed development. Preliminary experiments indicate that glucose deprivation during the induction of neurogenesis is sufficient to disturb neuronal differentiation in TSC2 knockout. Throughout my project, I have observed that NSCs involved in neurogenesis seem particularly vulnerable to TSC2 deficiency as well as to glucose deprivation, and especially to the combination of the two conditions. Other studies have demonstrated a similar vulnerability of NSCs to TSC1/TSC2 insufficiency as outlined in previous chapters. Activation of mTORC1 follows a specific pattern during neurodevelopment, even in TSC2 knockout cultures, with its highest activity in NSCs and relatively low mTORC1 activation in neurons. Further, pluripotent TSC2 -/- hES cells maintained their ability to appropriately lower mTORC1 activation in low glucose supply. In contrast, TSC2 -/- NSCs lacked such a metabolic response to glucose deprivation, leading to high mTORC1 activity even in sparse supply conditions. Wild-type NSCs, also, were unresponsive to glucose deprivation with regards to mTORC1 activity but their starting mTORC1 activation levels were considerably lower. The mismatch between the metabolic state and supply could explain the vulnerability of TSC2 knockout NSCs to glucose deprivation.

Neuronal vulnerability, on the other hand, did not appear to be exaggerated by glucose deprivation. During dual SMAD-inhibition differentiation, TSC2 knockout correlated

with increased neuronal vulnerability, independent of glucose supply. The NGN2 protocol produced very fragile neurons irrespective of TSC2 status as seen in the cell death assay (up to 50 % of cell death) and in the detected drop in cell numbers between day 10 and day 21. Differences in neuronal vulnerability depending on TSC2 status or glucose supply might have been masked by the inherently high cellular death in NGN2 neurons. NGN2 neurons are usually co-cultured with rat astrocytes to enhance cell viability and enable long-term culturing as NGN2 neurons maintained without glial support only survive a few weeks [138]. I consciously avoided glial co-culturing as I was interested in the effect of TSC2 deficiency on glio-neuronal differentiation tendencies and co-culturing with rat astrocytes could have confounded my results.

Interestingly, glucose deprivation reduced the efficiency of rapamycin in NSCs. Rapamycin is an antibiotic agent derived from *Streptomyces hygroscopicus* that blocks mTORC1 activity after forming a complex with the intracellular protein FKBP12 [147]. Rapamycin and related agents (*rapalogs*) further destabilise the interaction of mTOR with Raptor in the mTOR complex 1 [13]. The efficiency of rapamycin differs between *in vivo* and *in vitro* settings indicating that the extra-cellular environment interacts with rapamycin's mechanism of action [13]. However, how exactly rapalogs inhibit mTORC1 activity and how their mechanism-of-action might be influenced by extracellular conditions remains unclear.

Taken together, glucose deprivation in TSC2 deficiency led to disturbances in glio-neuronal cellular proportions, dysmorphic neurons and neuronal networks as well as likely giant balloon cells and can, thus, be considered an initiator of cortical malformation-like patterns in a TSC *in vitro* model system.

6.4 Is there a link between energy metabolism and cortical malformation in glucose-deprived TSC2-insufficient neuronal cultures?

I was unable to answer this question sufficiently as I could not perform crucial experiments due to constraints on laboratory opening by the COVID-19 pandemic and related restrictions. However, my results, taken together with previous studies, suggest that energy metabolism and disturbed neurodevelopment are causally connected in glucose-deprived TSC2 -/- neuronal cultures.

Neurons, irrespective of TSC2 genotype, increased glycolytic as well as mitochondrial activity as a response to glucose deprivation. This suggests that they do not run these pathways at full capacity in high glucose conditions leaving them with a reserve capacity to be recruited in deprivation. TSC2-deficient neurons notably increased mitochondrial activity as a reaction to low glucose supply. Previously, TSC2-insufficient neurons demonstrated disturbances in mitochondrial dynamics and function comprising a redistribution of mitochondria from neurites to the cell soma, a 2.5-times increase of mitochondrial mass and transcriptional changes in mitochondrial respiration genes [64]. Thus, mitochondrial metabolism seems to be highly affected by TSC2 deficiency in neurons although the exact mechanisms as well as physiological implications remain to be elucidated.

However, the largest changes in gene transcription and metabolic activity in response to TSC2 knockout and glucose deprivation were noticed **on the NSC** and not on the neuronal level. This highlights, once again, the importance of the NSC stage for the appropriate development of neuronal cultures against the background of TSC. When TSC2 -/- NSCs are challenged with low glucose supply, their energy metabolic activity is reduced and critical glycolytic genes are upregulated, a process which I interpret to

be compensatory. A similar phenomenon occurred in glucose-deprived wild-type NSCs, however, both groups differed in their expression levels of two critical gene groups: (i) the glycolysis gatekeepers HK2 and LDHB and (ii) genes of the Krebs cycle. The inability of TSC2-deficient NSCs to upregulate Krebs cycle genes suggests that TSC2 knockout prevents a shift from aerobic glycolysis to mitochondrial respiration, a mechanism that is important for neurogenesis. Previous studies have highlighted that TSC2 KO cells do not adjust their metabolic activity to low glucose levels and are running on aerobic glycolysis leading to pathological glucose addiction [35]. The inability to cover their energy demand through glycolysis due to a lack of glucose could drive the compensatory upregulation of HK2 and LDHB. Under sufficient supply, HK2 increases glycolytic rates whereas LDHB feeds pyruvate back into mitochondrial metabolism. Both attempts to enhance ATP production are ill-fated in glucose-deprived TSC2-deficient NSC as they lack glucose to drive glycolysis and are unable to upregulate mitochondrial genes sufficiently. This is reflected in the marked decrease in both, glycolytic and mitochondrial metabolism, detected in glucose-deprived TSC2-deficient NSCs. Subsequently, the upregulation of HK2 and LDHB likely causes a string of intracellular changes in these NSCs as both enzymes serve important non-metabolic regulatory functions as well. Both enzymes work in tandem with regard to apoptosis and autophagy, important mechanisms to control cellular and tissue homeostasis. HK2 increases the cellular ability to evade apoptosis and increase proliferation [170]. LDHB inhibition causes increased apoptotic activity and LDHB upregulation could counteract apoptotic tendencies in damaged cells undergoing cancerous transformations [270]. Both, HK2 and LDHB, are regulated by mTORC1 and promote autophagy, for example through negative-feedback mTORC1 inhibition. Dysregulated autophagy supports increased survival in cancer cells as it serves as a protection mechanism against cellular damage [270]. The compensatory upregulation of HK2

and LDHB could, thus, incidentally contribute to increased survival and proliferation of TSC2-deficient NSCs in glucose-deprived conditions and in turn, decrease their neurogenic potential.

It is interesting to note that, although TSC2-deficient NSCs do not respond to glucose deprivation with a general upregulation in TCA genes, they demonstrated a notable upregulation of isocitrate dehydrogenase (IDH), irrespective of glucose supply. IDH transforms isocitrate into α-ketoglutarate (α-KG), a TCA metabolite that has been associated with increased pluripotency levels and stemness [166]. I did not measure α-KG levels in my cellular systems but this could be the next step to investigate the effect of upregulated IDH on neurodevelopment in TSC2 deficiency. This is another example of how the state of cellular metabolic pathways could contribute to cell fate decisions in TSC2-deficient NSCs.

6.5 Do astrocytes disturb neuronal connectivity in the context of TSC?

To answer this question, I applied a Bayesian modelling tool to MEA recordings from TSC glio-neuronal co-cultures. Dynamic causal modelling allows inferences on the synaptic landscape underlying effective connectivity in neuronal populations. My DCM analysis was based on a canonical microcircuit model reflecting the cortical nature of the hES-derived TSC neuronal cultures. TSC2 +/+ and TSC2 -/- neurons were matured under presence of different glial populations including TSC2 +/+ and TSC2 -/- astrocytes as well as rat astrocytes.

The experiment relied on the generation of valid MEA LFP recordings from the TSC glio-neuronal co-cultures as every analysis can only be as valid as the initial data allows. Unfor-

tunately, I was unable to mature the neuronal cultures for a long enough period resulting in an insufficient level of spontaneous activity at the time of the final recording. However, analysis of conventional neuronal activity parameters demonstrated a trend of increased spontaneous firing in TSC2-deficient neurons when co-cultured with TSC2-deficient astrocytes. TSC2-insufficient neurons have previously been found to be less excitable and less spontaneously firing than their wild-type counterparts [44, 253]. However, TSC1/TSC2-insufficient neurons were also observed to form networks characterised by increased network activity [186] and the mechanism underlying these somewhat contradicting findings has not been fully elucidated.

My DCM analysis offers an explanation for this phenomenon. When co-cultured with TSC2 -/- astrocytes, TSC2-deficient excitatory neuronal populations saw a decrease in their stimulating effect on the inhibitory interneuron population which, in turn, could raise the excitatory state of the whole network. No increase in the network excitation state was seen for TSC2 -/- neurons co-cultured with wild-type astrocytes highlighting that TSC2 has an important role in astrocyte function as well. The maturation of TSC2 -/- hES-derived astrocytes was delayed and low gene expression levels of key glial proteins (as shown in chapter 3) could cause a reduction in their ability to provide a satisfactory extracellular environment for developing neurons. This is in line with previous *in vitro* and *in vivo* studies on TSC astrocytes providing evidence for altered glial potassium currents [118] and glial gap junction functioning [291]. Immature glutamate channels and glial gap junctions might hamper glial clearance of the synaptic space which could lead to disturbances in synaptogenesis and circuit formation. TSC2 -/- astrocytes had a contradictory effect in TSC2-sufficient neurons increasing the connection strength from the inhibitory to the excitatory populations. This highlights the close interaction of astrocytes and neurons during neurodevelopment and indicates that neurons respond differently to the extracellu-

lar environment provided by the supporting astrocytes depending on the neuronal TSC2 status. Next experimental steps should include patch-clamp experiments to determine electrophysiological features of TSC2 +/+ and TSC2 -/- neurons co-cultured with astrocytes of different TSC2 backgrounds as well as investigations on the extracellular media to examine the glial clearance of glutamate and potassium, for example.

In summary, my results suggest that TSC2-deficient astrocytes play a prominent role in driving disturbances of neuronal connectivity in TSC. Glial maturation was delayed in TSC2 -/- astrocytes, likely decreasing their ability to provide a neuro-supportive extracellular environment during circuit formation. TSC2 +/+ and TSC2 -/- neuronal networks reacted differently to these challenges resulting in less inhibition in TSC2 -/- neuronal networks. However, my experimental findings and the subsequent computational analysis are only preliminary and follow-up experiments are crucial to elucidate the exact mechanisms underlying glia-induced neuronal network excitability in TSC.

6.6 Limitations and outlook

I discussed various limitations of my project in previous chapters. In general, the main limitations I faced included

1. only one set of TSC2 -/- and isogenic control hES lines available
2. small numbers of replicates for various experiments
3. interruption of long-term differentiations by COVID-19-related laboratory closure and the resulting mix of different neuronal differentiation protocols for some experiments.

In chapter 3, I discussed my unsuccessful attempts to generate additional TSC2 hPSC lines. The reliance on a single set of mutated and control cell lines limits the interpretabil-

ity of my results. Phenotypic variability in stem cells and derived cellular systems can be significant, even between lines of the same genotype and even between individual experiments carried out on the same line [83, 275]. The variability is likely to be multi-factorial, for example, due to differences in batches of media and growth factors or differences in lab-internal procedures [278]. As a consequence, phenotypic differences detected in different genotypic lines need to be interpreted with caution and require careful analysis as to how much of the difference can confidently be explained by the genotype and how much is likely to be biological noise. This signal-to-noise ratio would be easier to overcome when increasing the number of individual lines per genotype which, unfortunately, was not possible for my project.

Due to limited laboratory resources and significant interruptions to experimental work during the COVID-19 pandemic, I was often only able to perform my experiments in a few replicates. More replicates per specific experiment are needed to reduce the signal-to-noise ratio and increase the confidence of my statistical analysis.

COVID-19-related laboratory closures hit my project in the early Summer of 2020, three years after starting my DPhil, and after I had carried out optimisation work and just started the crucial result-producing period of my project. The interruption meant that many of my long-term differentiations got lost and I had to perform the experiments using the NGN2 protocol although the dual SMAD inhibition protocol due to the close resemblance to human neurodevelopment, would have been more suitable.

My project further faced limitations and challenges related to specific experiments. For example, mTORC1 activity was only measured using the pS6/S6 ratio. However, mTORC1 activity can also be determined by 4E-BP phosphorylation. Previous studies have highlighted discrepancies between both mTORC1 activity measures so it is possible

that I missed specific patterns of mTORC1 activity by only focusing on its effect on S6. My western blots were generally of lower quality. Western blot equipment and pathways were introduced by myself and DPhil colleagues at the start of my project as they had not been established in the lab prior. Optimisation of western blotting techniques including adaptations to laboratory-specific facilities took time and resources. Again, due to the COVID-19 pandemic, I often had to use preliminary data produced during this optimisation period as I was unable to repeat them after the optimisation period was completed.

6.7 Conclusions

The aetiology of cortical tubers has mostly been investigated on the genetic and molecular level examining the impact that TSC1/TSC2 mutations and mTORC1 activity exerts on neurodevelopment. In contrast, I embedded the molecular biology of TSC in an environmental context acknowledging that molecular abnormalities alone likely do not represent the full picture. Some studies have concentrated on the interplay between different neural cell types in TSC, mostly focusing on neuronal-glial interactions. To my knowledge, my study is unique in investigating the interaction between genetics, different cell populations, and the extracellular environment in the pathogenesis of TSC.

My DPhil project demonstrated the role of cellular and non-cellular environmental modifiers in the genesis of cortical malformations in TSC. I showed that TSC-deficient NSCs harbour increased glial differentiation tendencies but that these transcriptional cell fate changes do not manifest in translational phenotypes without additional environmental triggers. Glucose deprivation was able to tip neurodevelopment in TSC cultures into a malformed state resembling features of cortical tubers *in vitro*. Further, TSC2-deficient astrocytes drove TSC2-deficient neuronal circuits into a more excitable state highlighting

the relevance of the glial-neuronal partnership for the development of disturbed neuronal network function and epileptogenesis.

Moreover, I presented the combination of stem cell-derived neuronal cultures with advanced computational modelling as a new tool to investigate the molecular landscape underlying neuronal connectivity *in vitro*. To my knowledge, my study is the first time DCM was applied to electrophysiological recordings from *in vitro* neuronal networks. I demonstrated the suitability of DCM analysis on MEA recordings and further, highlighted the potential of such analysis to detect disease-underlying mechanisms. In a specific TSC context, DCM analysis offered an explanation for the previously observed phenomenon that single TSC neurons show decreased excitation but TSC neuronal networks feature increased excitability.

Tuberous sclerosis is considered a rare neurodevelopmental disorder but TSC affects approx. 2 Million individuals worldwide [49], often with significant implications for the individual themselves as well as for family members and carers [96]. Moreover, TSC is often studied as an exemplar pathology representing either mTOR pathologies or the diverse group of cortical malformations [303]. Studying TSC can help widen our understanding of various aspects of neurodevelopment, the impact of mTOR-dependent and mTOR-independent effects of TSC1/TSC2 insufficiency on cortical development as well as the role that astrocytes play in the manifestation of neurological phenotypes. Stem cell-derived model systems promise access to developing human brain tissue and are thus particularly suited for the study of early neurodevelopmental stages and diseases thereof. Improvements in scientific models with the overall aim to increase their clinical relevance and experimental ease as well as advances to our understanding of disease mechanisms eventually benefit the development of new therapeutic options for patients who are at the heart of all our scientific efforts.

A | Stem cell models in TSC

Study	hPSC		NPC				Ref
	Size	mTORC1	Proliferation	Size	mTORC1	Marker	
Costa et al. 2016	↔	↑ in $TSC2^{-/-}$ ↔ in $TSC2^{+/-}$	↑ in $TSC2^{-/-}$ ↔ in $TSC2^{+/-}$	↔	↑ in $TSC2^{-/-}$ ↔ in $TSC2^{+/-}$	–	[44]
Grabole et al. 2016	–	–	–	–	↑ in $TSC2^{-/-}$	–	[93]
Ebrahimi-Fakhari et al. 2016	–	–	–	–	–	–	[64]
Li et al. 2017	↔	↑ in TSC line	↑ in TSC line	–	↑ in TSC line	↑ Pax6 in TSC line	[150]
Marinowic et al 2017	–	–	–	–	–	–	[162]
Sundberg et al. 2018	–	–	↑ in TSC lines and $TSC2^{-/-}$	–	↔ in TSC lines, ↑ in $TSC2^{-/-}$	–	[253]
Blair et al. 2018	↔	↑ in $TSC2^{-/-}$, $TSC1^{-/-}$ ↔ in $TSC2^{+/-}$, $TSC1^{+/-}$	↑ in $TSC2^{-/-}$ ↔ in $TSC2^{+/-}$, $TSC1^{+/-}$	↑ in $TSC2^{-/-}$ ↔ in $TSC2^{+/-}$, $TSC1^{+/-}$	↑ in $TSC2^{-/-}$ ↔ in $TSC2^{+/-}$, $TSC1^{+/-}$	↑ Pax6 in $TSC2^{-/-}$ ↔ Pax6 in $TSC2^{+/-}$, $TSC1^{+/-}$	[19]
Zucco et al. 2018	–	–	↔	–	↑ moderate	–	[304]
Nadadhur et al. 2019	–	–	–	–	–	–	[186]
Martin et al. 2020	–	–	↑ in $TSC2^{-/-}$ ↑ in $TSC2^{+/-}$	↑ in $TSC2^{-/-}$ ↑ in $TSC2^{+/-}$	↑ in $TSC2^{-/-}$ ↑ in $TSC2^{+/-}$	–	[164]

TABLE A.1: **Stem cell models of TSC; stem cell stage.** Overview of hPSC and NSC features detected in previous stem cell studies on TSC (–, no information given).

Study	Neurons			Glia			Glio-neuronal ratio
	Size	mTORC1	Function	Size	mTORC1	Biology	
[44]	↑ in $TSC2^{-/-}$ ↔ in $TSC2^{+/-}$	↑↑ in $TSC2^{-/-}$ ↑ in $TSC2^{+/-}$	In $TSC2^{-/-}$: Hypoexcitability, ↓ Synapse maturation, ↑ Dendritic arborisation, ↑ NSC markers				In $TSC2^{-/-}$: ↓ neurons & ↑ glia In $TSC2^{+/-}$: ↔
[93]	–	–	↓ Maturation	–	–	↓ Maturation	↓ neuronal markers, ↑ glial markers
[64]	–	↑	–	–	–	–	–
[150]	↑	↑	↑ Neuritic arborisation	↔	↑	↑ Proliferation	–
[162]	–	–	–	–	–	–	–
[253]	↑	↑ in het lines and $TSC2^{-/-}$	↑ Dendritic number, Hypoexcitability, ↓ synaptogenesis	–	–	–	↓ Neuronal markers ↑ Glial markers
[19]	↑ in $TSC1^{-/-}$ & $TSC2^{-/-}$, ↔ in $TSC1^{+/-}$ & $TSC2^{+/-}$	↑ in $TSC2^{-/-}$	–	–	↑ in $TSC2^{-/-}$	–	In homozygous lines: ↑ glia, ↓ neurons In heterozygous lines: ↔
[304]	↔	–	–	–	–	–	–
[186]	↑ in TSC neurons co-cultured with TSC OL ↔ in TSC neurons co-cultured with ctrl OL		In TSC neurons co-cultured with TSC OL: ↑ Spontaneous firing ↑ Dendritic branching	–	–	In TSC OL co-cultured with TSC neurons: ↓ Maturation	–
[164]	–	–	–	–	–	–	–

TABLE A.2: **Stem cell models of TSC; glial/neuronal stage.** Overview of glial and neuronal features detected in previous stem cell studies on TSC (–, no information given).

B | Cell culture materials

Name	Storage	Supplier	Supplier Ref
B27	-20 °C	Invitrogen	17504044
B27 without vitamin A	-20 °C	Invitrogen	12587010
N2	-20 °C	Invitrogen	17502048
β-mercaptoethanol	4 °C	Invitrogen	31350010
L-glutamine	RT	Thermo Fisher	25030024
GlutaMAX	RT	Thermo Fisher	35050061
Insulin	4 °C	Sigma	I9278
Sodium pyruvate	4 °C	Sigma	8636
MEM non-essential amino acids	4 °C	Thermo Fisher	11140050
Penicillin-streptomycin	4 °C	Thermo Fisher	15140122
Glucose	4 °C	Thermo Fisher	A2494001
Dorsomorphin	-20 °C	Tocris	3093
SB431542	-20 °C	Tocris	1614
FGF-2	-80 °C	Peprotech	AF-100-18B
EGF	-80 °C	R&D Systems	236-EG-01M)
BDNF	-80 °C	Peprotech	AF-450-02
Rock Inhibitor	-20 °C	Abcam	ab120129
DMSO	RT	Sigma	D2650

TABLE B.1: **Growth factors, small molecules and media supplements**

Name	Stock Storage Temp	Supplier	Supplier Ref
Matrigel	-80 °C	Scientific Laboratory Supplies	354277
KnockOut-DMEM	4 °C	Thermo Fisher	10829018
Laminin	-20 °C	Sigma	L2020
Poly-L-ornithine	4 °C	Sigma	P4957

TABLE B.2: **Coating materials**

Name	Stock Storage Temp	Supplier	Supplier Ref
EDTA	RT	Thermo Fisher	15575020
Accutase	-20 °C	StemCell Technologies	7920
Trypsin	RT	ThermoFisher	25300054
Dispase	-80 °C		
Trypan Blue 0.4 %	RT	ThermoFisher	15250-061

TABLE B.3: **Detachment agents**

Name	Function	Storage	Supplier	Supplier Item
Rapamycin	mTORC1 inhibitor	-20 °C	Tocris	1292
MHY1458	mTORC1 activator	-20 °C		
GABA	Inhibitory neurotransmitter			
Doxycycline	Antibiotic	-20 °C	Tocris	4090
Puromycin	Antibiotic, bacterial selection	-20 °C	InvivoGEN	ant-pr-1

TABLE B.4: **Drugs**

Name	Supplier	Supplier Ref
DNAse/RNAse-free water	Invitrogen	46-2224
RNase-free DNAse	Qiagen	79254
NuPAGE Novex 4-12 % Bis-Tris Protein Gels 1.0 mm	Thermo Fisher Scientific	NP0322BOX
Loading dye	ThermoFisher	NP0007
NuPAGE Sample Reducing Agent (10X)	Thermo Fisher Scientific	NP0004
SeeBlue Plus2 Pre-stained Protein Standard	Invitrogen	LC5925
Bovine serum albumin (BSA)	Sigma	H4522
TBS	Biorad	706435
Tween20	Sigma	P1379
NuPAGE™ MOPS SDS Running Buffer (20X)	Thermo Fisher	NP0001
NuPAGE™ MES SDS Running Buffer (20X)	Thermo Fisher	NP000202
Trans-Blot Turbo Midi 0.2 μm Nitrocellulose Transfer Packs	BioRad	1704159
Pierce ECL Western Blotting Substrate Kit	Thermo Scientific	32106
Blot Restore Kit	Millipore	2520)
4 % ParaFormAldehyde (PFA)	Alfa Aesar	J61899
Blot Restore Membrane Rejuvination Kit, 10x	Merck	2520

TABLE B.5: **Other molecular biology agents**

C | Antibodies

Antigen	Target cell type	Technique & Conc	Host species	Supplier
GFAP	Astrocytes, RGC	1:2000 (I,F)	Chicken	BioLegend
GFAP	Astrocytes, RGC	1:100 (F)	Mouse	Abcam
Nestin	NSCs	1:100 (F)	Mouse	BioLegend
Nestin	NSCs	1:1000 (I)	Mouse	Abcam
TUJ1	Neurons	1:200 (F)	Mouse	BioLegend
TUJ1	Neurons	1:1000 (I)	Mouse	Abcam
Huc/HuD	Neurons	1:400 (F)	Mouse	Life Technologies
S100β	Astrocytes	1:400 (F), 1:1000 (I)	Rabbit	DAKO
Tbr2, Enomer	IPC	1:200 (I)	Rabbit	Abcam
Ki67	Cycling cells	1:400 (F, I)	Rabbit	Cell Signaling
Pax6	NSCs	1:1000 (I)	Rabbit	R&D Systems
MAP-2	Neurons	1:1000 (I)	Mouse	BioLegend
TSC2	hES, NSCs	1:1000 (W)	Rabbit	Cell Signaling
S6	hES, NSCs	1:1000 (W)	Rabbit	Cell Signaling
pS6	hES, NSCs	1:8000 (W)	Rabbit	Cell Signaling

TABLE C.1: **Primary antibodies.** Techniques: W, western blotting; F, flowcytometry; I, immunostainings

Target species	Host species	Fluorophore	Supplier	Supplier Ref
Mouse	Rabbit	ECL	abcam	ab6728
Rabbit	Goat	ECL	abcam	ab6721
Chicken	Goat	488	Thermo Fisher	A11039
Chicken	Goat	647	Thermo Fisher	A21449
Rabbit	Goat	647	Thermo Fisher	A21244
Rabbit	Goat	488	Thermo Fisher	A11008
Rabbit	Goat	594	Thermo Fisher	A11012
Mouse	Goat	488	Thermo Fisher	A11011
Mouse	Goat	594	Thermo Fisher	A11005
Mouse	Goat	647	Thermo Fisher	A11001
Rat	Goat	594	Thermo Fisher	A11007
Rat	Goat	488	Thermo Fisher	A11006

TABLE C.2: **Secondary antibodies**

D | Primer sequences

Gene	Forward Primer	Reverse Primer
House keeping genes		
HPRT	TTGTTGTAGGATATGCCCTTGA	GCGATGTCAATAGGACTCCAG
ACTIN	GACCCAGATCATGTTTGAGACCT	GAGGCGTACAGGGATAGCAC
TSC2 KO Confirmation		
TSC2 Exon 11	GAGGCTGGACCTGGGAGAGG	TCATCGGGCATCCTGAGACC
Neomycin Casette	AATGGGCTGACCGCTTCCTC	TGTTCAATGGCCGATCCCAT
Cell type marker		
TUJ1	TCCAGGAGCTGTTCAAGCG	TCGGACACCAGGTCGTTC
Tbr2	AGCCGACAATAACATGCAGGG	TCCTGTCTCATCCAGTGGGA
Ctib2	TCCAGAGCAATCTCATCGTG	GCATGTGCGTCTTCATGTG
Brn2	TGTATGGCAACGTGTTCTCG	CCTCCTCCAACCACTTGTTC
NF1A	TAATCCAGGGCTCTGTGTCC	CCTGCAGCTATTGGTGTCTG
GFAP	AGAGATCCGCACGCAGTATG	TCTGCAAACTTGGAGCGGTA
Glial glutamate transporters		
EAAT1	AGGCAGTAGCAGCTGTGTTT	TGCACAGAATGCTTGGGGTC
EAAT2	GAGGATGGGGGTGACCTAGT	GATGACTGTCGTGCATTCGC

Metabolic pathways		
Gene	**Forward Primer**	**Reverse Primer**
ACO2	AATGGATGTACTCGTTGGGC	ACAGCCTACTGGTGACTCGG
GAPDH	TGTTGCCATCAATGACCCCTT	CTCCACGACGTACTCAGCG
IDH2	AACCGTGACCAGACTGATGAC	ATGGTGGCACACTTGACAGC
PGAM1	TCGCTCTCTTCTGCACTGAG	ACCTGGAGAACCGCTTCAG
PGC1a	CTGCTAGCAAGTTTGCCTCA	AGTGGTGCAGTGACCAATCA
PGK1	AGCAGAATTTGATGCTTGGG	TCTAACAAGCTGACGCTGGA
PKM	TCACTATGGGGCTTCGACAT	ATAACCTTGAGGCTGAGGCA
HK2	AAGCCCTTTCTCCATCTCCT	CTTCTTCACGGAGCTCAACC
LDHA	GCCAGAGACAATCTTTGGTG	GGCCTGTGCCATCAGTATCT
ATP5A1	AAGACACGCCCAGTTTCTTC	TTTGGGTTCATCTTTCATTGC
ATP5B	CAAGTCATCAGCAGGCACAT	GTGGGCTATCAGCCTACCCT
ATP5E	CTTCAGTGCATCTCTCACTGC	TACAGCATGGTGGCCTACTG
CS	GGGCTGCAAGAACAAGACA	CTCCCTTTCTTACCTCCCCA
COX5B	AGTCGCCTGCTCTTCATCAG	TGGCTTCAAGGTTACTTCGC
CYC1	GGTCACTGGCACTCACAGC	CCGCTACGGACACCTCAG
Enolase1	GCCTCCTGCTCAAAGTCAAC	AACGATGAGACACCATGACG
FH	CCTCATCTGCTGCCTTCATT	GGAGGTGTGACAGAACGCAT
NDUFA1	TTCTAGCAGGGGTAGATGGC	GAGATAGGCGCATCTCTGGA
NRF1	CCACGTTACAGGGAGGTGAG	TGTAGCTCCCTGCTGCATCT
OGDH	TTGGCTGGAAAACCCCAAAAG	TGTGCTTCTACCAGGGACTGT
SDHA	CGAACGTCTTCAGGTGCTTT	AAGAACATCGGAACTGCGAC
Sucla2	TTGCTTCAGGAGACTCAGCA	TTGCTTCAGGAGACTCAGCA
TPI1	ATGGCTGAAGTCCAACGTCT	AAGGAAGCCATCCACATCAG
HK1	CTGCTGGTGAAAATCCGTAGTGG	GTCCAAGAAGTCAGAGATGCAGG
LDHB	GGACAAGTTGGTATGGCGTGTG	AAGCTCCCATGCTGCAGATCCA
G6PD	CTGTTCCGTGAGGACCAGATCT	TGAAGGTGAGGATAACGCAGGC
Glut1	TTGCAGGCTTCTCCAACTGGAC	CAGAACCAGGAGCACAGTGAAG

NMDA and AMPA receptor subunits		
Gene	**Forward Primer**	**Reverse Primer**
GluN1	CCCCTGCGACCCTTACTTTT	GGATGGTACTGCTGCAGGTT
GluN2A	GGCCACTGCTGAGAACTATGT	AGGTAGACGTCGGATCCTTGT
GluN2B	CTCACCCCCTTTCCGCTTT	AAGGCATCCAGTTTCCCTGTT
GluN2C	ACTTCACAGCCCGAGTGACC	CCCTGAGCTGCTAAACACCA
GluN2D	CCCCAACAGAACAGGGTCAT	AGGTGGAGCCCTTCTCCTTG
GRIA1	GGGTCTGCCCTGAGAAATCC	AGCGCTTGTCTTGTCCTTGG
GRIA2	AACTCAGTGAGCAAGGCGTC	GGACTCACGTAAGGGACAGC
GRIA3	GGCTCAGCATTAGGAACGCC	TTGTCGCGAGTCTCAGAGTG
GRIA4	TAGTGGTGGGCCATAGTGGA	TTGCTGACGGGAATAGCTGG

E | Area bins

Area bins (in μ2) for used for grouped cell size histograms in figure 3.2

hES: 1, -Inf-148; 2, 149-241; 3, 242-333; 4, 334-426; 5, 427-518; 6, 519-611; 7, 612-703; 8, 704-796; 9, 797-888; 10, 889-981

NSC: 1, -Inf-2677; 2, 2678-4871; 3, 4872-7065; 4, 7066-9260; 5, 9261-11454; 6, 11455-13649; 7, 13650-15843; 8, 15844-18038; 9, 18039-20232; 10, 20233-22427

F | Seahorse Background

Seahorse Real-Time Cell Metabolic Analysis from Agilent offers a way to interrogate glycolytic activity and mitochondrial respiration in cell cultures. The Seahorse analyser directly measures two different metrics, the cellular oxygen consumption rate (OCR) and the extracellular acidification rate (ECAR). These measurements are then used to calculate the proton efflux rate (PER) which depends on glycolytic and mitochondrial acidification to varying degrees in each cellular system. The assay design, however, allows us to calculate the proportion of glycolysis contributing to PER, glycoPER, and thus provides an accurate and dynamic way of measuring glycolytic activity in live cells over time.

I measured the dynamics of ECAR, OCR and PER in all samples at baseline and after subsequent application of the mitochondrial blocker rotenone as well as the glycolysis inhibitor 2-DG. The percentage of the proton efflux rate directly caused by glycolysis (glycoPER) served as a further measure of glycolytic rate.

Seahorse analysers measure OCR and ECAR in a microplate by the transient creation of a microchamber containing only 2 μL of media above the cellular monolayer. Due to the small volume, changes in media oxygen and proton content induced by cellular metabolism are rapidly detected by solid-state sensor probes placed just 200 μm above the cells. After each measurement, the media in the transient microchamber is allowed to mix with the remaining media again to ensure viability of the cells and allow sequential drug delivery if required.

In my experiment, I first measured basal metabolic activity comprising glycolysis and mitochondrial respiration over 20 minutes. Rotenone, a mitochondrial complex I inhibitor, was then applied to remove the contribution of mitochondrial activity to extracellular

acidification and also, drive the cells into their maximum compensatory glycolysis. In the end, the glycolysis blocker 2-DG was injected into the media to confirm that the measured proton efflux was predominantly due to glycolysis.

Figure F.1 gives an overview of the theory behind the Seahorse Glycolysis Kit and demonstrates the expected dynamic pattern of ECAR, OCR and glycoPER over time in a usual cell culture dish.

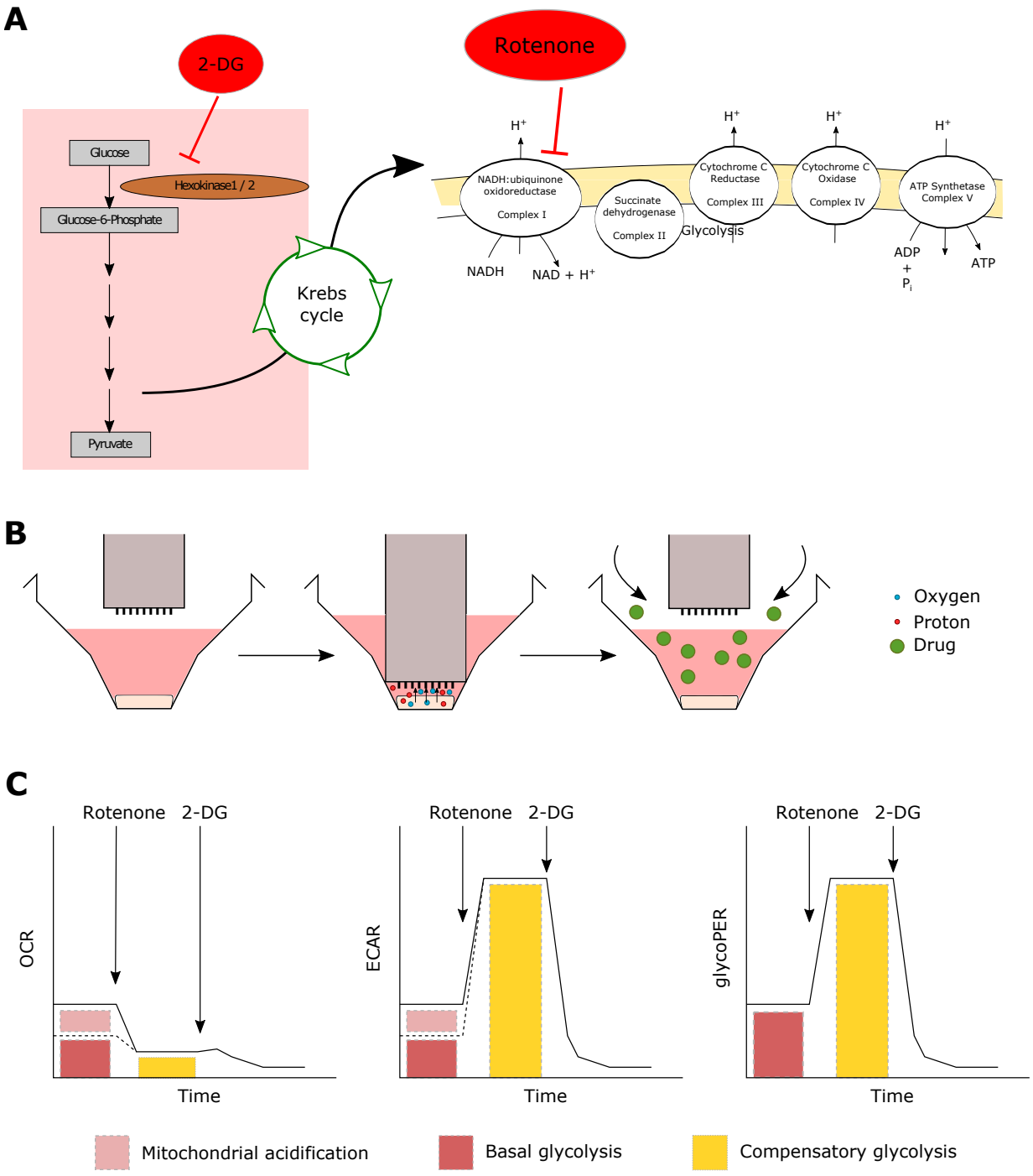


FIGURE F.1: **Schematic on Seahorse analysis of cellular metabolism.** The rate of mitochondrial activity and basal as well as maximum compensatory glycolysis was measured using a Seahorse Analyser from Agilent. (A) To interrogate the mitochondrial contribution to extracellular acidification, the mitochondrial complex I inhibitor rotenone was applied abolishing oxidative phosphorylation completely. I also used the hexokinase 1/2 inhibitor 2-Desoxyglucose (2-DG) as a mean to stop glycolysis and determine the glycolytic contribution to media acidification. (B) The cellular monolayer is attached to a small well below a movable solid-state sensor probe. Initially, the full media is covering the cellular monolayer to ensure viability of the cells. The sensor probe is then lowered down and locks a small microchamber containing 2 μL of media from the rest of the media. The cellular efflux of oxygen and protons into this microchamber is measured and averaged over 2-5 minutes before the probe moves up again and releases the remaining media back onto the cells. That step can be used to wash in additional drugs as required. (C) Schematics of dynamic changes of the three main Seahorse metrics OCR, ECAR and glycoPER as they would be expected in usual cell culture. Rotenone blocks mitochondrial oxygen consumption and thus, leads to a decrease in OCR. It, however, drives the cells towards maximum glycolysis so we expect to see an increase in ECAR and glycoPER. 2-DG application then abolishes glycolytic proton efflux causing a near-zero ECAR and glycoPER.

G | Bayes' Theorem and probabilistic inference.

In general, probability can be defined as *frequency in an ensemble* or *reasonable expectation* [46]. The frequency theory requires the possibility to perform a certain experiment for, theoretically, an indefinite number of times. The probability of a specific outcome is defined as the ratio of the number this specific outcome occurred and the total number the experiment was performed. In contrast, the *Bayesian* subjective view on probability as reasonable expectation is *the intuitively best guess* and reflects our degree of belief that a certain event would happen or not. It is particularly applied when the possibility of repeating a specific task indefinitely does not exist. Regardless of which interpretation of probability is used, the mathematical rules of probability theory are still valid [14].

Consider the two variables x and y that can take on the different states from their domains $dom(x) = \{x_1, x_2, \ldots, x_n\}$ and $dom(y) = \{y_1, y_2, \ldots, y_m\}$, respectively. $P(x = x_n)$, or $P(x_1)$ in short, is the probability that x is in the particular state x_n with $0 \leq P(x_n) \leq 1$ and $\sum_{x \in dom(x)} P(x) = 1$.
By definition, the term $P(x_n, y_m)$ shall denote the probability that $x = x_n$ and $y = y_m$. This joint probability is calculated with the help of the conditioned probability $P(x|y)$, that is the probability of x given the state of y, as follows:

$$P(x, y) = P(x|y)P(y) = P(y|x)P(x) \qquad \text{with } P(x) \neq 0, P(y) \neq 0. \tag{G.1}$$

The variables x and y are independent if knowledge about the current state of y does not

change our prediction on the current state of x so that

$$P(x|y) = P(x) \Leftrightarrow P(y|x) = P(y)$$

and $P(x, y) = P(x)P(y)$.

Bayes' rule, which is crucial in probabilistic reasoning and lays the foundation for modern machine learning algorithms, follows directly from the definition of joint probability in equation G.1:

$$P(x|y) = \frac{P(y|x)P(x)}{P(y)} \tag{G.2}$$

This theorem is crucial as it allows to invert between $P(x|y)$ and $P(y|x)$.

H | Dynamic Causal Modeling

First step: Defining the model. We define a system x that comprises n number of system variables X_n so that the n-vector $x(t)$ expresses the state of all system variables at the time t.

$$x(t) = \begin{bmatrix} x_1(t) \\ \dots \\ x_n(t) \end{bmatrix} \tag{H.1}$$

Each of the system variables does belong to a system element (individual neurons, neuronal units or similar) and describes specific properties of this element, such as membrane potential or ion channel status. These system variables interact with one another so that their individual dynamic is influenced by at least one other variable. The dynamics can be expressed as a set of ordinary differential equations that describe the change of the system over time:

$$F(x) = \frac{dx}{dt} = \begin{bmatrix} f_1(x_1, \dots, x_n) \\ \dots \\ f_n(x_1, \dots, x_n) \end{bmatrix}. \tag{H.2}$$

The evolution function F is further dependent on a set of specific parameters θ that describe the concrete nature of each dependency between the state variables, such as the synaptic

strength of the connection or specific time constants. Furthermore, most model systems in DCM analyses include external inputs in form of the input vector $u(t)$ as well, so that the complete evolution function can be written as

$$\frac{dx}{dt} = F(x, u, \theta). \tag{H.3}$$

This general form of a model for effective connectivity assumes that the system changes are deterministic and happen instantaneously. To model biological randomness and delay, one need to add stochastic and delay differential equations to express noise in the system.

In addition to the evolution model, the modelling part of DCM analysis comprises a second model, the so-called *forward or observation model*. It can be expressed in general as the observation function g that maps the neuronal system x onto the real-world measurements y with help of a set of observation parameters φ.

$$y = g(x, \varphi). \tag{H.4}$$

Second step: Inferring on parameter densities.

The model is fitted to the real-world data to keep the discrepancy between the predictive model outcome and the actual data to a minimum (*model inversion*). $P(y|\vartheta, m)$ is the likelihood of measuring y given the model m with the parameters $\vartheta = (\theta, \varphi)$. Given the defined priors $P(\vartheta|m)$ of the model parameters, the classic Bayesian theorem then allows the calculation of two statistical conclusions: (1) an estimate on the posterior mean value of the model parameters as well as their confidence interval via the posterior probability density function $P(\vartheta|y, m)$

$$P(\vartheta|y, m) = \frac{P(y|\vartheta, m)P(\vartheta|m)}{P(y|m)}. \tag{H.5}$$

and (2) the so-called model evidence $P(y|m)$ which follows directly from the rules of marginalisation and is a measure of how plausible the model is able to explain the data

$$P(y|m) = \int P(y|\vartheta, m)P(\vartheta|m)\delta\vartheta. \tag{H.6}$$

Acronyms

2DG 2-desoxyglucose.

4E-BPs eukaryotic translation initiation factor 4E-binding protein.

ACO2 aconitase 2.

ADM astrocyte differentiation media.

AIC Akaike information criterion.

AML angiomyolipoma.

AMM astrocyte maturation media.

AMPA α-amino-3-hydroxy-5-methyl-4-isoxazolepropionic acid.

AMPAR α-amino-3-hydroxy-5-methyl-4-isoxazolepropionic acid receptor.

AMPK 5' AMP-activated protein kinase.

ATP adenosine triphosphate.

BCA bicinchoninic acid.

BDNF brain-derived neurotrophic factor.

bFGF basic fibroblast growth factor.

BIC Bayesian information criterion.

Brn2 brain-specific homeobox / POU domain protein 2.

Brn3a brain-specific homeobox / POU domain protein 3a.

BSA bovine serum albumin.

cDNA complementary DNA.

CMM canonical microcircuit model.

COVID-19 coronavirus-associated disease 2019.

COX5B cytochrome c oxidase subunit 5B.

CRISPR clustered regularly interspaced Short palindromic repeats.

CS citrate synthetase.

CTIP-2 COUP-TF-interacting protein 2.

Cx43 connexin 43.

CYC1 cytochrome C1.

DCM dynamic causal modeling.

EAAT1 excitatory amino acid transporter 1.

ECAR extracellular acidification rate.

EEG electroencephalogram.

EGF epidermal growth factor.

eIF4E eukaryotic translation initiation factor 4E.

ES embryonic stem cells.

FCD focal cortical dysplasia.

FH fumarate hydratase.

fMRI functional magnetic resonance imaging.

FOXG1 forkhead box G1.

G6P glucose-6-phosphate.

G6PD glucose-6-phosphate dehydrogenase.

GABA γ-aminobutyric acid.

$\mathbf{GABA_AR}$ γ-aminobutyric acid A receptor.

GAPDH glycerinaldehyd-3-phosphat-Dehydrogenase.

GFAP glial fibrillary acidic protein.

GLM generalised linear model.

Glut1 glucose transporter 1.

glycoPER share of glycolysis on the total proton efflux.

GS glutamine synthetase.

GTP guanosine triphosphate.

hES human embryonic stem cells.

HIF hypoxia-induced factor.

HK hexokinase.

HPRT hypoxanthin guanin phosphoribosyltransferase.

hPSC human pluripotent stem cells.

IDH2 isocitratdehydrogenase 2.

IGF insulin-like growth factor.

IPC intermediate progenitor cells.

iPSC induced pluripotent stem cells.

Ki67 antigen KI-67.

LDH lactate dehydrogenase.

LFP local field potential.

MAP-2 microtubule-associated protein 2.

Map2 microtubule-associated protein 2.

MCD malformation of cortical development.

MEA multi-electrode array.

mLST8 mammalian lethal with Sec13 protein 8.

MNR multinomial logistic regression.

MOI multiplicity of infection.

MRI magnetic resonance imaging.

mTOR mechanistic target of rapamycin.

mTORC1 mechanistic target of rapamycin complex 1.

Nanog NK2-family homeobox transcription factor.

NDUF1A NADH:ubiquinone oxidoreductase subunit A1.

NEC neural epithelial cells.

NF1A nuclear factor 1A.

NGN1 neurogenin 1.

NGN2 neurogenin 2.

NIM neural induction media.

NMDA N-methyl-D-aspartate.

NMDAR N-methyl-D-aspartate receptor.

NMI no mutation identified.

NMM neural maintenance media.

NRF1 nuclear respiratory factor 1.

NSC neural stem cells.

NT-3 neurotrophin 3.

OCR oxygen consumption rate.

Oct4 octamer-binding transcription factor 4.

OGDH oxoglutarate dehydrogenase.

oRGC outer radial glial cells.

OXPHOS oxidative phosphorylation.

Pax6 paired Box 6.

PCC Pearson correlation coefficient.

PCR polymerase chain reaction.

PER proton efflux rate.

PGAM1 phosphoglycerate Mutase 1.

PGC-1α peroxisome-proliferator-activated γ co-activator-1α.

PGC1a PPARG coactivator 1 α.

PGK1 phosphoglycerate Kinase 1.

PI3K phosphoinositide 3-kinase.

PKM pyruvate kinase muscle isozyme.

pS6 phosphorylated S6.

qRT-PCR quantitative reverse transcription PCR.

RAPTOR regulatory-associated protein of mTOR.

RGC radial glial cells.

Rheb Ras homolog enriched in brain.

RICTOR rapamycin-insensitive companion of mTOR.

RT room temperature.

S6K ribosomal protein S6 kinases.

Sat2b special AT-rich sequence-binding protein 2.

SDHA succinate dehydrogenase complex, subunit A.

SEGAs subependymal giant cell astrocytomas.

sgRNA single-guide RNA.

shRNA short RNA.

SMAD protein family of homologies to the *Caenorhabditis elegans'* SMA (small worm phenotype) and *drosophila's* MAD family (Mothers Against Decapentaplegic).

SOX2 SRY-Box transcription factor 2.

SREBPs sterol regulatory element-binding proteins.

Sucla2 succinyl-CoA ligase subunit β.

SVZ subventricular zone.

TAND TSC-associated neuropsychiatric disorder.

Tbr1 T-box brain protein 1.

Tbr2 T-box brain protein 2.

TCA tricarboxylic acid cycle.

TPI1 triosephosphate isomerase 1.

TSC Tuberous Sclerosis Complex.

TUJ-1 β-tubulin.

VZ ventricular zone.

ZO-1 zona occludens 1.

Bibliography

[1] E. Aaku-Saraste, A. Hellwig, and W. B. Huttner. Loss of occludin and functional tight junctions, but not ZO-1, during neural tube closure - Remodeling of the neuroepithelium prior to neurogenesis. *Developmental Biology*, 180(2):664–679, 1996.

[2] W. Afshar Saber and M. Sahin. Recent advances in human stem cell-based modeling of Tuberous Sclerosis Complex, feb 2020.

[3] P. Agrawal et al. DEPTOR Is a Stemness Factor That Regulates Pluripotency of Embryonic Stem Cells *. *The Journal of Biological Chemistry*, 289(46):31818–31826, 2014.

[4] M. Alsaqati, V. M. Heine, and A. J. Harwood. Pharmacological intervention to restore connectivity deficits of neuronal networks derived from ASD patient iPSC with a TSC2 mutation. *Molecular Autism*, 11(1):1–13, 2020.

[5] N. D. Amin and S. P. Paşca. Building Models of Brain Disorders with Three-Dimensional Organoids. *Neuron*, 100(2):389–405, oct 2018.

[6] N. An, H. Xu, W. Q. Gao, and H. Yang. Direct conversion of somatic cells into induced neurons. *Molecular Neurobiology*, 55(1):642–651, jan 2018.

[7] T. E. Anthony, C. Klein, G. Fishell, and N. Heintz. Radial glia serve as neuronal progenitors in all regions of the central nervous system. *Neuron*, 41(6):881–890, mar 2004.

[8] K. Aravantinou-Fatorou et al. CEND1 and NEUROGENIN2 Reprogram Mouse Astrocytes and Embryonic Fibroblasts to Induced Neural Precursors and Differentiated Neurons. *Stem Cell Reports*, 5(3):405–418, 2015.

[9] K. Aravantinou-Fatorou and D. Thomaidou. In vitro direct reprogramming of mouse and human astrocytes to induced neurons. In *Methods in Molecular Biology*, volume 2155, pages 41–61. Humana Press Inc., 2020.

[10] J. L. Arbiser et al. Tuberous sclerosis-associated lesions of the kidney, brain, and skin are angiogenic neoplasms. *Journal of the American Academy of Dermatology*, 46(3):376–380, 2002.

[11] E. Aronica, A. J. Becker, and R. Spreafico. Malformations of Cortical Development. *Brain Pathology*, 22(3):380–401, may 2012.

[12] H. S. Bachelard. The subcellular distribution and properties of hexokinases in the guinea-pig cerebral cortex. *The Biochemical Journal*, 104(1):286–292, 1967.

[13] L. M. Ballou and R. Z. Lin. Rapamycin and mTOR kinase inhibitors. *Journal of Chemical Biology*, 1(1):27–36, nov 2008.

[14] D. Barber. *Bayesian Reasoning and Machine Learning*. Cambridge University Press, 2012.

[15] R. Beckervordersandforth et al. Role of Mitochondrial Metabolism in the Control of Early Lineage Progression and Aging Phenotypes in Adult Hippocampal Neurogenesis. *Neuron*, 93(3):560–573, feb 2017.

[16] B. J. Berry et al. Morphological and functional characterization of human induced pluripotent stem cell-derived neurons (iCell Neurons) in defined culture systems. *Biotechnology Progress*, 31(6):1613–1622, nov 2015.

[17] F. Birey et al. Assembly of functionally integrated human forebrain spheroids. *Nature*, 545(7652):54–59, may 2017.

[18] J. D. Blair and H. S. Bateup. New frontiers in modeling Tuberous Sclerosis with human stem cell-derived neurons and brain organoids. *Developmental Dynamics*, 249(1):46–55, may 2019.

[19] J. D. Blair, D. Hockemeyer, and H. S. Bateup. Genetically engineered human cortical spheroid models of tuberous sclerosis. *Nature Medicine*, 24(10):1568–1578, oct 2018.

[20] J. M. Brown and L. D. Attardi. The role of apoptosis in cancer development and treatment response. *Nature Reviews Cancer*, 5(3):231–237, mar 2005.

[21] G. Buzsáki, C. A. Anastassiou, and C. Koch. The origin of extracellular fields and currents - EEG, ECoG, LFP and spikes, jun 2012.

[22] I. Bystron, C. Blakemore, and P. Rakic. Development of the human cerebral cortex: Boulder Committee revisited. *Nature Reviews Neuroscience*, 9(2):110–122, feb 2008.

[23] I. Bystron, P. Rakic, Z. Molnár, and C. Blakemore. The first neurons of the human cerebral cortex. *Nature Neuroscience*, 9(7):880–886, jul 2006.

[24] M. Caiazzo et al. Direct Conversion of Fibroblasts into Functional Astrocytes by Defined Transcription Factors. *Stem Cell Reports*, 4(1):25–36, jan 2015.

[25] K. Campbell and M. Götz. Radial glia: Multi-purpose cells for vertebrate brain development. *Trends in Neurosciences*, 25(5):235–238, may 2002.

[26] B. W. Carey et al. Intracellular α-ketoglutarate maintains the pluripotency of embryonic stem cells. *Nature*, 518(7539):413–416, feb 2015.

[27] F. Cargnin et al. FOXG1 orchestrates neocortical organization and cortico-cortical connections. *Neuron*, 100(5):1083–1096, dec 2018.

[28] R. P. Carson, D. L. Van Nielen, P. A. Winzenburger, and K. C. Ess. Neuronal and glia abnormalities in Tsc1-deficient forebrain and partial rescue by rapamycin. *Neurobiology of disease*, 45(1):369–380, jan 2012.

[29] T. S. Catlett et al. RHOA signaling defects result in impaired axon guidance in iPSC-derived neurons from patients with tuberous sclerosis complex. *Nature Communications*, 12(1):1–15, 2021.

[30] S. M. Chambers et al. Highly efficient neural conversion of human ES and iPS cells by dual inhibition of SMAD signaling HHS Public Access Author manuscript. *Nat Biotechnol*, 27(3):275–280, 2009.

[31] W. Y. Chan et al. Normal and Abnormal Development of the Human Cerebral Cortex. *Neuroembryology*, 1:78–90, 2002.

[32] A. Chandrasekaran et al. Astrocyte Differentiation of Human Pluripotent Stem Cells: New Tools for Neurological Disorder Research. *Frontiers in Cellular Neuroscience*, 10, 2016.

[33] C. Chauvin et al. Ribosomal protein S6 kinase activity controls the ribosome biogenesis transcriptional program. *Oncogene*, 33(4):474–483, 2014.

[34] H. Chong-Kopera et al. TSC1 stabilizes TSC2 by inhibiting the interaction between TSC2 and the HERC1 ubiquitin ligase. *Journal of Biological Chemistry*, 281(13):8313–8316, 2006.

[35] A. Y. Choo et al. Glucose addiction of TSC-null cells is caused by failed mTORC1-dependent balancing of metabolic demand with supply. *Molecular C*, 38(4):487–499, 2010.

[36] M. Chouchane et al. Lineage Reprogramming of Astroglial Cells from Different Origins into Distinct Neuronal Subtypes. *Stem Cell Reports*, 9(1):162–176, jul 2017.

[37] C. C. Chow and Y. Karimipanah. Before and beyond the Wilson-Cowan equations. *Journal of Neurophysiology*, 123(5):1645–1656, 2020.

[38] C. J. Chu-Shore, P. Frosch, E. Grant, and E. A. Thiele. Progressive multifocal cystlike cortical tubers in tuberous sclerosis complex: Clinical and neuropathologic findings. *Epilepsia*, 50(12):2648–51, 2009.

[39] D. C. Chugani et al. Imaging Epileptogenic Tubers in Children with Tuberous Sclerosis Complex Using a-[11C] Methyl-L-Tryptophak Positronw Emission Tomography. *Annals of Neurology*, 44:858–866, 1998.

[40] F. Ciscato et al. Hexokinase 2 in cancer: A prima donna playing multiple characters. *International Journal of Molecular Sciences*, 22(9), 2021.

[41] D. Cloëtta et al. Inactivation of mTORC1 in the Developing Brain Causes Microcephaly and Affects Gliogenesis. *The Journal of Neuroscience*, 33(18):7799–7810, 2013.

[42] R. Cohen, J. Genizi, and L. Korenrich. Behavioral Symptoms May Correlate With the Load and Spatial Location of Tubers and With Radial Migration Lines in Tuberous Sclerosis Complex. *Frontiers in Neurology*, 12, 2021.

[43] K. J. Condon and D. M. Sabatini. Nutrient regulation of mTORC1 at a glance. *Journal of Cell Science*, 132(21), nov 2019.

[44] V. Costa et al. MTORC1 Inhibition Corrects Neurodevelopmental and Synaptic Alterations in a Human Stem Cell Model of Tuberous Sclerosis. *Cell Reports*, 15(1):86–95, 2016.

[45] A. M. Courtot et al. Morphological analysis of human induced pluripotent stem cells during induced differentiation and reverse programming. *BioResearch Open Access*, 3(5):206–216, oct 2014.

[46] R. T. Cox. Probability, frequency and rational expectation. *American Journal of Physics*, 14(1), 1946.

[47] P. B. Crino, K. L. Nathanson, and E. P. Henske. The Tuberous Sclerosis Complex. *The New England Journal of Medicince*, 355(13):1345–1356, sep 2006.

[48] P. B. Crino, J. Q. Trojanowski, M. A. Dichter, and J. Eberwine. Embryonic neuronal markers in tuberous sclerosis: Single-cell molecular pathology. *Proceedings of the National Academy of Sciences of the United States of America*, 93:14152–14157, 1996.

[49] P. Curatolo. Tuberous Sclerosis. *Orphanet Encyclopedia*, 2015.

[50] G. G. Curto et al. Pax6 Is Essential for the Maintenance and Multi-Lineage Differentiation of Neural Stem Cells, and for Neuronal Incorporation into the Adult Olfactory Bulb. *Stem Cells and Development*, 23(23):2813–2830, aug 2014.

[51] S. L. Dabora et al. Mutational analysis in a cohort of 224 tuberous sclerosis patients indicates increased severity of TSC2, compared with TSC1, disease in multiple organs. *American journal of human genetics*, 68(1):64–80, jan 2001.

[52] J. Daunizeau, O. David, and K. E. Stephan. Dynamic causal modelling: A critical review of the biophysical and statistical foundations. *NeuroImage*, 58(2):312–322, 2011.

[53] A. De Ciantis et al. Ultra-High-Field MR Imaging in Polymicrogyria and Epilepsy. *AM J Neuroradiol*, 36:309–16, 2015.

[54] C. De Lima E Santos, C. P. Arnoni, N. Schor, and M. A. Boim. Effects of glucose deprivation or glucose instability on mesangial cells in culture. *American Journal of Nephrology*, 29(3):222–229, 2009.

[55] B. Deneen et al. The Transcription Factor NFIA Controls the Onset of Gliogenesis in the Developing Spinal Cord. *Neuron*, 52:953–968, 2006.

[56] A. Di Nardo et al. Tuberous Sclerosis Complex Activity Is Required to Control Neuronal Stress Responses in an mTOR-Dependent Manner. *Journal of Neuroscience*, 29(18):5926–5937, may 2009.

[57] J. Díaz-Alonso et al. CB1 Cannabinoid Receptor-Dependent Activation of mTORC1/Pax6 Signaling Drives Tbr2 Expression and Basal Progenitor Expansion in the Developing Mouse Cortex. *Cerebral Cortex*, 25(9):2395–2408, sep 2015.

[58] S. Dooves, A. G. Nadadhur, L. Gasparotto, and V. M. Heine. Co-culture of Human Stem Cell Derived Neurons and Oligodendrocyte Progenitor Cells. *Bio-protocol*, 9(17):1–17, 2019.

[59] S. Dooves, A. J. van Velthoven, L. G. Suciati, and V. M. Heine. Neuron–glia interactions in tuberous sclerosis complex affect the synaptic balance in 2d and organoid cultures. *Cells*, 10(1):1–20, 2021.

[60] R. J. Dowling et al. mTORC1-mediated cell proliferation, but not cell growth, controlled by the 4E-BPs. *Science (New York, N.Y.)*, 328(5982):1172, may 2010.

[61] X. Du and J. M. Parent. Using Patient-Derived Induced Pluripotent Stem Cells to Model and Treat Epilepsies. *Current Neurology and Neuroscience Reports*, 15(10), 2015.

[62] K. Düvel et al. Activation of a metabolic gene regulatory network downstream of mTOR complex 1. *Molecular Cell*, 39(2):171–183, 2010.

[63] C. A. Easley et al. mTOR-Mediated Activation of p70 S6K Induces Differentiation of Pluripotent Human Embryonic Stem Cells. *Cellular reprogramming*, 12(3):263–273, 2010.

[64] D. Ebrahimi-Fakhari et al. Impaired Mitochondrial Dynamics and Mitophagy in Neuronal Models of Tuberous Sclerosis Complex. *Cell Reports*, 17(4):1053–1070, oct 2016.

[65] O. L. Eichmüller et al. Amplification of human interneuron progenitors promotes brain tumors and neurological defects. *Science*, 375(6579), 2022.

[66] M. Eiraku et al. Self-Organized Formation of Polarized Cortical Tissues from ESCs and Its Active Manipulation by Extrinsic Signals. *Cell Stem Cell*, 3(5):519–532, nov 2008.

[67] U. Ej, M. Wong, B. Rl, and B. Ml. Tsc1 Conditional Knockout Mice Exhibit Abnormal Neuronal Organization and Seizures. *Annals of Neurology*, 52(3):285–96, 2002.

[68] M. Endo, M. A. Antonyak, and R. A. Cerione. Cdc42-mTOR Signaling Pathway Controls Hes5 and Pax6 Expression in Retinoic Acid-dependent Neural Differentiation. *Journal of Biological Chemistry*, 284(8):5107–5118, feb 2009.

[69] S. J. Engle and D. Puppala. Integrating Human Pluripotent Stem Cells into Drug Development. *Cell Stem Cell*, 12(6):669–677, 2013.

[70] C. Englund et al. Pax6, Tbr2, and Tbr1 are expressed sequentially by radial glia, intermediate progenitor cells, and postmitotic neurons in developing neocortex. *Journal of Neuroscience*, 25(1):247–251, jan 2005.

[71] V. Eronique Ruppe et al. Developmental brain abnormalities in tuberous sclerosis complex: A comparative tissue analysis of cortical tubers and perituberal cortex. *Epilepsia*, 55(4):539–550, 2014.

[72] I. Espuny-Camacho et al. Pyramidal Neurons Derived from Human Pluripotent Stem Cells Integrate Efficiently into Mouse Brain Circuits In Vivo. *Neuron*, 77(3):440–456, 2013.

[73] M. J. Evans and M. H. Kaufman. Establishment in culture of pluripotential cells from mouse embryos. *Nature*, 292(5819):154–156, jul 1981.

[74] A. Fallah et al. Predictors of Seizure Outcomes in Children with Tuberous Sclerosis Complex and Intractable Epilepsy Undergoing Resective Epilepsy Surgery: An Individual Participant Data Meta-Analysis. *PLOS ONE*, 8(2):e53565, feb 2013.

[75] A. Fallah et al. Resective Epilepsy Surgery for Tuberous Sclerosis in Children: Determining Predictors of Seizure Outcomes in a Multicenter Retrospective Cohort Study. *Neurosurgery*, 77(4):517–524, oct 2015.

[76] H. Fan et al. Critical role of mTOR in regulating aerobic glycolysis in carcinogenesis (Review). *International Journal of Oncology*, 58:9–19, 2021.

[77] M. J. Farrell et al. FUNCTIONAL CONSEQUENCES OF GLUCOSE AND OXYGEN DEPRIVATION ON ENGINEERED MESENCHYMAL STEM CELL-BASED CARTILAGE CONSTRUCTS. *Osteoarthritis Cartilage*, 23(1):134–142, 2015.

[78] D. M. Feliciano. The Neurodevelopmental Pathogenesis of Tuberous Sclerosis Complex (TSC). *Frontiers in Neuroanatomy*, 14, jul 2020.

[79] D. M. Feliciano et al. Postnatal neurogenesis generates heterotopias, olfactory micronodules and cortical infiltration following single-cell TSC1 deletion. *Human Molecular Genetics*, 21(4):799–810, 2012.

[80] Y. Feng et al. Lactate dehydrogenase A: A key player in carcinogenesis and potential target in cancer therapy. *Cancer Medicine*, 7(12), dec 2018.

[81] A. R. Fernie, F. Carrari, and L. J. Sweetlove. Respiratory metabolism: glycolysis, the TCA cycle and mitochondrial electron transport. *Current Opinion in Plant Biology*, 7(3):254–261, jun 2004.

[82] D. C. Fingar et al. mTOR Controls Cell Cycle Progression through Its Cell Growth Effectors S6K1 and 4E-BP1/Eukaryotic Translation Initiation Factor 4E. *Molecular and Cellular Biology*, 24(1):200, jan 2004.

[83] V. Fossati, T. Jain, and A. Sevilla. The silver lining of induced pluripotent stem cell variation. *Stem cell investigation*, 3(86):341–54, 2016.

[84] W. J. Freeman. *Mass action in the nervous system : examination of the neurophysiological basis of adaptive behavior through the EEG.* Academic Press, 1975.

[85] R. T. Fremeau, S. Voglmaier, R. P. Seal, and R. H. Edwards. VGLUTs define subsets of excitatory neurons and suggest novel roles for glutamate. *Trends in Neurosciences*, 27(2):98–103, feb 2004.

[86] K. J. Friston, L. Harrison, and W. Penny. Dynamic causal modelling. *NeuroImage*, 19(4):1273–1302, 2003.

[87] A. Gallagher et al. MRI findings reveal three different types of tubers in patients with tuberous sclerosis complex. *Journal of neurology*, 257(8):1373–1381, aug 2010.

[88] J. Gao, M. Yao, D. Chang, and J. Liu. mTOR (Mammalian Target of Rapamycin): Hitting the Bull's Eye for Enhancing Neurogenesis After Cerebral Ischemia? *Stroke*, 54(1):279–285, 2023.

[89] N. Gaspard et al. An intrinsic mechanism of corticogenesis from embryonic stem cells. *Nature*, 455(7211):351–357, sep 2008.

[90] W.-p. Ge et al. Local generation of glia is a major astrocyte source in postnatal cortex. *Nature*, 484:376–381, 2012.

[91] T. Goji, K. Takahara, M. Negishi, and H. Katoh. Cystine uptake through the cystine/glutamate antiporter xCT triggers glioblastoma cell death under glucose deprivation. *Journal of Biol*, 292(48):19721–19732, 2017.

[92] M. P. Goldberg and D. W. Choi. Combined Oxygen and Glucose Deprivation in Cortical Cell Culture: Calcium-dependent and Calcium-independent Mechanisms of Neuronal Injury. *The Journal of Neuroscience*, 13(8):3510–3524, 1993.

[93] N. Grabole et al. Genomic analysis of the molecular neuropathology of tuberous sclerosis using a human stem cell model. *Genome Medicine*, 8(94), dec 2016.

[94] N. Guérout, X. Li, and F. Barnabé-Heider. Cell fate control in the developing central nervous system. *Experimental Cell Research*, 321:77–83, 2014.

[95] A. Gupta. Epilepsy surgery recipes galore: in quest for the epileptogenic tuber in tuberous sclerosis complex. *Epileptic Disorders*, 11(1):80–81, 2009.

[96] L. Hallett et al. Burden of disease and unmet needs in tuberous sclerosis complex with neurological manifestations: systematic review. *Current Medical Research and Opinion*, 27(8):1571–1583, 2011.

[97] J. Han et al. Mammalian target of rapamycin (mTOR) is involved in the neuronal differentiation of neural progenitors induced by insulin. *Molecular and Cellular Neuroscience*, 39(1):118–124, 2008.

[98] A. E. Handel et al. Assessing similarity to primary tissue and cortical layer identity in induced pluripotent stem cell-derived cortical neurons through single-cell transcriptomics. *Human Molecular Genetics*, 25(5):989–1000, mar 2016.

[99] N. W. Hartman et al. mTORC1 Targets the Translational Repressor 4E-BP2, but Not S6 Kinase 1/2, to Regulate Neural Stem Cell Self-Renewal In Vivo. *Cell Reports*, 5(2):433–444, oct 2013.

[100] J. T. Hees and A. B. Harbauer. Metabolic Regulation of Mitochondrial Protein Biogenesis from a Neuronal Perspective. *Biomolecules*, 12(11):1–16, 2022.

[101] C. Heinrich et al. Generation of subtype-specific neurons from postnatal astroglia of the mouse cerebral cortex. *Nature Protocols*, 6(2):214–228, feb 2011.

[102] J. O. Hernandez et al. A tissue-bioengineering strategy for modeling rare human kidney diseases in vivo. *Nature Communications*, 12(1), 2021.

[103] T. Hirose et al. Tuber and subependymal giant cell astrocytoma associated with tuberous sclerosis: an immunohistochemical, ultrastructural, and immunoelectron microscopic study. *Acta Neuropathologica*, 90(4):387–399, oct 1995.

[104] C. Hisatsune et al. Tuberous Sclerosis Complex (TSC) inactivation increases neuronal network activity by enhancing Ca2+ influx via L-type Ca2+ channels. *Journal of Neuroscience*, 41(39):8134–8149, 2021.

[105] A. L. HODGKIN and A. F. HUXLEY. Propagation of electrical signals along giant nerve fibres. *Proceedings of the Royal Society of London. Series B - Biological Sciences*, 140(899):177–183, oct 1952.

[106] C. A. Hoeffer and E. Klann. mTOR Signaling: At the Crossroads of Plasticity, Memory, and Disease. *Circulation*, 33(2), 2010.

[107] G. L. Holmes et al. Tuberous Sclerosis Complex and Epilepsy: Recent Developments and Future Challenges. *Epilepsia*, 48(4):617–630, apr 2007.

[108] C. C. Homem et al. Ecdysone and mediator change energy metabolism to terminate proliferation in drosophila neural stem cells. *Cell*, 158(4):874–888, aug 2014.

[109] Q. Huang et al. Cell Death Pathways in Astrocytes with a Modified Model of Oxygen-Glucose Deprivation. *PLoS ONE*, 8(4):61345, 2013.

[110] P. R. Huttenlocher and P. T. Heydemann. Fine Structure of Cortical Tubers in Tuberous Sclerosis: A Golg Study. *Annals of Neurology*, 16(5):595–602, 1984.

[111] W. B. Huttnerl and M. Brand. Asymmetric division and polarity of neuroepithelial cells. *Current Opinion in Neurobiology*, 7:29–39, 1997.

[112] Y. Imaizumi and H. Okano. Modeling human neurological disorders with induced pluripotent stem cells. *Journal of Neurochemistry*, 129(3):388–399, may 2014.

[113] R. Iwata, P. Casimir, and P. Vanderhaeghen. Mitochondrial dynamics in postmitotic cells regulate neurogenesis. *Science*, 369(6505):858–862, aug 2020.

[114] R. Iwata and P. Vanderhaeghen. Regulatory roles of mitochondria and metabolism in neurogenesis. *Current Opinion in Neurobiology*, 69, aug 2021.

[115] B. H. Jansen and V. G. Rit. Electroencephalogram and visual evoked potential generation in a mathematical model of coupled cortical columns. *Biological cybernetics*, 73(4):357–366, sep 1995.

[116] F. E. Jansen et al. Overlapping neurologic and cognitive phenotypes in patients with TSC1 or TSC2 mutations. *Neurology*, 70(12):908–915, 2008.

[117] F. E. Jansen et al. Identification of the Epileptogenic Tuber in Patients with Tuberous Sclerosis: A Comparison of High-resolution EEG and MEG. *Epilepsia*, 47(1):108–114, jan 2006.

[118] L. A. Jansen et al. Epileptogenesis and Reduced Inward Rectifier Potassium Current in Tuberous Sclerosis Complex-1-Deficient Astrocytes. *Epilepsia*, 46(12):1871–1880, dec 2005.

[119] X. Jiang, H. L. Kenerson, and R. S. Yeung. Glucose deprivation in tuberous sclerosis complex-related tumors. *Cell and Bioscience*, 1(1):1–15, 2011.

[120] J. Jozwiak and S. Jozwiak. Giant cells: Contradiction to two-hit model of tuber formation? *Cellular and Molecular Neurobiology*, 25(5):795–806, aug 2005.

[121] M. Kaczorowska et al. Cerebral tuber count and its impact on mental outcome of patients with tuberous sclerosis complex. *Epilepsia*, 52(1):22–27, jan 2011.

[122] A. Kakita. Surgical pathologic features of cerebral cortical lesions taken from 600 patients with intractable epilepsy. *Brain and Development*, 35(8):793–801, 2013.

[123] J. Kassiri et al. Cortical tubers, cognition, and epilepsy in tuberous sclerosis. *Pediatric Neurology*, 44(5):328–332, may 2011.

[124] I. Kelava et al. Stem Cell Models of Human Brain Development. *Cell stem cell*, 18(6):736–48, jun 2016.

[125] H. Kenerson, T. A. Dundon, and R. S. Yeung. Effects of rapamycin in the eker rat model of tuberous sclerosis complex. *Pediatric Research*, 57(1):67–75, 2005.

[126] M. Khacho et al. Mitochondrial Dynamics Impacts Stem Cell Identity and Fate Decisions by Regulating a Nuclear Transcriptional Program. *Cell Stem Cell*, 19(2):232–247, aug 2016.

[127] M. Khacho et al. Mitochondrial dysfunction underlies cognitive defects as a result of neural stem cell depletion and impaired neurogenesis. *Human Molecular Genetics*, 26(17):3327, sep 2017.

[128] S. J. Kiebel et al. Dynamic causal modeling for EEG and MEG. *Human Brain Mapping*, 30(6):1866–1876, jun 2009.

[129] T. Kikuchi et al. Human iPS cell-derived dopaminergic neurons function in a primate Parkinson's disease model. *Nature*, 548:592–596, 2017.

[130] J. Kim, M. Kundu, B. Viollet, and K. L. Guan. AMPK and mTOR regulate autophagy through direct phosphorylation of Ulk1. *Nature Cell Biology 2011 13:2*, 13(2):132–141, jan 2011.

[131] J. C. Kingswood et al. TuberOus SClerosis registry to increase disease Awareness (TOSCA) - Baseline data on 2093 patients. *Orphanet Journal of Rare Diseases*, 12(1):1–13, jan 2017.

[132] T. Kobayashi et al. A germ-line Tsc1 mutation causes tumor development and embryonic lethality that are similar, but not identical to, those caused by Tsc2 mutation in mice. *Proceedings of the National Academy of Sciences of the United States of America*, 98(15):8762, jul 2001.

[133] S. V. Kothare et al. Severity of manifestations in tuberous sclerosis complex in relation to genotype. *Epilepsia*, 55(7):1025–1029, jul 2014.

[134] R. Krencik et al. Specification of transplantable astroglial subtypes from human pluripotent stem cells. *Nature Biotechnology*, 29(6):528–534, jun 2011.

[135] A. R. Kriegstein and M. Götz. Radial glia diversity: A matter of cell fate. *GLIA*, 43(1):37–43, jul 2003.

[136] D. Krueger and H. Northrup. Tuberous Sclerosis Complex Surveillance and Management: Recommendations of the 2012 International Tuberous Sclerosis Complex Consensus Conference. *Pediatric Neurology*, 49(4):255–265, 2013.

[137] D. K. Lachhwani et al. Identification of candidates for epilepsy surgery in patients with tuberous sclerosis. *Neurology*, 64(9):1651–1654, may 2005.

[138] R. S. Lam et al. Functional Maturation of Human Stem Cell-Derived Neurons in Long-Term Cultures. *PLoS ONE*, 12(1):e0169506, 2017.

[139] M. A. Lancaster et al. Cerebral organoids model human brain development and microcephaly. *Nature*, 501(7467):373–379, aug 2013.

[140] S. C. Land and A. R. Tee. Hypoxia-inducible Factor 1a Is Regulated by the Mammalian Target of Rapamycin (mTOR) via an mTOR Signaling Motif. *Journal of Biological Chemistry*, 282(28):20534–43, 2007.

[141] M. Laplante, D. M. Sabatini, and C. B. Author. An emerging role of mTOR in lipid biosynthesis NIH Public Access Author Manuscript. *Curr Biol*, 19(22):1046–1052, 2009.

[142] S. Lautrup, D. A. Sinclair, M. P. Mattson, and E. F. Fang. NAD+ in Brain Aging and Neurodegenerative Disorders. *Cell metabolism*, 30(4), oct 2019.

[143] C. H. Lee et al. Constitutive mTOR activation in TSC mutants sensitizes cells to energy starvation and genomic damage via p53. *EMBO Journal*, 26(23):4812–4823, nov 2007.

[144] D. Y. Lee. Roles of mTOR Signaling in Brain Development. *Experimental Neurobiology*, 24(3):177–185, 2015.

[145] L. Lee et al. Efficacy of a rapamycin analog (CCI-779) and IFN-γ in tuberous sclerosis mouse models. *Genes Chromosomes and Cancer*, 42(3):213–227, 2005.

[146] J. C. Lewis, V. Thomas, and C. Murphy. Genotype and psychological phenotype in tuberous sclerosis. *J Med Genet*, 41:203–207, 2004.

[147] J. Li, S. G. Kim, and J. Blenis. Rapamycin: one drug, many effects. *Cell Metabolism*, 19(3), 2014.

[148] X.-J. Li et al. Specification of motoneurons from human embryonic stem cells. *Nature Biotechnology*, 23(2):215–221, 2005.

[149] X. J. Li et al. Coordination of sonic hedgehog and Wnt signaling determines ventral and dorsal telencephalic neuron types from human embryonic stem cells. *Development*, 136(23):4055–4063, sep 2009.

[150] Y. Li et al. Abnormal Neural Progenitor Cells Differentiated from Induced Pluripotent Stem Cells Partially Mimicked Development of TSC2 Neurological Abnormalities. *Stem Cell Reports*, 8:883–893, 2017.

[151] F. LiCausi and N. W. Hartman. Role of mTOR Complexes in Neurogenesis. *International Journal of Molecular Sciences*, 19(5), may 2018.

[152] F. W. Lindhout et al. Quantitative mapping of transcriptome and proteome dynamics during polarization of human iPSC-derived neurons. *eLife*, 9:e58124, 2020.

[153] J. O. Lipton and M. Sahin. The Neurology of mTOR. *Neuron*, 84(2):275–291, 2014.

[154] H. Liu and S.-C. Zhang. Specification of neuronal and glial subtypes from human pluripotent stem cells. *Cellular and Molecular Life Sciences*, 68:3995–4008, 2011.

[155] P. S. Liu et al. α-ketoglutarate orchestrates macrophage activation through metabolic and epigenetic reprogramming. *Nature immunology*, 18(9):985–994, aug 2017.

[156] J. Lui, D. Hansen, and A. Kriegstein. Development and Evolution of the Human Neocortex. *Cell*, 146(1):18–36, jul 2011.

[157] L. Magri et al. Sustained activation of mTOR pathway in embryonic neural stem cells leads to development of tuberous sclerosis complex-associated lesions. *Cell stem cell*, 9(5):447–62, nov 2011.

[158] P. Major et al. Are cortical tubers epileptogenic? Evidence from electrocorticography. *Epilepsia*, 50(1):147–154, jan 2009.

[159] P. Malatesta et al. Neuronal or Glial Progeny: Regional Differences in Radial Glia Fate. *Neuron*, 37(5):751–764, mar 2003.

[160] B. Manning et al. Identi cation of the tuberous sclerosis complex-2 tumor suppressor gene product tuberin as a target of the phosphoinositide 3-kinase/akt pathway. *Molecular and Cellular Biology*, 10(1):151–62., 2002.

[161] Z. Mao and W. Zhang. Role of mTOR in glucose and lipid metabolism. *International Journal of Molecular Sciences*, 19(7), jul 2018.

[162] D. R. Marinowic et al. Induced pluripotent stem cells from patients with focal cortical dysplasia and refractory epilepsy. *Molecular Medicine Reports*, 15:2049–2056, 2017.

[163] A. Marreiros, K. Stephan, and K. Friston. Dynamic causal modeling. *Scholarpedia*, 5(7):9568, 2010.

[164] P. Martin et al. TSC patient-derived isogenic neural progenitor cells reveal altered early neurodevelopmental phenotypes and rapamycin-induced MNK-eIF4E signaling. *Molecular autism*, 11(2), 2020.

[165] V. Martínez-Cerdeño et al. Evolutionary origin of Tbr2-expressing precursor cells and the subventricular zone in the developing cortex HHS Public Access. *J Comp Neurol*, 524(3):433–447, 2016.

[166] I. Martínez-Reyes and N. S. Chandel. Mitochondrial TCA cycle metabolites control physiology and disease. *Nature Communications*, 11(1), dec 2020.

[167] G. Masserdotti et al. Transcriptional Mechanisms of Proneural Factors and REST in Regulating Neuronal Reprogramming of Astrocytes. *Cell Stem Cell*, 17(1):74–88, jul 2015.

[168] R. Mathew, V. Karantza-Wadsworth, and E. White. Role of autophagy in cancer. *Nature Reviews Cancer*, 7(12):961–967, dec 2007.

[169] E. H. Mathews, B. A. Stander, A. M. Joubert, and L. Liebenberg. Tumor cell culture survival following glucose and glutamine deprivation at typical physiological concentrations. *Nutrition*, 30(2):218–227, 2014.

[170] S. P. Mathupala, Y. H. Ko, and P. L. Pedersen. Hexokinase II: Cancer's double-edged sword acting as both facilitator and gatekeeper of malignancy when bound to mitochondria. *Oncogene 2006*, 25(34):4777–4786, aug 2006.

[171] N. Matsuda et al. Detection of synchronized burst firing in cultured human induced pluripotent stem cell-derived neurons using a 4-step method. *Biochemical and Biophysical Research Communications*, 497(2):612–618, mar 2018.

[172] D. A. McCormick and D. A. Prince. Post-natal development of electrophysiological properties of rat cerebral cortical pyramidal neurones. *The Journal of Physiology*, 393(1):743–762, dec 1987.

[173] W. S. McCulloch and W. Pitts. A logical calculus of the ideas immanent in nervous activity. *The bulletin of mathematical biophysics*, 5(4):115–133, dec 1943.

[174] V. Mieulet and R. F. Lamb. Tuberous sclerosis complex: Linking cancer to metabolism. *Trends in Molecular Medicine*, 16(7):329–335, 2010.

[175] D. R. Miller et al. A bistable, multiport valve enables microformulators creating microclinical analyzers that reveal aberrant glutamate metabolism in astrocytes derived from a tuberous sclerosis patient. *Sens Actuators B Chem*, 341, 2022.

[176] A. G. Mitra and C. Dickerson. Central nervous system tumor with associated unilateral ventriculomegaly: unusual prenatal presentation of subsequently diagnosed tuberous sclerosis. *Journal of Ultrasound in Medicine*, 19(9):651–654, sep 2000.

[177] K. Mizuno et al. Genes associated with the formation of germ cells from embryonic stem cells in cultures containing different glucose concentrations. *Molecular Reproduction and Development*, 73(4):437–445, 2006.

[178] H. Mochizuki, Y. Ohnuki, and H. Kurosawa. Effect of glucose concentration during embryoid body (EB) formation from mouse embryonic stem cells on EB growth and cell differentiation. *Journal of Bioscience and Bioengineering*, 111(1):92–97, jan 2011.

[179] A. V. Molofsky and B. Deneen. Astrocyte Development: A Guide for the Perplexed. *GLIA*, 63:1320–1329, 2015.

[180] B. J. Molyneaux, P. Arlotta, J. R. Menezes, and J. D. Macklis. Neuronal subtype specification in the cerebral cortex. *Nature Reviews Neuroscience*, 8(6):427–437, jun 2007.

[181] J. Montagne et al. Drosophila S6 kinase: A regulator of cell size. *Science*, 285(5436):2126–2129, 1999.

[182] H. Monyer et al. Developmental and regional expression in the rat brain and functional properties of four NMDA receptors. *Neuron*, 12(3):529–540, mar 1994.

[183] R. Moran, D. A. Pinotsis, and K. Friston. Neural masses and fields in dynamic causal modelling. *Frontiers in Computational Neuroscience*, 7, apr 2013.

[184] A. Mühlebner et al. Novel Histopathological Patterns in Cortical Tubers of Epilepsy Surgery Patients with Tuberous Sclerosis Complex. *PLoS ONE*, 11(6):e0157396, 2016.

[185] M. P. Murphy and L. A. O'Neill. Krebs Cycle Reimagined: The Emerging Roles of Succinate and Itaconate as Signal Transducers. *Cell*, 174(4):780–784, aug 2018.

[186] A. G. Nadadhur et al. Neuron-Glia Interactions Increase Neuronal Phenotypes in Tuberous Sclerosis Complex Patient iPSC-Derived Models. *Stem Cell Reports*, 12:42–56, 2019.

[187] T. Namba et al. Time-lapse imaging reveals symmetric neurogenic cell division of GFAP-expressing progenitors for expansion of postnatal dentate granule neurons. *PLoS ONE*, 6(9), 2011.

[188] S. Nidhi et al. Novel crispr–cas systems: An updated review of the current achievements, applications, and future research perspectives. *International Journal of Molecular Sciences*, 22(7), apr 2021.

[189] K. Nishitani, K. Hayakawa, and S. Tanaka. Extracellular glucose levels in cultures of undifferentiated mouse trophoblast stem cells affect gene expression during subsequent differentiation with replicable cell line-dependent variation. *Journal of reproduction and developemt*, 65(1):19–27, 2019.

[190] W. Niu, B. Siciliano, and Z. Wen. Modeling tuberous sclerosis complex with human induced pluripotent stem cells. *World Journal of Pediatrics*, 2022.

[191] S. C. Noctor et al. Neurons derived from radial glial cells establish radial units in neocortex. *Nature*, 409(6821):714–720, feb 2001.

[192] S. C. Noctor, V. Martinez-Cerdeño, L. Ivic, and A. R. Kriegstein. Cortical neurons arise in symmetric and asymmetric division zones and migrate through specific phases. *Nature Neuroscience*, 7(2):136–144, jan 2004.

[193] H. Northrup et al. Updated International Tuberous Sclerosis Complex Diagnostic Criteria and Surveillance and Management Recommendations. *Pediatric Neurology*, 123:50–66, 2021.

[194] H. Northrup et al. Tuberous sclerosis complex diagnostic criteria update: Recommendations of the 2012 international tuberous sclerosis complex consensus conference. *Pediatric Neurology*, 49(4):243–254, oct 2013.

[195] A. Odawara, H. Katoh, N. Matsuda, and I. Suzuki. Physiological maturation and drug responses of human induced pluripotent stem cell-derived cortical neuronal networks in long-term culture. *Scientific Reports*, 6(26181), 2016.

[196] A. Odawara et al. Long-term electrophysiological activity and pharmacological response of a human induced pluripotent stem cell-derived neuron and astrocyte coculture. *Biochemical and Biophysical Research Communications*, 443(4):1176–1181, 2014.

[197] H. Onda et al. Tsc2 null murine neuroepithelial cells are a model for human tuber giant cells, and show activation of an mTOR pathway. *Molecular and Cellular Neuroscience*, 21(4):561–574, 2002.

[198] H. Onda et al. Tsc2+/– mice develop tumors in multiple sites that express gelsolin and are influenced by genetic background. *The Journal of Clinical Investigation*, 104(6):687–695, 1999.

[199] K. A. Orlova and P. B. Crino. The tuberous sclerosis complex. *Ann N Y Acad Sci*, 1184:87–105, 2010.

[200] J. J. Pang, F. Gao, and S. M. Wu. Dual-Cell Patch-Clamp Recording Revealed a Mechanism for a Ribbon Synapse to Process Both Digital and Analog Inputs and Outputs. *Frontiers in Cellular Neuroscience*, 15:1–15, 2021.

[201] M. T. Pankratz et al. Directed Neural Differentiation of Human Embryonic Stem Cells via an Obligated Primitive Anterior Stage. *Stem Cells*, 25(6):1511–1520, jun 2007.

[202] P. Paoletti, C. Bellone, and Q. Zhou. NMDA receptor subunit diversity: impact on receptor properties, synaptic plasticity and disease. *Nature Reviews Neuroscience*, 14(6):383–400, 2013.

[203] S. P. Pas. The rise of three-dimensional human brain cultures. *Nature*, 553(7689):437–445, jan 2018.

[204] S. Pasca, G. Panagiotakos, and R. E. Dolmetsch. Generating Human Neurons In Vitro and Using Them to Understand Neuropsychiatric Disease. *Annual Review of Neuroscience*, 37:479–501, 2014.

[205] I. Pascual-Castroviejo et al. Significance of tuber size for complications of tuberous sclerosis complex. *Neurología (English Edition)*, 28(9):550–557, 2013.

[206] R. Patani et al. Investigating the utility of human embryonic stem cell-derived neurons to model ageing and neurodegenerative disease using whole-genome gene expression and splicing analysis. *Journal of Neurochemistry*, 122(4):738–51, aug 2012.

[207] M. Peitz, J. Jungverdorben, and O. Brüstle. Disease-specific iPS cell models in neuroscience. *Current molecular medicine*, 13(5):832–41, 2013.

[208] W. D. Penny, K. E. Stephan, A. Mechelli, and K. J. Friston. Comparing dynamic causal models. *NeuroImage*, 22(3):1157–1172, 2004.

[209] N. A. Perez-Catalan, C. Q. Doe, and S. D. Ackerman. The role of astrocyte-mediated plasticity in neural circuit development and function. *Neural Development*, 16(1):1–14, jan 2021.

[210] O. A. Petroff. GABA and glutamate in the human brain. *Neuroscientist*, 8(6):562–573, 2002.

[211] J. Poulos. The limited application of stem cells in medicine: a review. *Stem cell research therapy*, 9(1), 2018.

[212] A. S. Prabowo et al. Fetal brain lesions in tuberous sclerosis complex: TORC1 activation and inflammation. *Brain Pathology*, 23(1):45–59, jan 2013.

[213] C. G. Proud. The multifaceted role of mTOR in cellular stress responses. *DNA Repair*, 3:927–934, 2004.

[214] W. Qin et al. Analysis of TSC cortical tubers by deep sequencing of TSC1, TSC2 and KRAS demonstrates that small second-hit mutations in these genes are rare events. *Brain pathology (Zurich, Switzerland)*, 20(6):1096–1105, nov 2010.

[215] M. A. Reid, Z. Dai, and J. W. Locasale. The impact of cellular metabolism on chromatin dynamics and epigenetics. *Nature Cell Biology*, 19(11):1298–1306, 2017.

[216] M. Rigoulet et al. Cell energy metabolism: An update. *Biochimica et Biophysica Acta (BBA) - Bioenergetics*, 1861(11):148276, nov 2020.

[217] J. R. Risner-Janiczek, M. A. Ungless, and M. Li. Electrophysiological Properties of Embryonic Stem Cell-Derived Neurons. *PLoS ONE*, 6(8):24169, 2011.

[218] S. Ritter. Monitoring and Maintenance of Brain Glucose Supply. In R. Harris, editor, *Appetite and Food Intake*, pages 177–204. CRC Press/Taylor Francis, jun 2017.

[219] D. J. Roberts and S. Miyamoto. Hexokinase II integrates energy metabolism and cellular protection: Akting on mitochondria and TORCing to autophagy. *Cell Death and Differentiation*, 22(2):248–257, feb 2015.

[220] A. M. Robitaille et al. Quantitative phosphoproteomics reveal mTORC1 activates de novo pyrimidine synthesis. *Science*, 339(6125):1320–1323, mar 2013.

[221] P. Rocktäschel, A. Sen, and M. Z. Cader. High glucose concentrations mask cellular phenotypes in a stem cell model of tuberous sclerosis complex. *Epilepsy Behavior*, page 106581, nov 2019.

[222] D. C. Rodrigues et al. Methylglyoxal couples metabolic and translational control of Notch signalling in mammalian neural stem cells. *Nature Communications*, 11(1), 2020.

[223] C. Rosset, C. Brinckmann, O. Netto, and P. Ashton-Prolla. TSC1 and TSC2 gene mutations and their implications for treatment in Tuberous Sclerosis Complex: a review. *Genetics and Molecular Biology*, 40(1):69–79, 2017.

[224] D. H. Rowitch. Glial specification in the vertebrate neural tube. *Nature Reviews Neuroscience*, 5(5):409–419, 2004.

[225] L. Roybon et al. Neurogenin2 Directs Granule Neuroblast Production and Amplification while NeuroD1 Specifies Neuronal Fate during Hippocampal Neurogenesis. *PLoS ONE*, 4(3):4779, 2009.

[226] G. Ruffolo et al. Functional aspects of early brain development are preserved in tuberous sclerosis complex (TSC) epileptogenic lesions. *Neurobiology of Disease*, 95:93–101, 2016.

[227] C. Rüschenschmidt, P. G. Koch, O. Brüstle, and H. Beck. Functional properties of ES cell-derived neurons engrafted into the hippocampus of adult normal and chronically epileptic rats. In *Epilepsia*, volume 46, pages 174–183. John Wiley Sons, Ltd, jul 2005.

[228] P. Sampath et al. A Hierarchical Network Controls Protein Translation during Murine Embryonic Stem Cell Self-Renewal and Differentiation. *Cell Stem Cell*, 2(5):448–460, 2008.

[229] O. Sancak et al. Mutational analysis of the TSC1 and TSC2 genes in a diagnostic setting: Genotype-phenotype correlations and comparison of diagnostic DNA techniques in tuberous sclerosis complex. *European Journal of Human Genetics*, 13(6):731–741, jun 2005.

[230] M. A. Saporta, M. Grskovic, and J. T. Dimos. Induced pluripotent stem cells in the study of neurological diseases. *Stem Cell Research Therapy*, 2(37), sep 2011.

[231] R. A. Saxton and D. M. Sabatini. mTOR Signaling in Growth, Metabolism, and Disease. *Cell*, 168(6):960–976, 2018.

[232] T. T. Schwindt et al. Effects of FGF-2 and EGF removal on the differentiation of mouse neural precursor cells. 81(3):443–452, 2009.

[233] S. Sengupta, T. R. Peterson, and D. M. Sabatini. Regulation of the mTOR Complex 1 Pathway by Nutrients, Growth Factors, and Stress. *Molecular Cell*, 40:310–322, 2010.

[234] E. B. Sequerra. Subventricular zone progenitors in time and space: generating neuronal diversity. *Frontiers in Cellular Neuroscience*, 8:1–6, 2014.

[235] C. Settembre et al. A lysosome-to-nucleus signalling mechanism senses and regulates the lysosome via mTOR and TFEB. *The EMBO Journal*, 31:1095–1108, 2012.

[236] Z.-H. Sheng and Q. Cai. Mitochondrial transport in neurons: impact on synaptic homeostasis and neurodegeneration. *Nature Reviews Neuroscience*, 13(2):77–93, 2016.

[237] C. W. SHEPHERD, M. R. GOMEZ, J. T. LIE, and C. S. CROWSON. Causes of Death in Patients With Tuberous Sclerosis. *Mayo Clinic Proceedings*, 66(8):792–796, aug 1991.

[238] Y. Shi, P. Kirwan, and F. J. Livesey. Directed differentiation of human pluripotent stem cells to cerebral cortex neurons and neural networks. *Nature Protocols*, 7(10):1836–1846, 2012.

[239] Y. Shi et al. Human cerebral cortex development from pluripotent stem cells to functional excitatory synapses. *Nature Neuroscience*, 15(3):477–486, mar 2012.

[240] H. Shima et al. Disruption of the p70 s6k /p85 s6k gene reveals a small mouse phenotype and a new functional S6 kinase. *The EMBO Journal*, 17(22):6649–6659, 1998.

[241] A. Shimbel and A. Rapoport. A statistical approach to the theory of the central nervous system. *The bulletin of mathematical biophysics*, 10(1):41–55, mar 1948.

[242] M. Shimobayashi and M. N. Hall. Making new contacts: the mTOR network in metabolism and signalling crosstalk. *Nature Reviews Molecular Cell Biology*, 15:155–162, 2014.

[243] S. A. Sloan et al. Human Astrocyte Maturation Captured in 3D Cerebral Cortical Spheroids Derived from Pluripotent Stem Cells. *Neuron*, 95(4):779–790.e6, aug 2017.

[244] J. F. Smythe, J. D. Dyck, J. F. Smallhorn, and R. M. Freedom. Natural history of cardiac rhabdomyoma in infancy and childhood. *American Journal of Cardiology*, 66(17):1247–1249, nov 1990.

[245] J. J. Soghomonian and D. L. Martin. Two isoforms of glutamate decarboxylase: Why? *Trends in Pharmacological Sciences*, 19(12):500–505, dec 1998.

[246] F. Soldner and R. Jaenisch. iPSC disease modeling. *Science*, 338(6111):1155–1156, nov 2012.

[247] A. A. Sosunov et al. Epileptogenic but MRI-normal perituberal tissue in Tuberous Sclerosis Complex contains tuber-specific abnormalities. *Acta neuropathologica communications*, 3:17, apr 2015.

[248] A. A. Sosunov et al. Tuberous sclerosis: A primary pathology of astrocytes? *Epilepsia*, 49(s2):53–62, jan 2008.

[249] O. Sporns. Brain connectivity. *Scholarpedia*, 2(10):4695, 2007.

[250] K. E. Stephan et al. Ten simple rules for dynamic causal modeling. *NeuroImage*, 49(4):3099–3109, 2010.

[251] K. E. Stephan et al. Dynamic causal models of neural system dynamics: Current state and future extensions. *Journal of Biosciences*, 32(1):129–144, 2007.

[252] M. Sundberg and M. Sahin. Modeling Neurodevelopmental Deficits in Tuberous Sclerosis Complex with Stem Cell Derived Neural Precursors and Neurons. In *Advances in Neurobiology*, volume 25, pages 1–31. Springer, 2020.

[253] M. Sundberg et al. Purkinje cells derived from TSC patients display hypoexcitability and synaptic deficits associated with reduced FMRP levels and reversed by rapamycin. *Molecular Psychiatry*, 23(11):2167–2183, 2018.

[254] E. N. Suspitsin et al. Pattern of TSC1 and TSC2 germline mutations in Russian patients with tuberous sclerosis. *Journal of Human Genetics*, 63(5):597–604, may 2018.

[255] M. Symmonds et al. Ion channels in EEG: isolating channel dysfunction in NMDA receptor antibody encephalitis. *Brain*, 141:1691–1702, 2018.

[256] K. Takahashi and S. Yamanaka. Induction of Pluripotent Stem Cells from Mouse Embryonic and Adult Fibroblast Cultures by Defined Factors. *Cell*, 126(4):663–676, aug 2006.

[257] K. Tamaki et al. Regional cerebral blood flow in relation to MRI and EEG findings in tuberous sclerosis. *Brain and Development*, 13(6):421–425, 1991.

[258] O. A. Tarazona and O. Pourquie. Exploring the Influence of Cell Metabolism on Cell Fate through Protein Post-translational Modifications. *Developmental Cell*, 54(2):282–292, 2020.

[259] J. Tchieu et al. NFIA is a gliogenic switch enabling rapid derivation of functional human astrocytes from pluripotent stem cells. *Nature Biotechnology*, 37:267–275, 2019.

[260] A. R. Tee et al. Tuberous Sclerosis Complex Gene Products, Tuberin and Hamartin, Control mTOR Signaling by Acting as a GTPase-Activating Protein Complex toward Rheb. *Current Biology*, 13:1259–1268, 2003.

[261] A. Thapar, M. Cooper, and M. Rutter. Neurodevelopmental disorders. *The Lancet Psychiatry*, 4(4):339–346, apr 2017.

[262] J. A. Thomson et al. Embryonic stem cell lines derived from human blastocysts. *Science*, 282(5391):1145–7, nov 1998.

[263] T. Tian et al. Neuroprotective effects of orientin on oxygen-glucose deprivation/ reperfusion-induced cell injury in primary culture of rat cortical neurons. *Experimental Biology and Medicine*, 243:78–86, 2018.

[264] M. Trawczynski, G. Liu, B. T. David, and R. G. Fessler. Restoring Motor Neurons in Spinal Cord Injury With Induced Pluripotent Stem Cells. *Frontiers in Cellular Neuroscience*, 13, aug 2019.

[265] I. K. Trombley and S. S. Mirra. Ultrastructure of tuberous sclerosis: Cortical tuber and subependymal tumor. *Annals of Neurology*, 9(2):174–181, feb 1981.

[266] TSA (The Tuberous Sclerosis Association). What is TSC?, 2022.

[267] M. Uhlen. The Human Protein Atlas - Hexokinase 2, 2023.

[268] M. Uhlen. The Human Protein Atlas - LDHB, 2023.

[269] E. J. Uhlmann et al. Astrocyte-specific TSC1 conditional knockout mice exhibit abnormal neuronal organization and seizures. *Annals of Neurology*, 52(3):285–296, 2002.

[270] K. Urbańska and A. Orzechowski. Unappreciated Role of LDHA and LDHB to Control Apoptosis and Autophagy in Tumor Cells. *International journal of molecular sciences*, 20(9), may 2019.

[271] J. Van Den Ameele and A. H. Brand. Neural stem cell temporal patterning and brain tumour growth rely on oxidative phosphorylation. *eLife*, 8, sep 2019.

[272] E. Vander Haar et al. Insulin signalling to mTOR mediated by the Akt/PKB substrate PRAS40. *Nature Cell Biology*, 9(3):316–23, 2001.

[273] T. J. Veersema et al. Changes in vascular density in resected tissue of 97 patients with mild malformation of cortical development, focal cortical dysplasia or TSC-related cortical tubers. *International Journal of Developmental Neuroscience*, 79:96–104, dec 2019.

[274] T. J. Veersema et al. 7 tesla T 2 *-weighted MRI as a tool to improve detection of focal cortical dysplasia. *Epileptic Disord*, 18(3):315–338, 2016.

[275] S. Velasco et al. Individual brain organoids reproducibly form cell diversity of the human cerebral cortex. *Nature*, 570(7762):523–527, jun 2019.

[276] I. Vercellino and L. A. Sazanov. The assembly, regulation and function of the mitochondrial respiratory chain. *Nature Reviews Molecular Cell Biology*, 23(2):141–161, oct 2021.

[277] T. Vierbuchen et al. Direct conversion of fibroblasts to functional neurons by defined factors. *Nature*, 463(7284):1035–1041, feb 2010.

[278] V. Volpato et al. Reproducibility of Molecular Phenotypes after Long-Term Differentiation to Human iPSC-Derived Neurons: A Multi-Site Omics Study. *Stem Cell Reports*, 11(4):897–911, oct 2018.

[279] T. Wälchli et al. Shaping the brain vasculature in development and disease in the single-cell era. *Nature Reviews Neuroscience*, 24(5):271–298, 2023.

[280] B. Wang et al. Nogo-66 promotes the differentiation of neural progenitors into astroglial lineage cells through mTOR-STAT3 pathway. *PLoS ONE*, 3(3), 2008.

[281] Q. Wang, L. Yang, and Y. Wang. Enhanced differentiation of neural stem cells to neurons and promotion of neurite outgrowth by oxygen–glucose deprivation. *International Journal of Developmental Neuroscience*, 43(1):50–57, jun 2015.

[282] H. R. Wilson and J. D. Cowan. EXCITATORY AND INHIBITORY INTERACTIONS IN LOCALIZED POPULATIONS OF MODEL NEURONS. *Biophysical Journal*, 12:1–24, 1972.

[283] J. E. Wilson. Hexokinases. *Reviews of physiology, biochemistry and pharmacology*, 126:65–198, 1995.

[284] S. W. Wilson and C. Houart. Early Steps in the Development of the Forebrain. *Developmental Cell*, 6(2):167–181, 2004.

[285] K. D. Winden et al. Biallelic Mutations in TSC2 Lead to Abnormalities Associated with Cortical Tubers in Human iPSC-Derived Neurons. *The Journal of neuroscience : the official journal of the Society for Neuroscience*, 39(47):9294–9305, 2019.

[286] P. Wintermark et al. Perfusion imaging of focal cortical dysplasia using arterial spin labeling: Correlation with histopathological vascular density. *Journal of Child Neurology*, 28(11):1474–1482, 2013.

[287] A. Wolf et al. Hexokinase 2 is a key mediator of aerobic glycolysis and promotes tumor growth in human glioblastoma multiforme. *The Journal of Experimental Medicine*, 208(2):313–326, 2011.

[288] M. Wong. Mammalian target of rapamycin (mTOR) pathways in neurological diseases. *Biomedical journal*, 36(2):40–50, mar 2013.

[289] M. Wong and P. B. Crino. Tuberous sclerosis and epilepsy: Role of astrocytes. *Glia*, 60(8):1244–1250, aug 2012.

[290] H. Wu et al. Central role of lactic acidosis in cancer cell resistance to glucose deprivation-induced cell death. *Journal of Pathology*, 227(2):189–199, 2012.

[291] L. Xu, L.-H. Zeng, and M. Wong. Impaired Astrocytic Gap Junction Coupling and Potassium Buffering in a Mouse Model of Tuberous Sclerosis Complex. *Neurobiology of disease*, 34(2):291–9, 2009.

[292] D. X. Yu, M. Marchetto, and F. Gage. Therapeutic Translation of iPSCs for Treating Neurological Disease. *Cell Stem Cell*, 12(6):678–688, 2013.

[293] M. Ždralević et al. Double genetic disruption of lactate dehydrogenases A and B is required to ablate the "Warburg effect" restricting tumor growth to oxidative metabolism. *The Journal of biological chemistry*, 293(41):15947–15961, oct 2018.

[294] L.-H. Zeng et al. ABNORMAL GLUTAMATE HOMEOSTASIS AND IMPAIRED SYNAPTIC PLASTICITY AND LEARNING IN A MOUSE MODEL OF TUBEROUS SCLEROSIS COMPLEX. *Neurobiol Dis*, 28(2):184–196, 2007.

[295] L.-H. Zeng, L. Xu, D. H. Gutmann, and M. Wong. Rapamycin Prevents Epilepsy in a Mouse Model of Tuberous Sclerosis Complex. *Ann Neurol*, 63:444–453, 2008.

[296] X. Zha et al. Lactate Dehydrogenase B Is Critical for Hyperactive mTOR-Mediated Tumorigenesis. *Cancer Research*, 71(1), 2011.

[297] F. Zhang, Y. Wen, and X. Guo. CRISPR/Cas9 for genome editing: Progress, implications and challenges. *Human Molecular Genetics*, 23(R1):R40–R46, sep 2014.

[298] L. Zhang et al. Small molecules efficiently reprogram human astroglial cells into functional neurons HHS Public Access. *Cell Stem Cell*, 17(6):735–747, 2015.

[299] S. Zhang, B. B. Lachance, M. P. Mattson, and X. Jia. Glucose metabolic crosstalk and regulation in brain function and diseases. *Progress in Neurobiology*, 204:102089, sep 2021.

[300] Y. Zhang et al. Rapid Single-Step Induction of Functional Neurons from Human Pluripotent Stem Cells. *Neuron*, 78(5):785–798, 2013.

[301] X. Zheng et al. Metabolic reprogramming during neuronal differentiation from aerobic glycolysis to neuronal oxidative phosphorylation. *eLife*, 5:e13374, 2016.

[302] J. Zhu and C. B. Thompson. Metabolic regulation of cell growth and proliferation. *Nature reviews. Molecular cell biology*, 20(7):436–450, jul 2019.

[303] T. S. Zimmer et al. Tuberous Sclerosis Complex as Disease Model for Investigating mTOR-Related Gliopathy During Epileptogenesis. *Frontiers in Neurology*, 11:1–18, 2020.

[304] A. J. Zucco et al. Neural progenitors derived from Tuberous Sclerosis Complex patients exhibit attenuated PI3K/AKT signaling and delayed neuronal differentiation. *Molecular and Cellular Neuroscience*, 92:149–163, oct 2018.